



A University of Sussex DPhil thesis

Available online via Sussex Research Online:

<http://sro.sussex.ac.uk/>

This thesis is protected by copyright which belongs to the author.

This thesis cannot be reproduced or quoted extensively from without first obtaining permission in writing from the Author

The content must not be changed in any way or sold commercially in any format or medium without the formal permission of the Author

When referring to this work, full bibliographic details including the author, title, awarding institution and date of the thesis must be given

Please visit Sussex Research Online for more information and further details

University of Sussex

School of Engineering and Informatics

On the Dynamic Analysis of Engineering Structures with
High and Low Level Random Uncertainties

A Thesis

Submitted in Accordance with the Requirements

for the Degree of Doctor of Philosophy

by

Thana Cheepsomsong

Sep 2014

Abstract

The ability to predict the effect of dimension and thickness variability on the dynamic response of realistically uncertain engineering structures is examined in this thesis. Initially, available methods for predicting key response statistics and probabilities, for both low and high frequencies are examined to establish their strengths and limitations for specified levels of random dimension variability. For low frequency applications, the ability of Direct Integration (DI) and the First-Order Reliability Method (FORM) to predict exceedance probability is examined. For high frequency applications, the ability of the methods of Statistical Energy Analysis (SEA) and DI to predict the mean and standard deviation of the energy response is examined.

The use of Extreme Value (EV) theory is included as a way to bound responses using simulated or measured responses. The strengths and limitations of Monte Carlo simulation methods are explored for both low and high frequency responses of randomly uncertain structures using both simple mode superposition plate-structure solutions and (commercially available) finite element solutions for coupled plate structures.

To address, without the need to undertake expensive Monte Carlo simulation, the problem of predicting response bounds for structures with varying levels of uncertainty, a novel DI-EV method is developed and examined. It is tested first on a simple plate structure, then on a coupled plate structure, with low-level and high-level random dimension and thickness uncertainty. In addition, the method is compared with the SEA-EV method.

The thesis shows that the results from the existing SEA-EV bounding approach gives good bounds only at particular frequencies and mainly for low levels of dimension variability. In contrast, the proposed DI-EV bounding approach compare extremely well with Monte Carlo simulations, which is not only at all frequencies but also with both low-level and high-level uncertainties, for simple and coupled plate structures with dimension and thickness variation.

Declaration

This research has been carried out in the Department of Engineering and Design, School of Engineering and Informatics, at the University of Sussex. I hereby declare that this thesis has not been submitted, either in the same or different form, to this, or any other University for a degree.

.....

Thana Cheepsomsong

Date.....

Acknowledgments

I would like to express my gratitude to my enthusiastic supervisor, Dr. J. F. DUNNE, whose expertise, understanding, encouragement and patience supported my graduate experience during this research.

I would sincerely like to thank Prof. R. S. Langley for his suggestions on how to improve this work.

I wish to express my sincere gratitude to Faculty of Engineering at Kamphaeng Saen Kasetsart University, Thailand for the financial support.

I would like to express my heartfelt thanks to my beloved wife, Ting, who was always beside me; my parents, Mom and Dad, for their many blessings, help, and best wishes for the successful completion of this research.

Special thanks to my uncle, Suwan, and Thai Café & Restaurant, London SW1V 2DY for providing me with superb food and accommodation.

Thanks also to my friend, Tik, for his help, and to also all my friends for advice and kindness to me.

Finally, thanks to Buddha.

Table of Contents

Abstract	i
Declaration	ii
Acknowledgments	iii
Abbreviations	vii
Nomenclature	viii
1 Introduction	1
1.1 Literature Survey.....	3
1.2 The Objectives of the Thesis.....	11
1.3 Outline of the Thesis	11
2 Theories for Predicting the Statistical Response of Uncertain Structures	15
2.1 Direct Integration Method (DI).....	15
2.2 First Order Reliability Method (FORM)	16
2.3 Statistical Energy Analysis (SEA)	18
2.3.1 Coupling Loss Factor (CLF)	19
2.3.2 Transmission Coefficient	19
2.3.3 Modal Density	27
2.3.4 Power Input	27
2.3.5 Variance of the Energy	28
2.3.6 Statistical Overlap Factor (SOF)	29
2.4 Extreme Value Theory (EV).....	29
2.4.1 Calibration of EV Parameters Using Monte Carlo Simulation Data or Measurement	30
2.4.2 Finite Sample Extreme Value Distributions.....	31
2.5 Monte Carlo Simulation Methods.....	32

2.5.1	Confidence Intervals	33
2.6	A Summary of the Findings of Chapter 2.....	34
3	Low Frequency Response of Simple Structures with High and Low-Level Uncertainties	35
3.1	Low Frequency Models with Parametric Uncertainty	35
3.2	Application of Direct Integration, FORM, and Monte Carlo Simulation	35
3.2.1	Single Degree of Freedom Model.....	36
3.2.2	Two Degree of Freedom Model	45
3.2.3	Three Degree of Freedom Model	53
3.3	Conclusions of Chapter 3.....	59
4	High Frequency Response Prediction for Simple Structures with High and Low-Level Uncertainties	60
4.1	A Single Plate Model.....	61
4.1.1	The SEA Model.....	61
4.1.2	Mode Superposition Method.....	64
4.1.3	Dimension Variation.....	66
4.1.4	Thickness Variation.....	68
4.1.5	Statistical Overlap Factor of a Simple Plate.....	72
4.1.6	Ratio Between Energy Variances from Monte Carlo Simulation and SEA.....	77
4.1.7	Evolution of pdf of Energy.....	81
4.2	Conclusions of Chapter 4.....	84
5	High frequency analysis of coupled plate structures with high and low-level uncertainties	86
5.1	L-Shaped Plate	87
5.1.1	The SEA Model.....	87
5.1.2	FE Solution Methodology (via ANSYS)	91
5.1.3	Dimension Variation.....	92

5.1.4	Thickness Variation	96
5.1.5	Evolution of Pdf of Energy	100
5.2	Conclusions of Chapter 5.....	105
6	A Novel Extreme-Value-based bounding Method for uncertain structures	106
6.1	The Basis of the Proposed Bounding Method	107
6.2	Calculating the Mean and Standard Deviation of the Spatially-averaged Response Energy via Direct Integration.....	112
6.3	Bounding via the SEA-EV Method and the New DI-EV Method.....	115
6.4	Conclusions of Chapter 6.....	116
7	Application of DI-EV and SEA-EV Bounding Predictions	117
7.1	Mean and Standard Deviation Predictions Using DI	117
7.2	Application of DI-EV and SEA-EV Bounding Methods.	140
7.2.1	Simple Structure: a Single Plate	140
7.2.2	Built-Up Structure: an L-Shaped Plate	146
7.3	Conclusions of Chapter 7.....	151
8	Conclusions	153
	References	155
	Appendix A	160
	Appendix B	165

Abbreviations

CV	Coefficient of Variation, defined as the ratio of the standard deviation to the mean (σ/μ)
DEA	Dynamical Energy Analysis
DI	Direct Integration
DOF	Degree Of Freedom
DSC	Discrete Singular Convolution
EV	Extreme Value Theory
FEA	Finite Element Analysis
FEM	Finite Element Method
FRF	Frequency Response Function
FORM	First Order Reliability Method
GEV	Generalised Extreme Value distribution
GOE	Gaussian Orthogonal Ensemble
pdf	Probability Function
SEA	Statistical Energy Analysis
SOF	Statistical Overlap Factor

Nomenclature

$ \cdot $	Determinant/Absolute value
$\langle \cdot \rangle$	Ensemble average
A	Area
\mathbf{a}	Edge displacements of the plate carrying incident wave vector
\mathbf{b}	Edge displacements vector
B'	Bandwidth
\mathbf{b}'	Edge displacements vector
C	Damp
c	Group speed
c_ϕ	Phase speed
D	Bending stiffness
E	Energy
E	Young's modulus
$E[\cdot]$	Ensemble average/Expected value
\tilde{E}	Exponential integral function
\hat{E}	Modal energy
F	force
\mathbf{F}, \mathbf{F}'	Force vector
\mathbf{f}	Dynamic loading vector
$f_{N(0,1)}$	Standardised normal probability density function
f_{χ^2}	Chi-square probability density function
$g(z)$	Failure surface with normalised variable z
h	Thickness
i	Imaginary unit/Index
j	Index
K	Spring constant
\mathbf{K}	Dynamic stiffness matrix
k	Wave number/Index
k_B	Bending wave number

k_L	Longitudinal wave number
k_S	Shear wave number
M, M'	Force at the connected edge of plate in z direction
m	Mass
m'	Modal overlap factor
N, N'	Moment at the connected edge of plate
N	The number of samples/ The number of plates
n	Modal density/Degree of freedom
$N(0,1)$	Standard normal distribution
p	Index
P_F	Probability of failure
\mathbf{P}_{in}	Power input vector
P_{in}	Power input
$\Pr\{\cdot\}$	Probability
\mathbf{R}	Matrix \mathbf{R}
r	Wave type r (r can be B, L, and S)/Index
r^2	Function r^2
Re	Real part
S, S'	Force at the connected edge of plate in y direction
S	Sample standard deviation
s	Index
T	Force at the connected edge of plate in x direction
t	Time
T'	Force at the connected edge of plate in x direction
T_F	The number of times that failure level is exceeded
u	Displacement in x direction
u_e	Edge displacement in x direction
v	Displacement in y direction
v_e	Edge displacement in y direction
$\text{Var}(\cdot)$	Variance
w	Displacement in z direction
w_e	Edge displacement in z direction

\bar{X}	Sample mean value of X
x_{limit}	Exceedance level
Y	Mobility
Z	Impedance
α	Wave amplitude
α'_k	Non-SEA parameter constant
α'_{ks}	Coupling coefficients
β	reliability index
η	Coupling/damping loss factor
θ	Angle of plate
θ_e	Edge moment
μ	Mean value
$\boldsymbol{\mu}$	Wave number
$\hat{\mu}$	Mean estimate
ν	Poisson ratio
ρ	Mass per unit area
Σ	Covariance matrix
σ	Standard deviation
σ^2	Variance
σ_E	Standard deviation of the energy
σ_{ω_n}	Standard deviation of the natural frequency mode n th
σ_X	Standard deviation of X
τ	Transmission coefficient
Φ	Standard (one-dimensional) normal distribution function
ϕ	Incident wave angle
χ^2	Chi-square variable
Ω	Failure surface
Ω_f	Failure region
Ω_s	Safe region
ω	Angular frequency
ω_n	The natural frequency mode n th
∇	Gradient

Chapter 1

Introduction

Uncertainty in engineering structures is of significant importance in many areas of design including automotive, aerospace, and marine structures. Automotive vehicles for example, require ever better fuel economy, higher efficiency, improved performance, and reduced cost. Therefore vehicle-bodies need to be strong, but light-weight. However 'light-weight' vehicles can suffer from vibration problems, making the analysis of vibration a vital part of vehicle-body design. The problem is how to predict the dynamic response, since manufacturing variability, assembly, and structural properties, combine to make a vehicle-body uncertain. Similar sources of uncertainty arise in other types of engineering structure, and also giving rise to complicated design issues.

Uncertainty in engineering structures can be modelled in several different ways including deterministically, in a fuzzy sense, and statistically (Langley, 2000; Clough 2003; Mace, 2005; Anderson and Naeim, 2012). The main focus in this thesis is to progress statistical modelling and analysis methods.

There are many approaches available to predict the response statistics and probabilities of uncertain structures specifically at either low or high frequency. Successful methods for prediction in the mid frequency region are fewer and still the subject of research (Secgin et al, 2012). At low frequency, the Direct Integration method (DI) (Kreyszig, 1994), and the First Order Reliability Method (FORM) (Breitung and Faravelli, 1996; Madsen et al, 2006), are able to quantify the effect of random parameters. But there are limitations to the application of this method in terms of the number of uncertain parameters that can be handled. The more uncertain parameters there are, the more complex the analysis. At high frequency, Statistical Energy Analysis (SEA), (Lyon and Dejong, 1995; Langley and Cotoni, 2004), is the best approach available, but neither the mean response level, or the standard deviation, which are typically available from SEA, are sensitive to changes in the uncertain parameter levels even though the levels of uncertainty in manufacturing processes or assembly, are not the same. In some applications the level of variability in terms of the coefficient of variation (CV) defined

by the ratio of the standard deviation to the mean, may be below 1%, whereas in other applications, such as turbine blade manufacture, the level of variability may be very much higher i.e. 25% (Moeckel, 2006).

The response statistics at low frequency by contrast, may be well predicted via the Finite Element Method (FEM) (Rao, 2004). The FEM is the most commonly used deterministic method to analyse the structural vibration characteristics of complex structures. This technique splits the structure into a mesh of discrete elements, and describes the elastic strain and kinetic energy of these elements in terms of displacements and their time derivatives. Rayleigh's variation principle can then be used to calculate mode shapes and natural frequencies (Rao, 2004). This method however suffers from the problem that the subsection dimensions of the mesh needed, becomes increasingly small at higher frequencies in order to describe accurately the variation of the modal displacement. In order to predict the dynamic response of a system, the FEM might be used within a Monte Carlo procedure applied to the system by assuming a specific probability distribution for each of the random parameters involved, and then using a deterministic computational procedure to generate the response of each member of the ensemble. This however is normally impractical, both owing to the computational expense involved, and also because of the inability to correctly model the multidimensional joint PDFs for all the variables that are likely to be involved.

Monte Carlo simulation (for example based on finite element solutions) is able to quantify response means and standard deviations with both high and low-level uncertain parameters. But simulation generally takes considerable computation time even for simple structural responses with a small number of uncertain parameters. In general, real structures have most complexity in geometry, and typically have a very large number of uncertain parameters. The computation time needed to repeat the analysis many hundreds of times or more, is a very major problem, even at low frequency. With increasing frequency, the problem rapidly becomes intractable for realistic built-up structures.

The goal of this thesis is to develop an approach that can predict accurate response bound for varying levels of uncertainty without the need to undertake expensive Monte Carlo simulation. In handling varying levels of uncertainty, it is evident that available

methods are still in the state of development. To assess the state of the art, a literature review is therefore appropriate.

1.1 Literature Survey

This section reviews some of the published work relating to various approaches to the prediction of the dynamic response of uncertain structures. Uncertainty affecting the system depends to a large extent on the frequency range. There are conventionally three different frequency regions identified for predicting the dynamic response, categorized as: low frequency, mid frequency, and high frequency. The methods for predicting the effect of uncertainty within a suitable frequency range are reviewed below according to this classification.

Low Frequency Uncertain Dynamics

At low frequency, a structure gives the response typically in only the first few modes. This means that the response is typically described by natural frequencies. Over the past decades, several probabilistic and non-probabilistic methods have been in use for analysing the dynamics of structures with uncertain structural parameters at low frequency.

Benaroya and Rehak (1988) demonstrated the stochastic finite element method in assessing the response statistics. A random field of material properties or forces was discretised. The resulting system of equations involving random variables was transformed into a system of deterministic equations by a perturbation technique. The zeroth-order equation represented the unperturbed response, and the higher-order equations represented the effects of the randomness. In this manner, the accuracy of the response statistics depends on the order of the perturbation expansion, and whether the uncertainty in the structural parameters is not too large.

Manohar and Ibrahim (1999) showed how the extent of the uncertainty affects the eigensolutions of perturbation equations. The rates of change of the response were examined by varying structural parameters. It was found that the first-order approximation is only valid for relatively small perturbations.

Langley (2000) described the reliability method, which, unlike the perturbation method, is non-probabilistic. In this method, the variables are transformed into uncorrelated zero-mean unit standard Gaussian random variables. The limit state surface is constructed to represent an undesirable level of response. The distance between the origin and the point on the surface closest to it, designated the design point, represents the failure probability. If at the design point, the surface is subject to linear approximation, the method is considered to be a first-order method. If the curvature of the surface is taken into account, the method is of second order. The author shows through the concept of safety factors, the mathematical equivalence between the ‘possibilistic’ and the probabilistic methods.

Manson (2005) develops a method called ‘complex affine analysis’, an alternative to complex interval analysis, which is a non-probabilistic approach to look at the propagation of the upper and lower bounds as a result of uncertainty. By means of this alternative method, the author examines uncertainty propagation for a simple lumped-mass model with varying mass, stiffness, and damping parameters, and obtains the FRFs.

De Gerssem et al (2005) use the interval approach for a wide range of structures. First, with a clamped-plate structure having uncertain boundary conditions, the authors show that the approach is conservative when tested against Monte Carlo results. Second, for an aircraft wing structure, the authors show the usefulness of the eigenvalue interval correction. The structural parameters are the thickness of the viscoelastic layer, the stiffness of the wing/fuselage connection, and the Young's modulus value of the wing material. Third, with the previous wing structure, the interval approach is found to be conservative in giving resonance peaks, compared with a vertex analysis approach. Fourth, the authors demonstrate the use of the interval approach to analyse a telescope baffle-cover, with six uncertain parameters.

Donders et al (2005) created the short transformation method to predict the FRFs of dynamic structures. It is a deterministic approach designed to be less computationally expensive than the reduced transformation method, where the number of model runs grows with the number of uncertain parameters. It is also designed to avoid the over-estimation issues related to interval arithmetic when evaluating the effects of the uncertainty. The short transformation method is tested against Monte Carlo simulation

for two models: a clamped plate, and a car front cradle, both of which have three uncertain parameters. It is found that with fewer computations the performance is however not compromised.

Moens and Hanss (2011) present an overview of advances in interval and fuzzy finite element analysis. For the former, two approaches exist. First, the prediction of intervals for the response quantities, natural frequencies, mode shapes, and FRFs, is given by the specification of input parameters as interval variables, and minimum and maximum possible values. Second, the response bounds are determined from optimization involving multiple solutions. This is non-intrusive, so it becomes a generic approach for interval finite element analysis. However, it is too computationally expensive to be feasible for engineering applications, and therefore, requires other methods to help reduce the number of re-analyses. In the fuzzy finite element analysis, the degree of possibility of a certain value of a parameter, is made into a level of ‘membership’, then, several levels of membership are fed into a series of interval analyses.

Arnoux et al (2012) studied automotive vehicles consisting of both stiff and flexible parts. Such dynamically sensitive structures have high modal density in the low-frequency region, and exhibit classical global elastic modes in the low-frequency range along with huge local elastic modes. The modes can be separated by first decomposing the domain of the structure into subdomains, then from the subdomains, formulating an adapted generalised eigenvalue problem. This is then solved to obtain an adapted vector basis, from which, a stochastic, reduced-order computational dynamical model, adapted to the low-frequency range, can be constructed. The results are in good agreement with the objectives of the work, which includes the construction of a model with very low dimension, capable of predicting frequency responses in the low-frequency range.

The methods described above are for low frequency uncertain dynamics. For the high frequency uncertain dynamics different methods are needed. These methods are reviewed in the following section.

High Frequency Uncertain Dynamics

Higher frequency structural responses correspond to short wavelengths that are much smaller than the structure dimensions. At high frequencies, the variation in response is

more sensitive to changes in structural parameters because of increasing modal overlap. In the alternative approach considered shortly, the randomness is assumed to be high enough such that full statistical knowledge of the parameters is not necessary. The variation across the ensemble is instead assumed to be high enough that the statistical overlap factor is greater than one. The higher the excitation frequency, the more likely this becomes true. Such systems may then be examined by a general approach known as statistical energy analysis (SEA).

SEA is a statistical method, as opposed to a deterministic method like the FEM. It is particularly applicable to structures consisting of complex, coupled components. The FEM is a nominally exact method, so it becomes impractical at high frequencies. SEA looks at the asymptotic behaviour of the structural response at high frequencies, like the ensemble average FRF. The vibrational or acoustical energies constituting the degrees of freedom of an SEA system, are considered in the time-averaged steady-state form. With this, and the splitting of the SEA system into several subsystems, the analysis can be made much less computationally expensive.

As a statistical method, SEA includes some estimates of ensemble variance, and confidence intervals. Cotoni et al (2005) validates variance estimates using a SEA model to predict the mean energy level for ensembles of structures with random properties. Experimentally, the randomisation is the addition of small point masses to the structure at random locations. In SEA, the authors assume that the natural frequency distributions of the split subsystems obey the Gaussian orthogonal ensemble (GOE) statistics. Variance estimates from both experiments and numerical simulations, are found to agree with exact calculation of the variance.

Pradlwarter and Schueller (2005) found that SEA is appropriate only when substructures are weakly coupled. In examining the energy response of a discrete model of a structure, they use deterministic modal analysis to find subsystem kinetic energies, which eventually lead to the structure's energy distribution model. The model shows similar form to the inverse of a SEA model, but does not seem to carry its limitations. In the modal analysis approach, the representation of the coupling between substructures is not too inaccurate, so the estimates are acceptable even without accurate eigenfrequencies and mode shapes. Variation of eigenfrequencies and mode shapes do not quite affect substructure energies, because the summation is carried out over the

frequency range and the domain of the substructure. It is argued that the amount by which the coupling between substructures (and subsequently the power flow) are influenced by uncertain structural properties, could be examined by Monte Carlo simulation.

Le Bot and Cotoni (2010) showed the validity of SEA on the basis of geometry of surfaces in the space of dimensionless parameters (obtained from a dimensional analysis of the equations governing the model concerned). This work examined with the equivalence between two sets of four dimensionless parameters. The set of SEA parameters is the mode count, modal overlap, normalized attenuation factor, and coupling strength, while the ‘primary’ set of parameters is the frequency, damping loss factor, shape, and transmission efficiency. The validity domain of SEA is demonstrated by the validity diagrams for a pair of rectangular plates coupled along the edge. Only one plane of the domain of validity can be focused on, for it contains the low frequency limit of SEA and all the conditions of validity. Some other assumptions such as the nature of the excitation, and the problem of variance, have been excluded.

Langley (2011) demonstrates how to predict the mean and variance of responses from a random built-up system at high frequency without knowledge of the statistics of the underlying system uncertainty. A random matrix is constructed from structural dynamics problems, and the statistics of its eigenvalues are considered, where the eigenvalues are the squares of the system natural frequencies. The statistics of neighbouring natural frequencies are independent of both the type of the system concerned and how the system is randomised. The key to this work is the joint probability density function of the eigenvalues, or alternatively a series of functions introduced independently within the random matrix theory and random point process theory. The work shows that if the random matrix exhibits the Vandermonde determinant, the universal eigenvalue statistics will be present, and the response statistics can be obtained by SEA. The theory is tested with a single structural component, e.g. a beam and a plate where the damping is uniformly distributed and the mode shapes are not localized. The theory is extended to built-up structures. The results demonstrate the ability of the theory.

SEA can be viewed as a low-resolution ray-tracing algorithm. Dynamical energy analysis (DEA) gives a better algorithm by including ray dynamics and interpolation

towards full ray-tracing treatment. DEA can predict vibrational energy distributions in complex vibro-acoustic structures at high frequencies. David et al (2012) show that DEA is reliable, highly versatile, and efficient. In one case, they examine two subsystems with a complex interface: aluminium plates connected by an aluminium beam. At high frequencies, they model the beam using Timoshenko beam theory, and estimate the reflection and transmission probabilities by means of the hybrid FE/WFE approach (Ichchou et al, 2009). Having complex interface means having a greater degree of separation. Vibrational energy distributions are then predicted under the DEA framework, and compared with simple open interface problems. As the complex interface produces a greater degree of separation between the subsystems, good approximations for low-order implementations of DEA are achieved.

Burroughs et al (1997), Lyon and Dejong (1995), and Langley (1999) give general introductions to SEA. Bremner (1999) develops commercial SEA computer packages.

Mid Frequency Uncertain Dynamics

Mid frequencies are too high for deterministic methods but too low for statistical methods. For the latter, several SEA modelling conditions cannot be assumed to hold, including high modal density and weak coupling. SEA exploits the balancing power flow between subsystems, which is through coupling loss factors proportional to subsystem energies. All analytical, semi-infinite system impedances give transmission coefficients, which in turn give subsystem CLFs (Lyon and Dejong, 1995). For deterministic methods like the FEM, the unknown parameters are too numerous for the computation of frequency response functions to be possible. In analysing mid-frequency vibrations, small variation in geometry and material properties leads to large changes in modal characteristics. Hybrid FE-SEA techniques are required.

One way is to decompose a structure into deterministic and statistical components depending on specific wavelengths. Shorter and Langley (2005) develop a hybrid FE-SEA method for coupling FE and SEA based on wave concepts. SEA is used to examine bending waves of the flexible members, whereas FE is used to model the in-plane flexible and stiff members. Separation of modes for complex members may require numerical evaluation. The following publications are some examples of the subsequent use of hybrid FE-SEA techniques.

Charpentier (2006) predicts a car response by analysing stiff components with FE, and modally-dense components with SEA. He also shows how detailed FE models are used to improve SEA descriptions of car panels and couplings.

Cotoni et al (2007) analyse the performance of hybrid FE-SEA method in predicting the ensemble average response. Hybrid FE-SEA method associates a direct field dynamic stiffness matrix with each SEA subsystem. To build a hybrid FE-SEA model, the system needed to be partitioned into deterministic and statistical parts. This partitioning is based on the wavelengths within various components of a system. The FE method is applied in the modelling of the deterministic components, while SEA is applied in the modelling of the random components. This work studies thin panels bolted to a stiff frame subjected to a point force, with the frequency up to 1000 Hz. Uncertainty is introduced by adding a number of small masses at random locations. The comparison between numerical and experimental examples shows good results for the ensemble average response of the example systems.

Cotoni et al (2007) develop a hybrid SEA-FE method to predict the vibration transmission problem for mid and high frequencies. There are two improvements with this method: i) the use of periodic structure theory as a basis for the periodic SEA subsystem, and ii) the use of complex ribbed panels as the SEA subsystem. This work is concentrated on the vibration transmission in aircraft sections: i.e. the stowage bin, and the connected floor structure. The stowage bin consists of four side panels modelled by SEA subsystems, and a frame modelled by FE. The bin and frame were assembled and connected through four hybrid point junctions subjected to excitation with the frequency range of 50 Hz to 1600 Hz. The floor structure consists of sidewall and floor panels connected through three stiff beams. The sidewall modelled by SEA and the floor panels modelled by FE were assembled into a hybrid SEA-FE model, and subjected to the rain-on-the-roof loading with the frequency range of 50 Hz to 3000 Hz. The results show that the agreement between experiments and the hybrid method is fairly satisfactory. There are some limitations of the hybrid model from the rough FE model becoming more important as the frequency increases, and as the model assumption affecting the SEA becomes questionable.

Ragnarsson et al (2010) demonstrate the use of the wave-based boundary condition to calculate point mobilities from subcomponents of a structure as a tool for evaluating

SEA parameters to increase the accuracy of SEA prediction. Boundary conditions are derived by the wave-based substructuring technique which requires two sub-procedures: the wave calculation, and component reduction. The wave calculation involves a full modal analysis to the complete structure in the interested frequency range. The component reduction is conventional but with the wave load vector applied to each wave participation factors. A vehicle B-pillar case is tested to validate the theory compared with full FE analysis. The results show a very good match with FE up to 150 Hz. And for a higher frequency range (150–700 Hz), the results are still good.

Xie et al (2012) model a car floor, consisting of a floor panel connected to rails through spotwelds, by analysing stiff rails with FE and flexible, modally dense floor panel with SEA. In addition, they also model the floor wholly in SEA, with the rails as beams and the floor structure as SEA subsystems. Structure-borne vibration analyses (in the 10 Hz to 3 kHz range), produce ensemble average responses, which compared well with Monte Carlo simulations based on mass-randomised floor structure. However, each approach has its disadvantages. The hybrid model exhibits a small discrepancy between predictions of ensemble average responses and the numerical results, whereas the SEA-only model cannot give detailed modal behaviour. In modelling complex engineering structures at mid and high frequencies, the authors show that the hybrid technique is viable for predicting mean response levels. The use of standard couplings also improves the efficiency of the hybrid modelling procedure, bypassing the need to individually model each SEA structure. It is believed that the hybrid technique is useful for examining structure-borne vibrations and structural modifications.

Secgin et al (2012) study a rectangular plate structure with random boundary conditions in the mid and high frequency regions. They use an extreme-value (EV) approach to show that EV-based statistical bounding of both the FRF and total energy density response is applicable across the entire frequency range. The bounding uses an asymptotic threshold exceedance model of Type I to repeatedly calibrate the threshold model at discrete frequencies using a small sample of response data generated by Monte Carlo simulation or measurement. As a result, the m -observational return period is extrapolated to an arbitrarily large batch of structures. To generate Monte Carlo samples, the discrete singular convolution (DSC) method is used. It is a transfrequency computation approach for deterministic vibration. DSC results are then compared with those of a mode superposition method and SEA.

The methods described above are a sample of the published approaches for low, mid, and high frequency uncertain dynamics. For the mean response, general methods are available but there is the gap in knowledge to predict the variance for structures with varying levels of uncertainty because SEA is not able to control the level of uncertainty whereas Monte Carlo simulation takes a very considerable time to compute the response for each member of the ensemble. These shortcomings justify the following objectives.

1.2 The Objectives of the Thesis

Having reviewed the literature and identified remaining problems areas, a position has been reached where specific objectives of the thesis can be set. The specific problem identified for which no adequate theory exists is the problem of predicting the response of uncertain structures with significant differences in the levels of uncertainty. The objectives of the thesis are therefore stated as follows:

- i) To study uncertain structures at both low and high frequency, at different levels of uncertainty, with different uncertainty prediction methods. A number of existing methods for predicting response statistics, such as mean levels and standard deviations, are examined, compared, and benchmarked by (potentially expensive) Monte Carlo simulations.
- ii) To attempt, given the implicit statistical natures of SEA, to relate SEA type predictions to dimension and thickness variabilities, in particular, for at least high frequency responses of both simple and built-up structures.
- iii) To develop and test a new approach based on EV theory, which will enable response bounds to be predicted for simple and built-up structures without the need for expensive Monte Carlo simulations.

1.3 Outline of the Thesis

Overall, two methods, namely SEA and Direct Integration (DI), are combined with extreme-value (EV) theory to produce a method for predicting the maximum amplitude i.e. a statistical bound in terms of an exceedance level for a specified number of uncertain systems. These DI-EV and SEA-EV-based bounding approaches are developed and applied to both simple and non-simple structures.

In Chapter 2, five methods for predicting the statistical response of uncertain structures will be presented. First, Direct Integration gives the probability of failure as an integral of the joint probability density function over the failure region. Second, FORM approximates the failure probability by finding the design point of the failure surface, and putting it into the standard distribution function. Third, SEA looks at the asymptotic behaviour of the structural response at high frequencies. It does this by using the power balance equation and predicts the mean total energy level of an ensemble of the structure with uncertain parameters. Fourth, EV theory predicts the exceedance probability of the response by selectively working with extreme data. Fifth, Monte Carlo simulation methods are used for simulating dynamic systems with many uncertain parameters. This method can predict the failure or exceedance probability of the response by counting the number of times when failure or exceedance occurs from simulation results. But it will be shown to be computationally very expensive.

In Chapter 3, after testing three methods (Direct Integration, FORM, and Monte Carlo simulation) for calculating the failure probability, the use of Direct Integration, which is a deterministic method, is shown allow the failure probability to be calculated exactly from the limit-state function obtained from the equation of motion. However, if the number of variables is more than two, the direct integration computational complexity, in obtaining the exceedance or failure probability, increases. Therefore in general, there is a clear limitation to the practical application of direct integration. For FORM, this method is the fastest, but more complicated than both Direct Integration and Monte Carlo simulation because the boundary function can be very complex and where the origin must be known. Then, it will be shown which function should be used to calculate the failure probability. Monte Carlo simulation is almost always used as a benchmark but it takes considerable time to compute even simple structural responses with a small number of uncertain parameters. The greatest advantage of this method is its capabilities to handle unlimited random parameters and complex systems. In general, real structures have great complexity in geometry, and a large number of uncertain parameters. The time for repeating the analysis many hundreds of times or more, is a very major problem.

Chapter 4 applies the SEA method to predict the mean and standard deviation of the energy for a simple plate structure when the plate dimension varies. However, when the local minima of (Statistical Overlap Factor) SOF is less than one, SEA will be shown to

overpredict the standard deviation of the energy. The behaviour of the mean and standard deviation of the energy for thickness variation, is different from that for dimension variation. For dimension variation, the trends of the mean and standard deviation obtained by Monte Carlo simulation are almost the same when the level of variability changes. In contrast, for the thickness variation, the trends are higher when the level of variability increases. The mean of the energy with thickness variation, is smoother than with dimension variation for all CV levels. For the plate thickness variation, SEA will be shown to predict the mean and standard deviation of the energy in some ranges of variation. For the standard deviation of energy, the SEA prediction can only handle cases with CV values from 1% to 10%. After that, the SEA gives underpredictions. The response variance is seemingly saturated to the SEA result when CV increases only with plate dimension variation but with plate thickness variation, the response variance continuously increases. The distribution functions of the mean energy responses are shown for a simple plate structure to be similar to the lognormal distribution (which actually becomes the basis for the assumption in Chapter 6). It has therefore been verified that the assumption of the lognormal distribution for the energy response of a simple structure can be used.

Chapter 5 applies the SEA method for a built-up structure. The results show the mean and standard deviation of the energy for an L-shaped plate, driven by the harmonic point force. This is made uncertain as a random structure by varying the plate dimensions from 1%, 5%, 10%, 20%, and 30%, and the plate thicknesses from 1%, 5%, 10%, 15%, and 20% using a uniform distribution. The results are obtained by using Monte Carlo simulations based on (commercially available) finite element solutions via ANSYS as a benchmark to compare with SEA. The comparison between SEA and Monte Carlo simulations shows better agreement for the mean and standard deviations of the energy for the dimension variation than those for the thickness variation. The mean responses obtained from Monte Carlo simulation and SEA, for the different variation levels, are different. When the CV increases, the mean response is higher (especially on one of the plates for the plate thickness variation). The distribution functions of the spatial average FRFs are shown for a non-simple built-up structure to be similar to the lognormal distribution, which, together with the results from Chapter 4, underlies assumption made in Chapter 6. It will be shown that the assumption of the

lognormal distribution for the energy response of a non-simple built-up structure can be used.

Chapter 6 focuses on the basis of a new approach for bounding the response of uncertain structures based on a number of assumptions and a hypothesis. Chapter 6 also contains more details of the use of DI prediction of the mean and standard deviation based on the law of the ‘unconscious statistician’ theorem, and thus more fully describes the bounding methods based on EV theory. With the advantages given for constructing finite sample extreme value distributions, it is hypothesised that the combined SEA-EV and DI-EV methods can predict the bounds of the FRFs of uncertain structures without the need to undertake (potentially very expensive) Monte Carlo simulation. Two versions of an Extreme Value based method use finite sample extreme value distribution to construct a response bound for any level of variability and at any frequency. These methods are both mainly based on the assumption that the responses are log-normally distributed about the mean value at any given frequency. Evidence drawn from Chapter 4 and 5 will be shown support this assumption for both single plate and coupled plate structures.

In Chapter 7, the results show that the DI method has high ability to predict the mean and standard deviation of the energy for both simple and coupled plate structures with plate dimension and thickness variability. However, this essentially deterministic method takes much longer computation time than SEA but is still quicker than Monte Carlo simulations when working with many different CVs (for example, five CVs in our experiment).

Chapter 8 draws conclusions from the major findings and novelty of the thesis, and gives suitable recommendations for further work.

Chapter 2

Theories for Predicting the Statistical Response of Uncertain Structures

The purpose of this chapter is to present theories for predicting the statistical response of uncertain structures. These theories will be used throughout the remainder of the thesis, to establish their limitations, but also to assist in the development of a new approach in Chapter 6. Several theories mentioned in Chapter 1 have been developed to predict response statistics associated with uncertain structures. At low frequencies, a number of approaches exist which potentially allow levels of uncertainty in parameters to be varied. Whether these approaches can readily be implemented for more than just a few degrees-of-freedom, needs to be explored. Two methods are initially outlined, the first being the Direct Integration method (DI), and second, the First Order Reliability Method (FORM). The focus then switches to a high frequency prediction approach using Statistical Energy Analysis (SEA). This powerful approach, which massively simplifies the treatment of structures with natural variability, will be overviewed, and its potential explored. Then a somewhat different approach, based on extreme-value theory is discussed. This is generally implemented by calibrating EV distribution parameters using simulated data. The basis of the method has been verified across the entire frequency range but the practicality of simulation-based calibration at high frequency on non-simple built-up structures is questionable. To benchmark all of the methods, an overview of Monte Carlo simulation will also be discussed.

2.1 Direct Integration Method (DI)

In this section, the direct integration method (DI) is presented, and a general method discussed to predict the probability of exceeding a safe level for an ensemble set of uncertain FRFs.

To start with, the failure probability is discussed associated with the response of a SDOF model $m\ddot{x} + C\dot{x} + Kx = F(t)$, with failure surface $g(z) = x_{limit} - x_{max}(z)$;

where z is normalised to zero mean and normal standard deviation of the random parameters.

The probability of failure can usually be expressed as an integral (Guoqing and Dunne, 2010):

$$P_F(z) = \int_{\Omega_f} f(z) dz \quad (2.1)$$

where $f(z)$ is the joint probability density function of the normalized random variable parameters, and Ω_f is the failure area defined by the condition $g(z) < 0$. Eq. (2.1) shows that the failure probability can only be obtained via this direct route if the failure area, and the joint probability density function can be determined. To find the failure area Ω_f , a reasonable range for the basic random variable parameters should be adopted according to practical design requirements.

The joint probability density function $f(z)$, associated with the random parameters should therefore be determined in advance. The basic random parameters are assumed to be normally distributed with a multi-dimensional joint probability density function, which is given in the general form as (Guoqing and Dunne, 2010):

$$f(z) = \frac{1}{(2\pi)^{\frac{n}{2}} |\Sigma|^{\frac{1}{2}}} \exp \left[-\frac{1}{2} (z)^T \Sigma^{-1} (z) \right] \quad (2.2)$$

where z is a vector of n random variable parameters, Σ is the CVariance matrix (and $|\Sigma|$ is its determinant). This Direct Integration method will be tested in Chapter 3 to assess its potential.

2.2 First Order Reliability Method (FORM)

The first-order reliability method (FORM) provides a streamlined route to calculate failure probabilities. This method gives exact results when the random parameters are normally distributed and the failure surface is linear (Melchers et al, 2003). The principal requirement of FORM is to compute the so-called reliability index β . Then, the Hasofer-Lind reliability index, which is defined as the shortest distance from the origin to the failure surface in the normalised z -coordinate system, is adopted. For the two-

dimensional case shown in Fig. 2.1, β is the distance OA—point ‘A’ is known as the ‘design point’.

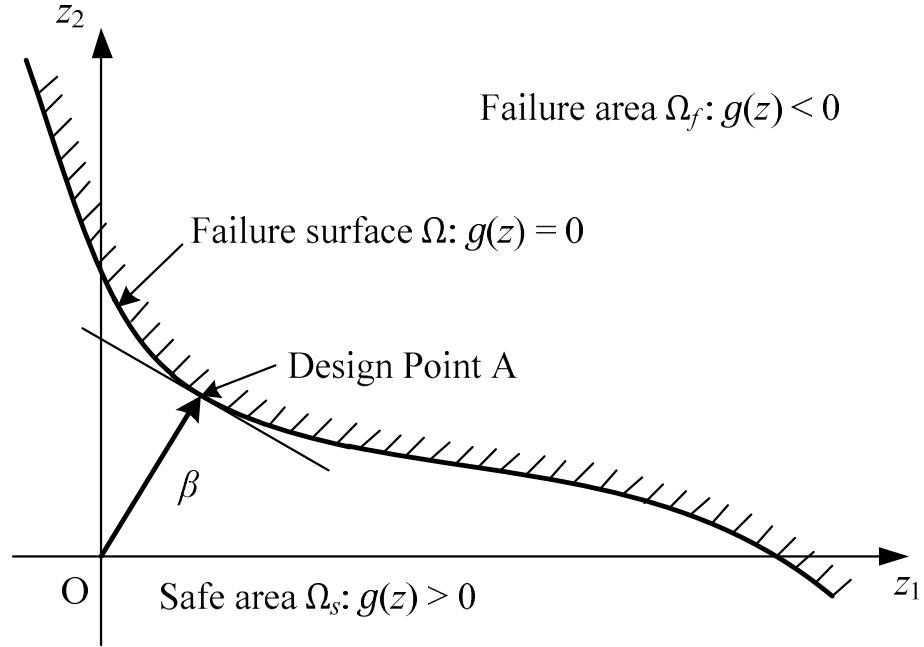


Figure 2.1: Failure surface and reliability index β (Guoqing and Dunne, 2010).

When the failure surface (Ω) in the z -coordinate system is linear, and the basic random variable parameters are normally distributed according to $N(\mu_i, \sigma_i)$, then the following (exact) relationship exists as:

$$P_F = \Phi(-\beta) = 1 - \Phi(\beta) \quad (2.3)$$

where Φ is the standard (one-dimensional) normal distribution function. The Hasofer-Lind reliability index β is defined formally as:

$$\beta = \min_{\bar{z} \in \Omega} \left(\sum_{i=1}^n z_i^2 \right)^{1/2} \quad (2.4)$$

where \bar{z} is any point on the failure surface. When the failure surface is nonlinear, β can generally be obtained by iteration. This method will also be explored in Chapter 3 to assess its ability to predict low frequency responses.

2.3 Statistical Energy Analysis (SEA)

At high frequency, SEA becomes a practical approach. SEA is a class of methods that look at the asymptotic behaviour of the structural response at high frequencies, like the ensemble average FRF. The vibrational or acoustical energies constituting the degrees of freedom of an SEA system are considered in the time-averaged steady-state form. With this, and the splitting of the SEA system into several subsystems, the analysis can be made much less computationally expensive.

The principal equation used in SEA is the power balance equation among subsystems (Lyon and Dejong, 1995). The power balance equation for subsystem j interconnected to subsystem k , with k varying, can be written as (Lyon and Dejong, 1995)

$$\omega \eta_j E_j + \sum_k \omega \eta_{jk} n_j \left(\frac{E_j}{n_j} - \frac{E_k}{n_k} \right) = P_{in,j} \quad (2.5)$$

where ω is the vibration frequency (rad/s), η_j is the loss factor of subsystem j , η_{jk} is the coupling loss factor from subsystem j to subsystem k , E_j is the energy of subsystem j , n_j is the modal density of subsystem j (The modal density will be described again in Section 2.3.3), and $P_{in,j}$ is the external input power into subsystem j . Eq. (2.5) can be written in matrix form as

$$\mathbf{C}\hat{\mathbf{E}} = \mathbf{P}_{in} \quad (2.6)$$

where

$$\mathbf{C} = \omega \begin{pmatrix} \left(\eta_1 + \sum_{j=1, j \neq k}^k \eta_{1j} \right) n_1 & -\eta_{12} n_1 & \cdots & -\eta_{1k} n_1 \\ -\eta_{21} n_2 & \left(\eta_2 + \sum_{j=1, j \neq k}^k \eta_{2j} \right) n_2 & \ddots & -\eta_{2k} n_2 \\ \vdots & \vdots & \ddots & \vdots \\ -\eta_{k1} n_k & -\eta_{k2} n_k & \cdots & \left(\eta_k + \sum_{j=1, j \neq k}^k \eta_{kj} \right) n_k \end{pmatrix}$$

$\hat{\mathbf{E}} = (\hat{E}_1 \ \hat{E}_2 \ \cdots \ \hat{E}_k)^T$ is the modal energy matrix, where $\hat{E}_k = E_k/n_k$ is the modal energy of subsystem k . $\mathbf{P}_{in} = (P_{in,1} \ P_{in,2} \ \cdots \ P_{in,k})^T$ is the external power input matrix.

A form of SEA will be used in Chapters 4 and 5, to explore its potential, in particular to examine high frequency sensitivity to varying levels of uncertainty. The parameters which are required by SEA are presented in the following sections.

2.3.1 Coupling Loss Factor (CLF)

The coupling loss factor parameter needed in Eq. (2.5) is a function of the transmission coefficient. For a line connection, it can be written as follows (Langley and Heron, 1990):

$$\langle \eta_{pr}^{ij}(\omega) \rangle = \frac{c_{pi}L\langle \tau_{pr}^{ij}(\omega) \rangle}{\pi\omega A_i} \quad (2.7)$$

where $\langle \eta_{pr}^{ij}(\omega) \rangle$ represents the average coupling loss factor between wave type p of plate i and wave type r of plate j , c_{pi} is the appropriate group speed of plate i , A_i is the area of plate i , L is the length of the junction, and $\langle \tau_{pr}^{ij}(\omega) \rangle$ represents the average transmission coefficient. The method used to calculate the transmission coefficient is presented in the following section.

2.3.2 Transmission Coefficient

The transmission coefficient needed in Eq. (2.7) is the most complicated and important parameter for SEA. The method used to calculate the transmission coefficients of a line junction for plate/plate in this work originated from the publication by Langley and Heron (1990). Because this is so particularly relevant to the work in Chapter 5, it is repeated here. This method is based on the wave approach including bending, longitudinal, and shear waves. The advantage of this method is the ability to calculate the transmission coefficients of an arbitrary number of semi-infinite plates coupled to each other at one junction.

A schematic of N semi-infinite plates each connected to a line junction is shown in Fig. 2.2a, where θ_1 , θ_j , and θ_N are the angles between the global y axis and plate 1, j , and N , respectively. The co-ordinate system, displacements and tractions for plate j are shown in Fig. 2.2b.

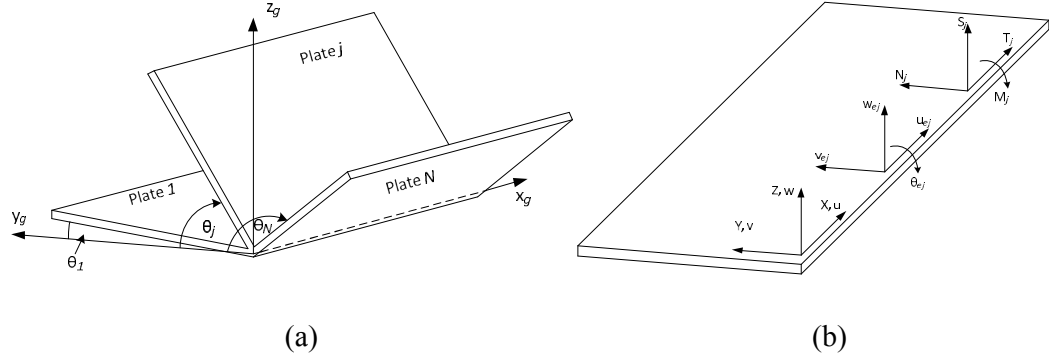


Figure 2.2: (a) Schematic of plate/plate junction with global axes, (b) Co-ordinate system, displacements and tractions for plate j .

The equations of motion governing the deflections of plate j can be written as follows (Langley and Heron, 1990):

$$D_j \nabla^4 w + \rho_j \ddot{w} = 0 \quad (2.8)$$

$$A_j(1 + \gamma_j) \frac{\partial^2 u}{\partial x^2} + A_j \frac{\partial^2 u}{\partial y^2} + A_j \gamma_j \frac{\partial^2 v}{\partial x \partial y} - \rho_j \ddot{u} = 0 \quad (2.9)$$

$$A_j(1 + \gamma_j) \frac{\partial^2 v}{\partial y^2} + A_j \frac{\partial^2 v}{\partial x^2} + A_j \gamma_j \frac{\partial^2 u}{\partial x \partial y} - \rho_j \ddot{v} = 0 \quad (2.10)$$

where D_j is the bending stiffness of plate j defined as $D_j = E_j h_j^3 / 12(1 - \nu_j^2)$, ρ_j is the mass per unit area of plate j , and A_j and γ_j are related to the thickness of plate j (h_j), $A_j = \frac{E_j h_j}{(2 + \nu_j)}$ and $\gamma_j = (1 + \nu_j) / (1 - \nu_j)$, E_j is Young's modulus of plate j and ν_j is Poisson ratio of plate j . The relationship between the displacements and tractions shown in Fig. 2.2b can be written as follows:

$$M_j = D_j \left(\frac{\partial^2 w}{\partial y^2} + \nu_j \frac{\partial^2 w}{\partial x^2} \right) \quad (2.11)$$

$$S_j = -D_j \left[\frac{\partial^3 w}{\partial y^3} + (2 - \nu_j) \frac{\partial^3 w}{\partial y \partial x^2} \right] \quad (2.12)$$

$$N_j = A_j(1 + \gamma_j) \left(\frac{\partial v}{\partial y} + \nu_j \frac{\partial u}{\partial x} \right) \quad (2.13)$$

$$T_j = A_j \left(\frac{\partial v}{\partial x} + \frac{\partial u}{\partial y} \right) \quad (2.14)$$

For a plate/plate line junction, the relationship between the edge displacements of the plate carrying incident wave $\mathbf{a} = (u \ v \ w \ \theta)^T$, and the edge displacements of plate j , $\mathbf{b}_j = (u_{ej} \ v_{ej} \ w_{ej} \ \theta_{ej})^T$, can be written as follows:

$$\mathbf{b}_j = \mathbf{R}_j^T \mathbf{a} \quad (2.15)$$

where

$$\mathbf{R}_j = \begin{pmatrix} 1 & 0 & 0 & 0 \\ 0 & \cos \theta_j & -\sin \theta_j & 0 \\ 0 & \sin \theta_j & \cos \theta_j & 0 \\ 0 & 0 & 0 & 1 \end{pmatrix} \quad (2.16)$$

and where θ_j is the angle of plate j shown in Fig. 2.2a. Eq. (2.16) is reduced from the plate/beam junction case in Langley and Heron (1990).

The wave numbers of plate j for three wave types may be calculated from the equations below as follows (Langley and Heron, 1990):

$$k_B = \left(\frac{\rho_j \omega^2}{D_j} \right)^{1/4} \quad (2.17)$$

$$k_L = \sqrt{\frac{\rho_j \omega^2 (1 - \nu_j^2)}{E_j h_j}} \quad (2.18)$$

$$k_S = \sqrt{\frac{2\rho_j \omega^2 (1 + \nu_j^2)}{E_j h_j}} \quad (2.19)$$

When a plane wave propagates towards the junction, the incident wave depends on $\exp(-ikx + i\boldsymbol{\mu}y + i\omega t)$ where $\boldsymbol{\mu}$ is a wave number. The fact that all plates share the same edge, implies that the response is in the form $\exp(-ikx + i\omega t) f(y)$, where $f(y)$ is to be determined from the plate equation of motion. The out of plane displacement of plate j is assumed to have a y dependency of $\exp(\boldsymbol{\mu}y)$, which implies that $\boldsymbol{\mu}$ must satisfy the equations for three wave types.

For bending waves:

$$(\boldsymbol{\mu}_B)^2 = (\kappa_r^i)^2 \pm (\kappa_B^j)^2 \quad (2.20)$$

where k_r and i represent the wave number and carrier plate of the incident wave type r , and k_B and j represent the bending wave number and carrier plate of the generated wave.

There are two valid roots as follows:

$$\boldsymbol{\mu}_{B1} = -\sqrt{(\kappa_r^i)^2 + (\kappa_B^j)^2}, \boldsymbol{\mu}_{B2} = -\sqrt{(\kappa_r^i)^2 - (\kappa_B^j)^2} \quad (2.21), \quad (2.22)$$

For longitudinal waves:

$$(\boldsymbol{\mu}_L)^2 = (\kappa_r^i)^2 - (\kappa_L^j)^2 \quad (2.23)$$

where k_r and i represent the wave number and carrier plate of the incident wave type r , and k_L and j represent the longitudinal wave number and carrier plate of the generated wave. There is only one valid root as follows:

$$\boldsymbol{\mu}_L = -\sqrt{(\kappa_r^i)^2 - (\kappa_L^j)^2} \quad (2.24)$$

For shear waves:

$$(\boldsymbol{\mu}_S)^2 = (\kappa_r^i)^2 - (\kappa_S^j)^2 \quad (2.25)$$

where k_r and i represent the wave number and carrier plate of the incident wave type r , and k_S and j represent the shear wave number and carrier plate of the generated wave.

There is only one valid root as follows:

$$\boldsymbol{\mu}_S = -\sqrt{(\kappa_r^i)^2 - (\kappa_S^j)^2} \quad (2.26)$$

The out of plane displacement of the plate can be written as follows:

$$w = \sum_{n=1}^2 \alpha_{Bn} \exp(-ikx + \boldsymbol{\mu}_{Bn}y + i\omega t) \quad (2.27)$$

where $\boldsymbol{\mu}_{B1}$ and $\boldsymbol{\mu}_{B2}$ are from Eqs. (2.21), and (2.22), and α_{B1} and α_{B2} are the complex amplitudes of the two functions in summation. Considering the edge of plate j , Eq. (2.27) can be used to express the displacement w_{ej} and rotation θ_{ej} of the edge of plate j as follows:

$$\begin{pmatrix} w_{ej} \\ \theta_{ej} \end{pmatrix} = \begin{pmatrix} 1 & 1 \\ \boldsymbol{\mu}_{B1} & \boldsymbol{\mu}_{B2} \end{pmatrix} \begin{pmatrix} \alpha_{B1} \\ \alpha_{B2} \end{pmatrix} \exp(-ikx + i\omega t) \quad (2.28)$$

Eqs. (2.11), (2.12), and (2.28) can be used to express the edge tractions S_j and M_j in terms of α_{B1} and α_{B2} . The relationship between the edge displacements and the edge tractions can be written as follows:

$$\begin{pmatrix} S_j \\ M_j \end{pmatrix} = \frac{D_j}{\mu_{B1} - \mu_{B2}} \begin{pmatrix} \mu_{B1}^3 \mu_{B2} - \mu_{B2}^3 \mu_{B1} & \mu_{B2}^3 - \mu_{B1}^3 + (2 - \nu_j)(\mu_{B1} - \mu_{B2})k^2 \\ \text{Symm.} & \mu_{B1}^2 - \mu_{B2}^2 \end{pmatrix} \begin{pmatrix} w_{ej} \\ \theta_{ej} \end{pmatrix} \quad (2.29)$$

see Appendix A for a full derivation. The in-plane displacement of the plate can be written as follows:

$$\begin{pmatrix} u \\ v \end{pmatrix} = \left\{ \alpha_L \begin{pmatrix} k \\ i\mu_L \end{pmatrix} e^{\mu_L y} + \alpha_S \begin{pmatrix} i\mu_S \\ -k \end{pmatrix} e^{\mu_S y} \right\} \exp(-ikx + i\omega t) \quad (2.30)$$

where μ_L and μ_S are obtained from Eqs. (2.24) and (2.26), and α_L and α_S are the complex amplitudes of the two associated complementary functions. Eq (2.30) can be used to express the displacement u_{ej} and rotation v_{ej} of the edge of plate j as follows:

$$\begin{pmatrix} u_{ej} \\ v_{ej} \end{pmatrix} = \begin{pmatrix} k & i\mu_S \\ i\mu_L & -k \end{pmatrix} \begin{pmatrix} \alpha_L \\ \alpha_S \end{pmatrix} \exp(-ikx + i\omega t) \quad (2.31)$$

Eqs. (2.13), (2.14), and (2.31) can be used to express the edge tractions T_j and N_j in terms of α_L and α_S . The relationship between the edge displacements and the edge tractions can be written as follows:

$$\begin{pmatrix} T_j \\ N_j \end{pmatrix} = \frac{E_j h_j}{k^2 - \mu_S \mu_L} \begin{pmatrix} \frac{-(\mu_S^2 - k^2)\mu_L}{2(1 + \nu_j)} & \frac{-i(\mu_L^2 - \nu_j^2 k^2)k}{1 - \nu_j^2} + \frac{i\mu_S \mu_L k}{1 + \nu_j} \\ \frac{i(\mu_L^2 - \nu_j^2 k^2)k}{1 - \nu_j^2} - \frac{i\mu_S \mu_L k}{1 + \nu_j} & \frac{(\nu_j k^2 - \mu_L^2)\mu_S}{1 - \nu_j^2} + \frac{k^2 \mu_S}{1 + \nu_j} \end{pmatrix} \begin{pmatrix} u_{ej} \\ v_{ej} \end{pmatrix} \quad (2.32)$$

Eqs. (2.29) and (2.32) can be written as the combination of the complete set of the edge displacement \mathbf{b}_j and tractions \mathbf{F}_j as follows:

$$\mathbf{F}_j = \mathbf{K}_j \mathbf{b}_j \quad (2.33)$$

where $\mathbf{F}_j = (T_j \ N_j \ S_j \ M_j)^T$ and \mathbf{K}_j is known as the dynamic stiffness matrix as follows:

$$\mathbf{K}_j = \begin{pmatrix} K_{11} & K_{12} & 0 & 0 \\ K_{21} & K_{22} & 0 & 0 \\ 0 & 0 & K_{33} & K_{34} \\ 0 & 0 & K_{43} & K_{44} \end{pmatrix} \quad (2.34)$$

where

$$K_{11} = \frac{-(\boldsymbol{\mu}_S^2 - k^2)\boldsymbol{\mu}_L}{2(1 + \nu_j)} \left(\frac{\mathbf{E}_j h_j}{k^2 - \boldsymbol{\mu}_S \boldsymbol{\mu}_L} \right) \quad (2.35)$$

$$K_{12} = \left(\frac{-i(\boldsymbol{\mu}_L^2 - \nu_j^2 k^2)k}{1 - \nu_j^2} + \frac{i\boldsymbol{\mu}_S \boldsymbol{\mu}_L k}{1 + \nu_j} \right) \left(\frac{\mathbf{E}_j h_j}{k^2 - \boldsymbol{\mu}_S \boldsymbol{\mu}_L} \right) \quad (2.36)$$

$$K_{21} = \left(\frac{i(\boldsymbol{\mu}_L^2 - \nu_j^2 k^2)k}{1 - \nu_j^2} + \frac{i\boldsymbol{\mu}_S \boldsymbol{\mu}_L k}{1 + \nu_j} \right) \left(\frac{\mathbf{E}_j h_j}{k^2 - \boldsymbol{\mu}_S \boldsymbol{\mu}_L} \right) \quad (2.37)$$

$$K_{22} = \left(\frac{(\nu_j k^2 - \boldsymbol{\mu}_L^2)\boldsymbol{\mu}_S}{1 - \nu_j^2} + \frac{k^2 \boldsymbol{\mu}_S}{1 + \nu_j} \right) \left(\frac{\mathbf{E}_j h_j}{k^2 - \boldsymbol{\mu}_S \boldsymbol{\mu}_L} \right) \quad (2.38)$$

$$K_{33} = (\boldsymbol{\mu}_{B1}^3 \boldsymbol{\mu}_{B2} - \boldsymbol{\mu}_{B2}^3 \boldsymbol{\mu}_{B1}) \left(\frac{D_j}{\boldsymbol{\mu}_{B1} - \boldsymbol{\mu}_{B2}} \right) \quad (2.39)$$

$$K_{34} = (\boldsymbol{\mu}_{B2}^3 - \boldsymbol{\mu}_{B1}^3 + (2 - \nu_j)(\boldsymbol{\mu}_{B1} - \boldsymbol{\mu}_{B2})k^2) \left(\frac{D_j}{\boldsymbol{\mu}_{B1} - \boldsymbol{\mu}_{B2}} \right) \quad (2.40)$$

$$K_{43} = (\boldsymbol{\mu}_{B2}^3 - \boldsymbol{\mu}_{B1}^3 + (2 - \nu_j)(\boldsymbol{\mu}_{B1} - \boldsymbol{\mu}_{B2})k^2) \left(\frac{D_j}{\boldsymbol{\mu}_{B1} - \boldsymbol{\mu}_{B2}} \right) \quad (2.41)$$

$$K_{44} = (\boldsymbol{\mu}_{B1}^2 - \boldsymbol{\mu}_{B2}^2) \left(\frac{D_j}{\boldsymbol{\mu}_{B1} - \boldsymbol{\mu}_{B2}} \right) \quad (2.42)$$

Eq. (2.33) is valid for the case in which the incident wave is not carried by plate j . If the incident wave is carried by plate j , \mathbf{F}_j must be replaced by $\mathbf{F}_j - \mathbf{F}'_j$ and \mathbf{b}_j must be replaced by $\mathbf{b}_j - \mathbf{b}'_j$, where \mathbf{F}'_j and \mathbf{b}'_j are the edge tractions and the edge displacements caused by the incident wave, hence Eq. (2.33) becomes

$$\mathbf{F}_j = \mathbf{K}_j \mathbf{b}_j - \mathbf{f}_j \quad (2.43)$$

$$\mathbf{f}_j = \mathbf{K}_j \mathbf{b}'_j - \mathbf{F}'_j \quad (2.44)$$

where \mathbf{f}_j can be called as a dynamic loading vector acting on the semi-infinite plate. There are three cases for \mathbf{F}'_j and \mathbf{b}'_j , depending on the incident wave type. First, for a bending wave which is incident to the connected edge with an angle ϕ , \mathbf{F}'_j and \mathbf{b}'_j are

$$\mathbf{F}'_j = \begin{pmatrix} T'_j \\ N'_j \\ S'_j \\ M'_j \end{pmatrix} = \begin{pmatrix} 0 \\ 0 \\ -\alpha D_j [\boldsymbol{\mu}^3 - (2 - \nu_j)k^2 \boldsymbol{\mu}] \\ \alpha D_j (\boldsymbol{\mu}^2 - \nu_j k^2) \end{pmatrix} \quad (2.45)$$

$$\mathbf{b}'_j = \begin{pmatrix} u'_{ej} \\ v'_{ej} \\ w'_{ej} \\ \theta'_{ej} \end{pmatrix} = \begin{pmatrix} 0 \\ 0 \\ \alpha \\ \alpha\boldsymbol{\mu} \end{pmatrix} \quad (2.46)$$

where α is the wave amplitude and

$$k = k_B \cos \phi \quad (2.47)$$

$$\boldsymbol{\mu} = ik_B \sin \phi \quad (2.48)$$

Second, for a longitudinal wave which is incident to the connected edge with an angle ϕ , \mathbf{F}'_j and \mathbf{b}'_j are

$$\mathbf{F}'_j = \begin{pmatrix} T'_j \\ N'_j \\ S'_j \\ M'_j \end{pmatrix} = \begin{pmatrix} \alpha E_j h_j k \boldsymbol{\mu} / (1 + \nu_j) \\ \alpha i E_j h_j (\boldsymbol{\mu}^2 - \nu_j k^2) / (1 - \nu_j^2) \\ 0 \\ 0 \end{pmatrix} \quad (2.49)$$

$$\mathbf{b}'_j = \begin{pmatrix} u'_{ej} \\ v'_{ej} \\ w'_{ej} \\ \theta'_{ej} \end{pmatrix} = \begin{pmatrix} \alpha k \\ \alpha i \boldsymbol{\mu} \\ 0 \\ 0 \end{pmatrix} \quad (2.50)$$

where α is the wave amplitude and

$$k = k_L \sin \phi \quad (2.51)$$

$$\boldsymbol{\mu} = ik_L \cos \phi \quad (2.52)$$

Finally, for a shear wave which is incident to the connected edge with an angle ϕ , \mathbf{F}'_j and \mathbf{b}'_j are

$$\mathbf{F}'_j = \begin{pmatrix} T'_j \\ N'_j \\ S'_j \\ M'_j \end{pmatrix} = \begin{pmatrix} \alpha i E_j h_j (\boldsymbol{\mu}^2 + k^2) / 2(1 + \nu_j) \\ \alpha E_j h_j k \boldsymbol{\mu} / (1 + \nu_j) \\ 0 \\ 0 \end{pmatrix} \quad (2.53)$$

$$\mathbf{b}'_j = \begin{pmatrix} u'_{ej} \\ v'_{ej} \\ w'_{ej} \\ \theta'_{ej} \end{pmatrix} = \begin{pmatrix} \alpha i \boldsymbol{\mu} \\ -\alpha k \\ 0 \\ 0 \end{pmatrix} \quad (2.54)$$

where α is the wave amplitude and

$$k = k_S \sin \phi \quad (2.55)$$

$$\boldsymbol{\mu} = ik_S \cos \phi \quad (2.56)$$

The vibration of plate j is governed by Eq. (2.43). The relationship between Eqs. (2.43) and (2.15) can be written as Eq. (2.57) for plate/plate junction, which yields the edge displacement \mathbf{a} .

$$\left\{ \sum_{j=1}^N \mathbf{R}_j \mathbf{K}_j \mathbf{R}_j^T \right\} \mathbf{a} = \mathbf{R}_i \mathbf{f}_i \quad (2.57)$$

where i indicates the plate carrying the incident wave and N is the number of plates connected at the junction. The edge displacements \mathbf{b}_j of plate j can be calculated from Eq. (2.15), and then \mathbf{b}_j is used to solve the response wave amplitudes ($\alpha_{B1}, \alpha_{B2}, \alpha_L, \alpha_S$) of plate j , which govern the y dependency, by using Eqs. (2.28) and (2.31). The magnitude of the power transmitted for three types of waves can be evaluated from Eqs. (2.58)–(2.60) by using an appropriate amplitude α_r :

$$P_B = (\rho_j \omega^3 \alpha_{B2}^2 / k_B) \sin \phi \quad (2.58)$$

$$P_L = \frac{1}{2} \rho_j \omega^3 k_L \alpha_L^2 \sin \phi \quad (2.59)$$

$$P_S = \frac{1}{2} \rho_j \omega^3 k_S \alpha_S^2 \sin \phi \quad (2.60)$$

where P_r is the incident power for a wave type r . ϕ is the transmitted wave heading $\phi = \cos^{-1} k^i / k_r^j$, where k and i represent the wave number and carrier plate of the incident wave and k_r and j represent the wave number and carrier plate of the generated wave type r . The transmission coefficient associated with each of the generated waves can be calculated by taking the ratio of the transmitted power to the total power which is incident on the junction.

The transmission coefficient for the complete set can be written in the form of $\tau_{pr}^{ij}(\omega, \phi)$, where i, p, ω and ϕ are the carrier plate, wave type, frequency and heading of the incident wave, and j and r are the carrier plate and wave type of a generated wave. For $i = j$, τ is known as a reflection coefficient. The conservation of energy can be written as follows:

$$\sum_r \sum_j \tau_{pr}^{ij}(\omega, \phi) = 1 \quad (2.61)$$

The average transmission coefficient can be written as follows:

$$\langle \tau_{pr}^{ij}(\omega) \rangle = \frac{1}{2} \int_0^\pi \tau_{pr}^{ij}(\omega, \phi) \sin \phi \, d\phi \quad (2.62)$$

This completes the restatement of the essential derivations of the SEA parameters for coupled plates as given by Langley and Heron (1990).

2.3.3 Modal Density

The modal density (mode/rad) of a plate as needed in Eq. (2.5) is given (Lyon and Dejong, 1995) as

$$n_r(\omega) = \frac{Ak_r^2}{4\pi c_{\phi r}} \quad (2.63)$$

where n_r , k_r , and $c_{\phi r}$ are the modal density, wave number, and phase speed for a wave type r , respectively. A is the area of a plate. The wave number for each wave type can be obtained by using Eqs. (2.17)–(2.19). A phase speed is defined as $c_{\phi r} = \omega/k_r$.

2.3.4 Power Input

The power input subjected to a point force as needed in Eq. (2.5) can be written in form of (Lyon and Dejong, 1995)

$$P_{in} = \frac{|F|^2 \text{Re}\{Y(\omega)\}}{2} \quad (2.64)$$

where $|F|$ is the force amplitude and $\text{Re}\{Y(\omega)\}$ is the real part of the point mobility. For an infinite plate $Y(\omega) = 1/(8\sqrt{D\rho})$ (Cremer et al, 1973), the power input subjected to a unit point force can be written as follows:

$$P_{in}^\infty = \frac{1}{16\sqrt{D\rho}} \quad (2.65)$$

2.3.5 Variance of the Energy

Prediction of the variance of the energy response has been quite difficult via SEA. The most up-to-date method to predict the energy variance for built-up structures (which is of particular importance in Chapter 5) originated from the publication by Langley and Cotoni (2004). The variance equations can be written in the form of

$$\text{Var}[\hat{E}_j] = \sum_k (D_{0,jk}^{-1})^2 \text{Var}[P_{\text{ran},k}] + \sum_k \sum_{s \neq k} [(D_{0,jk}^{-1} - D_{0,js}^{-1}) \hat{E}_s]^2 \text{Var}[D_{\text{ran},ks}] \quad (2.66)$$

where $\text{Var}[\]$ is the variance, and $D_{0,jk}^{-1}$ represents the jk entry of the matrix \mathbf{D}_0^{-1} , which is the inverse of the SEA matrix \mathbf{C} in Eq. (2.6). \hat{E}_s is the ensemble averaged modal energy obtained by SEA. The input power variance can be written below:

$$\text{Var}[P_{\text{ran},k}] = P_{\text{in},k}^2 r^2(\alpha'_k, m'_k, B'_k) \quad (2.67)$$

where $P_{\text{in},k}$ is the input power of the subsystem k , α'_k is a non-SEA parameter depending upon the nature of loading (for single point load, $\alpha'_k = 2.75$), B'_k is a bandwidth within the frequency-averaging band parameter of the subsystem k , m'_k is the modal overlap factor of the subsystem k defined as

$$m' = \omega \eta n(\omega) \quad (2.68)$$

and the function r^2 is defined as

$$r^2(\alpha', m', B') = \frac{\alpha' - 1}{\pi m'} \left(\frac{1}{B'^2} \right) \left\{ 2B' \left[\frac{\pi}{2} - \tan^{-1} \left(\frac{1}{B'} \right) \right] - \ln(1 + B'^2) \right\} + \frac{1}{(\pi m')^2} \left(\frac{1}{B'^2} \right) \ln(1 + B'^2) \quad (2.69)$$

For no frequency averaging ($B' = 0$), the function r^2 is defined as

$$r^2(\alpha', m', 0) = \frac{1}{\pi m'} \left[\alpha' - 1 + \frac{1}{2\pi m'} (1 - e^{-2\pi m'}) + \tilde{E}(\pi m') \left(\cosh \pi m' - \frac{1}{\pi m'} \sinh \pi m' \right) \right] \quad (2.70)$$

where \tilde{E} is the exponential integral function, $\tilde{E}(x) = \int_x^\infty \exp(-t)/t dt$. The relative variance of the term D_{ks} can be written as follows:

$$\text{Var}[D_{\text{ran},ks}] = D_{0,k}^2 r^2(\alpha'_{ks}, m'_k, B'_k) \quad (2.71)$$

where α'_{ks} is a non-SEA parameter called the coupling coefficients depending upon the nature of loading applied to subsystem k by subsystem s (for a line connection $\alpha'_{ks} = 2$).

This method will be explored in Chapter 4 and 5 to assess its ability to predict variance of energy.

2.3.6 Statistical Overlap Factor (SOF)

SEA is a high frequency method. SEA predictions will be reliable above certain frequency. The frequency range above that frequency threshold has often been given in terms of the modal overlap factor. An alternative measure is the statistical overlap factor (SOF). The vibration responses of a system are affected by any uncertainty in the system parameters caused by variation in material parameters, dimensions, and manufacturing processes. The SOF can be used to measure the amount of crossing and veering modes occurring due to uncertainty in a system. The term SOF of the n th mode, originated from Manohar and Keane (1994), and is defined as follows:

$$\text{SOF}_n = \frac{2\sigma_{\omega_n}}{\langle \omega_{n+1} - \omega_n \rangle} \quad (2.72)$$

where σ_{ω_n} is the standard deviation of the n th natural frequency and $\langle \omega_{n+1} - \omega_n \rangle$ is the mean frequency spacing between the natural frequency mode n th and $n + 1$ th.

If the SOF is greater than unity, systems will have enough mixing between the modes and veering of the modes (Langley, 2004) and therefore SEA can be used with confidence. The SOF will be used in Chapter 3 to validate which levels of the random parameter variation is SEA able to handle.

2.4 Extreme Value Theory (EV)

Classical Extreme Value (EV) theory (Coles, 2001) concerns the statistical behaviour of a variable $M_n = \max\{X_1, X_2, \dots, X_n\}$, where X_i are independent random variable parameters with identical distribution. It can predict the exceedance probability associated with M_n as follows:

$$\Pr\{M_n > x\} = P_F \quad (2.73)$$

A significant aspect of extreme-value analysis is the prediction, with specified exceedance probability P_F , of the level x that will be exceeded by random variable parameter M_n . Here the asymptotic extreme value theory will be summarised before discussing the ‘extreme’ values associated with finite (rather than infinite) samples of data.

An important EV theorem (Coles, 2001) shows that:

$$\lim_{n \rightarrow \infty} \Pr \left\{ \frac{M_n - b_n}{a_n} \leq x \right\} = F(x) \quad (2.74)$$

where $F(x)$ is the generalised EV distribution (GEV):

$$F(x) = e^{-A^{-1/\xi}}; \mathbf{A} > 0 \quad (2.75)$$

$$\mathbf{A} = 1 + \xi \left(\frac{x - \mu}{\sigma} \right)$$

$$\sigma > 0; -\infty < \mu < \infty; -\infty < \xi < \infty;$$

a_n is scale parameter ($a_n > 0$), b_n is location parameters, σ is called the scale parameter, μ location parameter, and ξ shape parameter. If $\xi \rightarrow 0$, the distribution becomes:

$$F(x) = \lim_{\xi \rightarrow 0} e^{-A^{-1/\xi}} = e^{-e^{-(x-\mu)/\sigma}} \quad (2.76)$$

This is called the ‘‘Type I (Gumbel family)’’. If $\xi > 0$, the distribution becomes:

$$F(x) = \begin{cases} 0, & x \leq b \\ e^{-[(x-\mu)/\sigma]^{-\alpha}}, & x > b \end{cases} \quad (2.77)$$

This is called the ‘‘Type II (Fréchet family)’’. If $\xi < 0$, the distribution becomes:

$$F(x) = \begin{cases} e^{[(x-\mu)/\sigma]^{-\alpha}}, & x \leq b \\ 0, & x > b \end{cases} \quad (2.78)$$

This is called the ‘‘Type III (Weibull family)’’.

If the underlying distribution of the random parameters is known, the EV distribution can be constructed for a finite sample size such that it is subject to the accuracy of that underlying distribution. In Chapter 6, it is hypothesised that a particular underlying distribution is lognormal, and as such it is known that the EV distribution tends to Type I.

2.4.1 Calibration of EV Parameters Using Monte Carlo Simulation Data or Measurement

A calibrated GEV can predict the level x that will be exceeded by random variable M_n by considering the inverse problem:

$$\Pr\{M_n \geq x\} = P_F \quad (2.79)$$

where the exceedance probability is known to be:

$$P_F = 1 - F(x) \quad (2.80)$$

The solution x is called the ‘return level’ associated with a ‘return period’ $1/P_F$. The return level can be approximately viewed as the threshold where $N_B=1/P_F$ blocks of data would on average be exceeded just once. The return level is only appropriate for extrapolating to exceedance levels for mN_B , where m is integer, because the parameter in the GEV are locked to the number of data point per block N_{pb} . The return level cannot be used to extrapolate to different values of N_{pb} which are often required for FRF bounding. Moreover the distribution types I–III given by Eqs. (2.76)–(2.78) are asymptotic, i.e. , which only approximate finite sample extreme value distributions. With fairly weak assumptions, finite sample distributions can indeed be obtained.

2.4.2 Finite Sample Extreme Value Distributions

There are occasions where the underlying distribution of a random variable $F(x)$ corresponds to:

$$\Pr\{X < x\} = p \quad (2.81)$$

Assuming variable X is identically distributed and independent, then the distribution function associated with n realisations of X is then:

$$\Pr\{M_n < x\} = F_n(x) = F(x)^n \quad (2.82)$$

where X_n is the largest of the n realisations. If $F(x)$ is known, then it is possible to construct the distribution function $F_n(x)$ simply by raising $F(x)$ to the power n . Only when $n \rightarrow \infty$ does $F_n(x)$ approach one of the extreme-value distributions such as Eqs. (2.76), (2.77), and (2.78).

The finite sample extreme-value distribution (2.82) can be used to supply a return level or bound with some specified probability p . By solving for the value x satisfying:

$$1 - F_n(x) = p \quad (2.83)$$

The level $x = a$ i.e. the root of Eq. (2.83), is the threshold value that will be exceeded by n realisations with probability p . These ideas associated with finite sample ‘extreme’ will be used in Chapter 6 and 7.

2.5 Monte Carlo Simulation Methods

Monte Carlo simulation methods are a class of computation algorithms that hinge on repeated random sampling to compute their results. These methods are frequently used in simulations of physical and mathematical systems. They are most suitable for calculation by a computer and tend to be applied when it is unfeasible to compute an exact result with a deterministic algorithm (Anderson, 1986).

Monte Carlo methods are useful for simulating dynamic systems with many coupled degrees of freedom, such as fluids, disordered materials, strongly coupled solids, and cellular structures (see cellular Potts model (Chen et al, 2007)). They are used to model phenomena with many uncertainties in parameters and inputs. They are also broadly used for problem solving in mathematics such as multidimensional integration. When Monte Carlo simulations have been used in space exploration and oil exploration, their predictions of failures, cost overruns, and schedule overruns, are routinely better than human intuition or alternative "soft" methods (Baeurle, 2009).

To compute a sample mean $\mu = E[g(X)]$ from Monte Carlo simulations where X is a random variable generated in N finite samples, the estimate can be written as follows:

$$\hat{\mu}_N = \frac{1}{N} \sum_{j=1}^N g(X_j) \quad (2.84)$$

Estimating the failure probability obtained from a Monte Carlo simulation method involves the use of an appropriate random number generator to create independent sample values for each of the N basic random variable parameters x_i . For all of the random variable realizations x_i , by counting the number of times when $g(x_1, x_2, \dots, x_N) \leq 0$, i.e. when failure occurs, a failure probability estimate can be obtained from the ratio between the the number of times that failure level is exceeded T_F and the total number of realizations N , i.e.:

$$P_F \approx \frac{T_F}{N} \quad (2.85)$$

2.5.1 Confidence Intervals

To compute confidence intervals (error bars) associated with Monte Carlo simulations from the finite number of samples for mean α of an approximate $100(1 - \delta)$, construction of % confidence intervals are useful (Papanicolaou, 2011). To do this suppose that the random variable X with N samples takes on the following values:

$$X = X_1, X_2, X_3, \dots, X_N \quad (2.86)$$

so that

$$\bar{X} = \frac{1}{N}(X_1 + X_2 + \dots + X_N) \quad (2.87)$$

and

$$S = \sqrt{\frac{1}{N-1} \sum_{j=1}^n (X_j - \bar{X})^2} \quad (2.88)$$

The $100(1 - \delta)$ % confidence intervals of mean μ_X are then computed by

$$\left[\bar{X} - \frac{z_{1-\delta/2} S}{\sqrt{N}} \leq \mu_X < \bar{X} + \frac{z_{1-\delta/2} S}{\sqrt{N}} \right] \quad (2.89)$$

where z_a is defined by $\int_{-\infty}^{z_a} f_{N(0,1)}(z) dz = \Pr\{z_a \leq z\} = a$, then

$$\Pr\{-z_{1-\delta/2} \leq x \leq z_{1-\delta/2}\} = 1 - \delta; X \sim N(0,1) \quad (2.90)$$

To compute confidence intervals associated with Monte Carlo simulations for standard deviation α (Bendat and Piersol, 2000), the $100(1 - \delta)$ % confidence intervals for the standard deviation σ_X of the random variable X are computed by

$$\left[\frac{\sqrt{n}S}{\chi_{n;1-\delta/2}^2} \leq \sigma_X < \frac{\sqrt{n}S}{\chi_{n;\delta/2}^2} \right] \quad (2.91)$$

where n is equal $N - 1$ and χ_n^2 is a chi-square variable with n degree of freedom. $\chi_{n;a}^2$ is defined by $\int_0^{\chi_{n;a}^2} f_{\chi^2}(\chi^2) d\chi^2 = \Pr\{\chi_{n;a}^2 \leq \chi^2\} = a$.

Sufficient tools have now been identified to enable in Chapter 6, a novel approach to be constructed. These tools are now summarised.

2.6 A Summary of the Findings of Chapter 2

Five methods for predicting the statistical response of uncertain structures have been identified. First, Direct Integration gives the probability of failure as an integral of the joint probability density function over the failure region. Second, FORM approximates the failure probability by finding the design point of the failure surface, and putting it into the standard distribution function. Third, SEA obtains the asymptotic behaviour of the structural response at high frequencies. It does this by using the power balance equation and predicts the mean total energy level of an ensemble of a structure with uncertain parameters. Fourth, EV theory predicts the exceedance probability of the response by selectively working with extreme data. Fifth, Monte Carlo simulation methods are used for simulating dynamic systems with many uncertain parameters. This method can predict the failure or exceedance probability of the response by counting the number of times when failure or exceedance occurs from simulation results. It is however computationally very expensive, and in some cases simply not practical.

Direct Integration, FORM, and Monte Carlo methods are assessed in Chapter 3 particularly in examining low frequency responses of uncertain structures. SEA is examined in Chapter 4 and 5. In Chapter 6, EV theory will be combined to create a new method, which is extensively tested in Chapter 7.

Chapter 3

Low Frequency Response of Simple Structures with High and Low-Level Uncertainties

In Chapter 2 several methods were discussed that are potentially suitable for predicting response statistics of structures with varying levels of uncertainty. The aim of this chapter is to demonstrate the application and assess the limitations of FORM, and Direct Integration compared with Monte Carlo simulation for SDOF, 2DOF, and 3DOF systems. A number of low frequency discrete dynamic (lumped-mass) models with parameter uncertainty, are adopted, and then used specifically as a vehicle to test theoretical predictions. The focus will be on the capability to handle varying levels of uncertainty.

3.1 Low Frequency Models with Parametric Uncertainty

A total of three lumped-mass dynamic models are adopted as a vehicle to test the capability of the prediction methods, which are benchmarked with Monte Carlo simulation. This starts with a single degree of freedom model with two random variables, then two 2DOF model with three random parameters, and finally a 3DOF system with three random parameters. In all cases, the uncertain parameters are assumed to be normally distributed, with specific parameter statistics.

3.2 Application of Direct Integration, FORM, and Monte Carlo Simulation

The study commences with a SDOF model with two parameter variation and looks at three failure conditions (referred to as Case I and II in Figs. 3.5 and 3.6, respectively). Then a 2DOF system is examined involving random variation in 3 parameters. Finally a 3DOF system is studied to show up the full capabilities and limitations of these methods. Because in each case the FRF can be written explicitly, this response measure is used for Monte Carlo simulation along with a (parameter) random number generator.

Evaluating the failure probability by using Direct Integration and FORM, the limit-state function needs to be constructed to serve Eqs. (2.1) and (2.3), respectively. Then, the random parameters are normalised to zero mean and unit variance. For Direct Integration, the range of the normalised random parameters is limited to $[-5, 5]$. For Monte Carlo simulation, Eq (2.85) is used to calculate the failure probability. The variable T_F is defined as the number of FRFs that exceed a level L and N is a number of simulations. The number of Monte Carlo runs for all of Monte Carlo simulations in this chapter was selected to be 10^4 . The confidence level was selected to be 95%. Eq. (2.89) is then used to calculate the confidence interval of the exceedance probability. However, normally, the confidence level and confidence interval are chosen to determine the (minimum) number of Monte Carlo runs.

3.2.1 Single Degree of Freedom Model

The lumped-mass SDOF model is shown in Fig. 3.1. This is a standard linear system excited with a harmonic force $F_1(t)$. The study looks at the steady-state harmonic response to $F_1(t)$.

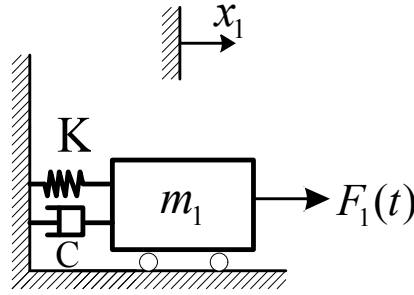


Figure 3.1: The SDOF model.

The equation of motion is given for the system as:

$$m_1 \ddot{x}_1 + C \dot{x}_1 + K x_1 = F_1 \sin \omega t \quad (3.1)$$

Its steady-state solution is $X_1 = F_1/Z(i\omega)$, where $Z(i\omega) = -\omega^2 m_1 + i\omega C + K$ is the impedance. Therefore, the solution for Eq. (3.1) is

$$X_1 = \frac{1}{-\omega^2 m_1 + i\omega C + K} \quad (3.2)$$

and

$$|X_1| = \frac{1}{\sqrt{(-\omega^2 m_1 + K)^2 + (\omega C)^2}} \quad (3.3)$$

Choosing nominal parameter values $m_1 = 10$ kg, $C = 17.89$ Ns/m, $K = 80,000$ N/m, and $F_1 = 1$ N, the natural frequency for this SDOF model is 89.44 rad/s. FRFs (for 10^4 samples from Monte Carlo simulation) with 1% and 10% CV in the two random parameters m_1 and K are shown in Fig. 3.2, where CV stands for coefficient of variation, defined by the ratio of the standard deviation to the mean (σ/μ).

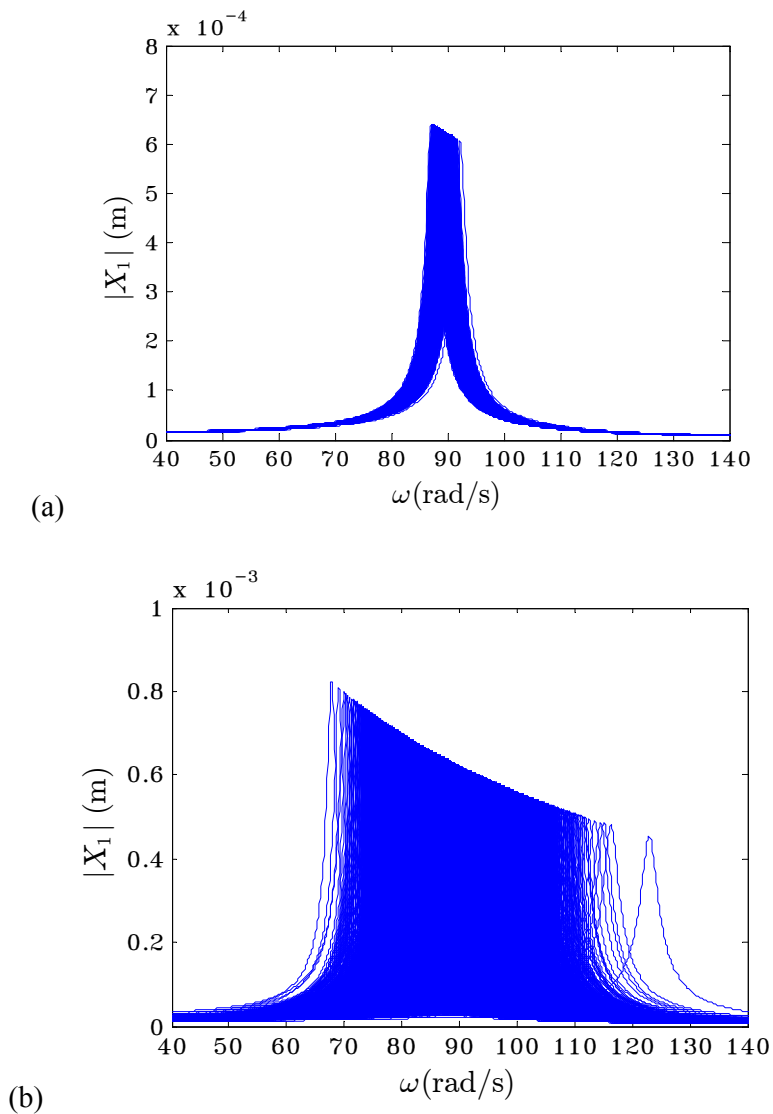


Figure 3.2: The FRFs (10^4 samples) of SDOF model with two random parameters: (a) 1% CV, (b) 10% CV.

Here the limit-state function $g(m_1, K)$ is defined in terms of the frequency response function. Failure is deemed to occur if the frequency response exceeds level L , in other words, if the response exceeds level L , then $g < 0$, and the system fails, where g is defined as:

$$g(m_1, K) = L - |X_1| \quad (3.4)$$

where m_1 and K are random parameters. The random parameters m_1 and K are normalised to zero mean and unit standard deviation:

$$z_1 = \frac{m_1 - \mu_{m_1}}{\sigma_{m_1}}, \text{ and } z_2 = \frac{K - \mu_K}{\sigma_K}$$

The random normalized parameters z_1 and z_2 are substituted for m_1 and K , respectively, in Eq. (3.4) which make g a function of z_1 and z_2 i.e. $g(z_1, z_2)$.

The limit-state function $g(z_1, z_2)$ of the SDOF model Eq. (3.4) with two normalised random parameters and with 1% and 10% CV at various frequencies, is shown in Figs. 3.3 and 3.4. The frequencies are chosen at the natural frequency and near the natural frequency. The lines are the failure surfaces $g(z_1, z_2) = 0$. The dotted area between each pair of lines is the failure area. The failure area moves when frequency changes and the failure area reduces when level L increases.

There are two cases of the failure surface for the SDOF model with two random parameters shown in Figs. 3.5 and 3.6. In contrast to Fig.2.1, the failure area is only a single strip. The calculation of failure probability is slightly more complicated. In all cases of the limit-state function of the SDOF model, the failure probability can be calculated from two probability areas.

In Case I, the origin is outside of the failure area as shown in Fig. 3.5. In Case II, the origin is inside the failure area as shown in Fig.3.6.

Comparisons of the predicted results for FORM, Monte Carlo simulation (10^4 samples) with 95% confidence interval, and Direct Integration for Case I and Case II are shown in Tables 3.1–3.4, respectively. Direct Integration can in these cases, within the limitations of numerical integration accuracy, be treated as exact.

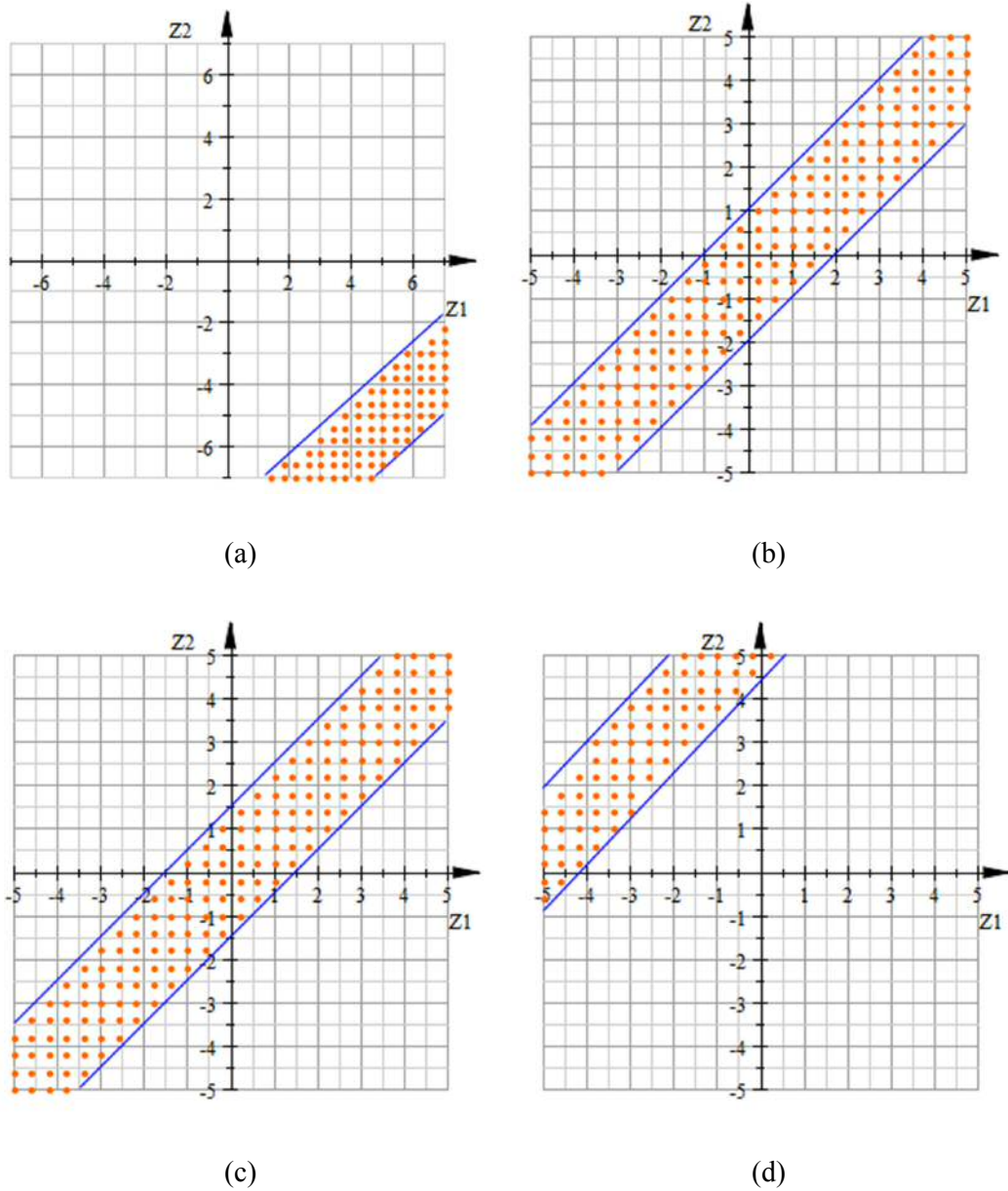
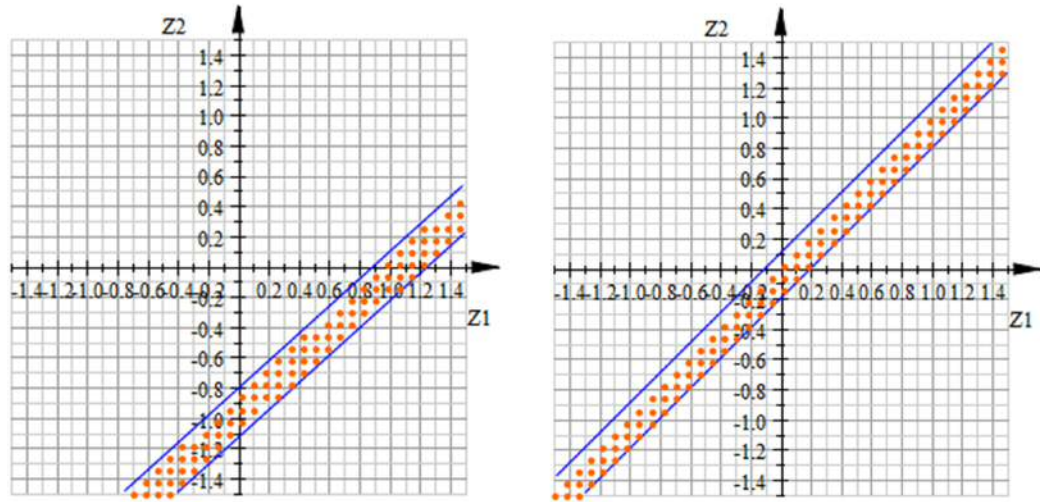
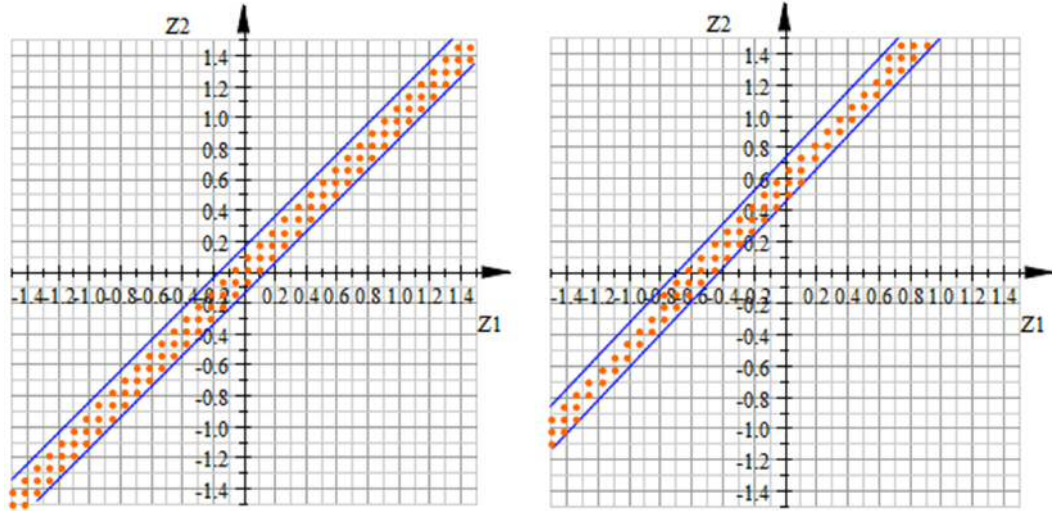


Figure 3.3: The limit-state function $g(z_1, z_2)$ of the SDOF model with 1% CV and level $L = 5.0 \times 10^{-4} \text{ m}$, at frequencies: (a) 85 rad/s, (b) 89.22 rad/s, (c) 89.44 rad/s, (d) 92 rad/s. The dotted area between each pair of lines for each frequency is the failure area.



(a)

(b)



(c)

(d)

Figure 3.4: The limit-state function $g(z_1, z_2)$ of the SDOF model with 10% CV and level $L = 5.0 \times 10^{-4}$ m, at frequencies: (a) 85 rad/s, (b) 89.22 rad/s, (c) 89.44 rad/s, (d) 92 rad/s. The dotted area between each pair of lines for each frequency is the failure area.

Case I: The origin is outside of the failure area $P_f(F) = \Phi(-\beta_0) - \Phi(-\beta_1)$

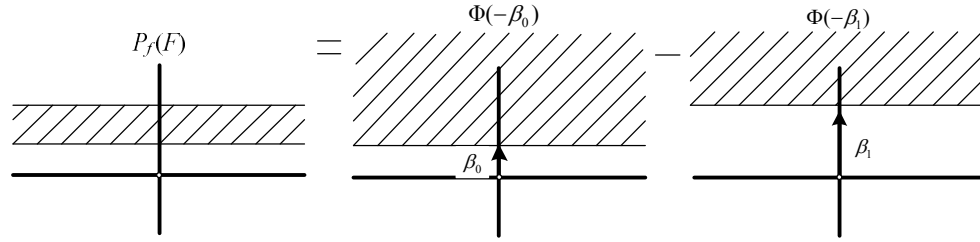


Figure 3.5: Diagrammatic representation of Case I.

Table 3.1: Comparison of results from FORM, Monte Carlo simulation, and Direct Integration for Case I with 1% CV.

ω (rad/s)	Failure level $\times 10^{-4}$ (m)	FORM				Monte Carlo simulation 95% confidence	Direct Integration
		β_0	β_1	Function of $P_f(F)$	$P_f(F)$	$P_f(F)$	$P_f(F)$
85	1.40	0.7151	15.6691	$\Phi(-\beta_0) - \Phi(-\beta_1)$	0.2389	0.2378 ± 0.0083	0.2373
	1.45	0.9492	15.3386	$\Phi(-\beta_0) - \Phi(-\beta_1)$	0.1736	0.1661 ± 0.0073	0.1713
	1.50	1.1680	15.0303	$\Phi(-\beta_0) - \Phi(-\beta_1)$	0.1230	0.1226 ± 0.0064	0.1214
	1.55	1.3731	14.7421	$\Phi(-\beta_0) - \Phi(-\beta_1)$	0.0853	0.0814 ± 0.0054	0.0849
	1.60	1.5657	14.4721	$\Phi(-\beta_0) - \Phi(-\beta_1)$	0.0594	0.0595 ± 0.0046	0.0587
	1.65	1.7471	14.2185	$\Phi(-\beta_0) - \Phi(-\beta_1)$	0.0409	0.0398 ± 0.0038	0.0403
92	1.70	1.9181	13.9799	$\Phi(-\beta_0) - \Phi(-\beta_1)$	0.0281	0.0278 ± 0.0032	0.0276
	2.50	0.8537	8.9005	$\Phi(-\beta_0) - \Phi(-\beta_1)$	0.1977	0.1960 ± 0.0078	0.1966
	2.60	0.9993	8.7016	$\Phi(-\beta_0) - \Phi(-\beta_1)$	0.1611	0.1528 ± 0.0071	0.1588
	2.70	1.1352	8.5158	$\Phi(-\beta_0) - \Phi(-\beta_1)$	0.1292	0.1314 ± 0.0066	0.1281
	2.80	1.2626	8.3418	$\Phi(-\beta_0) - \Phi(-\beta_1)$	0.1038	0.1009 ± 0.0059	0.1034
	2.90	1.3823	8.1783	$\Phi(-\beta_0) - \Phi(-\beta_1)$	0.0838	0.0859 ± 0.0055	0.0834
	3.00	1.4956	8.0241	$\Phi(-\beta_0) - \Phi(-\beta_1)$	0.0681	0.0674 ± 0.0049	0.0674

Table 3.2: Comparison of results from FORM, Monte Carlo simulation, and Direct Integration for Case I with 10% CV.

ω (rad/s)	Failure level $\times 10^{-4}$ (m)	FORM				Monte Carlo simulation 95% confidence	Direct Integration
		β_0	β_1	Function of $P_f(F)$	$P_f(F)$	$P_f(F)$	$P_f(F)$
85	2.5	0.3757	1.0622	$\Phi(-\beta_0) - \Phi(-\beta_1)$	0.2111	0.2101 ± 0.0080	0.2095
	3.0	0.4438	0.9941	$\Phi(-\beta_0) - \Phi(-\beta_1)$	0.1689	0.1694 ± 0.0074	0.1685
	3.5	0.4946	0.9433	$\Phi(-\beta_0) - \Phi(-\beta_1)$	0.1385	0.1365 ± 0.0067	0.1377
	4.0	0.5349	0.9030	$\Phi(-\beta_0) - \Phi(-\beta_1)$	0.1140	0.1153 ± 0.0063	0.1131
	4.5	0.5686	0.8693	$\Phi(-\beta_0) - \Phi(-\beta_1)$	0.0928	0.0917 ± 0.0057	0.0924
	5.0	0.5984	0.8395	$\Phi(-\beta_0) - \Phi(-\beta_1)$	0.0743	0.0758 ± 0.0052	0.0742
	5.5	0.6265	0.8114	$\Phi(-\beta_0) - \Phi(-\beta_1)$	0.0587	0.0549 ± 0.0045	0.0569
	6.0	0.6557	0.7822	$\Phi(-\beta_0) - \Phi(-\beta_1)$	0.0402	0.0396 ± 0.0038	0.0387
92	2.0	0.0070	0.8038	$\Phi(-\beta_0) - \Phi(-\beta_1)$	0.2881	0.2913 ± 0.0089	0.2920
	2.5	0.0854	0.7114	$\Phi(-\beta_0) - \Phi(-\beta_1)$	0.2293	0.2291 ± 0.0082	0.2276
	3.0	0.1495	0.6473	$\Phi(-\beta_0) - \Phi(-\beta_1)$	0.1832	0.1860 ± 0.0076	0.1819
	3.5	0.1979	0.5989	$\Phi(-\beta_0) - \Phi(-\beta_1)$	0.1471	0.1492 ± 0.0070	0.1470
	4.0	0.2368	0.5600	$\Phi(-\beta_0) - \Phi(-\beta_1)$	0.1213	0.1205 ± 0.0064	0.1187
	4.5	0.2702	0.5266	$\Phi(-\beta_0) - \Phi(-\beta_1)$	0.0920	0.0960 ± 0.0058	0.0943
	5.0	0.3008	0.4960	$\Phi(-\beta_0) - \Phi(-\beta_1)$	0.0700	0.0710 ± 0.0050	0.0718
	5.5	0.3321	0.4647	$\Phi(-\beta_0) - \Phi(-\beta_1)$	0.0479	0.0464 ± 0.0041	0.0488

Case II: The origin is inside the failure area $P_f(F) = \Phi(\beta_0) - \Phi(-\beta_1)$

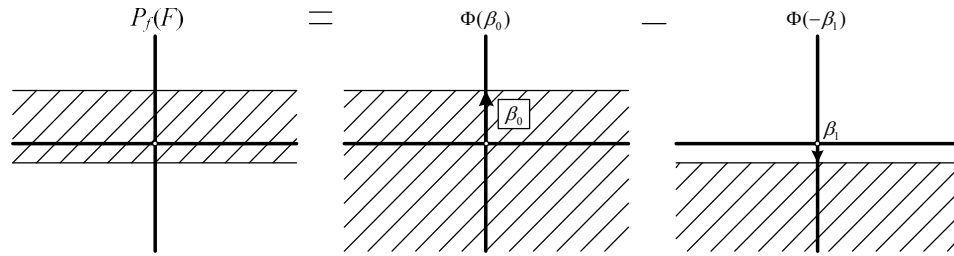


Figure 3.6: Diagrammatic representation of Case II.

Table 3.3: Comparison of results from FORM, Monte Carlo simulation, and Direct Integration for Case II with 1% CV.

ω (rad/s)	Failure level $\times 10^{-4}$ (m)	FORM				Monte Carlo simulation 95% confidence	Direct Integration
		β_0	β_1	Function of $P_f(F)$	$P_f(F)$	$P_f(F)$	$P_f(F)$
89.22	5.900	0.8578	0.1526	$\Phi(\beta_0) - \Phi(-\beta_1)$	0.3620	0.3638 ± 0.0094	0.3651
	5.925	0.8386	0.1334	$\Phi(\beta_0) - \Phi(-\beta_1)$	0.3484	0.3467 ± 0.0093	0.3523
	5.950	0.8189	0.1137	$\Phi(\beta_0) - \Phi(-\beta_1)$	0.3348	0.3379 ± 0.0093	0.3389
	5.975	0.7986	0.0934	$\Phi(\beta_0) - \Phi(-\beta_1)$	0.3211	0.3193 ± 0.0091	0.3250
	6.00	0.7776	0.0725	$\Phi(\beta_0) - \Phi(-\beta_1)$	0.3073	0.3128 ± 0.0091	0.3105
	6.025	0.7558	0.0506	$\Phi(\beta_0) - \Phi(-\beta_1)$	0.2933	0.2997 ± 0.0090	0.2953
89.44	6.100	0.3150	0.3150	$\Phi(\beta_0) - \Phi(-\beta_1)$	0.2434	0.2485 ± 0.0085	0.2473
	6.125	0.2866	0.2866	$\Phi(\beta_0) - \Phi(-\beta_1)$	0.2205	0.2237 ± 0.0082	0.2256
	6.150	0.2554	0.2554	$\Phi(\beta_0) - \Phi(-\beta_1)$	0.1974	0.2010 ± 0.0079	0.2016
	6.175	0.2203	0.2203	$\Phi(\beta_0) - \Phi(-\beta_1)$	0.1741	0.1778 ± 0.0075	0.1744
	6.200	0.1791	0.1791	$\Phi(\beta_0) - \Phi(-\beta_1)$	0.1350	0.1395 ± 0.0068	0.1421
	6.225	0.1256	0.1256	$\Phi(\beta_0) - \Phi(-\beta_1)$	0.0955	0.0985 ± 0.0058	0.0999

Table 3.4: Comparison of results from FORM, Monte Carlo simulation, and Direct Integration for Case II with 10% CV.

ω (rad/s)	Failure level $\times 10^{-4}$ (m)	FORM				Monte Carlo simulation 95% confidence	Direct Integration
		β_0	β_1	Function of $P_f(F)$	$P_f(F)$	$P_f(F)$	$P_f(F)$
89.22	2.0	0.4551	0.3846	$\Phi(\beta_0) - \Phi(-\beta_1)$	0.3217	0.3213 ± 0.0092	0.3252
	2.5	0.3603	0.2897	$\Phi(\beta_0) - \Phi(-\beta_1)$	0.2508	0.2561 ± 0.0086	0.2547
	3.0	0.2946	0.2240	$\Phi(\beta_0) - \Phi(-\beta_1)$	0.2012	0.2041 ± 0.0079	0.2045
	3.5	0.2452	0.1747	$\Phi(\beta_0) - \Phi(-\beta_1)$	0.1623	0.1657 ± 0.0073	0.1662
	4.0	0.2058	0.1352	$\Phi(\beta_0) - \Phi(-\beta_1)$	0.1310	0.1343 ± 0.0067	0.1353
	4.5	0.1723	0.1017	$\Phi(\beta_0) - \Phi(-\beta_1)$	0.1073	0.1095 ± 0.0061	0.1089
	5.0	0.1420	0.0715	$\Phi(\beta_0) - \Phi(-\beta_1)$	0.0836	0.0849 ± 0.0055	0.0850
89.44	5.5	0.1124	0.0419	$\Phi(\beta_0) - \Phi(-\beta_1)$	0.0598	0.0602 ± 0.0047	0.0615
	2.0	0.4183	0.4183	$\Phi(\beta_0) - \Phi(-\beta_1)$	0.3182	0.3234 ± 0.0092	0.3246
	2.5	0.3236	0.3236	$\Phi(\beta_0) - \Phi(-\beta_1)$	0.2510	0.2532 ± 0.0085	0.2541
	3.0	0.2585	0.2585	$\Phi(\beta_0) - \Phi(-\beta_1)$	0.1974	0.2038 ± 0.0079	0.2040
	3.5	0.2092	0.2092	$\Phi(\beta_0) - \Phi(-\beta_1)$	0.1585	0.1619 ± 0.0072	0.1657
	4.0	0.1698	0.1698	$\Phi(\beta_0) - \Phi(-\beta_1)$	0.1271	0.1314 ± 0.0066	0.1348
	4.5	0.1363	0.1363	$\Phi(\beta_0) - \Phi(-\beta_1)$	0.1034	0.1056 ± 0.0060	0.1085
	5.0	0.1061	0.1061	$\Phi(\beta_0) - \Phi(-\beta_1)$	0.0797	0.0830 ± 0.0054	0.0844
5.5	0.0763	0.0763	$\Phi(\beta_0) - \Phi(-\beta_1)$	0.0558	0.0586 ± 0.0046	0.0609	

Tables 3.1–3.4 show the comparison of the predicted results for FORM, Monte Carlo simulation, and Direct Integration for the SDOF model with 1% and 10% CV at frequencies 85 rad/s, 89.22 rad/s, 89.44 rad/s, and 92 rad/s. The results from FORM and Direct Integration are similar, and give good agreement with Monte Carlo simulation.

3.2.2 Two Degree of Freedom Model

The 2DOF model is shown in Fig. 3.7. This is a standard linear system excited by a pair of in-phase harmonics of different amplitude. The study looks at the steady-state harmonic response to $F_1(t)$ and $F_2(t)$.

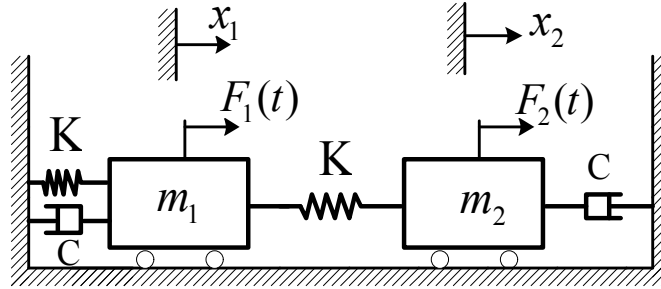


Figure 3.7: The 2DOF model.

The equation of motion is for this system is

$$[m]\ddot{\mathbf{x}} + [C]\dot{\mathbf{x}} + [K]\mathbf{x} = \mathbf{F} \quad (3.5)$$

where

$$\mathbf{x} = \begin{Bmatrix} x_1 \\ x_2 \end{Bmatrix}, [m] = \begin{bmatrix} m_1 & 0 \\ 0 & m_2 \end{bmatrix}, [C] = \begin{bmatrix} C & 0 \\ 0 & C \end{bmatrix}, [K] = \begin{bmatrix} 2K & -K \\ -K & K \end{bmatrix}, \mathbf{F} = \begin{Bmatrix} F_1 \sin \omega t \\ F_2 \sin \omega t \end{Bmatrix}$$

Its steady-state solution is $\mathbf{x} = \mathbf{Z}(i\omega)^{-1}\mathbf{F}$, where

$$\mathbf{Z}(i\omega) = \begin{bmatrix} Z_{11} & Z_{12} \\ Z_{21} & Z_{22} \end{bmatrix}; Z_{ij}(i\omega) = -\omega^2 m_{ij} + i\omega C_{ij} + K_{ij}$$

is the impedance and \mathbf{F} is $\{F_1 \ F_2\}^T$. Therefore, the solutions for Eq. (3.5) are

$$X_1 = \frac{Z_{22}F_1 - Z_{12}F_2}{Z_{11}Z_{22} - Z_{12}Z_{21}} \quad \text{and} \quad X_2 = \frac{-Z_{12}F_1 + Z_{11}F_2}{Z_{11}Z_{22} - Z_{12}Z_{21}}$$

The limit-state function $g(m_1, m_2, K)$ is defined in terms of the frequency response function. Failure is deemed to occur if the frequency response X_1 exceeds level L , in other words, if the response exceeds level L , then $g < 0$, and the system fails, where g is defined as:

$$g(m_1, m_2, K) = L - |X_1| \quad (3.6)$$

The random parameters (m_1, m_2, K) are normalised to zero mean and unit standard deviation:

$$z_1 = \frac{m_1 - \mu_{m_1}}{\sigma_{m_1}}, \quad z_2 = \frac{m_2 - \mu_{m_2}}{\sigma_{m_2}}, \quad \text{and} \quad z_3 = \frac{K - \mu_K}{\sigma_K}$$

The random normalized parameters z_1 , z_2 , and z_3 are substituted for m_1 , m_2 , and K , respectively, in Eq. (3.6) to convert the limit-state function to $g(z_1, z_2, z_3)$.

Choosing nominal parameter values $m_1 = 10$ kg, $m_2 = 15$ kg, $C = 10$ Ns/m, $K = 8,000$ N/m, and $F_1 = F_2 = 1$ N, the FRF of this 2DOF model is shown in Fig. 3.8 and the FRFs (with 10^4 samples of Monte Carlo simulation) with 10% CV in the three random parameters (m_1 , m_2 , and K) are shown in Fig. 3.9.

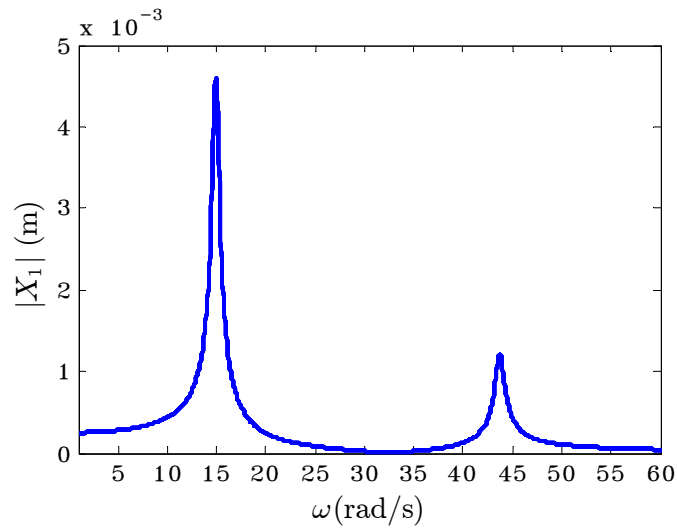


Figure 3.8: The FRF of 2DOF model with nominal parameters.

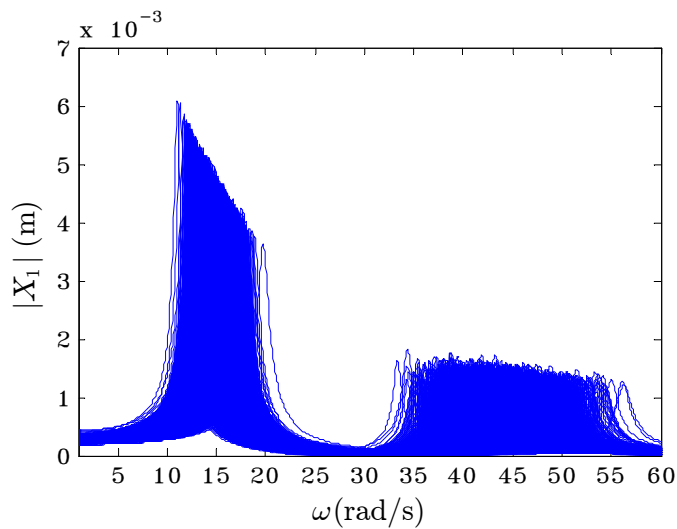


Figure 3.9: The FRFs (10^4 samples) of 2DOF model with three random parameters.

The failure surface for three random parameters now forms a three-dimensional space. Here to make use of FORM, it is necessary to define β_0 (the distance from the origin to the nearest point on the surface), given that the normal vector of the tangential plane at that point points to the origin. Define β_1 as the distance from the origin to the next-to-nearest point on the surface, given that the normal vector of the tangential plane at that point also points to the origin. There are two cases for calculating the failure probability. If the origin is inside the failure surface, the failure probability is $\Phi(\beta_0) - \Phi(-\beta_1)$. If the origin is outside of the failure surface, the failure probability is $\Phi(-\beta_0) - \Phi(-\beta_1)$.

The limit-state functions $g(z_1, z_2, z_3)$ for the 2DOF model from Eq. (3.6) with 10% CV in the three normalised random parameters at certain frequencies are shown in Figs. 3.10–3.16. The small black circles show the failure space and the large black circle shows the origin of z -coordinate.

Figs. 3.10 and 3.11 show the limit-state functions $g(z_1, z_2, z_3)$ for the 2DOF model at frequency 15 rad/s with failure levels $L = 2.75 \times 10^{-3}$ m and $L = 3.75 \times 10^{-3}$ m. It shows that when the failure level increases from $L = 2.75 \times 10^{-3}$ m to $L = 3.75 \times 10^{-3}$ m, the failure space reduces. The origins are inside of the failure space and the failure surface $g(z_1, z_2, z_3) = 0$ looks like two flat planes, then β_0 and β_1 are the shortest lines from the origin to the planes. The failure probability is $\Phi(\beta_0) - \Phi(-\beta_1)$ when β_0 is less than β_1 . When zoomed out, as in Fig. 3.12, the failure surfaces are found to be more complex.

Figs. 3.13–3.15, show the limit-state functions $g(z_1, z_2, z_3)$ of the 2DOF model at frequency 45 rad/s with failure levels $L = 0.3 \times 10^{-3}$ m, $L = 0.5 \times 10^{-3}$ m, and $L = 1.0 \times 10^{-3}$ m, respectively. The failure surfaces $g(z_1, z_2, z_3) = 0$ look like folded plane. In Figs 3.13, the origin is in the failure surface. When the failure level increases to $L = 0.5 \times 10^{-3}$ m as shown in Fig. 3.14, it is found that the failure surface shifts away from the origin causing a change in how the failure probability is calculated. The failure space obviously reduces when the failure level $L = 1.0 \times 10^{-3}$ m shown in Fig 3.15. When zoomed out, as in Fig. 3.16, the failure surfaces are found to be more complex.

In 2D, The failure surface changes its width, or moves when failure level changes. However, in 3D, it is more complicated. The failure surface should be plotted in order to see its shape and position.

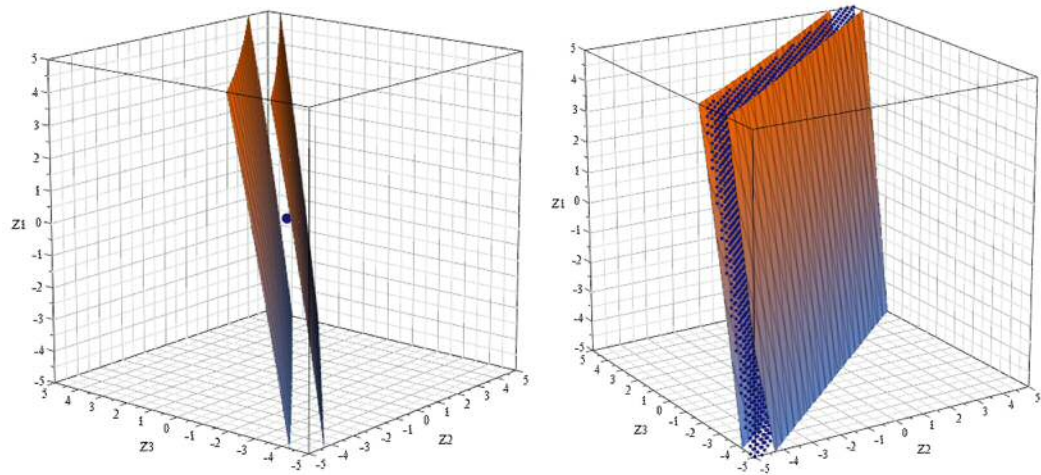


Figure 3.10: The limit-state function $g(z_1, z_2, z_3)$ of the 2DOF model at frequency 15 rad/s for $L = 2.75 \times 10^{-3}$ m.

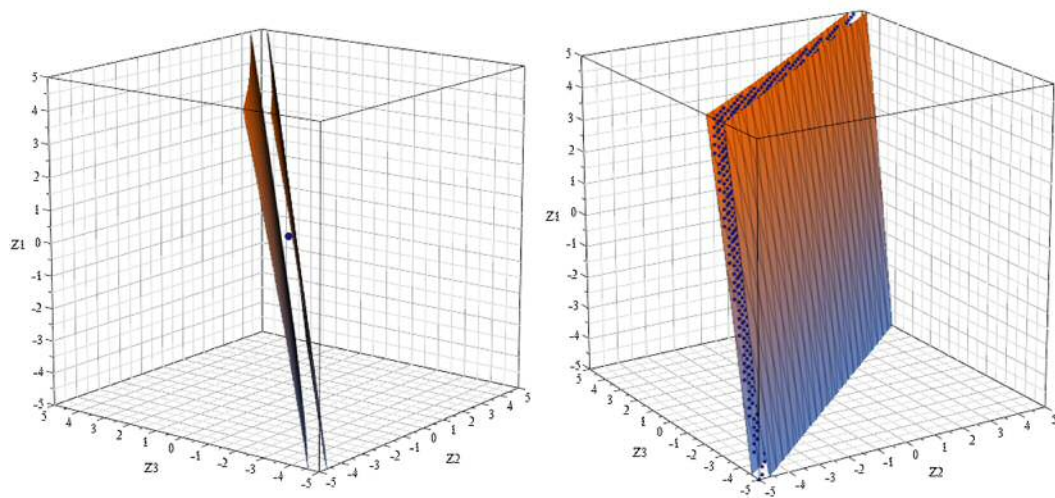


Figure 3.11: The limit-state function $g(z_1, z_2, z_3)$ of the 2DOF model at frequency 15 rad/s for $L = 3.75 \times 10^{-3}$ m.

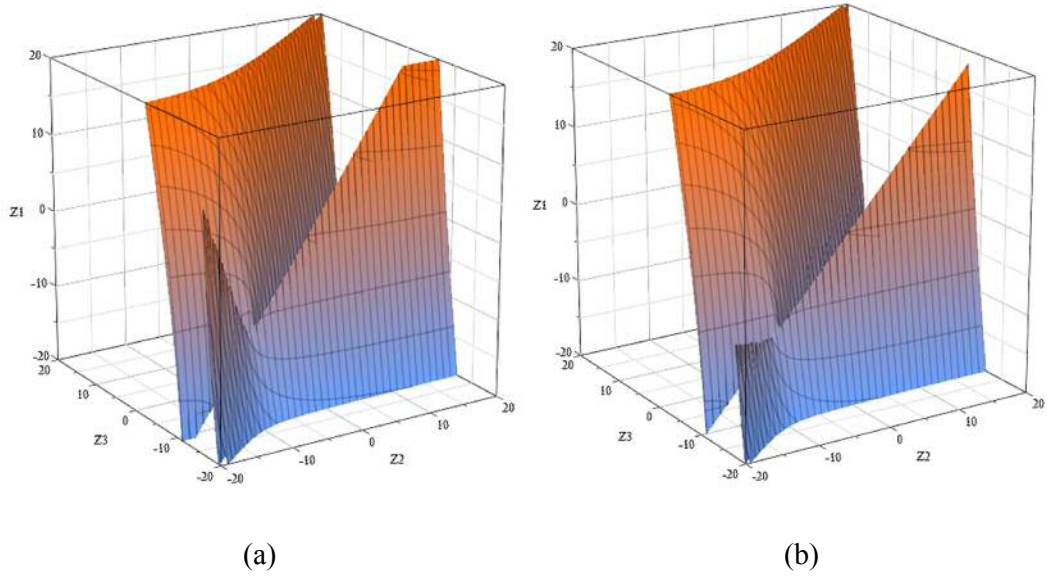


Figure 3.12: The limit-state function $g(z_1, z_2, z_3)$ of the 2DOF model at frequency 15 rad/s when zoomed out: (a) $L = 2.75 \times 10^{-3}$ m, (b) $L = 3.75 \times 10^{-3}$ m.

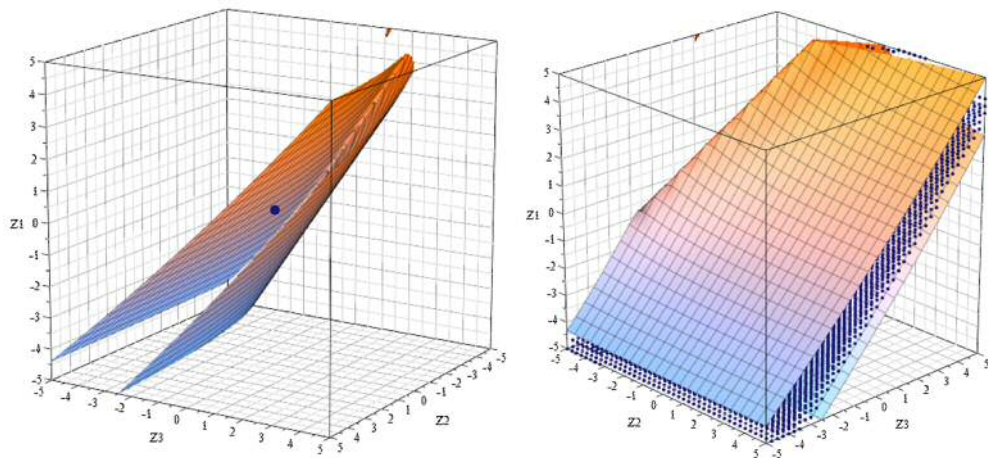


Figure 3.13: The limit-state function $g(z_1, z_2, z_3)$ of the 2DOF model at frequency 45 rad/s, $L = 0.3 \times 10^{-3}$ m.

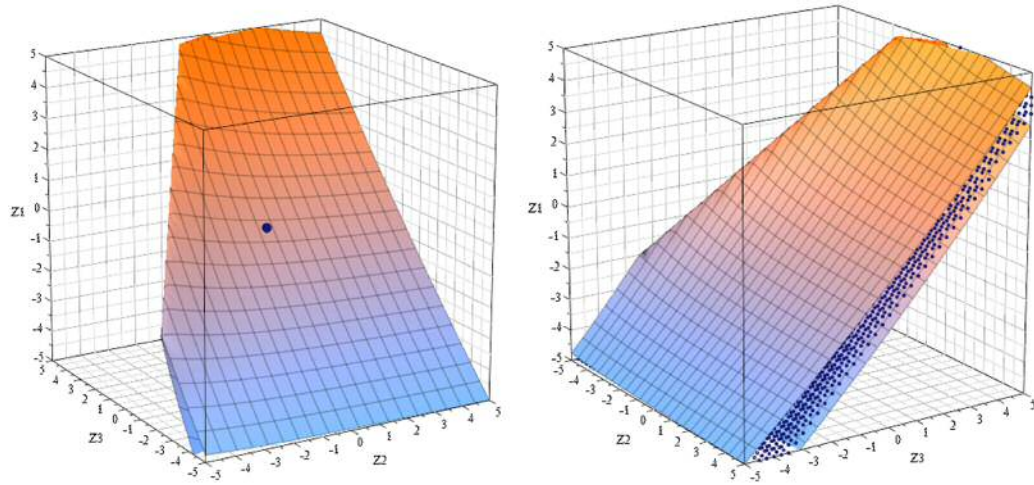


Figure 3.14: The limit-state function $g(z_1, z_2, z_3)$ of the 2DOF model at frequency 45 rad/s, $L = 0.5 \times 10^{-3}$ m.

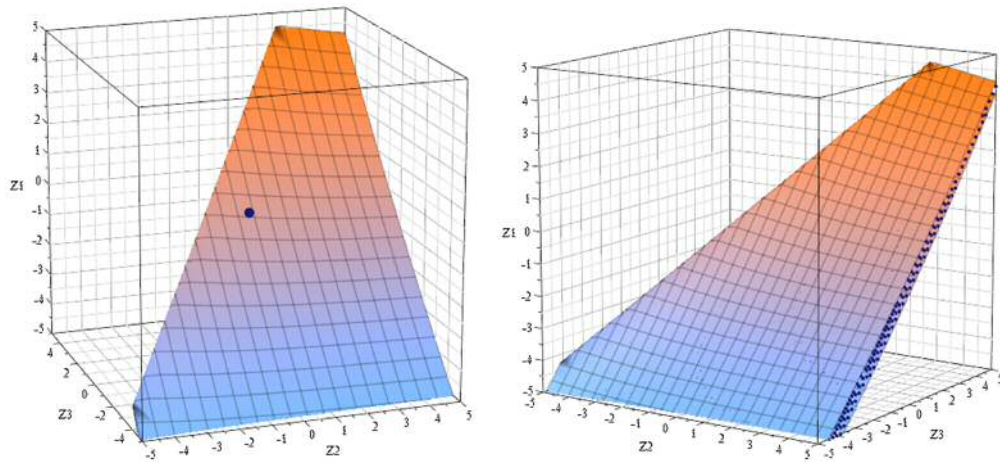


Figure 3.15: The limit-state function $g(z_1, z_2, z_3)$ of the 2DOF model at frequency 45 rad/s, $L = 1.0 \times 10^{-3}$ m.

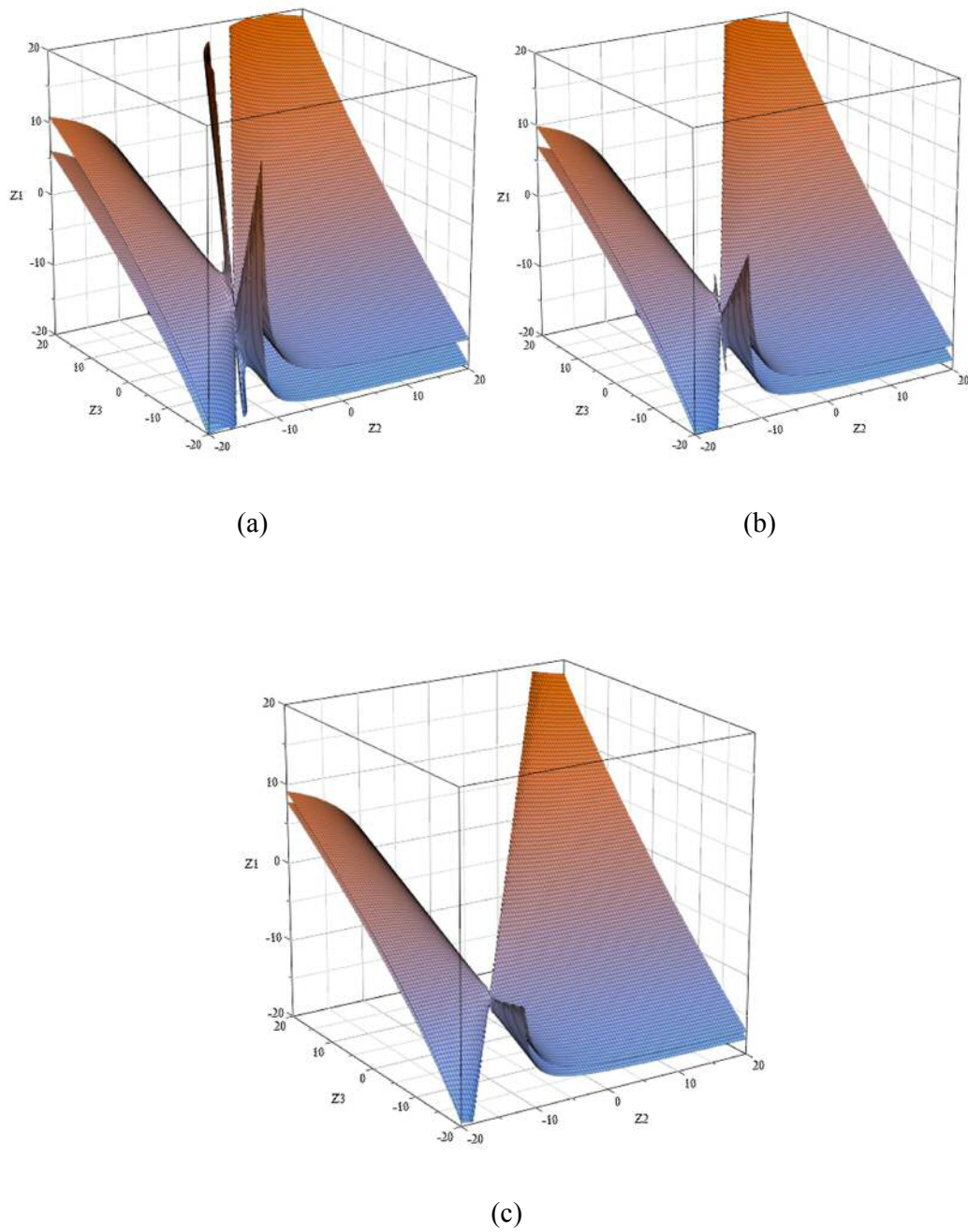


Figure 3.16: The limit-state function $g(z_1, z_2, z_3)$ of the 2DOF model at frequency 45 rad/s when zoomed out: (a) $L = 0.3 \times 10^{-3}$ m, (b) $L = 0.5 \times 10^{-3}$ m, (c) $L = 1.0 \times 10^{-3}$ m.

The comparison of the results from FORM, Monte Carlo simulation (10^4 simulations) with 95% confidence interval, and Direct Integration for the 2DOF model with 10% CV in the three random parameters at certain frequencies is shown in Table 3.5.

Table 3.5: Comparison of results from FORM, Monte Carlo simulation, and Direct Integration for the 2DOF model with 10% CV in the three random parameters.

ω (rad/s)	Failure level $\times 10^{-3}$ (m)	FORM				Monte Carlo simulation 95% confidence	Direct Integration
		β_0	β_1	Function of $P_f(F)$	$P_f(F)$	$P_f(F)$	$P_f(F)$
15	2.75	0.4336	0.5617	$\Phi(\beta_0) - \Phi(-\beta_1)$	0.3806	0.3763 ± 0.0095	0.3808
	3.00	0.3795	0.4937	$\Phi(\beta_0) - \Phi(-\beta_1)$	0.3371	0.3345 ± 0.0092	0.3333
	3.25	0.3097	0.4325	$\Phi(\beta_0) - \Phi(-\beta_1)$	0.2889	0.2873 ± 0.0089	0.2892
	3.50	0.2550	0.3760	$\Phi(\beta_0) - \Phi(-\beta_1)$	0.2472	0.2501 ± 0.0085	0.2474
	3.75	0.2024	0.3219	$\Phi(\beta_0) - \Phi(-\beta_1)$	0.2064	0.2092 ± 0.0080	0.2066
	4.00	0.1494	0.2677	$\Phi(\beta_0) - \Phi(-\beta_1)$	0.1649	0.1659 ± 0.0073	0.1650
	4.25	0.0916	0.2090	$\Phi(\beta_0) - \Phi(-\beta_1)$	0.1193	0.1196 ± 0.0064	0.1191
	4.50	0.0130	0.1294	$\Phi(\beta_0) - \Phi(-\beta_1)$	0.0567	0.0540 ± 0.0044	0.0499
45	0.3	0.2363	1.056	$\Phi(\beta_0) - \Phi(-\beta_1)$	0.4479	0.4396 ± 0.0097	0.4466
	0.4	0.0452	0.8999	$\Phi(\beta_0) - \Phi(-\beta_1)$	0.3339	0.3274 ± 0.0092	0.3325
	0.5	0.0705	0.8003	$\Phi(-\beta_0) - \Phi(-\beta_1)$	0.2601	0.2541 ± 0.0085	0.2584
	0.6	0.1497	0.7299	$\Phi(-\beta_0) - \Phi(-\beta_1)$	0.2078	0.2074 ± 0.0079	0.2056
	0.7	0.2088	0.6761	$\Phi(-\beta_0) - \Phi(-\beta_1)$	0.1678	0.1682 ± 0.0073	0.1649
	0.8	0.2560	0.6323	$\Phi(-\beta_0) - \Phi(-\beta_1)$	0.1354	0.1325 ± 0.0066	0.1311
	0.9	0.2962	0.5944	$\Phi(-\beta_0) - \Phi(-\beta_1)$	0.1074	0.1030 ± 0.0060	0.1012
	1.0	0.3329	0.5592	$\Phi(-\beta_0) - \Phi(-\beta_1)$	0.0816	0.0782 ± 0.0053	0.0739

From Table 3.5 at frequency 15 rad/s, the origin is always inside of the failure space for all failure levels but at frequency 45 rad/s, the origin is not always inside of the failure space. When the failure level increases from $L = 0.4 \times 10^{-3}$ m to $L = 0.5 \times 10^{-3}$ m, the origin moves away from failure space, causing the failure probability function to change from $\Phi(\beta_0) - \Phi(-\beta_1)$ to $\Phi(-\beta_0) - \Phi(-\beta_1)$.

Tables 3.5 shows a comparison of the predicted results for FORM, Monte Carlo simulation, and Direct Integration for the 2DOF model with three random parameters. The results from FORM and Direct Integration are again similar, and give good agreement with Monte Carlo simulation.

3.2.3 Three Degree of Freedom Model

The free body diagram of a 3DOF model is shown in Fig. 3.17. This is a standard linear system excited with an equal phased harmonic forcing at the same frequency but different amplitude. The study looks at the steady-state harmonic response to $F_1(t)$, $F_2(t)$, and $F_3(t)$.

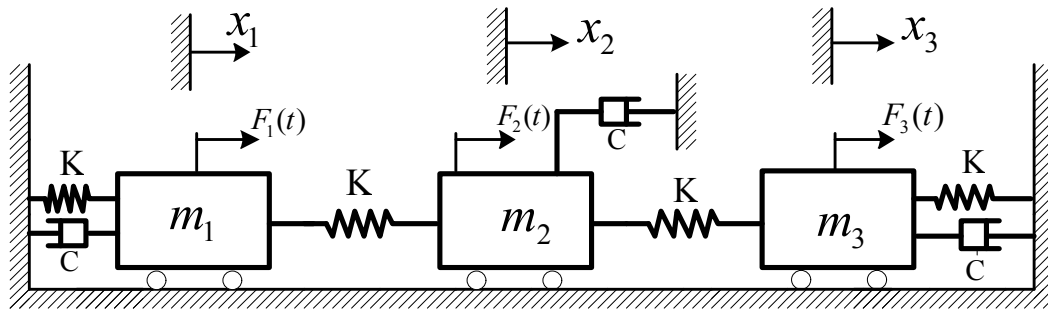


Figure 3.17: The 3DOF model.

The equation of motion is given for the system as:

$$[m]\ddot{\mathbf{x}} + [C]\dot{\mathbf{x}} + [K]\mathbf{x} = \mathbf{F} \quad (3.7)$$

where

$$\mathbf{x} = \begin{Bmatrix} x_1 \\ x_2 \\ x_3 \end{Bmatrix}, [m] = \begin{bmatrix} m_1 & 0 & 0 \\ 0 & m_2 & 0 \\ 0 & 0 & m_3 \end{bmatrix}, [C] = \begin{bmatrix} C & 0 & 0 \\ 0 & C & 0 \\ 0 & 0 & C \end{bmatrix},$$

$$[\mathbf{K}] = \begin{bmatrix} 2K & -K & 0 \\ -K & 2K & -K \\ 0 & -K & 2K \end{bmatrix}, \text{ and } \mathbf{F} = \begin{Bmatrix} F_1 \sin \omega t \\ F_2 \sin \omega t \\ F_3 \sin \omega t \end{Bmatrix}$$

Its steady-state solution is $\mathbf{X} = \mathbf{Z}(i\omega)^{-1}\mathbf{F}$, where

$$\mathbf{Z}(i\omega) = \begin{bmatrix} Z_{11} & Z_{12} & Z_{13} \\ Z_{21} & Z_{22} & Z_{23} \\ Z_{31} & Z_{32} & Z_{33} \end{bmatrix}; \quad Z_{ij}(i\omega) = -\omega^2 m_{ij} + i\omega C_{ij} + K_{ij}$$

is the impedance and \mathbf{F} is $\{F_1 \ F_2 \ F_3\}^T$. Therefore, the solutions are

$$X_1 = \frac{(Z_{12}Z_{23} - Z_{13}Z_{22})F_3 - (Z_{12}Z_{33} - Z_{13}Z_{32})F_2 + (Z_{22}Z_{33} - Z_{23}Z_{32})F_1}{Z_{11}Z_{22}Z_{33} + Z_{12}Z_{23}Z_{31} + Z_{13}Z_{21}Z_{32} - Z_{11}Z_{23}Z_{32} - Z_{12}Z_{21}Z_{33} - Z_{13}Z_{22}Z_{31}} \quad (3.8)$$

$$X_2 = \frac{(Z_{11}Z_{33} - Z_{13}Z_{31})F_2 - (Z_{11}Z_{23} - Z_{13}Z_{21})F_3 - (Z_{21}Z_{33} - Z_{23}Z_{31})F_1}{Z_{11}Z_{22}Z_{33} + Z_{12}Z_{23}Z_{31} + Z_{13}Z_{21}Z_{32} - Z_{11}Z_{23}Z_{32} - Z_{12}Z_{21}Z_{33} - Z_{13}Z_{22}Z_{31}} \quad (3.9)$$

and

$$X_3 = \frac{(Z_{11}Z_{22} - Z_{12}Z_{21})F_3 - (Z_{11}Z_{32} - Z_{12}Z_{31})F_2 + (Z_{21}Z_{32} - Z_{22}Z_{31})F_1}{Z_{11}Z_{22}Z_{33} + Z_{12}Z_{23}Z_{31} + Z_{13}Z_{21}Z_{32} - Z_{11}Z_{23}Z_{32} - Z_{12}Z_{21}Z_{33} - Z_{13}Z_{22}Z_{31}} \quad (3.10)$$

The limit-state function $g(m_1, m_2, K)$ is defined in terms of the frequency response function. Failure is deemed to occur if the frequency response X_1 exceeds level L , in other words, if the response exceeds level L , then $g < 0$, and the system fails, where g is defined as:

$$g(m_1, m_2, K) = L - |X_1| \quad (3.11)$$

The random parameters (m_1, m_2, K) are normalised to zero mean and normal standard deviation:

$$z_1 = \frac{m_1 - \mu_{m_1}}{\sigma_{m_1}}, \quad z_2 = \frac{m_2 - \mu_{m_2}}{\sigma_{m_2}}, \quad \text{and} \quad z_3 = \frac{K - \mu_K}{\sigma_K} \quad (3.12)$$

The random normalized parameters $z_1, z_2,$ and z_3 are substituted for $m_1, m_2,$ and K , respectively, in Eq. (3.11) to convert the limit-state function to $g(z_1, z_2, z_3)$.

Choosing nominal parameter values $m_1 = 10$ kg, $m_2 = 20$ kg, $m_3 = 50$ kg, $C = 10$ Ns/m, $K = 8,000$ N/m, and $F_1 = F_2 = 1$ N, the FRF of 3DOF model with nominal parameters is shown in Fig. 3.18. The FRFs (with 10^4 samples from Monte Carlo simulation) of the

3DOF model system with 10% CV in the three random parameters are shown in Fig. 3.19.

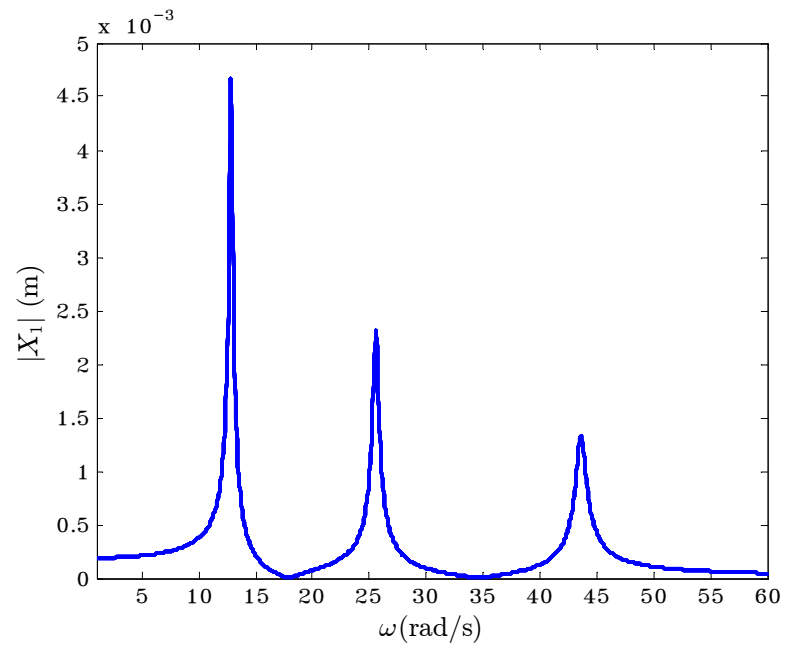


Figure 3.18: The FRF of 3DOF model with nominal parameters.

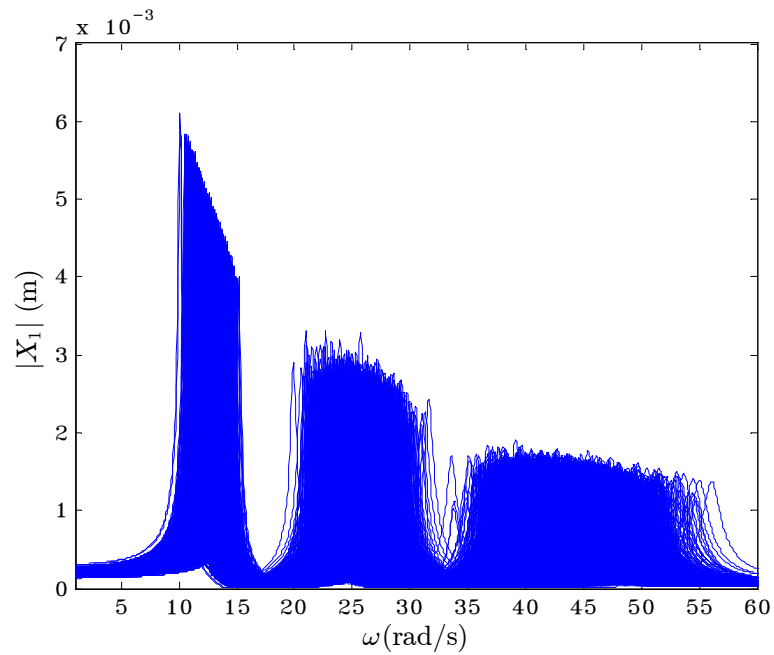


Figure 3.19: The FRFs (10^4 samples) of 3DOF model with three random parameters.

The limit-state functions $g(z_1, z_2, z_3)$ of the 3DOF model from Eq. (3.11) with 10% CV in the three normalised random parameters at certain frequencies are shown in Figs. 3.20–3.22. The small black circles show the failure space and the large black circle shows the origin.

Fig. 3.20 shows the limit-state function $g(z_1, z_2, z_3)$ of the 3DOF model at frequency 12 rad/s with failure levels $L = 2.0 \times 10^{-3}$ m. The failure surface $g(z_1, z_2, z_3) = 0$ looks like two flat planes, then the β_0 and β_1 are the shortest distances from the origin to the planes. The origin is outside of the failure space, so the failure probability is $\Phi(-\beta_0) - \Phi(-\beta_1)$ when β_0 is less than β_1 .

Fig. 3.21 shows the limit-state function $g(z_1, z_2, z_3)$ of the 3DOF model at frequency 25 rad/s with failure levels $L = 1.2 \times 10^{-3}$ m. The failure surface $g(z_1, z_2, z_3) = 0$ looks like two bent planes, then the β_0 and β_1 are the shortest lines from the origin to the planes. The origin is outside of the failure space, so the failure probability is $\Phi(-\beta_0) - \Phi(-\beta_1)$ when β_0 is less than β_1 .

Fig. 3.22 shows the limit-state function $g(z_1, z_2, z_3)$ of the 3DOF model at frequency 45 rad/s with failure levels $L = 0.6 \times 10^{-3}$ m. The failure surface $g(z_1, z_2, z_3) = 0$ looks like folded plane. The origin is outside of the failure space, hence the failure probability is $\Phi(-\beta_0) - \Phi(-\beta_1)$ when β_0 is less than β_1 .

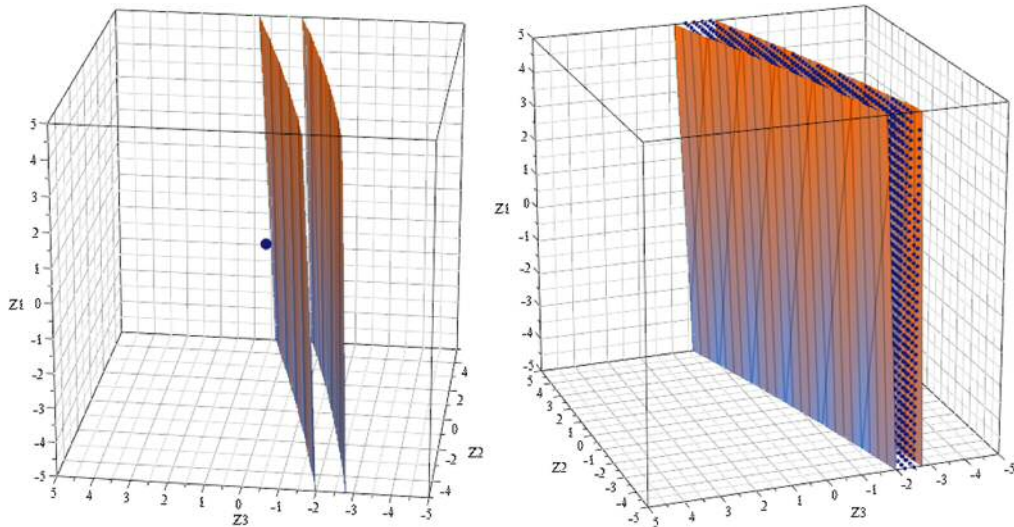


Figure 3.20: The limit-state function $g(z_1, z_2, z_3)$ of the 3DOF model at frequency 12 rad/s, $L = 2.0 \times 10^{-3}$ m.

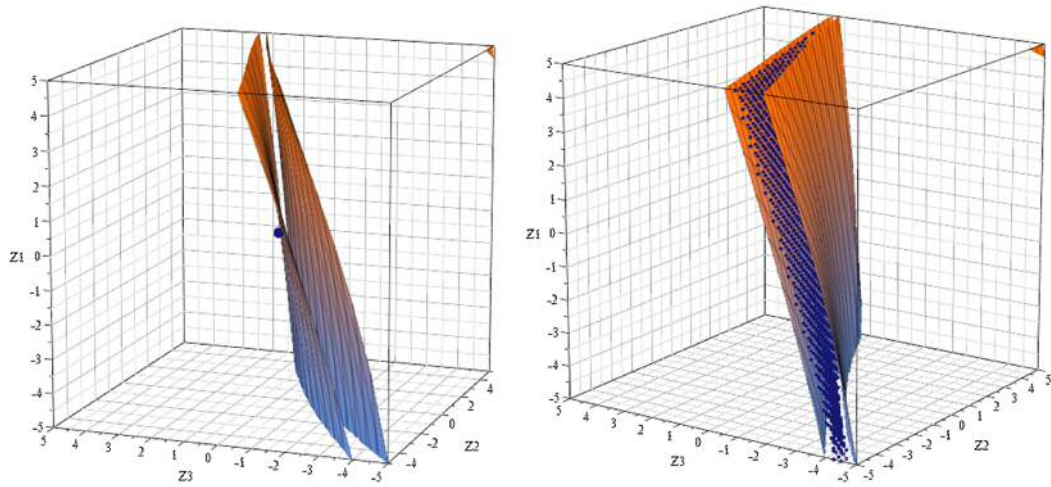


Figure 3.21: The limit-state function $g(z_1, z_2, z_3)$ of the 3DOF model at frequency 25 rad/s, $L = 1.2 \times 10^{-3}$ m.

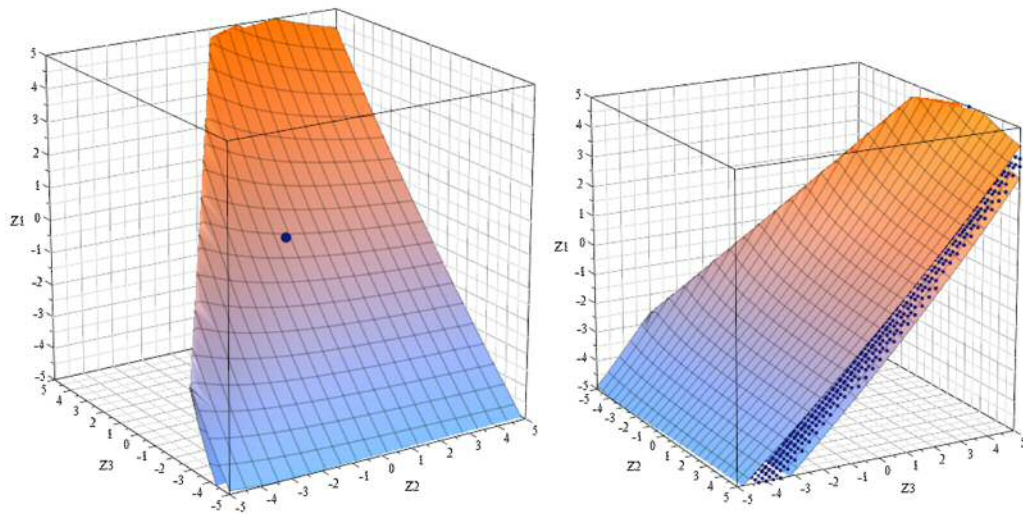


Figure 3.22: The limit-state function $g(z_1, z_2, z_3)$ of the 3DOF model at frequency 45 rad/s, $L = 0.6 \times 10^{-3}$ m.

The comparison of the results from FORM, Monte Carlo simulation (10^4 simulations) with 95% confidence interval, and Direct Integration for the 3DOF model with 10% CV in the three random parameters at certain frequencies is shown in Table 3.6.

Table 3.6: Comparison of results from FORM, Monte Carlo simulation, and Direct Integration for the 3DOF model with 10% CV in the three random parameters.

ω (rad/s)	Failure level $\times 10^{-3}$ (m)	FORM				Monte Carlo simulation 95% confidence	Direct Integration
		β_0	β_1	Function of $P_f(F)$	$P_f(F)$	$P_f(F)$	$P_f(F)$
12	2.0	0.6837	1.7181	$\Phi(-\beta_0) - \Phi(-\beta_1)$	0.2042	0.2087 ± 0.0080	0.2050
	2.5	0.8185	1.6027	$\Phi(-\beta_0) - \Phi(-\beta_1)$	0.1520	0.1533 ± 0.0071	0.1527
	3.0	0.9128	1.5189	$\Phi(-\beta_0) - \Phi(-\beta_1)$	0.1163	0.1158 ± 0.0063	0.1168
	3.5	0.9856	1.4524	$\Phi(-\beta_0) - \Phi(-\beta_1)$	0.0890	0.0912 ± 0.0056	0.0894
	4.0	1.0472	1.3949	$\Phi(-\beta_0) - \Phi(-\beta_1)$	0.0660	0.0663 ± 0.0049	0.0662
25	1.25	0.1147	0.6505	$\Phi(-\beta_0) - \Phi(-\beta_1)$	0.1967	0.1987 ± 0.0078	0.1974
	1.5	0.1815	0.5874	$\Phi(-\beta_0) - \Phi(-\beta_1)$	0.1495	0.1449 ± 0.0069	0.1499
	1.75	0.2349	0.5362	$\Phi(-\beta_0) - \Phi(-\beta_1)$	0.1112	0.1101 ± 0.0061	0.1109
	2.0	0.2830	0.4895	$\Phi(-\beta_0) - \Phi(-\beta_1)$	0.0763	0.0727 ± 0.0051	0.0738
	2.25	0.3372	0.4355	$\Phi(-\beta_0) - \Phi(-\beta_1)$	0.0364	0.0373 ± 0.0037	0.0353
45	0.6	0.1680	0.7896	$\Phi(-\beta_0) - \Phi(-\beta_1)$	0.2184	0.2191 ± 0.0081	0.2162
	0.7	0.2287	0.7356	$\Phi(-\beta_0) - \Phi(-\beta_1)$	0.1786	0.1797 ± 0.0075	0.1757
	0.8	0.2764	0.6923	$\Phi(-\beta_0) - \Phi(-\beta_1)$	0.1467	0.1441 ± 0.0069	0.1430
	0.9	0.3160	0.6557	$\Phi(-\beta_0) - \Phi(-\beta_1)$	0.1200	0.1165 ± 0.0063	0.1148
	1.0	0.3507	0.6230	$\Phi(-\beta_0) - \Phi(-\beta_1)$	0.0963	0.0920 ± 0.0057	0.0898

From Table 3.6, the origin is always inside of the failure space for all failure levels and frequencies, hence the failure probability from FORM is $\Phi(-\beta_0) - \Phi(-\beta_1)$.

The results from FORM and Direct Integration are again similar, and give good agreement with Monte Carlo simulation.

3.3 Conclusions of Chapter 3

After testing three methods (Direct Integration, FORM, and Monte Carlo simulation) for calculating the failure probability, the use of Direct Integration, which is a deterministic method, allows the failure probability to be calculated exactly from the limit-state function obtained from the equation of motion. However, if the number of variables is more than two, the Direct Integration computational complexity, in obtaining the exceedance or failure probability, increases. Therefore in general, there is a clear limitation to the practical application of Direct Integration.

For FORM, this method is the fastest, but more complicated than both Direct Integration and Monte Carlo simulation because the boundary function can be very complex and where the origin must be known. Then, it should be clear which function to be used to calculate the failure probability.

Monte Carlo simulation is almost always used as a benchmark but it takes considerable time to compute even simple structural responses with a small number of uncertain parameters. The greatest advantage of this method is its capabilities to handle unlimited random parameters and complex systems. In general, real structures have great complexity in geometry, and a large number of uncertain parameters. The time for repeating the analysis many hundreds of times or more, is a very major problem.

Objective (i) (of the thesis, given in the introduction) has been partially met in this chapter because the results are generated only at low frequency, the frequency range for the systems examined being below 100 rad/s, but with both high and low-level uncertainties. In summary then, it is evident that for low frequencies, Direct Integration and FORM are practically difficult to implement as the number of degrees of freedom increases. The next question is what is the scope and potential of SEA to handle low and high levels of uncertainty at high frequency.

Chapter 4

High Frequency Response Prediction for Simple Structures with High and Low-Level Uncertainties

The potential capability of several uncertain structure statistical prediction methods at low frequency was discussed in Chapter 3. The focus now switches to exploring the potential of high frequency methods in handling varying levels of uncertainty. These methods were discussed in Chapter 2, in particular, statistical energy analysis (SEA). The aim of this chapter is to demonstrate an application of SEA to simple plate structures with high and low-level uncertainties to predict mean levels and standard deviations. In Chapter 5, SEA is applied to a more complicated built-up structure but a simpler application is initially justified. Monte Carlo simulation, based on simple mode superposition, is used on this simple plate structure as a benchmark. The mean levels and standard deviations obtained using Monte Carlo simulations are compared with SEA predictions.

To be specific, in this chapter two types of uncertainty are examined namely i) dimension variability, and ii) thickness variability. This is to establish the capability and limitations of SEA prediction of both the mean and standard deviation of the energy response at the simplest level, i.e. a single plate as the level of variability is changed. This is followed by the use of the so-called ‘Statistical Overlap Factor (SOF)’ to establish its effectiveness in deciding for a plate structure the uncertainty range over which SEA can be confidentially used. The focus then switches to an examination of the probability distribution of the energy response for a single plate. To confirm the SEA prediction for an accurate and efficient transfrequency. Monte Carlo simulation method is developed using a mode superposition method and compared with ANSYS. These results are generated as a built-up (along with more complicated results in Chapter 5) to the development of an extreme value approach to handle different levels of variability.

4.1 A Single Plate Model

There are many methods available to obtain natural frequencies and forced response predictions of deterministic rectangular plates e.g., the Ritz method (Aydogdu, 2005), the mode superposition method (Gorman, 1999); the method DSC (Secgin et al, 2012), and mode superposition using mode shapes from a virtual work method (Arenas, 2003). The mode superposition method will be used to undertake Monte Carlo simulation in this chapter. Before then, the simple plate theory and a SEA modelling approach are described.

Simple Plate Theory

For a thin plate, the bending wave equation for transverse vibration of an isotropic, undamped plate subjected to a concentrated load at point (x_0, y_0) is given (Crocker, 1967) as:

$$D\nabla^4 w + \rho \frac{\partial^2 w}{\partial t^2} = F(t)\delta(x - x_0)\delta(y - y_0) \quad (4.1)$$

where w is the plate displacement, D is the bending stiffness defined by the relation $D = Eh^3/12(1 - \nu^2)$, E is the modulus of elasticity (Young's modulus), ν is Poisson's ratio, h is the thickness of the plate, ρ is the mass density per unit area of the plate, and $F(t)$ represents the dynamic amplitude of an external point force, where δ is the Dirac delta function.

4.1.1 The SEA Model

In this section, an SEA model for a single plate is constructed by using Eq. (2.6) and Eq. (2.66) to predict the mean and variance of the energy, respectively. The power input subjected to a unit point force is as given in Eq. (2.65).

The following material, the velocity square and energy levels in dB scale are quantified as the American National Standard definitions given in Beranek (1971) as follows:

$$L_{V^2} = 10\log_{10}\left(\frac{V^2}{V_{ref}^2}\right) = 20\log_{10}\left(\frac{V}{V_{ref}}\right) \quad \text{dB ref. } V_{ref} \text{ m/s}$$

$$L_E = 10 \log_{10} \left(\frac{E}{E_{ref}} \right) \quad \text{dB ref. } E_{ref} \text{ J}$$

Fig. 4.1 shows the SEA prediction of the mean energy compared with Fig. 9a from Cotoni et al. (2005) for a single plate structure. The properties of the plate are $E = 2.1 \times 10^{11} \text{ Nm}^{-2}$, $\nu = 0.3$, mass density = 7800 kg m^{-3} , $A = 2 \text{ m}^2$, $h = 1 \text{ mm}$, $\eta = 1.39\%$, $m = 15.6 \text{ kg}$, and external force is a single point load. Both SEA predictions are identical.

For a single plate, there is only one subsystem, hence Eq. (2.66) can be rewritten as $\text{Var}(\hat{E}) = (D_0^{-1})^2 \text{Var}(P_{ran})$.

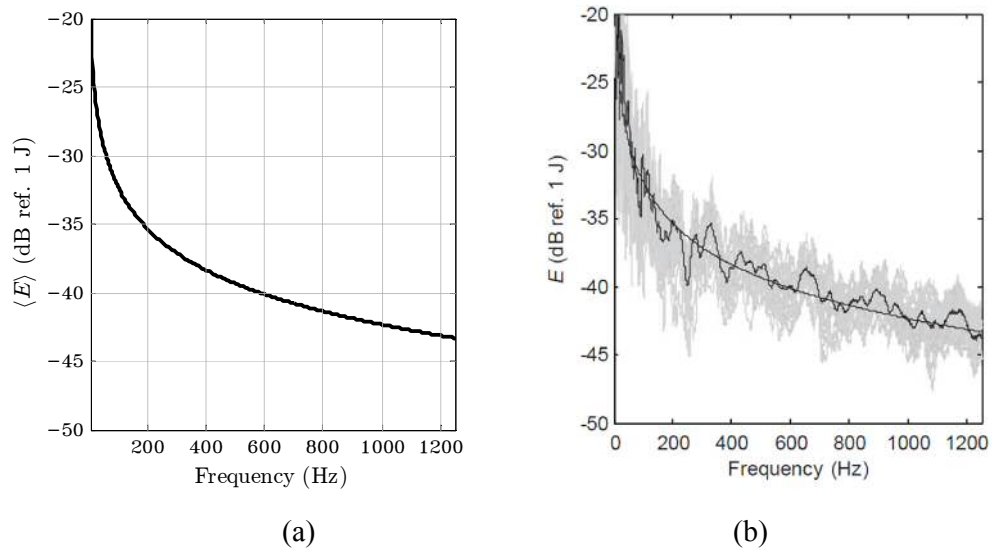


Figure 4.1: The mean energy of the plate with a single point load as a function of frequency: (a) Using Eq. (2.6); (b) figure taken from Cotoni et al (2005). Grey: response of each experimental sample, fluctuating black: mean response over all 19 samples, smooth line: SEA prediction.

Fig. 4.2 shows the SEA prediction of the relative variance of the pure-tone energy ($B' = 0$) is compared with Fig. 10 taken from Cotoni et al (2005) for this single plate structure with the single point load ($\alpha'_1 = 2.7$ given from Cotoni et al (2005)) and five point loads ($\alpha'_1 = 1.34$ given from Cotoni et al (2005)). The properties of the plate are the same as Fig. 4.1. Both SEA predictions are identical.

Fig. 4.3 shows the SEA prediction of the relative variance of the frequency-band-averaged energy ($B' = 10$ given from Cotoni et al (2005)) is compared with Fig. 11 taken from Cotoni et al (2005) for the single plate structure with the single point load

($\alpha'_1=2.7$ given from Cotoni et al (2005)) and five point loads ($\alpha'_1=1.34$ given from Cotoni et al (2005)). The properties of the plate are the same as Fig. 4.1. Both SEA predictions are identical.

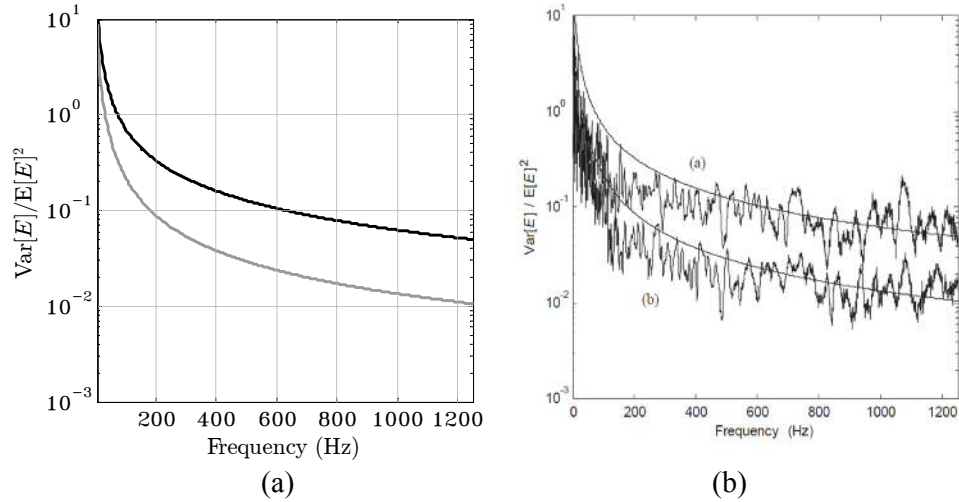


Figure 4.2: Relative variance of the pure-tone energy of the plate with a single point load as a function of frequency: (a) Using Eq. (2.66), black line: one point load, grey line: five point loads; (b) figure taken from Cotoni et al (2005): [a] one point load, [b] five point loads. Fluctuating curves: experimental results, smooth lines: prediction.

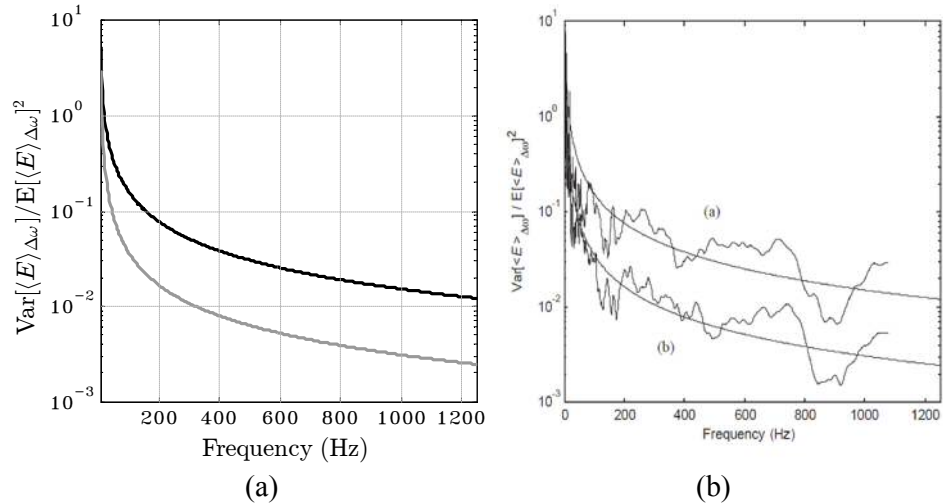


Figure 4.3: Relative variance of the frequency-band-averaged energy of the plate with a single point load as a function of frequency: (a) Using Eq. (2.65), black line: one point load, grey line: five point loads; (b) figure taken from Cotoni et al (2005): [a] one point load, [b] five point loads. Fluctuating curves: experimental results, smooth lines: prediction.

The next section will present the method that is used to generate FRFs of a simply-supported plate for Monte Carlo simulations used as a benchmark to validate SEA.

4.1.2 Mode Superposition Method

To create a simple plate Monte Carlo simulation capability the FRF response of a simply-supported plate with material damping, subjected to a harmonic point force, can be obtained by using mode superposition. The solution is given by Gorman (1999) as

$$w(x, y) = \sum_{m=1}^{\infty} \sum_{n=1}^{\infty} W_{mn} \sin \frac{m\pi x}{L_x} \sin \frac{n\pi y}{L_y} \quad (4.2)$$

where

$$W_{mn} = \frac{\frac{4F}{L_x L_y \rho} \sin \frac{m\pi x_0}{L_x} \sin \frac{n\pi y_0}{L_y}}{\left\{ \sqrt{\frac{D}{\rho}} \left[\left(\frac{m\pi}{L_x} \right)^2 + \left(\frac{n\pi}{L_y} \right)^2 \right] \right\}^2 - \omega^2} \quad (4.3)$$

and (x_0, y_0) is a coordinate of a point force. The natural frequency equation is given as

$$\omega_{mn} = \sqrt{\frac{D}{\rho} \left[\left(\frac{m\pi}{L_x} \right)^2 + \left(\frac{n\pi}{L_y} \right)^2 \right]} \quad (4.4)$$

where $D = Eh^3/12(1 - \nu^2)$ and ρ_j is the mass per unit area of plate. The absolute velocity at (x, y) location can be converted from Eq. (4.2) as follows:

$$|V(x, y)| = \omega |w(x, y)|$$

Then spatially averaged velocity square of the plate can be defined as

$$\langle |V|^2 \rangle = \frac{1}{N_x N_y} \sum_{i=1}^{N_x} \sum_{j=1}^{N_y} |V(x_i, y_j)|^2 \quad (4.5)$$

where N_x and N_y are the number of the points in x and y axis, respectively.

The energy of the plate can then be defined as:

$$E = m \langle |V|^2 \rangle \quad (4.6)$$

where m is the mass of the plate.

It is necessary to validate that FEM program ANSYS can be applied to a simply-supported plate comparing with the mode superposition before proceeding to built-up structure in Chapter 4. Hence, a simply-supported plate subjected to a single point load located at the point (0.14, 0.12) is tested, with a 1 Hz frequency step at frequency from 10 Hz to 1000 Hz and the bending motion is considered. The properties of the plate are shown in Table 4.1. Fig. 4.4 shows that the spatially averaged velocity obtained from the mode superposition in Eq. (4.5) agrees with FEM (ANSYS).

The following section will show capability of the SEA by comparing with Monte Carlo simulations using the mode superposition method for plate dimension and plate thickness variation.

Table 4.1: Properties of the simply-supported plate used to benchmark the Monte Carlo simulation method.

Plate width (m)	0.3
Plate length (m)	0.4
Thickness (mm)	1
Loss factor	0.01
Young's modulus (N/m ²)	2×10^{11}
Density (kg/m ³)	7900
Poisson ratio	0.3

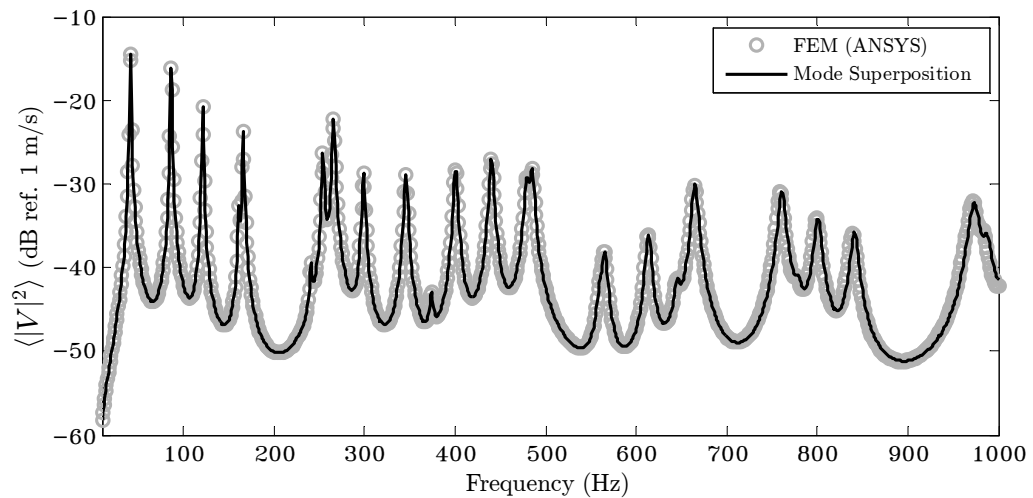


Figure 4.4: Comparison the spatially averaged velocity of the simply-supported plate with a single point load between mode superposition in Eq. (4.5) and FEM (ANSYS).

4.1.3 Dimension Variation

In this section, the plate dimension (i.e. the length along the x-axis) will be randomised by a uniform distribution with variability levels of CV 1%, 5%, 10%, 20%, and 30%. An ensemble of 1000 systems has been considered for each example. The properties of the plate are shown in Table 4.1 and a single point load is applied and located at point (0.14, 0.12). In Monte Carlo simulation, the mode superposition method has been used to generate the displacements, which is then converted to energy by using Eq. (4.6), with frequencies from 10 Hz up to 10000 Hz in 201 intervals.

The energy of the plate, for each of the 1000 generated samples, and the ensemble mean energy value, for variability levels of CV 1%, 5%, 10%, 20%, and 30% of the plate dimension as a function of frequency, are shown in Fig. 4.5. It is clear that the scatter in the energy is higher when the degree of variability increases.

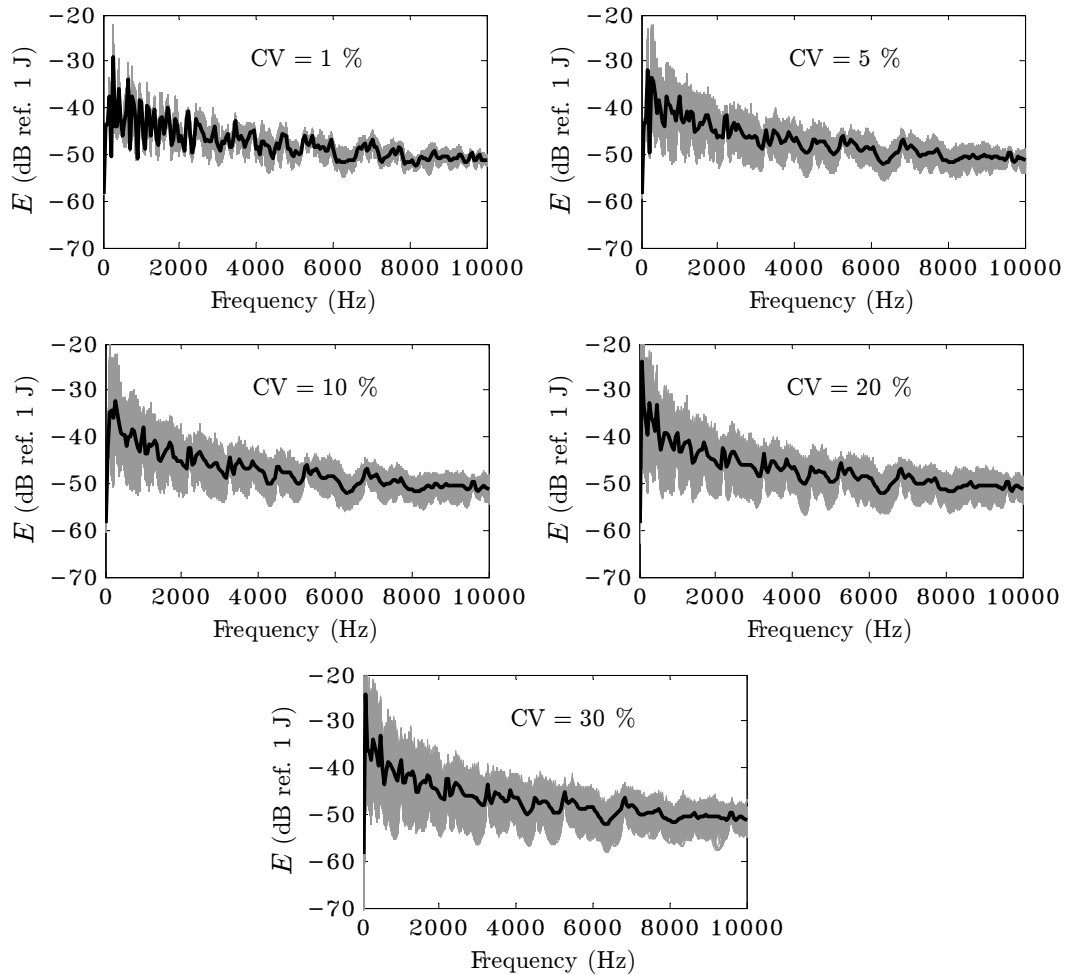


Figure 4.5: The energy of the plate subjected to a single point load via Monte Carlo simulation with CV values of 1%, 5%, 10%, 20%, and 30% for the plate dimension variation as a function of frequency.

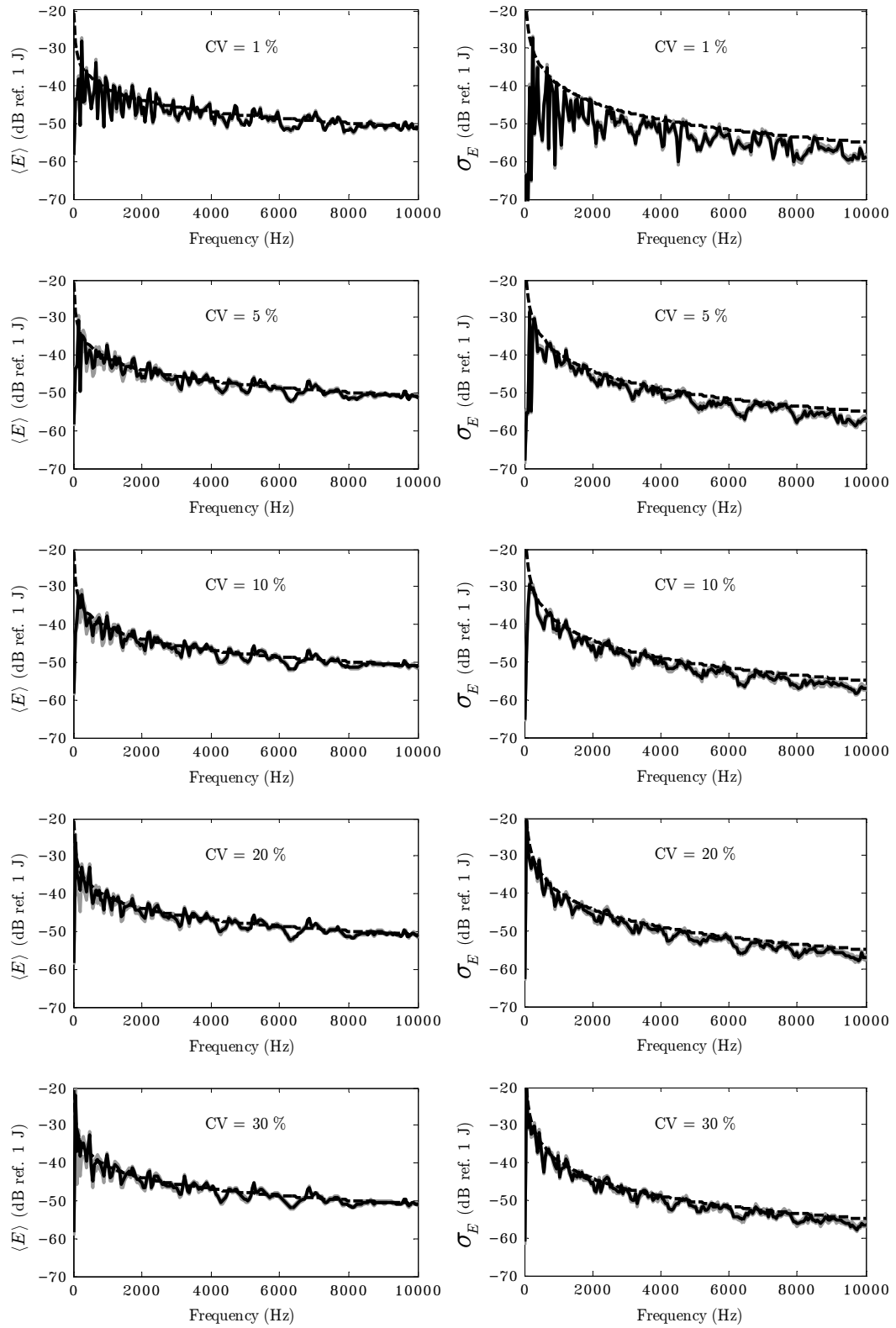


Figure 4.6: The mean and standard deviation of the energy of the plate via SEA and Monte Carlo simulation with CV values of 1%, 5%, 10%, 20%, and 30% for the plate dimension variation as a function of frequency.

Fig. 4.6 shows the SEA predictions for the mean and standard deviation of the energy of the plate with variability levels of CV 1%, 5%, 10%, 20%, and 30% of the plate dimension as a function of frequency compared with the corresponding mean and standard deviation obtained from Monte Carlo simulation. The SEA predictions are smooth dashed curves and Monte Carlo simulations are fluctuating curves. The number of Monte Carlo runs for all of Monte Carlo simulations was selected to be 1000. The confidence level was selected to be 95%. Eqs. (2.89) and (2.91) are then used to calculate the confidence interval of the mean of energy and standard deviation of energy, respectively. The bounds of the confidence intervals are shown in grey lines along the mean and standard deviation of the energy. However, normally, the confidence level and confidence interval are chosen to determine the (minimum) number of Monte Carlo runs.

Fig. 4.6 demonstrates that the comparisons of the mean and the standard deviation of energy between the SEA and Monte Carlo results give good agreement for all CV values. The mean and standard deviation obtained by Monte Carlo simulations become increasingly smooth (with less scatter) as the level of variability increases. The mean curves at high frequency are smoother than at low frequency. Besides, the predicted SEA mean is increasingly accurate within the high frequency region

In the next section, randomization of the plate is achieved by thickness variation.

4.1.4 Thickness Variation

In this section, the thickness of the plate will be randomised by a uniform distribution with variability levels of CV 1%, 5%, 10%, 20%, and 30%. The properties of the plate are shown in Table 4.1 and a single point load is applied and located at the point (0.14, 0.12). The number of simulations is selected at 1000 samples. For each simulation, the mode superposition method has been used to generate the displacements, which are then converted to energy by using Eq. (4.6) For Monte Carlo simulation, the mode superposition method has been used to generate the displacements, which is then converted to energy by using Eq. (4.6), with frequencies from 10 Hz up to 10000 Hz in 201 intervals.

Fig. 4.7 shows the energy of the plate for each of the 1000 generated samples and the ensemble mean with variability levels of CV 1%, 5%, 10%, 20%, and 30% of the plate thickness as a function of frequency. It is evident that the scatter in energy is higher when the degree of variability increases. On the contrary, the ensemble mean is smoother when the degree of variability increases for entire frequency range. The mean curves at high frequency are smoother than at low frequency.

Fig. 4.8 shows the SEA predictions for the mean and standard deviation of the energy of the plate with variability levels of CV 1%, 5%, 10%, 20%, and 30% of the plate thickness as a function of frequency compared with the results from Monte Carlo simulations. The SEA predictions are smooth dashed curves and Monte Carlo simulations are fluctuating curves.

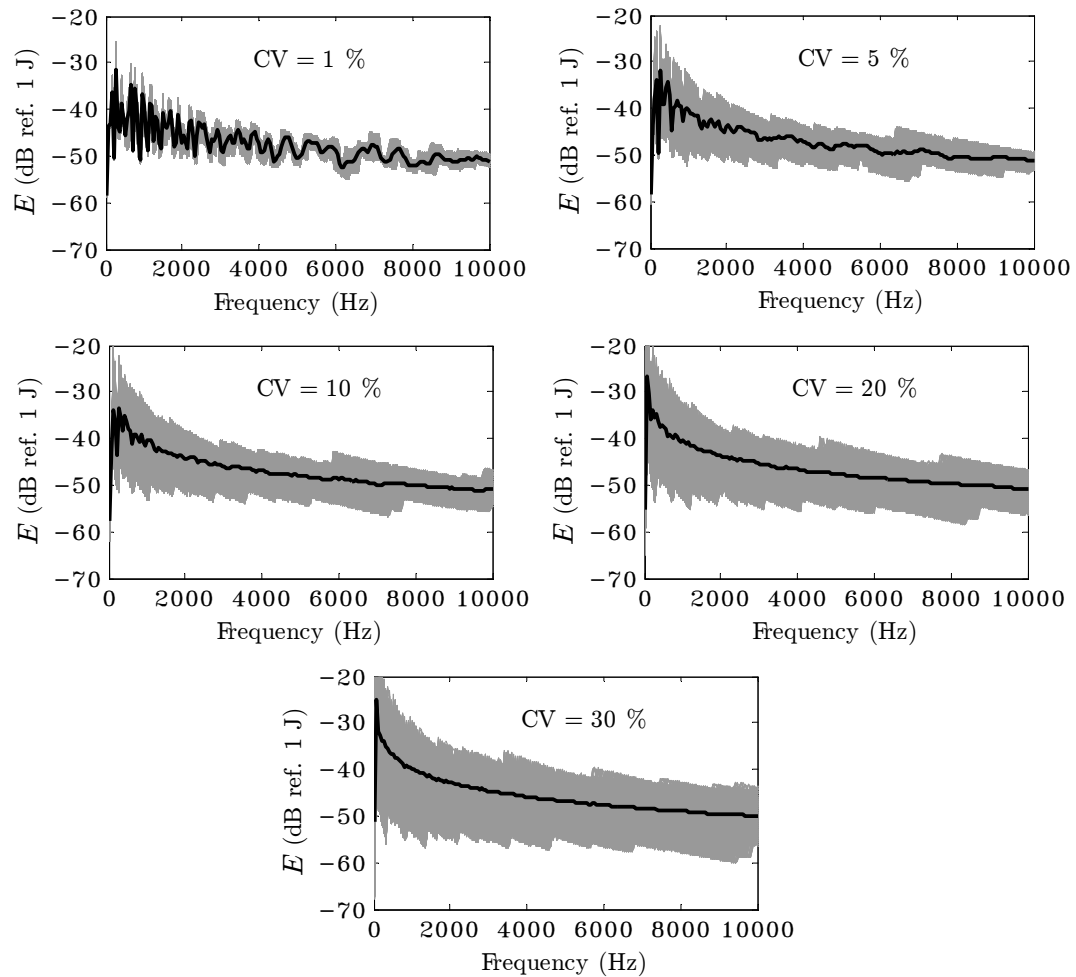


Figure 4.7: The energy of the plate with a single point load via Monte Carlo simulation with CV values of 1%, 5%, 10%, 20%, and 30% for the plate thickness variation as a function of frequency.

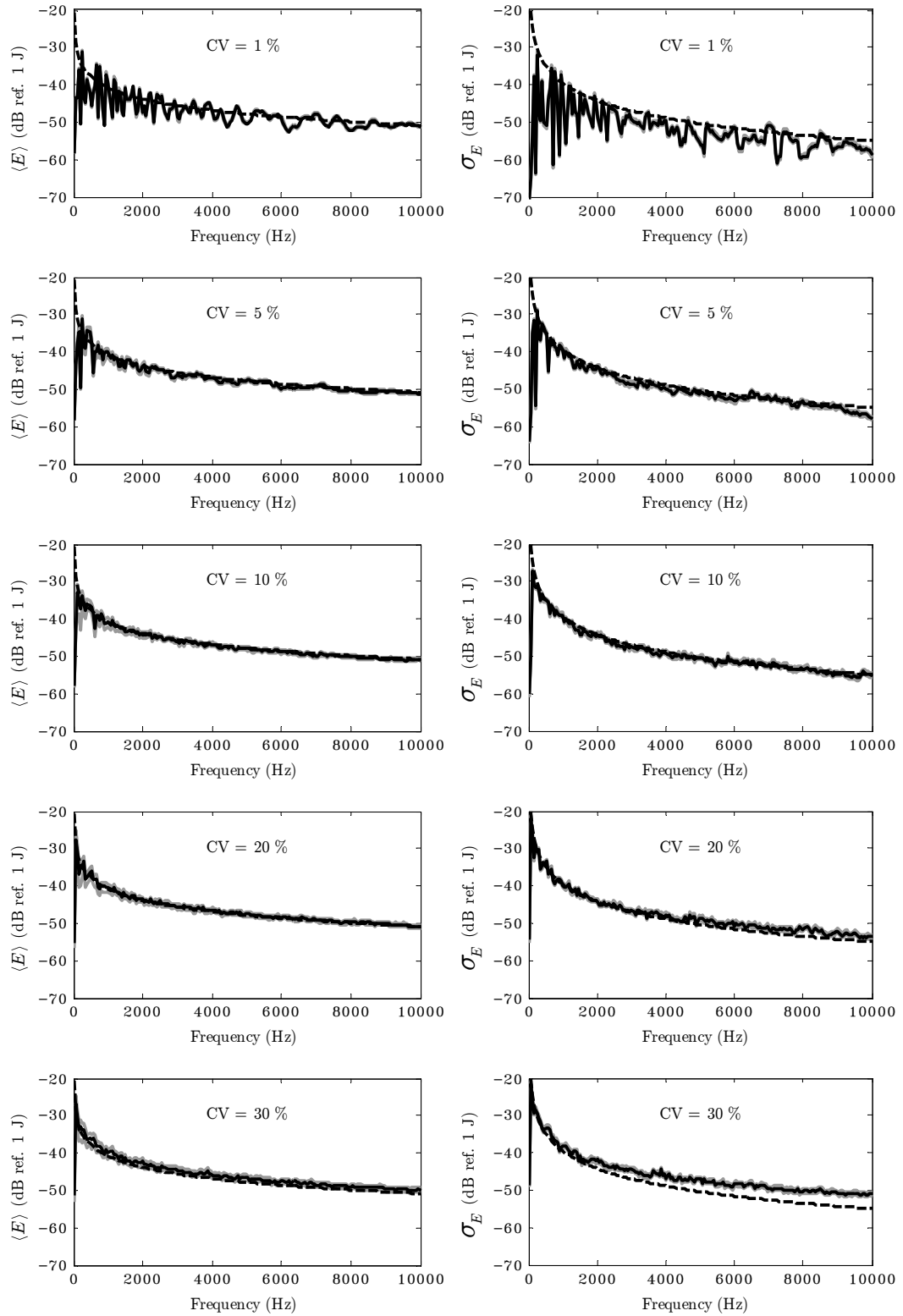


Figure 4.8: The mean and standard deviation of the energy of the plate via SEA and Monte Carlo simulation with CV values of 1%, 5%, 10%, 20%, and 30% for the plate thickness variation as a function of frequency.

The number of Monte Carlo runs for all of Monte Carlo simulations was selected to be 1000. The confidence level was selected to be 95%. Eqs. (2.89) and (2.91) are then used to calculate the confidence interval of the mean of energy and standard deviation of energy, respectively. The bounds of the confidence intervals are shown in grey lines along the mean and standard deviation of the energy. However, normally, the confidence level and confidence interval are chosen to determine the (minimum) number of Monte Carlo runs.

Fig. 4.8 demonstrates that the comparisons of the mean of energy between the results from the SEA and Monte Carlo give good agreement for CV values of 5%–10%. The mean and standard deviation obtained by Monte Carlo simulations become increasingly smooth (with less scatter) as the levels of variability and frequency increase. It would appear that at a variability level of CV 1% almost throughout frequency range, SEA standard deviation prediction is overestimated and at a variability level of CV 20% for the frequency range above 4500 Hz, SEA standard deviation prediction is underestimated. Besides, at a variability level of CV 30% across the entire frequency range, SEA mean and standard deviation predictions are underestimated. It seems that the trend of the mean and standard deviation of the energy increases when CV value is higher.

In particular, the change in thickness does not randomise the mode shapes because the natural frequency is linearly related to thickness parameter, as seen from Eq. (4.4). This leads to a fully correlated upwards shift of all the natural frequencies, hence translational symmetry of the natural frequencies. Because the system has at least one symmetry, GOE statistics is not applicable (Langley and Cotoni, 2004) to the natural frequency distribution, and the SEA variance formula will not work. To make more general randomisations, with more random parameters, SEA will lead to better results because the mode shapes will be highly randomised and mixed up between the modes.

The next section will present the parameter for validating the level of variation that the SEA can handle.

4.1.5 Statistical Overlap Factor of a Simple Plate

In this section, the statistical overlap factor (SOF) from Eq. (2.72) will be used to validate the levels of the random parameter variation at which SEA is able to handle. From previous sections, the results show that SEA is capable of handling the dimension variation with CV values of 1%–30%.

To validate the minimum that SEA can handle, the Monte Carlo simulation with 1000 samples used to generate to obtain the mean and standard deviation of the energy of the plate subjected to a single point load with CV values of 0.1%, 0.3%, 0.5%, and 0.8% of the plate dimension as a function of frequency compared with the SEA results are shown in Fig. 4.9. The SEA predictions are smooth dashed curves and Monte Carlo simulations are fluctuating curves. The 95% confidence intervals of Monte Carlo simulations with 1000 samples for the mean and standard deviation of the energy are calculated from the finite number of samples by using Eqs. (2.89) and (2.91), and shown in grey lines along the mean and standard deviation of the energy.

Fig. 4.9 shows that for all CV values, SEA mean prediction give a good agreement with Monte Carlo results. For standard deviation predictions, SEA gives a good agreement from CV values 0.3%–0.8% but at CV value 0.1%, SEA standard deviation is highly overestimated.

To examine why SEA standard deviation prediction cannot handle the CV value of 0.1%, the SOF parameter will be used to investigate the levels that SEA works.

Figs. 4.10 and 4.11 on the left hand side show SOF of the plate dimension variation with CV values of 0.1%, 0.3%, 0.5%, 0.8%, 1%, 5%, 10%, 20% and 30% as a function of the mode number and on the right hand side show the mean $\langle \omega_n \rangle$ and standard deviation σ_{ω_n} of the natural frequencies, and the mean frequency spacing $\langle \omega_{n+1} - \omega_n \rangle$.

Fig. 4.10 demonstrates that the local minima of SOF is less than one at CV value 0.1%, and higher than one at mode number above 150 for CV values of 0.3%–0.8%. At CV value of 0.1%, it can be clearly seen that the trend of standard deviations of the natural frequencies is less than that of the mean frequency spacing for all mode number range.

For the plate variation, it seems that if the local minima of SOF is less than one, SEA standard deviation prediction is overestimated.

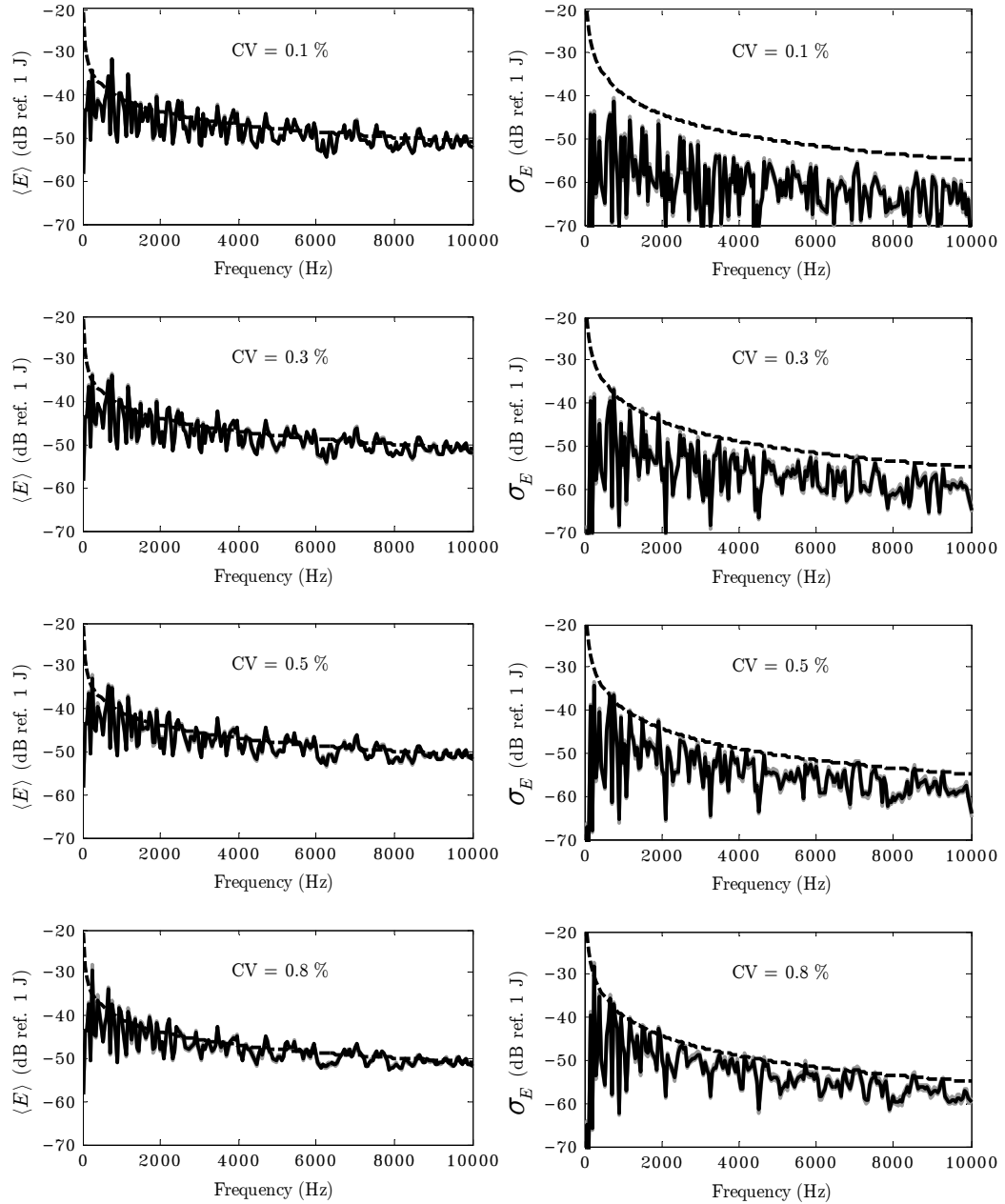


Figure 4.9: The mean and standard deviation of the energy of the plate via SEA and Monte Carlo simulation with CV values of 0.1%, 0.3%, 0.5 and 0.8% for the plate dimension variation versus frequency. The 95% confidence intervals calculated from Monte Carlo simulations are shown in grey.

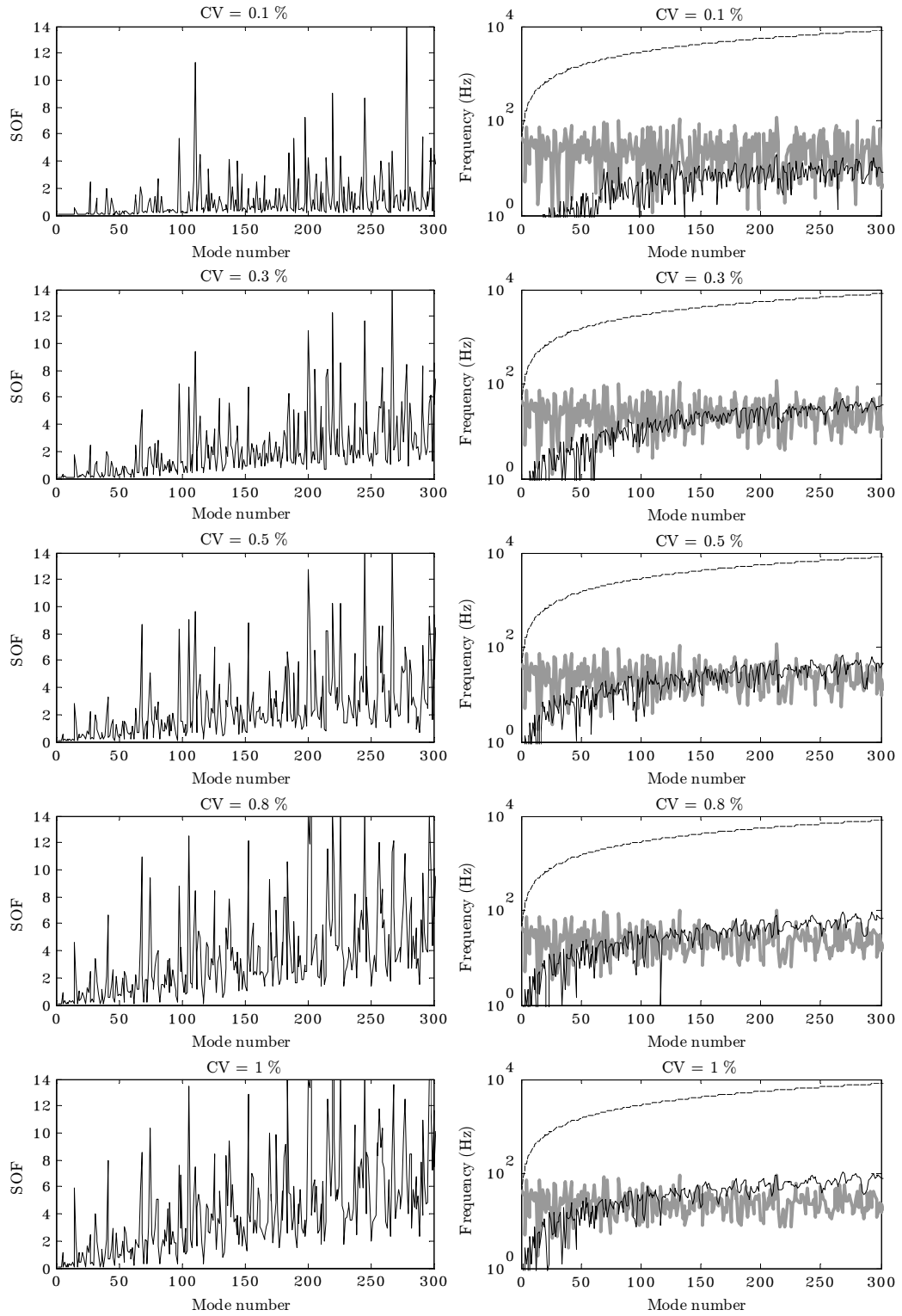


Figure 4.10: SOF of the plate versus the mode number with CV values of 0.1%, 0.3%, 0.5%, 0.8% and 1% for the plate dimension variation. Right hand side figures; $--: \langle \omega_n \rangle$; $-: \langle \omega_{n+1} - \omega_n \rangle$; $-: \sigma_{\omega_n}$.

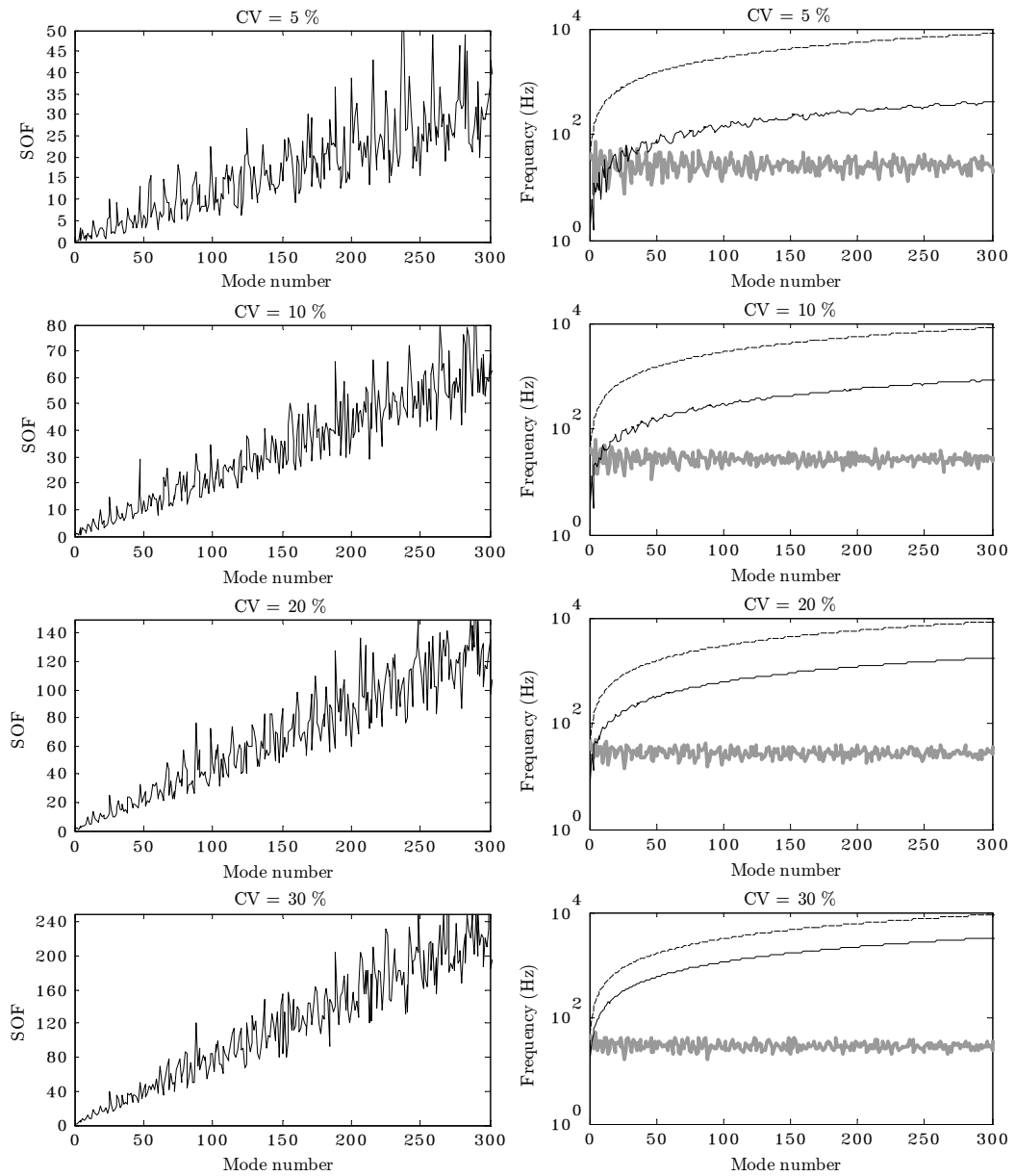


Figure 4.11: SOF of the plate versus the mode number with CV values of 5%, 10%, 20%, and 30% for the plate dimension variation. Right hand side figures; $--$: $\langle \omega_n \rangle$; $-$: $\langle \omega_{n+1} - \omega_n \rangle$; $-$: σ_{ω_n} .

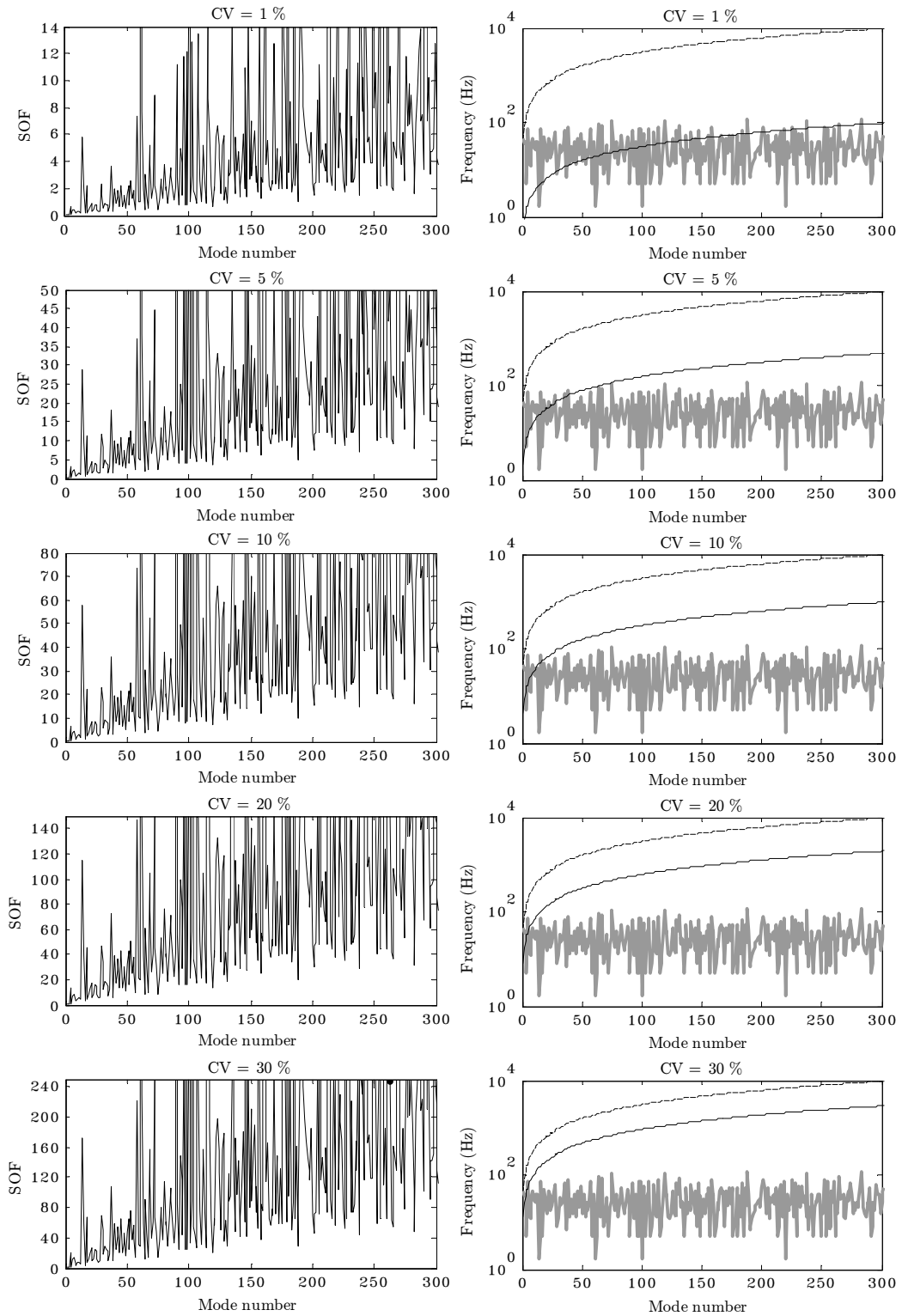


Figure 4.12: SOF of the plate versus the mode number with CV values of 5%, 10%, 20%, and 30% for the plate thickness variation. In figure on the right hand side; $-\cdot-$: $\langle \omega_n \rangle$; $-$: $\langle \omega_{n+1} - \omega_n \rangle$; $-$: σ_{ω_n} .

Turning attention to the plate thickness variation, Fig. 4.12 on the left hand side shows SOF of the plate thickness variation with CV values 1%, 5%, 10%, 20% and 30% as a function of the mode number and on the right hand side show the mean $\langle \omega_n \rangle$ and standard deviation σ_{ω_n} of the natural frequencies, and the mean frequency spacing $\langle \omega_{n+1} - \omega_n \rangle$. It can be clearly seen that the scatter in the SOF value and mean frequency spacing for the thickness variation are significantly higher than that for the dimension variation.

The mode shapes of the system for thickness variation correlate with thickness changes (i.e. the natural frequencies of all modes correlatively increase when thickness increases), leading to large fluctuation of the mean frequency spacing. According to Eq. (2.72), this in turn leads to large fluctuation in the SOF, and therefore SEA is not applicable. For the dimension variation, system has enough mixing between the modes, so SEA gives good results.

The following section will present the ratio of the energy variance between Monte Carlo and SEA as a function of CV.

4.1.6 Ratio Between Energy Variances from Monte Carlo Simulation and SEA

In Section 4.1.3 and 4.1.4, the results show that SEA standard deviation prediction cannot handle thickness variation at high levels of CV. This section will compare the behaviour of the variance of energy obtained by Monte Carlo simulation with SEA energy variance when the level of CV changes.

Fig. 4.13 shows the ratio between the energy variance from Monte Carlo Simulation and SEA. The energy variances are of the plate with the following variability levels: CV 1%, 5%, 10%, 20%, and 30% of the plate dimension as a function of frequency. Fig. 4.13 also shows SOF as a function of frequency. The ratios and SOFs are shown in black and grey curves, respectively.

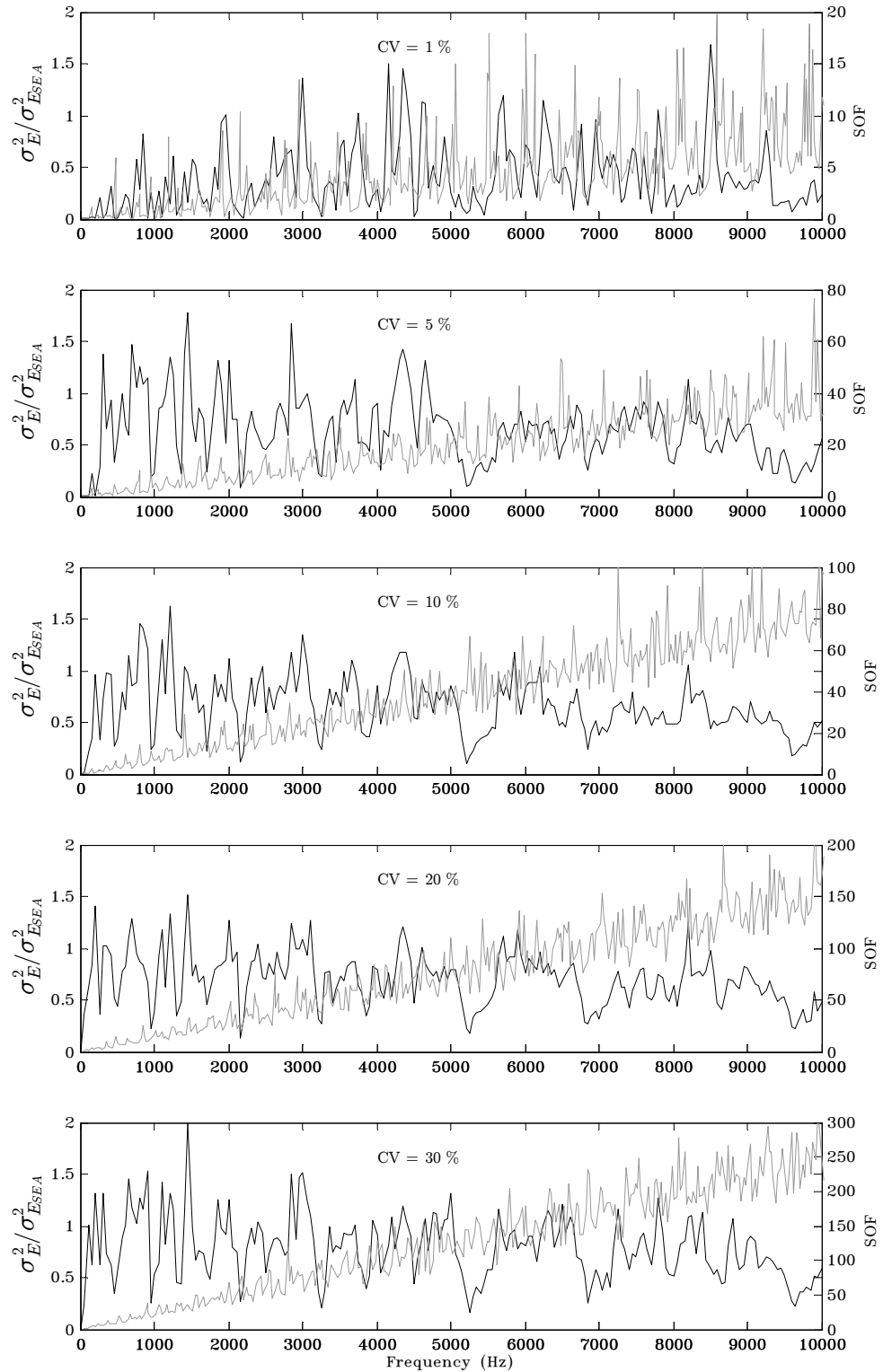


Figure 4.13: The ratio between the energy variance from Monte Carlo Simulation and SEA with dimension variation (black curves). The SOF as a function of frequency (grey curves).

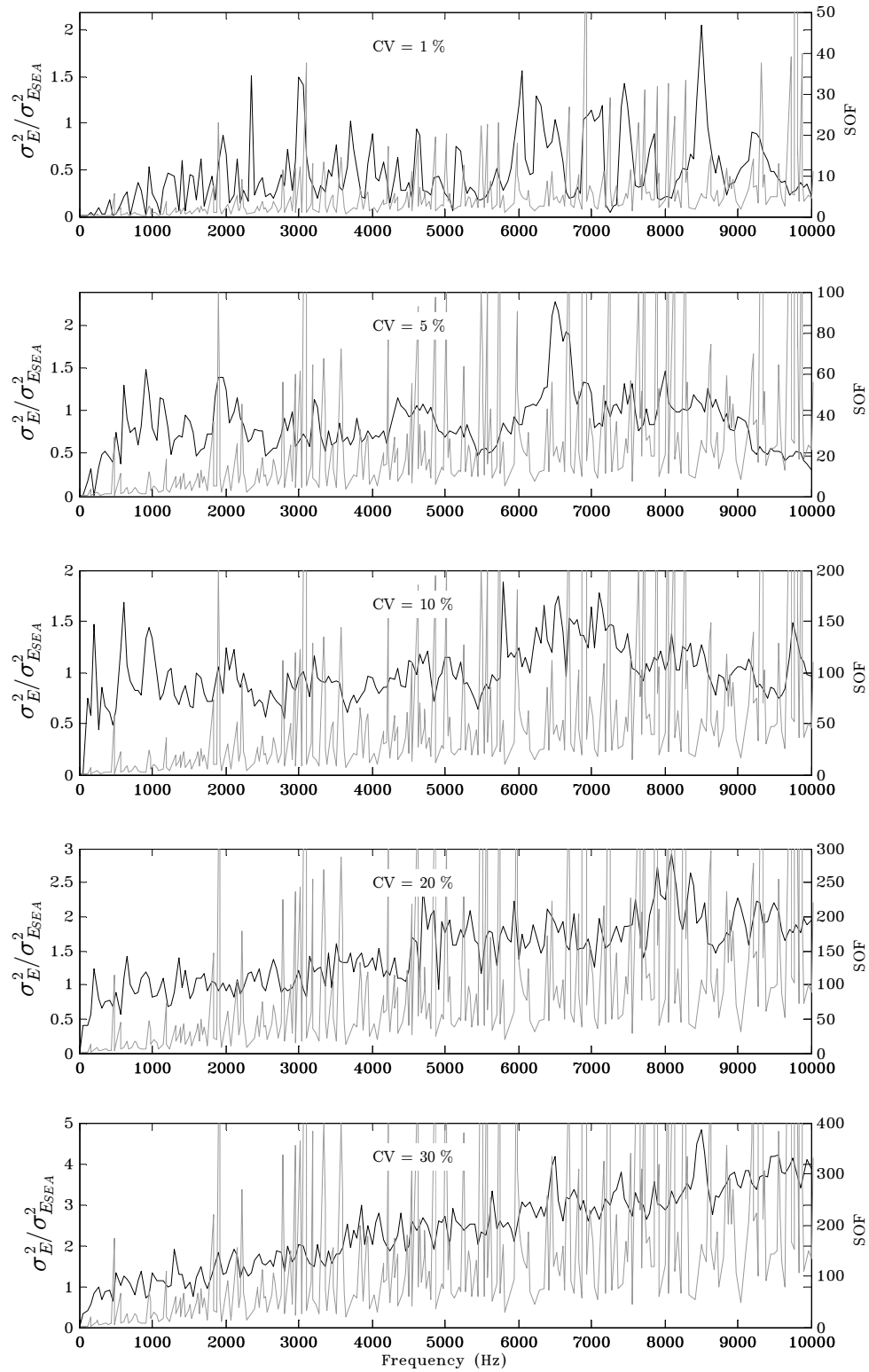


Figure 4.14: The ratio between the energy variance from Monte Carlo Simulation and SEA with thickness variation (black curves). The SOF as a function of frequency (grey curves).

Fig. 4.14 shows the ratio between the energy variance from Monte Carlo Simulation and SEA. The energy variances are of the plate with the following variability levels: CV 1%, 5%, 10%, 20%, and 30% of the plate dimension as a function of frequency. Fig. 4.14 also shows SOF as a function of frequency. The ratios and SOFs are shown in black and grey curves, respectively.

Fig. 4.13 demonstrates that the ratio increases when CV increases. At CV of 1%, it can be seen that the ratios in the low frequency range are lower than those in the high frequency range. In contrast, at CV of 5% and 10%, the ratios in the low frequency range are higher than those in the high frequency range. At CV of 1%, the ratio has more scatter in all frequency range than that at other CV values. At CV of 5%, 10%, 20%, and 30%, the ratios have higher scatter in the low frequency range than that in the high frequency range.

Fig. 4.14 demonstrates that the fluctuation of the ratio decreases when CV increases. It is also evident that the ratio increases when CV increases. At CV of 1%, most ratios are below unity for all frequency range. At CV value of 10%, the ratios approximately equal unity for all frequency range. At CV of 20% and 30%, it can be clearly seen that the ratio rapidly increases when the frequency increases. Besides, most local minima of the ratios are higher than unity for CV of 20% and 30%.

Comparing Figs. 4.13 and 4.14 shows that the scatter in the ratio with dimension variation is higher than that with thickness variation. In contrast, the scatter in SOF with dimension variation is lower than that with thickness variation.

From Figs. 4.13 and 4.14, we cannot find the relationship between SOF and the ratio between the energy variance from Monte Carlo Simulation and SEA.

To clearly see the behaviour of the ratio between the energy variance from Monte Carlo Simulation and SEA when CV changes, the frequency-averaged ratio between the energy variance from Monte Carlo Simulation and SEA is shown in Fig 4.15. The energy variances are of the plate with variability levels of CV 1%, 5%, 10%, 20%, and 30% of the plate dimension and thickness as a function of CV.

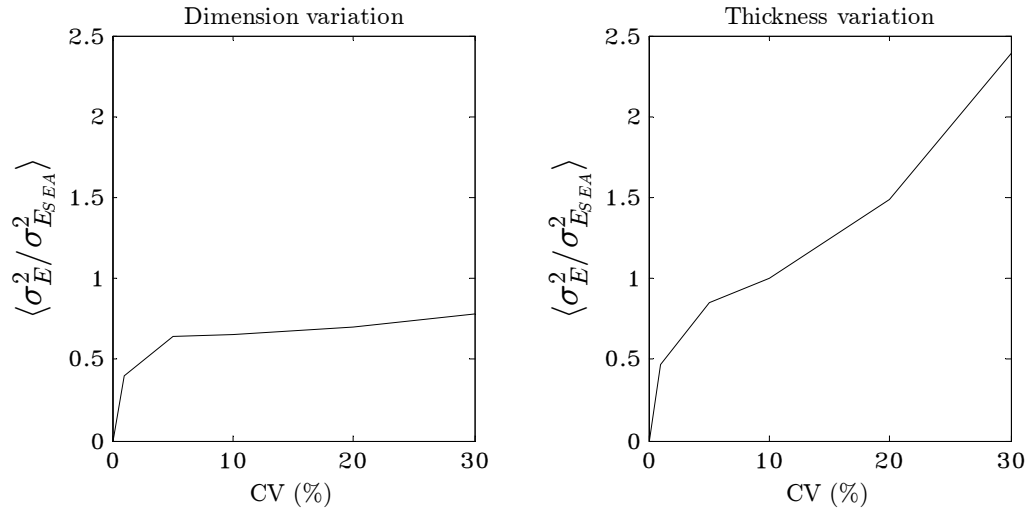


Figure 4.15: The frequency-averaged ratios between the energy variance from Monte Carlo Simulation and SEA with plate dimension and thickness variation.

From Fig 4.15, it is evident that the behaviour of the frequency-averaged ratio as a function of CV with plate dimension variation seems to approach certain limit whereas that with plate thickness variation continue to increase.

The following section will present the evolution of the pdf of the energy when the level of variability changes. The variation involves both dimension and thickness.

4.1.7 Evolution of pdf of Energy

In this section, the pdf of the energy of a random dynamic system for a simply-supported plate with plate dimension and thickness variation is examined. Langley et al. (2013) presented that the pdf of the energy of a simply-supported plate with a random system is very similar to lognormal when the modal overlap factor is greater than two. To see how the response distribution of the energy looks like when a level of variability increases, the probability density functions of the normalised energy (the energy is normalised by the mean value) obtained from Monte Carlo simulations at particular frequencies are shown in Figs 4.16 and 4.17. The continuous line represents the fitted lognormal distribution curve. In order to confidently plot the pdf of the energy obtained from Monte Carlo simulations, an ensemble of 10^5 systems has been considered for each example.

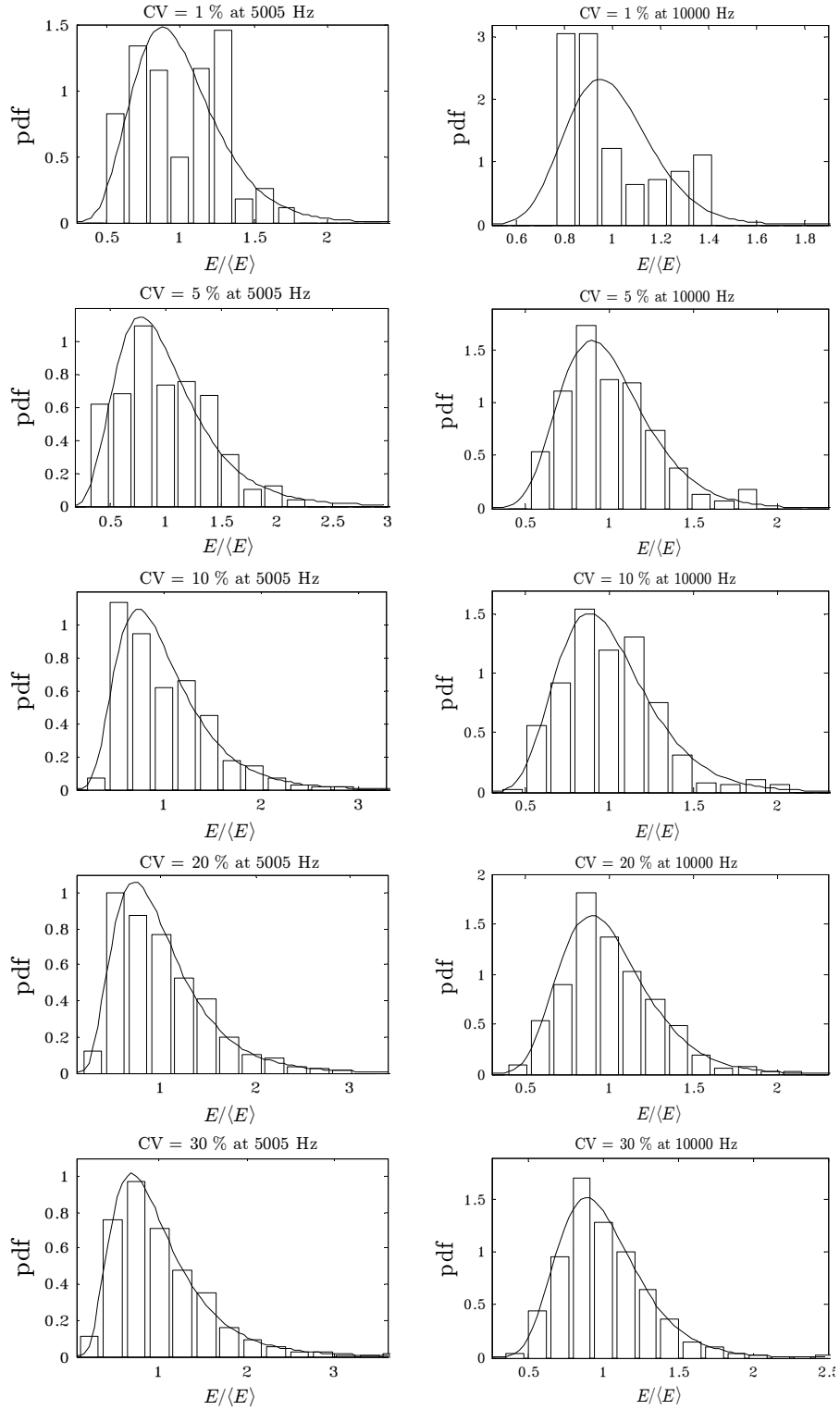


Figure 4.16: The estimated pdf versus the energy compared with a lognormal pdf, for the plate with CV values of 1%, 5%, 10%, 20% and 30% for the plate dimension variation.

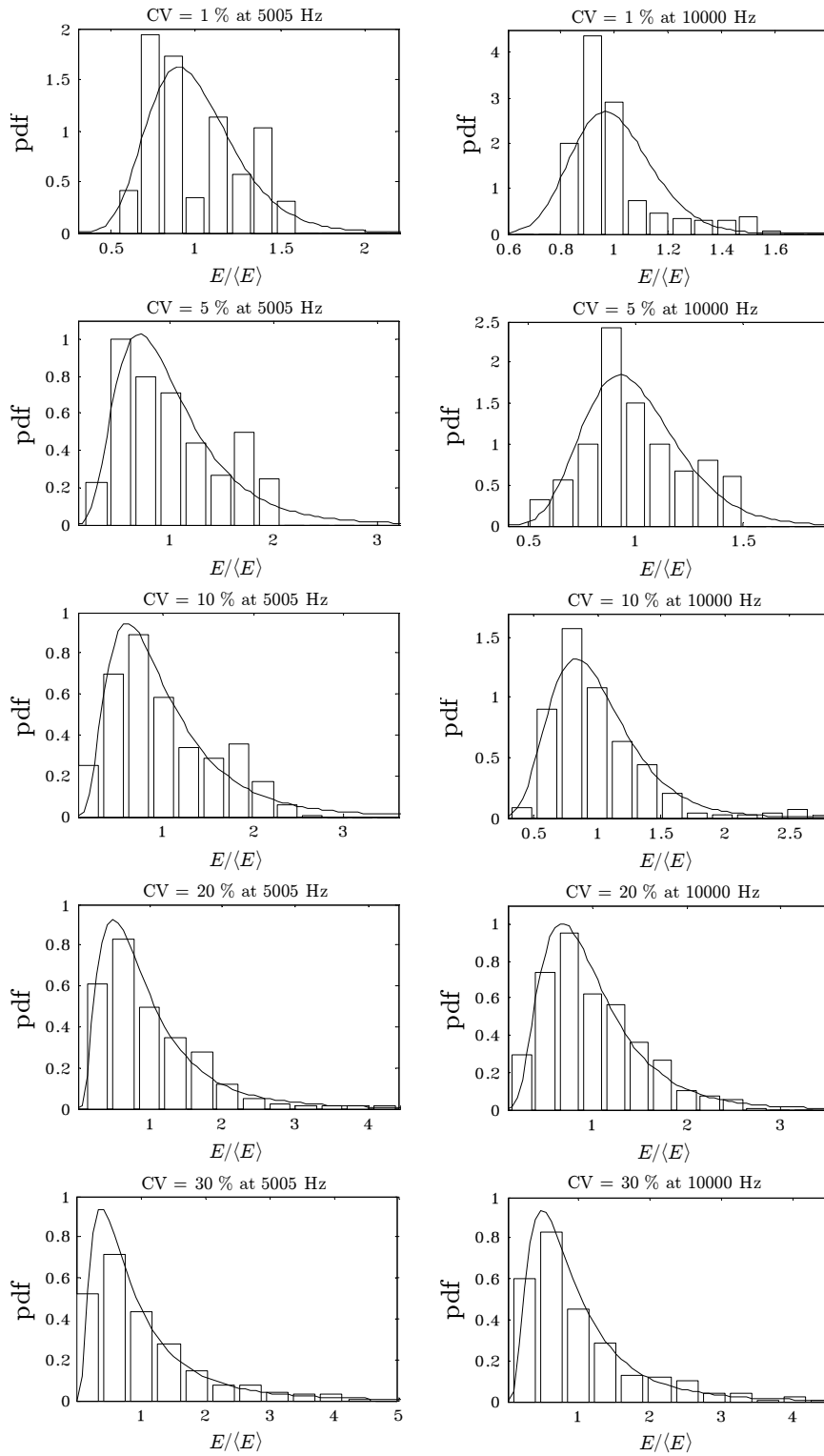


Figure 4.17: The estimated pdf versus the energy compared with a lognormal pdf, for the plate with CV values of 1%, 5%, 10%, 20% and 30% for the thickness variation.

Fig. 4.16 shows the pdf versus the normalised energy of a simply-supported plate, for the plate with CV values of 1%, 5%, 10%, 20% and 30% for the plate dimension variation at frequencies 5005 Hz and 10000 Hz.

Fig. 4.17 shows the pdf versus the normalised energy of a simply-supported plate, for the plate with CV values of 1%, 5%, 10%, 20% and 30% for the plate thickness variation at frequencies 5005 Hz and 10000 Hz.

The modal overlap factor for a simply-supported plate (bending motion) obtained by using Eq. (2.68) with frequencies 5005 Hz and 10000 Hz are equal to 0.1972 and 0.3941, respectively.

It can be clearly seen that when the level of variability increases, the pdf of normalised energy is more similar to lognormal. There is roughly no difference of the pdf of normalised energy between frequency of 5005 Hz and 10000 Hz.

4.2 Conclusions of Chapter 4

The results show that for a simple plate structure, the SEA has the ability to predict the mean and standard deviation of the energy when the plate dimension varies. However, when the local minima of SOF is less than unity, SEA will overpredict the standard deviation of the energy.

The behaviour of the mean and standard deviation of the energy for thickness variation, is different from that for dimension variation. For dimension variation, the trends of the mean and standard deviation obtained by Monte Carlo simulations are almost the same when the level of variability changes. In contrast, for the thickness variation, the trends are higher when the level of variability increases. The mean of the energy with thickness variation, is smoother than with dimension variation for all CV levels.

For the plate thickness variation, SEA is able to predict the mean and standard deviation of the energy in some ranges of variation. For the standard deviation of energy, the SEA prediction can only handle cases with CV values from 1% to 10%. After that, the SEA gives underpredictions.

The response variance is seemingly saturated to the SEA result when CV increases only with plate dimension variation but with plate thickness variation, the response variance continuously increases.

The distribution functions of the mean energy responses are shown for a simple plate structure to be similar to the lognormal distribution (which actually becomes the basis for the assumption in Chapter 6). It has therefore been verified that the assumption of the lognormal distribution for the energy response of a simple structure can be used.

Together with Chapter 3, Objective i) of the thesis (given in the introduction) has been met because evidence has now been generated at both low and high frequency with different levels of uncertainty. The SEA method has been used and tested against Monte Carlo simulation.

Objective ii) of the thesis has also been partially met in this chapter because the SEA model was only applied to a simple structure with both high and low-level uncertainties. In the next chapter, SEA will be applied to a non-simple built-up structure.

Chapter 5

High frequency analysis of coupled plate structures with high and low-level uncertainties

In Chapter 4, Statistical Energy Analysis (SEA) was applied to a simple uncertain structure (a rectangular plate) at high frequency. Although the findings are useful, the same information needs to be examined on a ‘built-up’ structure involving a more sophisticated SEA model that approaches a more realistic engineering structure. To benchmark the predictions, Monte Carlo simulations can no longer be based on the availability of an exact ‘plate’ solution. The aim of this chapter is twofold: i) to demonstrate the applicability of SEA to an L-shaped plate structure subjected to a single point force with high and low-level uncertainties to predict the mean levels and standard deviations as the level of variability is changed; and ii) as a vehicle to test in Chapter 7, a newly developed extreme value (EV) approach discussed in Chapter 6. Monte Carlo simulation based on (commercially available) finite element solutions (ANSYS) is used as a benchmark. Vibration analyses are carried out for frequencies from 10 Hz up to 10000 Hz in 201 intervals and results are compared with FE Monte Carlo simulations. Before showing SEA-based FRF predictions, the built-up structure, in the form of an L-shaped plate, is described, followed by the SEA model.

To be specific, in this chapter two types of uncertainty are examined namely i) dimension variability, and ii) thickness variability. This is to establish the capability and limitations of SEA prediction of both the mean and standard deviation of the energy response in a built-up structure, i.e. an L-shaped plate, as the level of variability is changed. The focus then switches to an examination of the probability distribution of the energy response for an L-shaped plate on both plates. To confirm the accuracy of SEA predictions, Monte Carlo simulation based on (commercially available) finite element solutions (ANSYS) is used to generate the results to compare with SEA. These results are generated as a build-up to the development of an extreme value approach in Chapter 6 to handle different levels of variability.

5.1 L-Shaped Plate

The structure of the L-shaped plate consists of two plates with 90° joint as shown in Fig. 5.1. The properties of Plates 1 and 2 are shown in Table 5.1. A single point (harmonic) force is applied on Plate 1 at the point defined by $x = 0.14$ m and $z = 0.12$ m. The boundary condition is simply-supported at the edges $z = 0$ and $z = 0.3$ m of Plate 1. This L-shaped plate model will be used as the built-up structure to examine the mean and standard deviation by using SEA, and be modelled for the FE method in the following sections.

Table 5.1: Properties of the L-shaped plate considered.

Dimension of Plate 1 (m \times m)	0.4×0.3
Dimension of Plate 2 (m \times m)	0.3×0.2
Thickness of Plates 1 and 2 (mm)	1
Loss factor	0.01
Young's modulus (N/m ²)	2×10^{11}
Density (kg/m ³)	7900
Poisson ratio	0.3

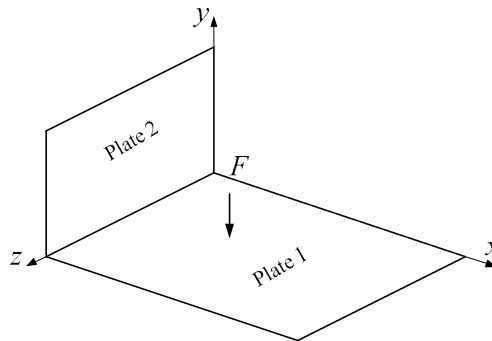


Figure 5.1: L-shaped plate.

5.1.1 The SEA Model

The SEA model of the L-shaped plate (corresponding to the details in Section 5.1), consists of 6 ‘subsystems’, which are the bending wave subsystem for Plate 1, the longitudinal waves of Plate 1, the shear waves of Plate 1, the bending waves of Plate 2, the longitudinal waves of Plate 2, and the shear wave of Plate 2. They are connected along the z axis with a line junction.

The SEA method was discussed in Chapter 2. The SEA model for this L-shaped plate is modelled by using Eqs. (2.6) and (2.66) to predict the mean and variance of the energy, respectively. The input power as in Eq. (2.65) is applied on the bending wave subsystem of Plate 1.

Because the SEA model consists of 6 subsystems, the CLFs in Eq. (2.7) are needed to serve Eq. (2.6). To compute the CLFs, the transmission coefficients are calculated first. To verify that the method used to calculate the transmission coefficients of a line junction for the plate/plate in Section 2.3.2 is correctly used, a comparison between the reproduced result and an original published result is essential. Fig. 5.2 shows the comparison of the full set of transmission coefficients from the bending wave of the carrier plate for an L-shaped plate junction with $k_L/k_B = 0.3$, which is in agreement with Fig. 3 of Langley and Heron (1990).

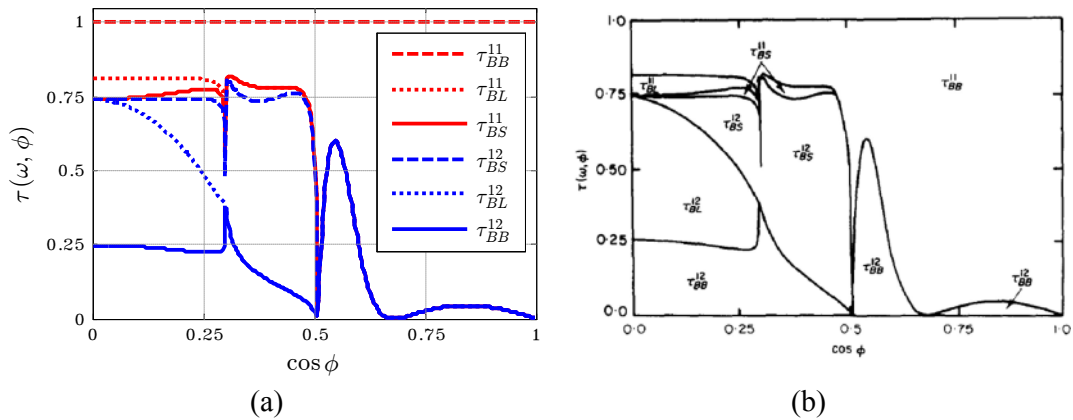


Figure 5.2: The full set of transmission coefficients from the bending wave of the carrier plate for an L-shaped plate junction with $k_L/k_B = 0.3$: (a) reproduced result, (b) taken from Fig. 3 of Langley and Heron (1990).

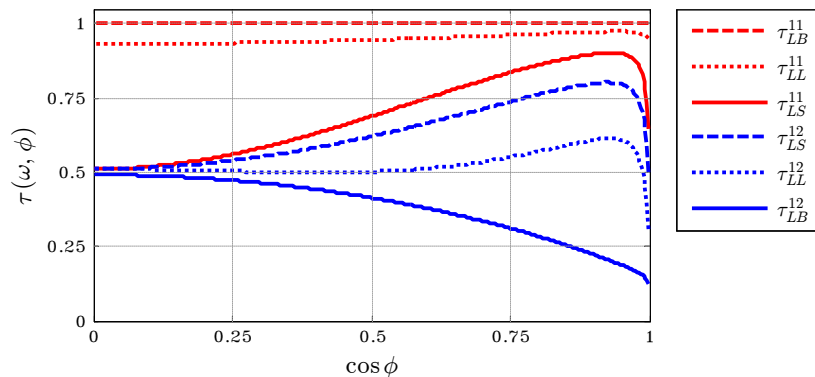


Figure 5.3: The full set of transmission coefficients from the longitudinal wave of the carrier plate for an L-shaped plate junction with $k_L/k_B = 0.3$.

The full set of transmission coefficients from the longitudinal and shear waves of the carrier plate for an L-shaped plate junction with $k_L/k_B = 0.3$ is also shown in Figs. 5.3 and 5.4.

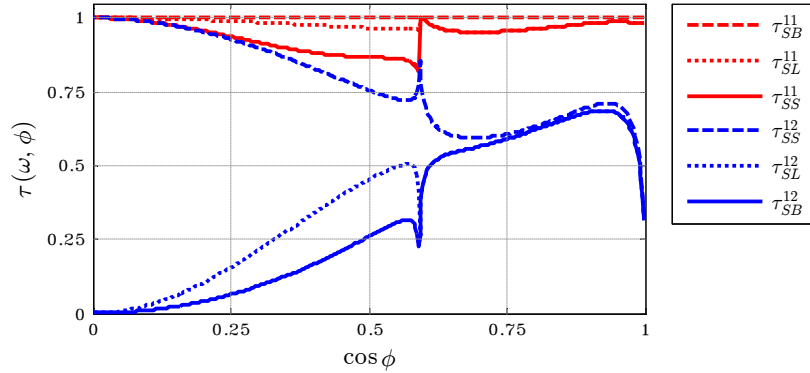


Figure 5.4: The full set of transmission coefficients from the shear wave of the carrier plate for an L-shaped plate junction with $k_L/k_B = 0.3$.

The SEA mean and variance calculations for a built-up system in Eqs. (2.6) and (2.66) are also essential in comparing with the original results for correct use. The two coupled plates modelled as in Langley and Heron (1990) with the properties shown in Table 4.2 is used to calculate the reproduced results for the mean and relative variance of the energy of Plates 1 and 2 to compare with original results. The bending waves of two edge-coupled plates are considered. The coefficient α'_1 , used in Eq. (2.67), is equal to 2.75 for a single point load, and α'_{12} as needed in Eq. (2.67) is equal to 2 for a line connection. Eq. (2.70) is used to calculate the function r^2 for no frequency averaging ($B' = 0$).

Table 4.2: Properties of the two coupled plates in Langley and Cotoni (2004).

Dimension of Plate 1 (m × m)	1.35×1.2
Dimension of Plate 2 (m × m)	1.05×1.2
Thickness of Plate 1 (mm)	5
Thickness of Plate 2 (mm)	15
Loss factor of Plates 1 and 2	0.01
The angle between Plate 1 and 2	60°
Young's modulus (N/m^2)	7.2×10^{10}
Density (kg/m^3)	2800
Poisson ratio	0.3

Fig. 5.5 shows the comparison of the mean and relative variance of the energy of Plates 1 and 2 versus frequency, for two coupled plates with a point load on Plate 1, which is in agreement with Fig. 3 of Langley and Cotoni (2004).

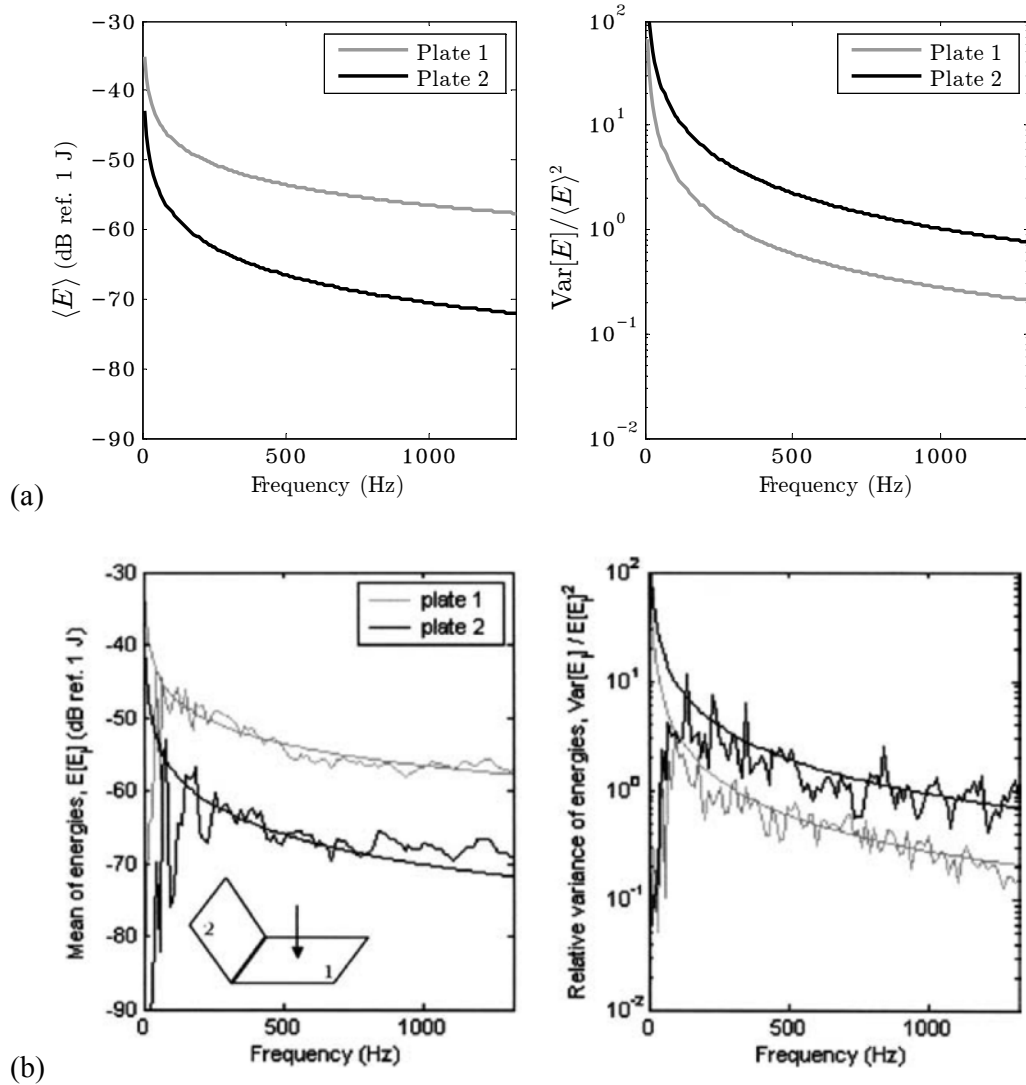


Figure 5.5: Mean and relative variance of the energy of Plates 1 and 2 versus frequency, for two coupled plates with a point loading on Plate 1: (a) reproduced result; (b) taken from Fig. 3 of Langley and Cotoni (2004). Fluctuating curves: simulation results, smooth lines: SEA prediction.

The energy of a plate for the built-up structure shown here (and thereafter) is the energy obtained by combining bending, longitudinal, and shear waves.

For an L-shaped plate model, α'_1 is equal to 2.75, and α'_{ks} (k and s from 1 to 6) are equal to 2. Fig. 5.6 shows the mean and standard deviation of the energy of Plates 1 and

2, for an L-shaped plate subjected to a single harmonic load on Plate 1 as a function of frequency obtained by using Eqs. (2.6) and (2.66)

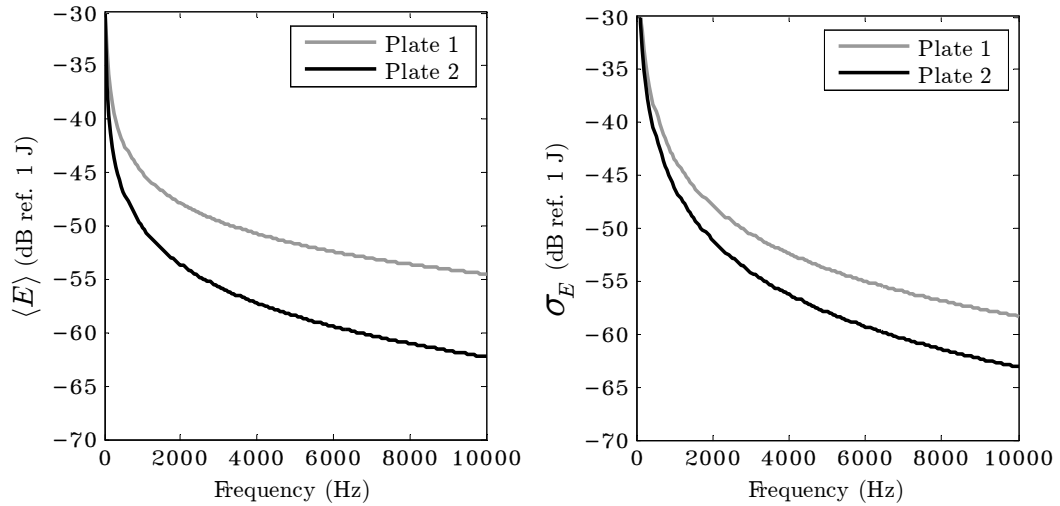


Figure 5.6: Mean and standard deviation of the energy of Plates 1 and 2, for an L-shaped plate subjected to a point load on Plate 1 as a function of frequency.

The SEA results for an L-shaped plate, compared with Monte Carlo simulation based on finite element solutions (ANSYS), will be given shortly after the FE solution in Monte Carlo simulation is described.

5.1.2 FE Solution Methodology (via ANSYS)

The FE method (via ANSYS) is used to calculate the displacements for L-shaped plate model (details and properties as in Section 5.1) of Plates 1 and 2 with frequencies from 10 Hz up to 10000 Hz in 201 intervals. Bending, longitudinal, and shear waves are all considered, and then the displacements of Plates 1 and 2 are converted to energy by using Eq. (4.6). The result from the FE method will be used to serve Monte Carlo simulation in the following sections to compare with SEA.

5.1.3 Dimension Variation

In this section, the dimension (i.e. the length along the z-axis) of the L-shaped plate (details in Section 5.1) will be randomised by a uniform distribution with CV values of 1%, 5%, 10%, 20%, and 30%. FE Monte Carlo simulation (via ANSYS) is used to calculate the mean and standard deviation of the energy for Plates 1 and 2, and compared with SEA. An ensemble of 100 systems has been generated. Fig. 5.7 shows the energy of Plates 1 and 2 versus frequency for each of the 100 generated samples and the ensemble mean value, for an L-shaped plate subjected to a single point load on Plate 1 with CV values of 1%, 5%, 10%, 20%, and 30% for the dimension variation. It shows that when the level of variability increases, the scatter in energy is higher and the mean of Plate 1 is higher than Plate 2. The mean curves at high frequency are smoother than those at low frequency.

Fig. 5.8 and 5.9 shows the mean and standard deviation of the energy of Plates 1 and 2, for an L-shaped plate subjected to a single load on Plate 1 with CV values of 1%, 5%, 10%, 20%, and 30% for the dimension variation as a function of frequency. The number of Monte Carlo runs for all of Monte Carlo simulations was selected to be 100. The confidence level was selected to be 95%. Eqs. (2.89) and (2.91) are then used to calculate the confidence interval of the mean of energy and standard deviation of energy, respectively. The bounds of the confidence intervals are shown in grey lines along the mean and standard deviation of the energy. However, normally, the confidence level and confidence interval are chosen to determine the (minimum) number of Monte Carlo runs. It is clear that the mean and standard deviation of the energy of Plate 1 obtained by Monte Carlo simulation are smoother than Plate 2. At frequencies above 7000 Hz for all CV values, predicted SEA mean is underestimated for Plate 1. At frequencies above 7000 Hz, for CV values from 5%–30%, predicted SEA standard deviations are underestimated for Plate 1. At a CV value of 1%, SEA standard prediction is underestimated for Plate 2 throughout the frequency range.

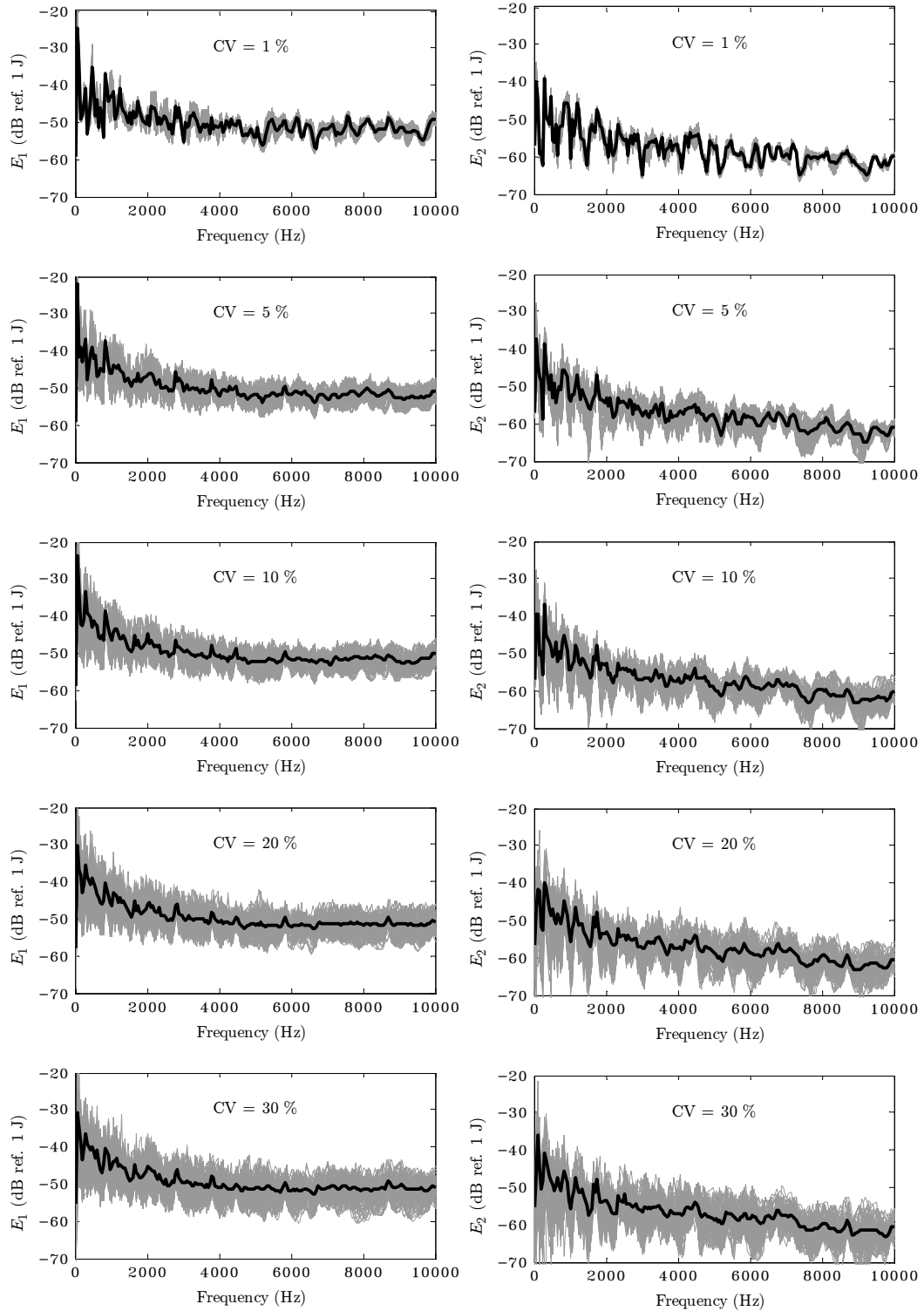


Figure 5.7: The energy of Plates 1 and 2 versus frequency via FE Monte Carlo simulation, for an L-shaped plate with CV values of 1%, 5%, 10%, 20%, and 30% for the dimension variation. The ensemble energy for 100 plates, along with the mean energy is shown.

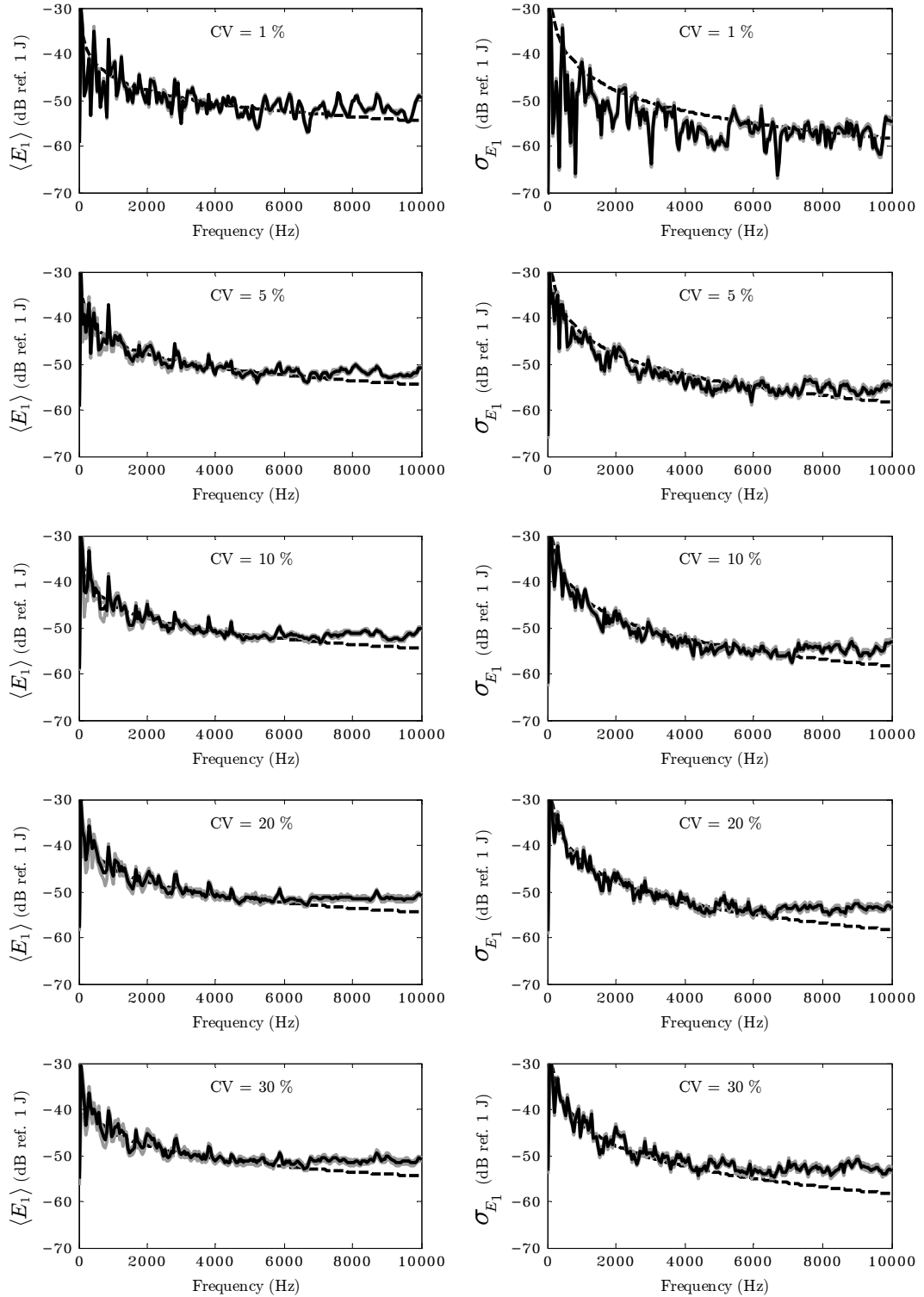


Figure 5.8: The mean and standard deviation of the energy of Plate 1 via SEA and Monte Carlo simulation, for an L-shaped plate with CV values of 1%, 5%, 10%, 20%, and 30% for the dimension variation.

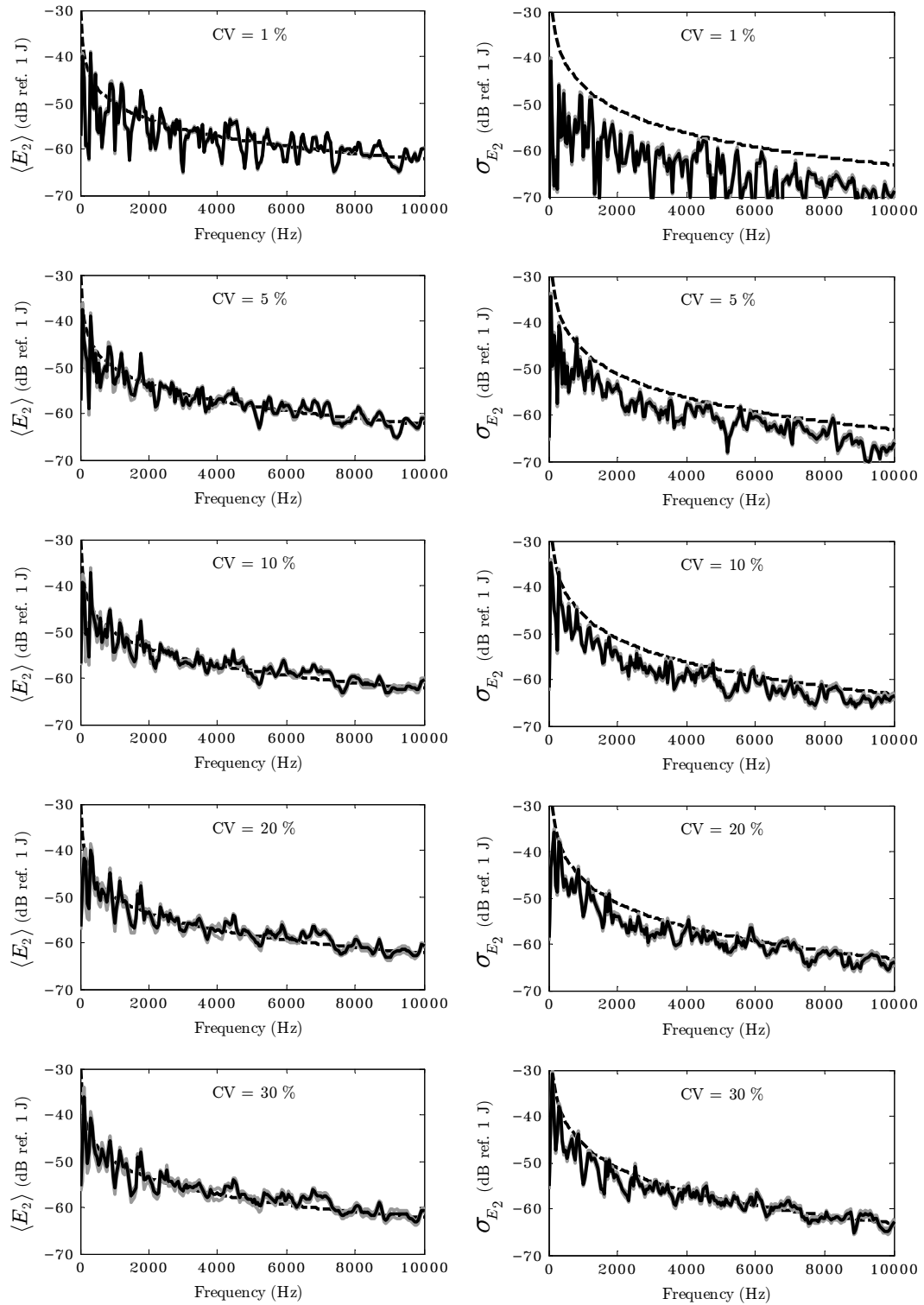


Figure 5.9: The mean and standard deviation of the energy of Plate 2 via SEA and Monte Carlo simulation, for an L-shaped plate with CV values of 1%, 5%, 10%, 20%, and 30% for the dimension variation.

5.1.4 Thickness Variation

In this section, the thickness of Plate 1 of the L-shaped plate in Section 5.1 will be randomised by a uniform distribution with CV values of 1%, 5%, 10%, 15%, and 20%. The thickness of Plate 2 is the same as that of Plate 1. (There is a limitation of ANSYS for minimum thickness at CV value of 30%). FE Monte Carlo simulation (via ANSYS) is used to calculate the mean and standard deviation of the energy for Plates 1 and 2, and compared with SEA. The number of simulations is selected at 100 samples.

Fig. 5.10 shows the energy of Plates 1 and 2 versus frequency, for an L-shaped plate subjected to a single point load on Plate 1 with CV values of 1%, 5%, 10%, 15%, and 20% of the plate thickness as a function of frequency. It is clearly seen that when a level of variability increases, the mean curve is smoother and the scatter in energy is higher. The mean of Plate 1 is also higher than that of Plate 2.

Fig. 5.11 and 5.12 show the mean and standard deviation of the energy of Plates 1 and 2, for an L-shaped plate subjected to a single load on Plate 1 with CV values of 1%, 5%, 10%, 15%, and 20% for the plate thickness variation as a function of frequency. The number of Monte Carlo runs for all of Monte Carlo simulations was selected to be 100. The confidence level was selected to be 95%. Eqs. (2.89) and (2.91) are then used to calculate the confidence interval of the mean of energy and standard deviation of energy, respectively. The bounds of the confidence intervals are shown in grey lines along the mean and standard deviation of the energy. However, normally, the confidence level and confidence interval are chosen to determine the (minimum) number of Monte Carlo runs.

It is clearly seen that the mean and standard deviation of the energy of Plate 1 are smoother than that of Plate 2. At frequencies above 7000 Hz for all CVs, SEA mean predictions are underestimated for Plate 1. At a frequency above 7000 Hz for CV values of 5% to 30%, SEA standard predictions are underestimated for Plate 1. At CV value of 1%, 5%, and 10%, SEA standard predictions are underestimated for Plate 2 for the entire frequency range. This seems to suggest again that SEA is not applicable in case of thickness variation, as in Section 4.1.4. The similarity between Figs. 5.11, 5.12, and 4.8 in that SEA tends to overpredict the mean and standard deviation as CV increases may also suggest that the mode shapes correlate with thickness changes.

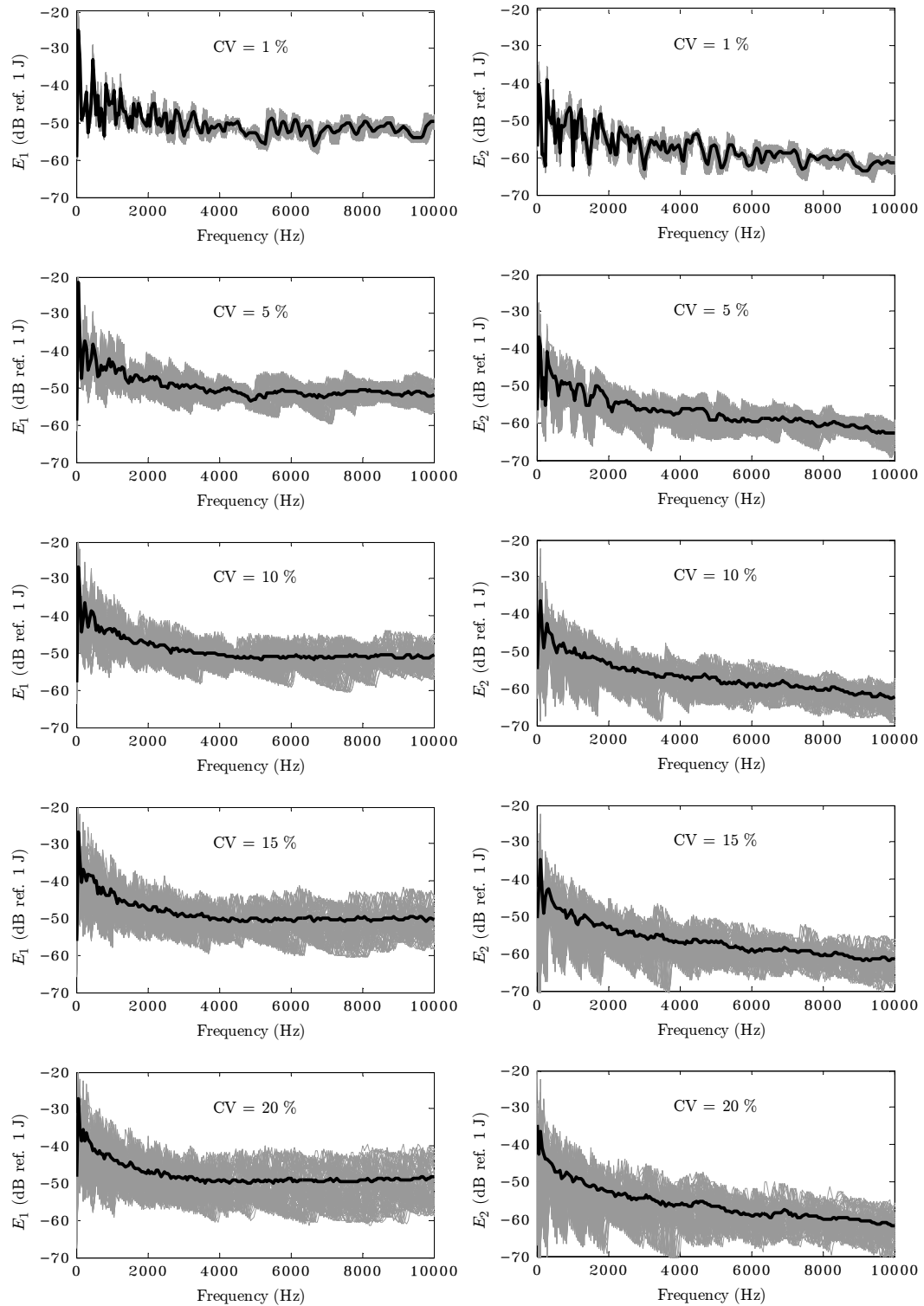


Figure 5.10: The energy of Plates 1 and 2 versus frequency via FE Monte Carlo simulation, for an L-shaped plate with CV values of 1%, 5%, 10%, 15%, and 20% for the plate thickness variation. The ensemble energy for 100 plates, along with the mean energy is shown.

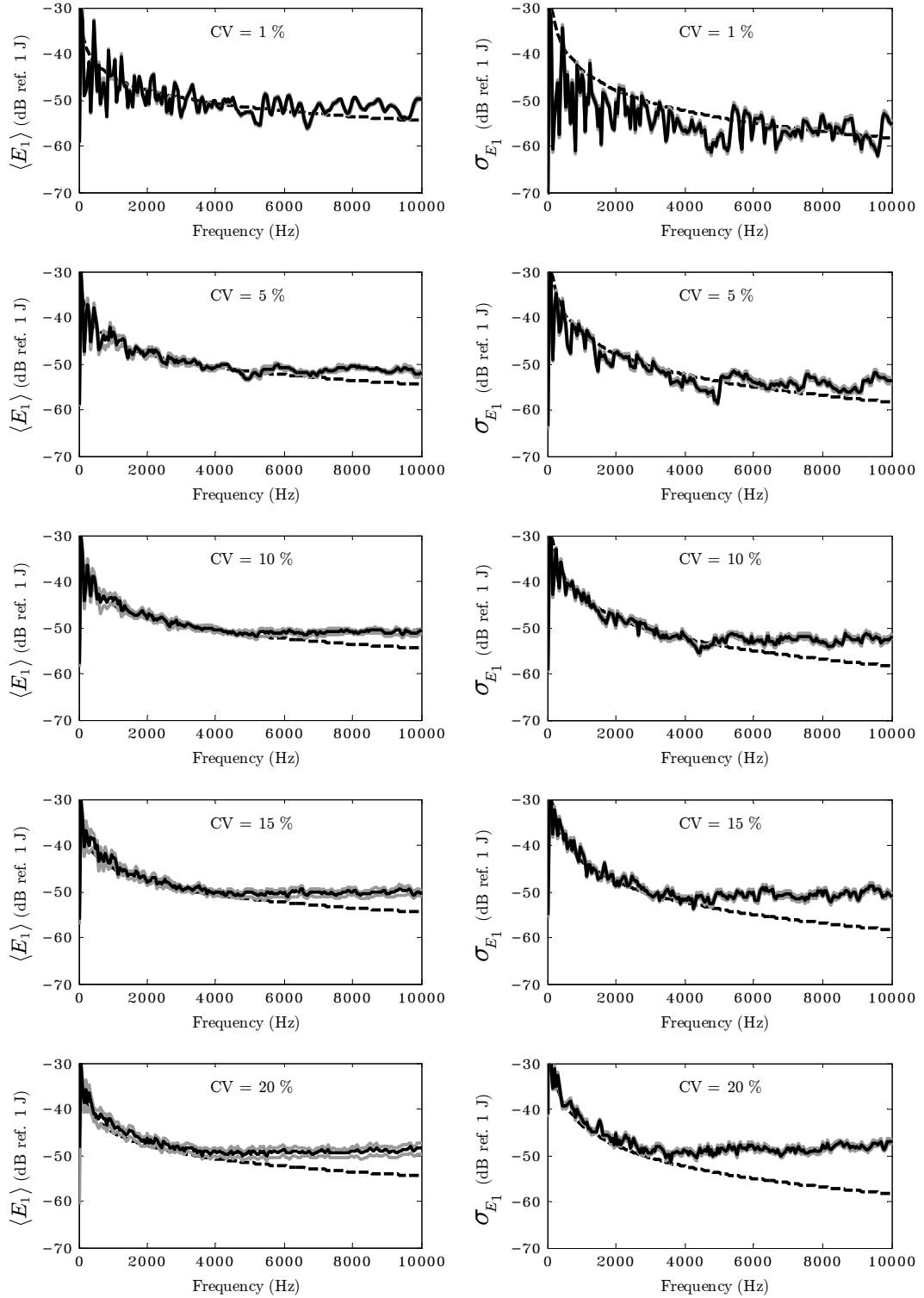


Figure 5.11: The mean and standard deviation of the energy of Plate 1, for an L-shaped plate with CV values of 1%, 5%, 10%, 15%, and 20% for the plate thickness variation as a function of frequency.

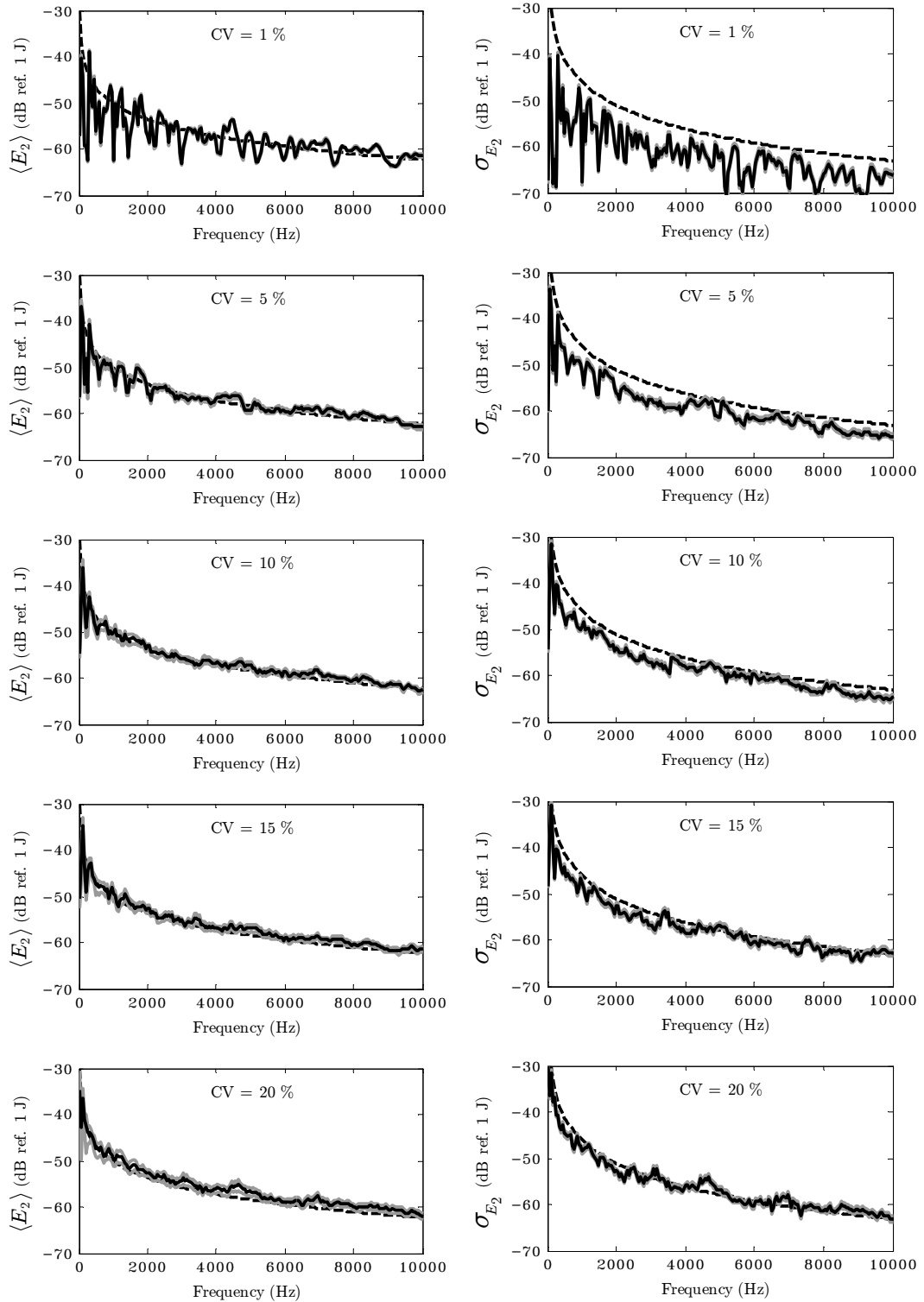


Figure 5.12: The mean and standard deviation of the energy of Plate 2, for an L-shaped plate with CV values of 1%, 5%, 10%, 15%, and 20% for the plate thickness variation as a function of frequency.

In the next section, the probability density function associated with the energy responses of Plates 1 and 2 for an L-shaped plate will be plotted as a function of a level of variability.

5.1.5 Evolution of Pdf of Energy

In this section, the pdf of energy response of an L-shaped plate subjected to a point load on Plate 1 is examined. Langley et al. (2013) shows that the pdf of energy response for a built-up structure (two coupled plates) with a random system conforms to a lognormal distribution. The probability density functions of energy of Plates 1 and 2 obtained from Monte Carlo simulations at particular frequencies are shown in Figs. 5.13–5.16. The continuous line represents a fitted lognormal distribution curve. In order to confidently plot the pdf of the energy obtained from Monte Carlo simulations, an ensemble of 1000 systems has been generated for each frequency.

Figs. 5.13 and 5.14 show the pdf versus the energy of Plates 1 and 2, respectively, for an L-shaped plate subjected to a single load on Plate 1 with CV values of 1%, 5%, 10%, 20%, and 30% for the plate dimension variation as a function of frequency.

Figs. 5.15 and 5.16 show the pdf versus the energy of Plates 1 and 2, for an L-shaped plate subjected to a single load on Plate 1 with CV values of 1%, 5%, 10%, 15%, and 20% for the plate thickness variation as a function of frequency.

It is evident that when the level of variability increases, respectively, for both dimension and thickness, the pdf of energy is more similar to that of the lognormal type. There is roughly no difference in the pdf of energy between the frequency of 5005 Hz and 10000 Hz.

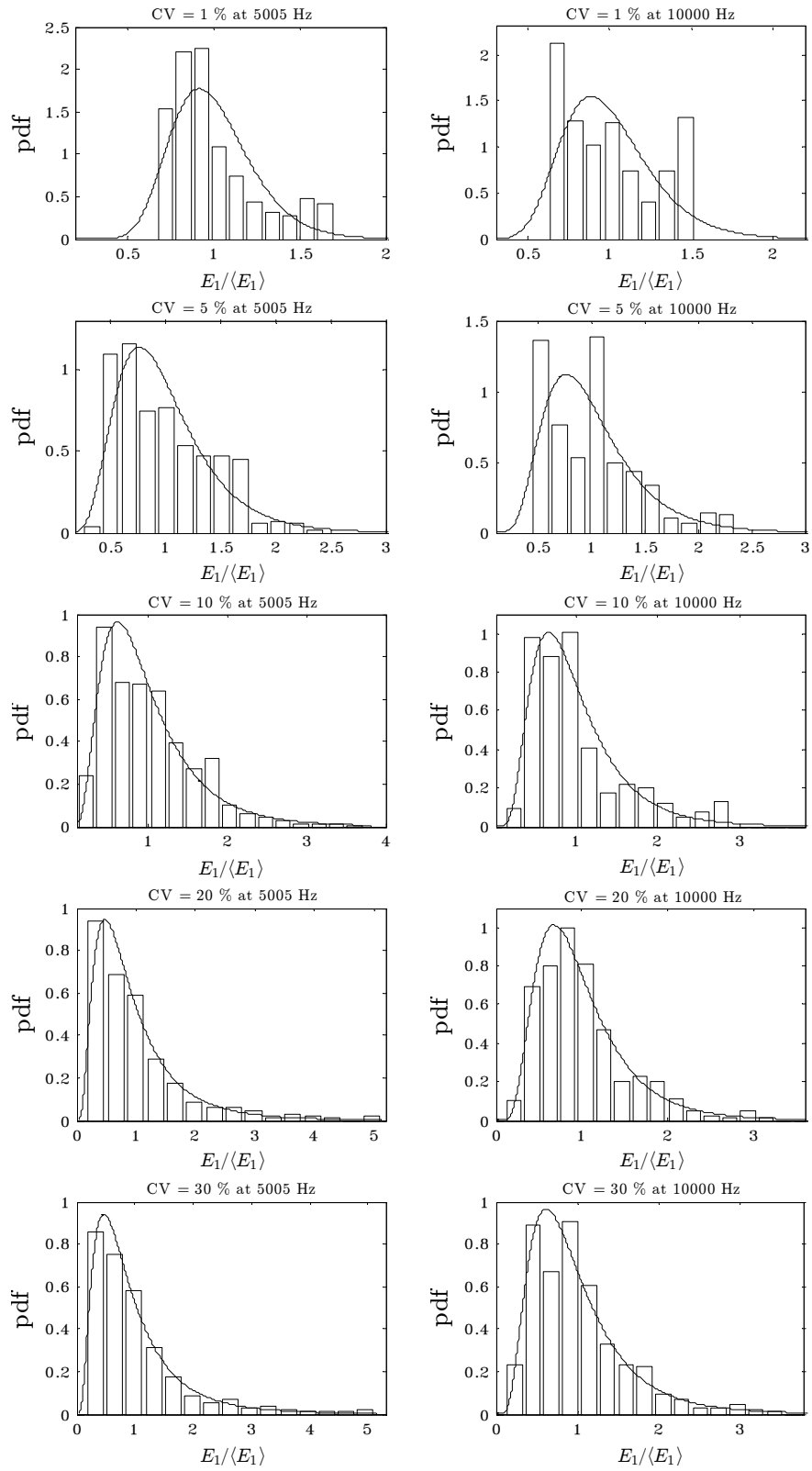


Figure 5.13: The pdf versus the normalised energy of Plate 1, for an L-shaped plate with CV values of 1%, 5%, 10%, 20%, and 30% for the dimension variation.

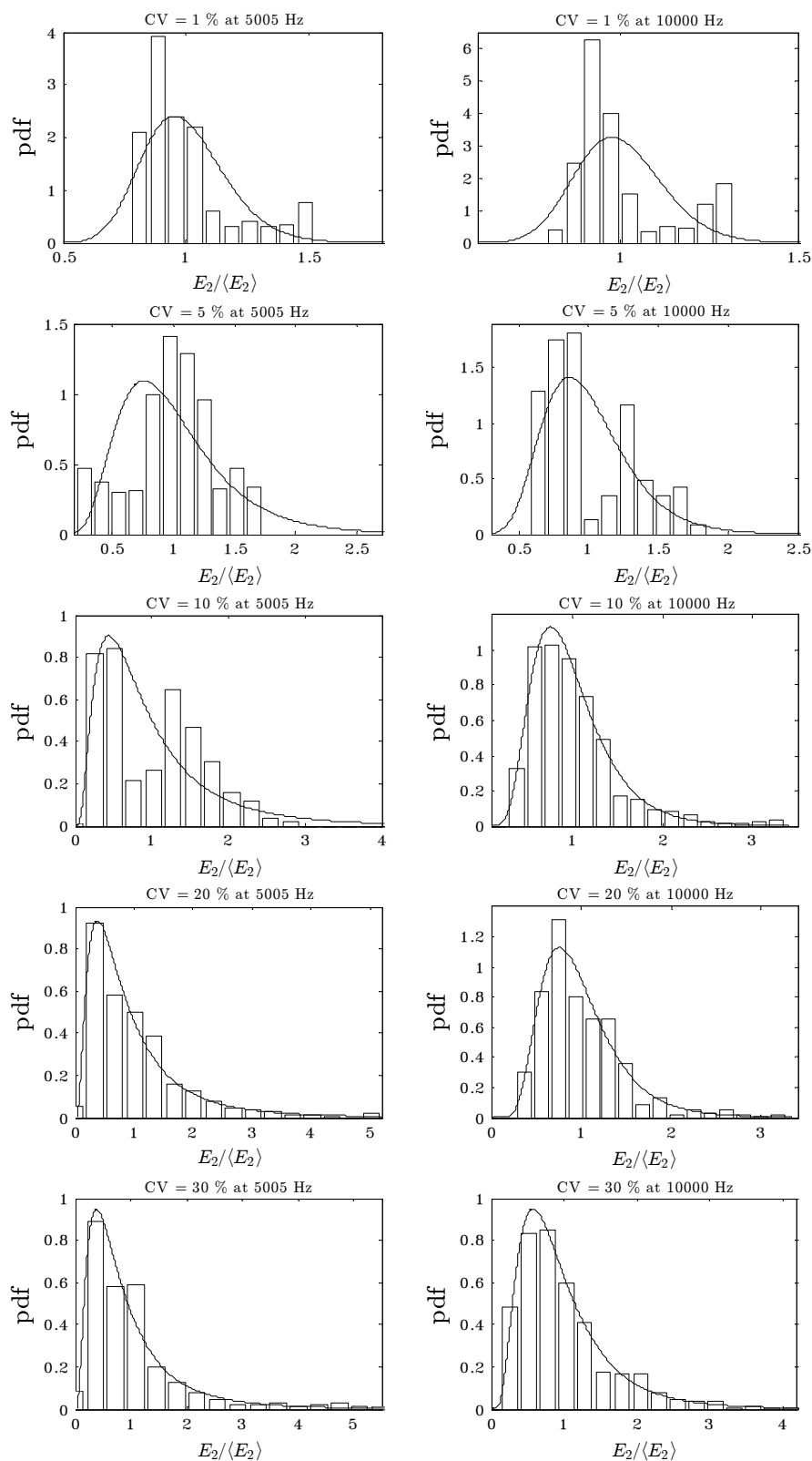


Figure 5.14: The pdf versus the normalised energy of Plate 2, for an L-shaped plate with CV values of 1%, 5%, 10%, 20%, and 30% for the dimension variation.

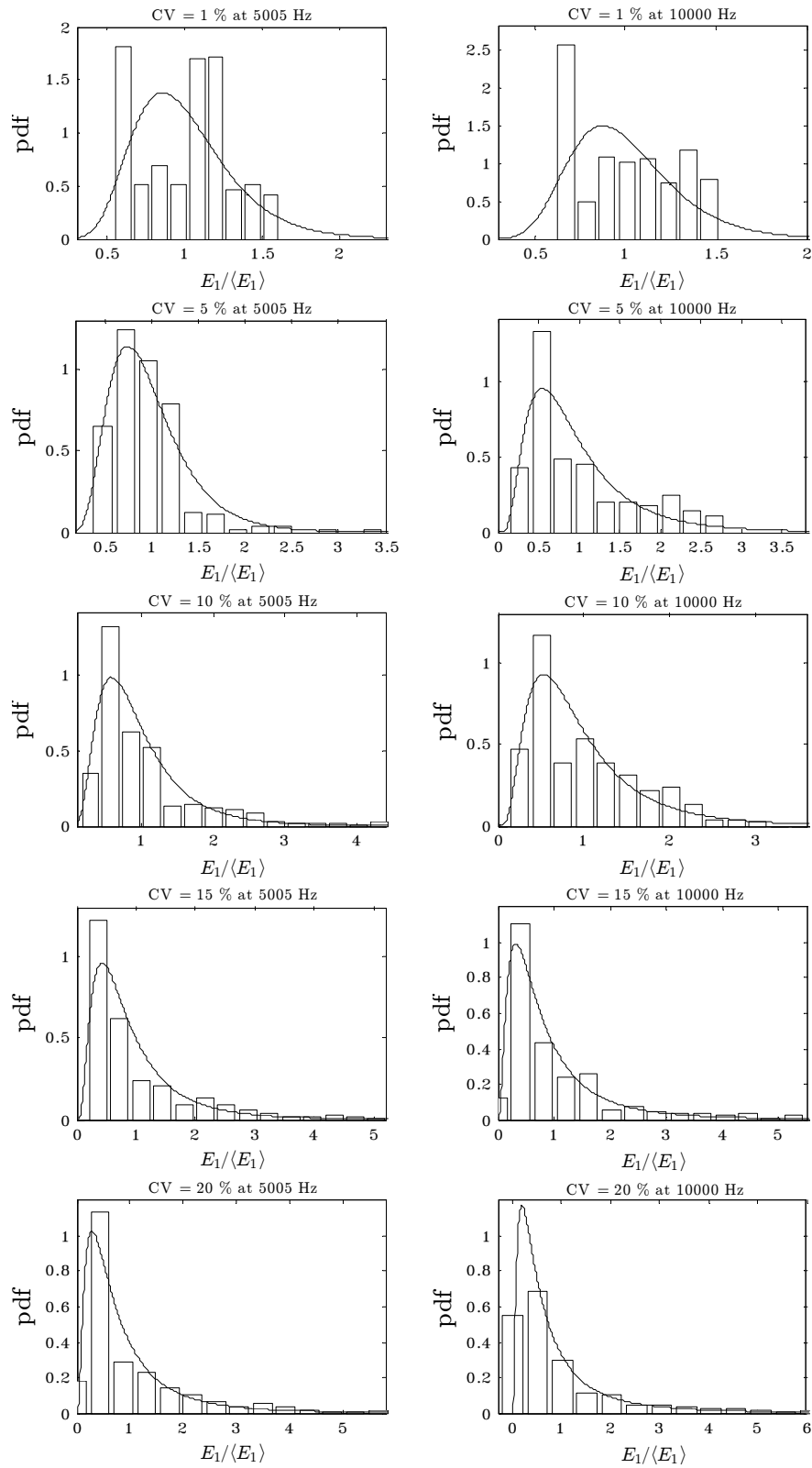


Figure 5.15: The pdf versus the normalised energy of Plate 1, for an L-shaped plate with CV values of 1%, 5%, 10%, 15%, and 20% for the plate thickness variation.

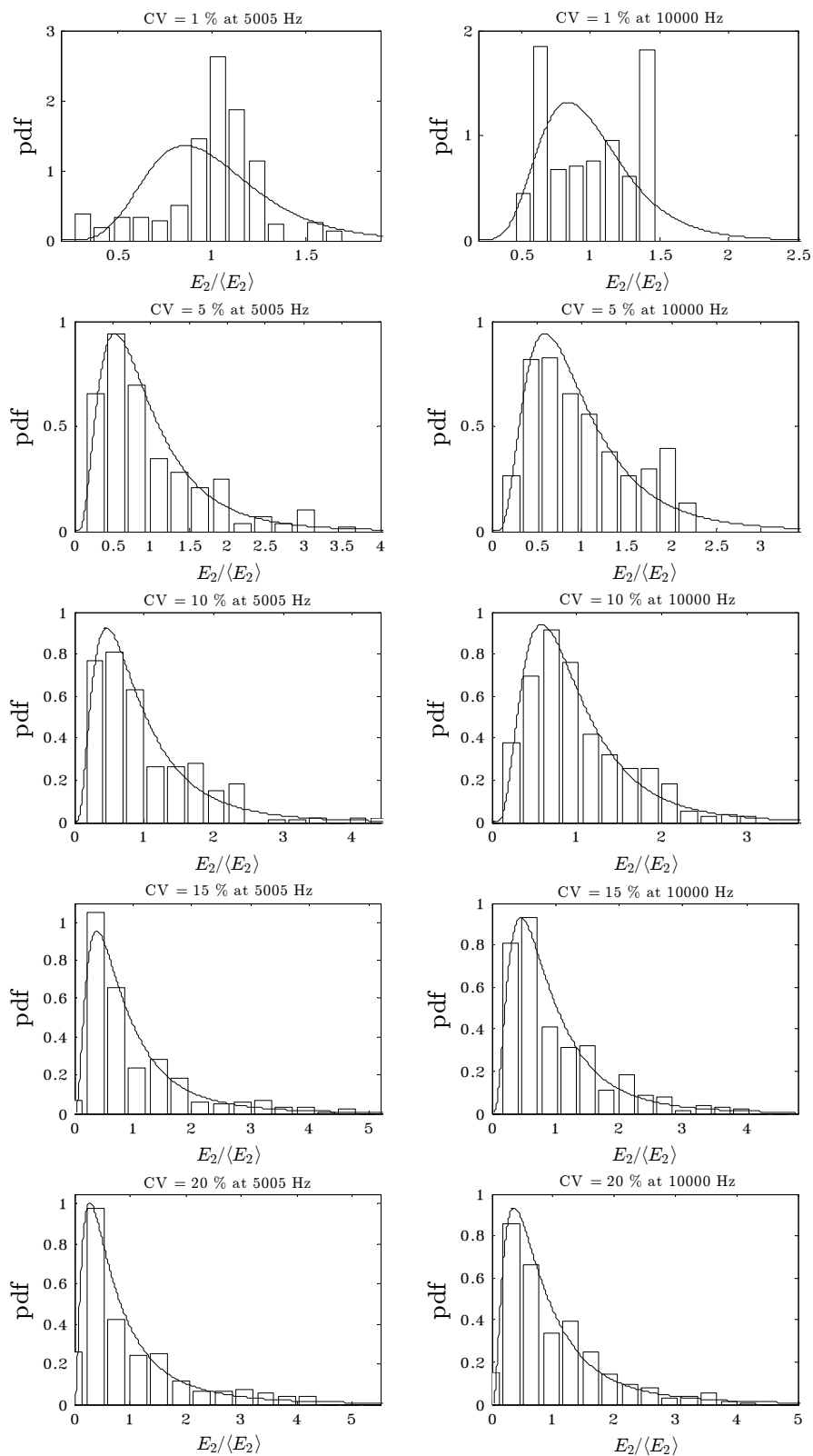


Figure 5.16: The pdf versus the normalised energy of Plate 2, for an L-shaped plate with CV values of 1%, 5%, 10%, 15%, and 20% for the plate thickness variation.

5.2 Conclusions of Chapter 5

The results shown for a non-simple built-up structure, are the mean and standard deviation of the energy for an L-shaped plate, driven by the harmonic point force. This is made uncertain as a random structure by varying the plate dimensions from 1%, 5%, 10%, 20%, and 30%, and the plate thicknesses from 1%, 5%, 10%, 15%, and 20% using a uniform distribution. The results are obtained by using Monte Carlo simulations based on (commercially available) finite element solutions via ANSYS as a benchmark to compare with SEA.

The comparison between SEA and Monte Carlo simulations shows better agreement for the mean and standard deviations of the energy for the dimension variation than those for the thickness variation. The mean responses obtained from Monte Carlo simulation and SEA for the different variation levels are different. When the CV increases, the mean response is higher, especially on Plate 1 for the plate thickness variation.

The distribution functions of the spatial average FRFs are shown for a non-simple built-up structure to be similar to the lognormal distribution, which, together with the results from Chapter 4, underlies the assumption to be made in Chapter 6. It has therefore been verified that the assumption of the lognormal distribution for the energy response of a non-simple built-up structure can be used.

Together with Chapter 4, Objective ii) of the thesis has now been met in this chapter because the SEA model has been applied to a non-simple built-up structure with both high and low-level uncertainties.

Chapter 6

A Novel Extreme-Value-based bounding Method for uncertain structures

A novel bounding method is proposed that allows a statistical bound to be computed associated with the response level of an ensemble of uncertain structures. The form of this statistical bound is expressed in terms of the probability of exceedance for a specified number of structures. In particular, it enables a frequency response exceedance level associated with n uncertain structures to be specified with particular probability p in terms of the level of uncertainty in the uncertain parameters. In simple terms, at a particular frequency, the statistical bound obtained is the level that would be exceeded with probability p by the response of the entire ensemble of n uncertain structures with a particular level of uncertainty. The more structures that are considered in the sample, the more likely a fixed level will be exceeded. Conversely, if a fixed exceedance probability is specified, as the number of structures considered is increased, the exceedance level will increase. At the same time as the level of variability in the uncertain parameters increases then bound will increase. Now to construct a statistical bound at a particular frequency for a particular level of parameter uncertainty, this is effectively specifying the proportion of all n realised FRFs of a random structure, falling above a certain level which is directly related to the specified probability level p .

The proposed approach makes use of finite sample extreme value distributions. The idea of using Extreme Value theory for bounding responses of uncertain structures is not new (see Dunne and Dunne, 2009). In that approach, asymptotic threshold-crossing extreme value theory was used to enable a limited amount of Monte Carlo simulation corresponding to a small number of structures, to be used to make statements about response bounds for a much largely sample of structures, at lower (more practically relevant) probability levels. The Monte Carlo simulation data was used to calibrate asymptotic threshold-crossing extreme value models. The limitations of the Dunne and Dunne (2009) approach was that asymptotic extreme value models might not always apply at lower levels involving finite samples of data, and second, some Monte Carlo

simulation had to take place (which could be computationally demanding) but also prone to statistical scatter.

The proposed approach also makes a number of key assumptions to make use of finite-sample extreme value distributions. Ultimately the only information needed, if all the assumptions hold, are accurate values of the mean and standard deviation associated with the spatially-averaged structural response energy. It will become apparent that the main advantage of the method is that it allows several routes to be used to obtain the required mean and standard deviation, opening-up the possibility of having a fast highly-efficient approximate bound prediction (using SEA for example), or a virtually exact approach via Direct Integration that involves only deterministic FRF prediction resulting in a calculation method that is much slower than SEA but much faster than Monte Carlo simulation.

The objective of this chapter is to create the basis of this new, relatively simple method that will allow a practical bound to be imposed on the FRF of a randomly-varying structure for different levels of parameter variability without the need for Monte Carlo simulation. To create this method, the evidence built up in Chapters 4 and 5 will be used to construct a hypothesis, which, in turn, will be used to develop an efficient predictive method. First, the basis of the method will be outlined in detail. This culminates in the need for accurate values of the mean and standard deviation of the spatially averaged energy level. A direct route to these two moments is then developed which along with an SEA route discussed earlier leads to two variants of the approach. These two variants namely where Direct Integration is used and where SEA is used, are applied in Chapter 7 and compared with predictions.

6.1 The Basis of the Proposed Bounding Method

The proposed method computes the bound from a ‘finite sample’ extreme value distribution $G_X(x) = F_n(x)$ associated with an ensemble of n uncertain structures. Here the variable X represents the spatially-averaged energy variable and is useful because additional key response statistics for displacement and velocity can be obtained when the external excitation is harmonic. The distribution:

$$G_X(x) = F_n(x) = \Pr(X < x) \quad (6.1)$$

i.e. the probability that the energy X associated with the ensemble of n uncertain structures is less than the energy level x .

Now as explained in Section 2.5.2, if the exceedance probability level is specified at some level p i.e. $1 - G_X(x) = p$ then $x = G_X^{-1}(1 - p)$. This level x is then deemed to be the statistical bound. In general, for an uncertain structure subject to harmonic excitation, the bound depends on the excitation frequency and would in general need to be computed separately for each (discrete) frequency. The first question is how in general is the distribution $G_X(x) = F_n(x)$ obtained?

To answer this question that will lead to the construction of an efficient method for bounding the FRF of a randomly-varying structure without using Monte Carlo simulation, a number of important assumptions need to be made:

Assumption-1 - independent identically-distributed random variables

The first assumption needed, is to hypothesise that the spatially-averaged energy levels $X_1, X_2, X_3, \dots, X_n$ associated with each structure, are independent identically-distributed random variables. When this assumption holds good, the distribution of the largest (extreme energy level) i.e. $\text{Max}(X_1, X_2, X_3, \dots, X_n)$ is of interest. Now in general, for (any) independent identically-distributed random variables, the distribution function $F_n(x)$ of the largest observation M_n is given (Madsen et al., 2006) as:

$$F_n(x) = F(x)^n \quad (6.2)$$

where $F(x)$ is underlying probability distribution function for the variable associated with any single sample. For any differentiable distribution function, the corresponding density function is given as:

$$f_n(x) = nF(x)^{n-1}f(x) \quad (6.3)$$

Eqs (6.2) and (6.3) are illustrated in Fig. 6.1 for both the normal and lognormal distribution functions with the mean and standard deviation values of 1.5 and 1, respectively (since an additional assumption will need to be made shortly).

It follows from Eq. (6.2) that for any value of x , where $0 < F(x) < 1$, when the sample size n increases, the location of the distribution function $F_n(x)$ for the normal

distribution increases more rapidly than the location of a lognormal distribution. But in general, that the expected value of M_n increases with increasing sample size n regardless of the underlying distribution.

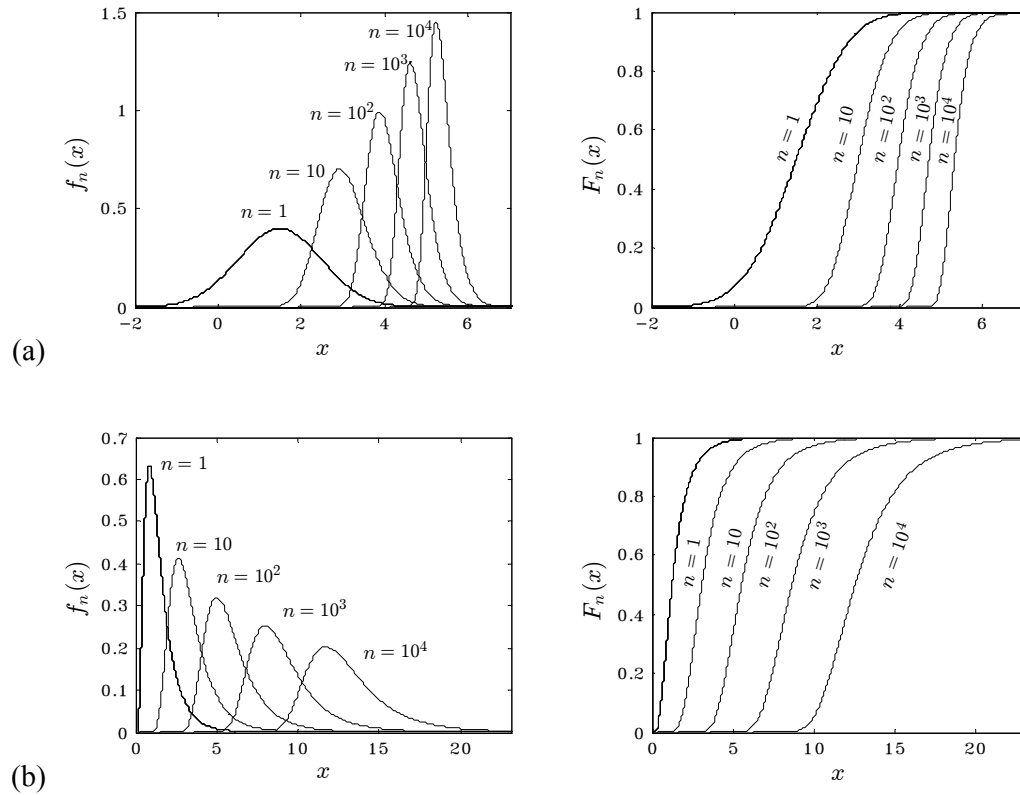


Figure 6.1: The probability densities and distribution functions for the largest of n independent variables, (from left to right) when $n = 1, 10, 10^2, 10^3, 10^4$: (a) normal distribution, (b) lognormal distribution.

By assuming that each realised response, at a given frequency, is independent, and identically distributed, then for an ensemble of responses, it is possible to construct the probability of exceedance or obtain the statistical bound. As mentioned earlier, the required response bound can be obtained by setting the probability level p associated with the finite sample distribution $F_n(x)$ (as explained in Section 2.5.2) by solving the equation $1 - F_n(x) = p$. For example, when $p = 0.5$, the bound effectively becomes the mean level M_n of the finite extreme value distribution. For example, the bounding parameter (M_n) with 50% probability (or confidence) level, for 10^4 samples, is computed from Eq. (6.2) and shown in Fig. 6.2.

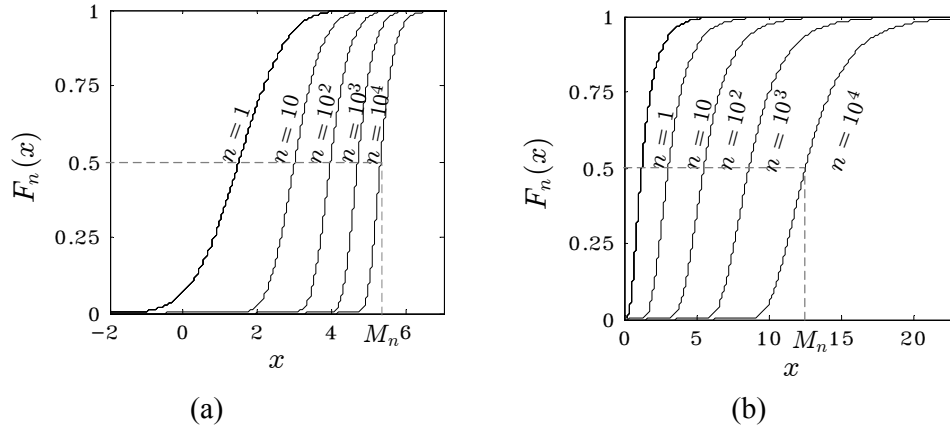


Figure 6.2: The probability level F_n as a function of the bounding parameter estimate: (a) normal distribution, (b) lognormal distribution.

Fig. 6.2 shows the distribution function for different numbers of samples up to 10^4 . The curves on the far-right-hand side of Fig. 6.2 are the distribution function for 10^4 samples. At 50% probability level (i.e. horizontal dashed lines), the estimate is found to be M_n (the vertical dashed line). If the sample size n decreases, the estimate M_n decreases. As the number of realisations n becomes very large, the exceedance probability would tend asymptotically to an extreme value (EV) distribution. The usual use of asymptotic extreme value distributions (such as Type I (Coles, 2001)) is to calibrate the distribution function (using simulated or measured data). It should be noted that this approach is not based on the use of an asymptotic Extreme Value distribution (as described in Section 2.5) but rather using the underlying distribution when it is known. But if the underlying distribution is known (or hypothesised, as is done shortly) then the finite number ensemble EV distribution can be constructed exactly (as also described in Section 2.4.2) and will therefore be subject to the accuracy of the assumed underlying distribution.

With the assumption of independent identically-distributed random variables, a response bound can therefore be calculated for any finite sample Extreme Value distribution corresponding to n structures. In general, the underlying distribution here could be of any type, depending on the actual random parameters in a real system, and providing the distribution parameters (such as the required moments) are available to describe it. Fortunately both the normal distribution and the lognormal distribution require only two moments—the mean and standard deviation. This then leads to the next important assumption:

Assumption-2 - the individual spatially-averaged energies are log-normally distributed.

There is strong evidence that the density function associated with the individual spatially-averaged energies is log-normal. The log-normal distribution function depends only on two moments: the mean and standard deviation. If these two moments are known then $F_n(x)$ is known, and for n structures, the distribution $G_X(x) = F_n(x)$ can be constructed using Eq. (6.2). It is therefore assumed that the spatially-averaged energy response FRF of an uncertain structure is log-normally distributed around the mean value for a particular level of variability. The results from Chapter 4, for all but very low uncertainty levels (regardless of the underlying distribution of variables) mainly support this assumption for simple structures. For example, in Figs 4.16 and 4.17, as concluded in Chapter 4, the estimated density functions of the FRFs look rather like a lognormal distribution. But more importantly, the results in Section 5.1.4 further support this assumption for a built-up structure.

The basis of the EV prediction method is therefore to assume that the underlying response energy level $F(x)$ is lognormal. The mean and standard deviation are needed as input values for the EV prediction, therefore an accurate mean and standard deviation prediction is essential. Before making additional assumptions on which to base development of a prediction method, an obvious implication of assuming that the underlying response distribution $F(x)$ is lognormal is the need for a computationally accurate and efficient way of obtaining the mean and standard deviation. Chapters 4 and 5 presented SEA-based mean and standard deviation predictions. However, the agreement of SEA based moments (as compared with Monte Carlo simulation) is not good for all cases. Where SEA does give good predictions of the mean and standard deviation of the spatially-averaged structural response energy, it is still necessary to make an important assumption. This is because SEA does not take account of the level of variability in the uncertain parameters.

Assumption-3 (only applicable to SEA-EV) - the spatially-averaged energy mean and standard deviation is constant and not a function of the parameter variability.

Because SEA does not take account of the level of variability in the uncertain parameters, regardless of the type of uncertainty, for use of SEA based predictions, it is necessary to assume that mean and standard deviation of the spatially-averaged structural response energy is constant and not a function of the parameter variability. To support this assumption, some evidence can be found in Section 2.3 that the SEA prediction for the mean energy (Lyon and Dejong, 1995) does not have the relationship with the level of parameter variability in the method. In Section 2.3.5, Langley and Cotroni (2004) energy variance prediction approach also has no relationship with the level of parameter variability in the method.

6.2 Calculating the Mean and Standard Deviation of the Spatially-averaged Response Energy via Direct Integration

This section will present calculation of the mean and standard deviation by using the Direct Integration (DI) method. To understand this approach, first consider in general a structure excited by a harmonic forcing function. If a single parameter (such as the length dimension or the thickness) were varied by a relatively small percentage from the nominal magnitude (for the crisp structure), a deterministic relationship at a particular frequency (of excitation) exists between the spatially-averaged structural response energy and the parameter value. In general this is a strongly nonlinear (deterministic) relationship of the form $y = g(x)$, where here x is the parameter value (or the variation from the nominal) and y is the spatially-averaged structural response energy.

Fig. 6.3 shows an example of the relationship $y = g(x)$, for a simply-supported plate structure subjected to a single harmonic load at the frequency of 10000 Hz. The plate length or thickness is varied with 150 subintervals between the minimum and maximum values. The nominal values of the plate length and thickness are 0.4 m and 1 mm, respectively.

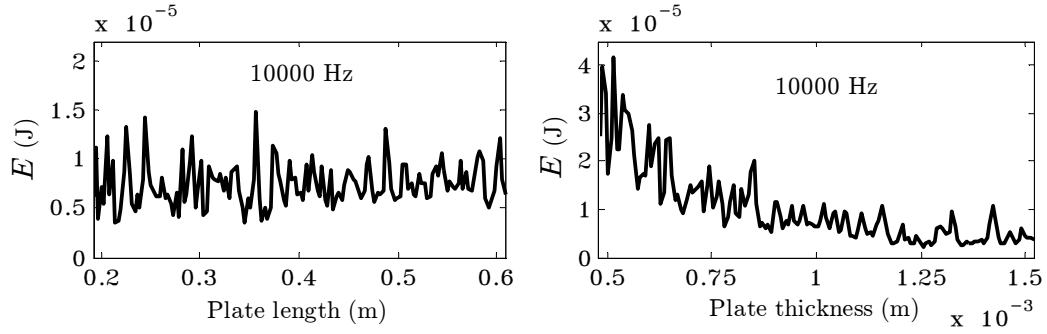


Figure 6.3: The energy of a plate as functions of the plate length and thickness at frequency 10000 Hz, for a simply-supported plate subjected to a single harmonic point load.

In general the function $y = g(x)$, would be obtained for a real structure using Finite Element solution. It is important to appreciate that this is a deterministic calculation (involving no statistical variation) i.e. this is not Monte Carlo simulation. An attractive feature is that such a function can be constructed using a standard FE model of the structure, and only needs to be constructed once. The difficulty however is that to construct $y = g(x)$ at a sufficient number of discrete values of parameter value x , at all frequencies, can involve a substantial amount of computing.

Turning to the calculation of the mean and standard deviation of y (i.e. the mean and standard deviation of the spatially-averaged structural response energy), if $y = g(x)$, assuming x is an input random variable with a uniform distribution with mean μ_x and standard deviation σ_x , then the pdf of variable x can be written as:

$$f_X(x) = \begin{cases} \frac{1}{2a} & \mu_x - a \leq x \leq \mu_x + a \\ 0 & x < \mu_x - a, x > \mu_x + a \end{cases} \quad (6.4)$$

where a corresponds to a particular value of CV associated with the uncertain variable x (Note it is shown in Appendix B using simple probability theory that parameter $a = \sqrt{3}\mu_x CV$ always, where $CV = \sigma_x/\mu_x$). For each value of CV, the value of a must therefore change if the nominal value of mean μ_x is to stay fixed. Before writing down expressions for the two required moments it is helpful to write σ_y^2 as:

$$\sigma_y^2 = E[g(X)^2] - E[g(X)]^2 \quad (6.5)$$

To calculate $E[g(X)]$ and $E[g(X)^2]$ when the distribution of X is known but that of $g(X)$ is not known, the law of the ‘unconscious statistician’ theorem (Ringner, 2009) can be used as follows:

$$E[g(X)] = \mu_y(a) = \begin{cases} \int_{\mu_x-a}^{\mu_x+a} g(x)f_X(x)dx & \text{if } X \text{ is continuous} \\ \sum_{x=\mu_x-a}^{\mu_x+a} g(x) f_X(x) & \text{if } X \text{ is discrete} \end{cases} \quad (6.6)$$

and

$$E[g(X)^2] = \begin{cases} \int_{\mu_x-a}^{\mu_x+a} g(x)^2 f_X(x)dx & \text{if } X \text{ is continuous} \\ \sum_{x=\mu_x-a}^{\mu_x+a} g(x)^2 f_X(x) & \text{if } X \text{ is discrete} \end{cases} \quad (6.7)$$

So to obtain σ_y^2 corresponding to a particular value of CV, where μ_x is chosen as the ‘crisp’ mean value, set $a = \sqrt{3}\mu_x\text{CV}$, then calculate the integrals in Eqs. (6.6) and (6.7) and substitute them into Eq. (6.5).

To demonstrate this method on a simple nonlinear function, consider an example where $y = g(x) = x^2 + 1$, and where x has a uniform distribution with $\mu_x = 1$. Substituting $g(x)$ into Eqs. (6.6) and (6.7) yields

$$E[g(X)] = \mu_y(a) = \frac{a^2}{3} + 2 \quad (6.8)$$

and

$$E[g(X)^2] = \frac{a^4}{5} + \frac{8a^2}{3} + 4 \quad (6.9)$$

Substituting $E[g(X)]$ and $E[g(X)^2]$ into Eq. (6.5) yields

$$\sigma_y^2 = \frac{4a^4}{45} + \frac{4a^2}{3} \quad (6.10)$$

or

$$\sigma_y = 2a \sqrt{\frac{a^2}{45} + \frac{1}{3}} \quad (6.11)$$

Therefore when the CV is 10%, such that $a = \sqrt{3}(1)(0.1)$, substituting a into Eqs. (6.8) and (6.11) yields $\mu_y = 2.01$ and $\sigma_y = 0.2002$. When the CV is 20% such that $a = \sqrt{3}(1)(0.2)$, substituting a into into Eqs. (6.8) and (6.11) yields $\mu_y = 2.04$ and $\sigma_y = 0.4016$.

This result can be compared with one from a MATLAB simulation for 10^6 samples of parameter x . The values of μ_y and σ_y from this MATLAB simulation are almost exactly identical to those obtained from Direct Integration (DI) to within four decimal points.

6.3 Bounding via the SEA-EV Method and the New DI-EV Method

As mentioned earlier the required mean and standard deviation can be obtained either via SEA or DI. Here we therefore refer to these versions of the bounding method as being either an SEA-EV method or a DI-EV method. The common basis of both the SEA-EV and DI-EV prediction methods are to assume Assumption-1 – that underlying spatially-averaged structural response energy is independent identically-distributed random variables, and Assumption-2 that the distribution of the underlying spatially-averaged structural response energy is lognormal. The mean and standard deviation needed for the normal distribution is obtained from SEA or DI for each frequency point. In each case different assumptions need to be made. In particular for use of the SEA-EV version Assumption-3 needs to be made, namely that the spatially-averaged structural response energy is constant and not a function of the parameter variability. For use of the DI-EV version Assumption-3 is not needed.

To test these versions of the bounding method, the response bounds first need to be obtained from the respective SEA-EV and DI-EV methods, and compared with Monte Carlo simulation.

The Monte Carlo simulation results in Chapter 4 (based on a simple Mode Superposition solution), and in Chapter 5 (based on finite element solutions), can act as a benchmark. These tests involve comparing the energy response bounds obtained from the SEA-EV and DI-EV bounding methods with the Monte Carlo simulation results. To

establish the accuracy of the SEA-EV and DI-EV versions, predictions of the bounds at each frequency will shortly be undertaken in Chapter 7.

6.4 Conclusions of Chapter 6

With the advantages given for constructing finite sample extreme value distributions, it is hypothesised that the combined SEA-EV and DI-EV methods can predict the bounds of the FRFs of uncertain structures without the need to undertake (potentially very expensive) Monte Carlo simulation. Two versions of an Extreme Value based method use finite sample extreme value distribution to construct a response bound for any level of variability and at any frequency. These methods are both mainly based on the assumption that the responses are log-normally distributed about the mean value at any given frequency. Evidence drawn from Chapter 4 and 5 supports this assumption for both simple and built-up structures. Both methods now need to be tested and this is done in Chapter 7.

Chapter 7

Application of DI-EV and SEA-EV Bounding Predictions

Regarding the Extreme Value based bounding method proposed in Chapter 6, this chapter is to test both the DI-EV and SEA-EV versions of the method. First more evidence is shown of the approach to calculate the mean and standard deviation of an uncertain structure, using the DI approach with simple and built-up structures before combining it with Extreme-Value (EV) theory. The bounding methods proposed in Chapter 6 allow the effect of variability to be included within either SEA-EV-based or DI-EV-based approaches. This chapter is to test their hypothesis.

The initial purpose of this chapter is to demonstrate application of SEA-Extreme-Value-based method (SEA-EV) and Direct-Integration-Extreme-Value-based method (DI-EV) in bounding the probability of exceedance, is to verify accurate computation of mean and standard deviation of the energy for models with high and low-level random dimension and thickness uncertainties. Testing then involves demonstrating the EV approach applied to a simple plate model. This is followed by a test on a non-simple built-up structure (Chapter 5) also with high and low-level random dimension and random thickness uncertainties. Monte Carlo simulation methods, using both simple Mode Superposition plate-structure solutions, and (commercially available) Finite Element (ANSYS) solutions for the (non-simple) built-up structure is used for comparisons with Both SEA-EV and DI-SEA methods. The response bounds obtained from the SEA-EV and DI-EV, with appropriate probability level are also presented.

7.1 Mean and Standard Deviation Predictions Using DI

The aim of this section is to present the applicability of Direct Integration (DI) method in predicting the mean level and standard deviation of the energy for a simply-supported plate and an L-shaped plate subjected to a single point force with high and low-level uncertainties as the level of variability is changed. Monte Carlo simulation based on Mode Superposition in Chapter 4 and (commercially available) finite element solutions (ANSYS) in Chapter 5 are used as a benchmark.

The mean and standard deviation of the energy are obtained by using Eqs. (6.7)–(6.11) as a discrete input parameter, because it is very complicated to write the energy as a function of the plate length (dimension) or thickness. Therefore, a comparison of the results with a different number of subintervals in DI prediction is necessary.

First, the energy as a function of the plate length or thickness ($g(X)$ in Eq. (6.5)) for each frequency needs to be constructed by selecting a used in Eq. (6.4) as the highest CV value with which to compare. In this case, the highest CV value is 30%. The function $g(X)$ of each frequency can be used to calculate the mean level and standard deviation of the energy for CV values of 1%–30%. The advantage of this method is it is a deterministic method. Besides, the most important advantage of this method will appear when it is used to compare with many variability levels of CV in the selected range. For example, if the highest CV value is 30%, $g(X)$ of each frequency can be used to serve for Eqs. (6.6) and (6.7) to calculate the mean and standard deviation of the energy for any variability level of CV from 1% to 30%.

Fig. 7.1 shows a comparison of the energy as a function of the plate length and a function of thickness with 100, 150, and 1000 subintervals at frequencies 5005 Hz and 10000 Hz, for a simply-supported plate. For the dimension (plate length) variation, its nominal value and the parameter a for CV value 30% are 0.4 m and 0.2078 m, respectively. For the thickness variation, its nominal value and the parameter a for CV value 30% are 1 mm and 0.520 mm, respectively.

In computing the energy as functions of the plate length and thickness, different subintervals are used to serve the numerical integration in Eqs. (6.6) and (6.7), which is via the Trapezoidal rule, to calculate the mean level and standard deviation of the energy for each frequency.

Figs. 7.2 and 7.3 show comparison of the mean and standard deviation of the energy as a function of frequency with frequencies from 10 Hz up to 10000 Hz in 201 intervals, for a simply-supported plate with the plate dimension variation at CV value of 1% and 20% between Monte Carlo and DI with 100, 150, and 1000 subintervals.

Figs. 7.4 and 7.5 show comparison of the mean and standard deviation of the energy as a function of frequency with frequencies from 10 Hz up to 10000 Hz in 201 intervals,

for a simply-supported plate with the plate thickness variation at CV value of 1% and 20% between Monte Carlo and DI with 100, 150, and 1000 subintervals.

Figs. 7.2–7.5 demonstrate that the mean and standard deviation of the energy obtained with 150-subinterval DI are similar to those with 1000-subinterval DI and significantly better than those with 100-subinterval DI, especially for the standard deviation of the energy with CV value of 1% for both plate dimension and thickness variation.

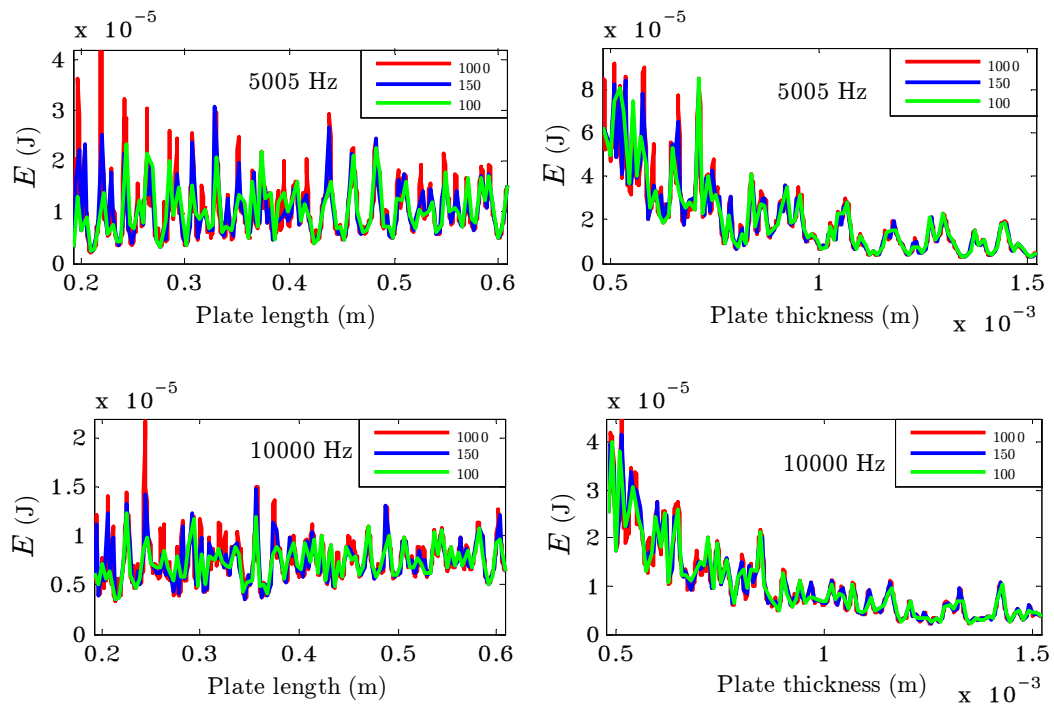


Figure 7.1: Comparison of the energy as functions of the plate length and thickness, with 100, 150, and 1000 subintervals at frequencies 5005 Hz and 10000 Hz, for a simply-supported plate.

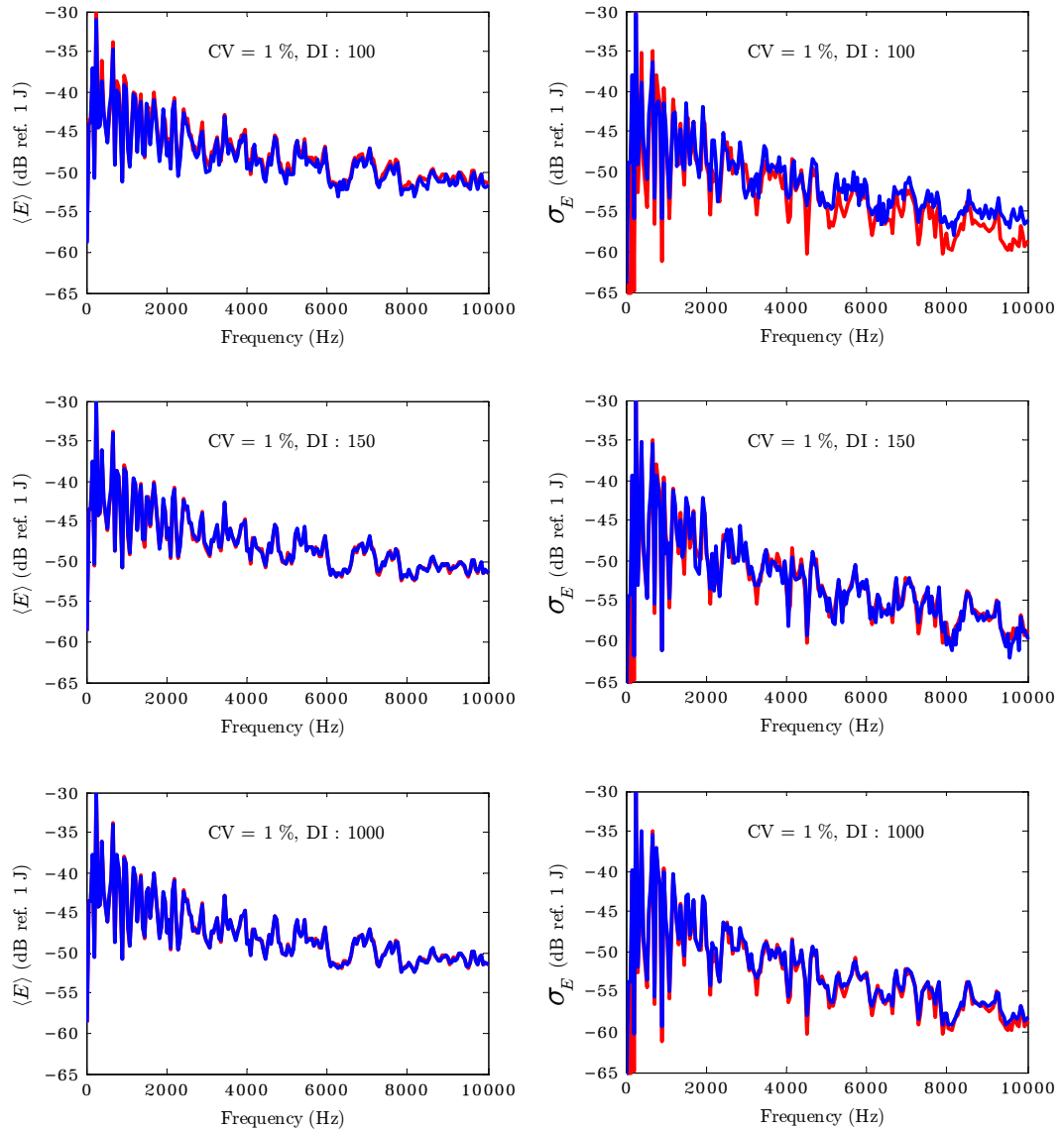


Figure 7.2: Comparison of the mean and standard deviation of the energy, for a simply-supported plate with CV values of 1% for the dimension variation between Monte Carlo and DI with 100, 150, and 1000 subintervals. —: Monte Carlo; —: DI.

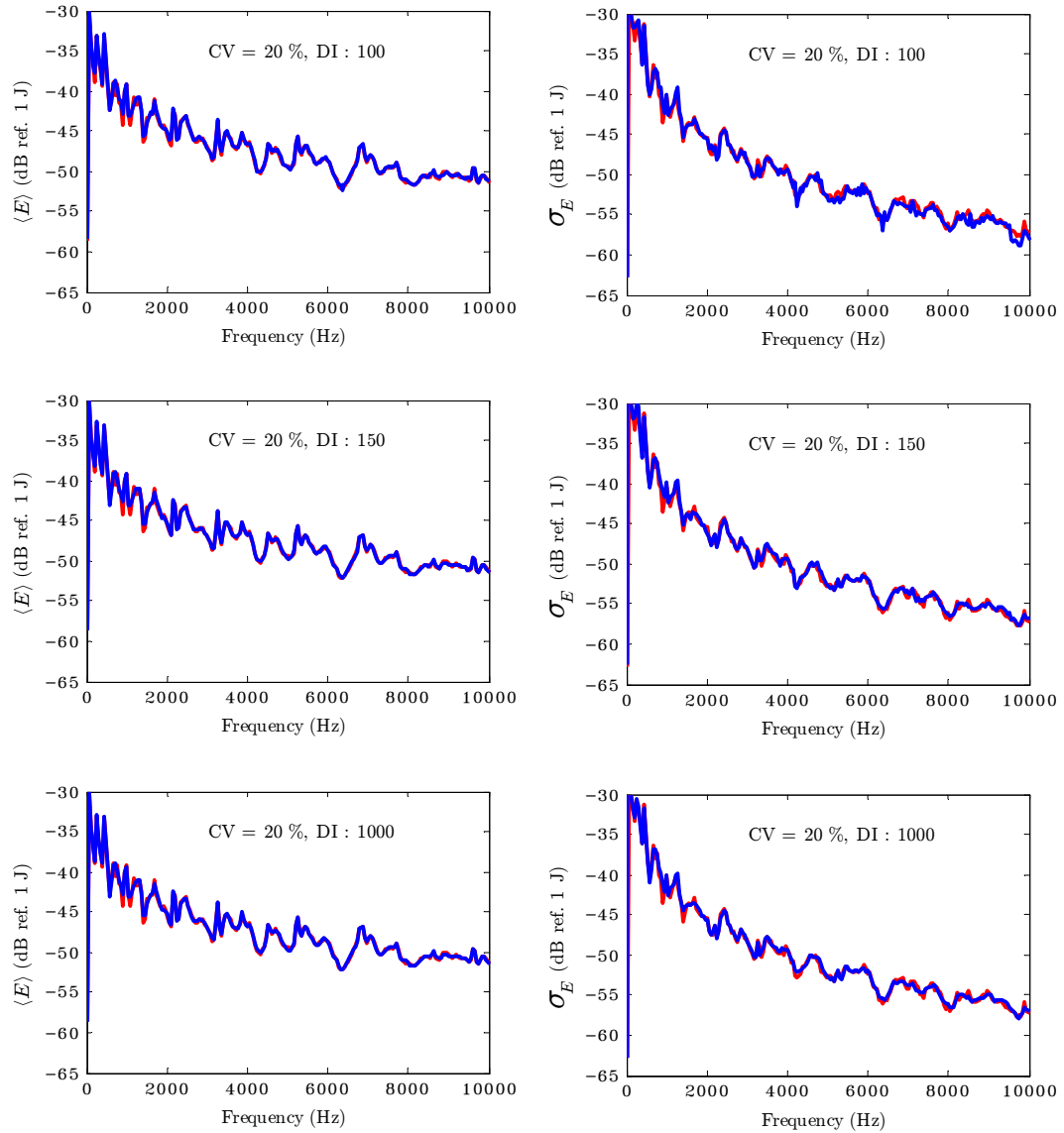


Figure 7.3: Comparison of the mean and standard deviation of the energy, for a simply-supported plate with CV values of 20% for the dimension variation between Monte Carlo and DI with 100, 150, and 1000 subintervals. —: Monte Carlo; —: DI.

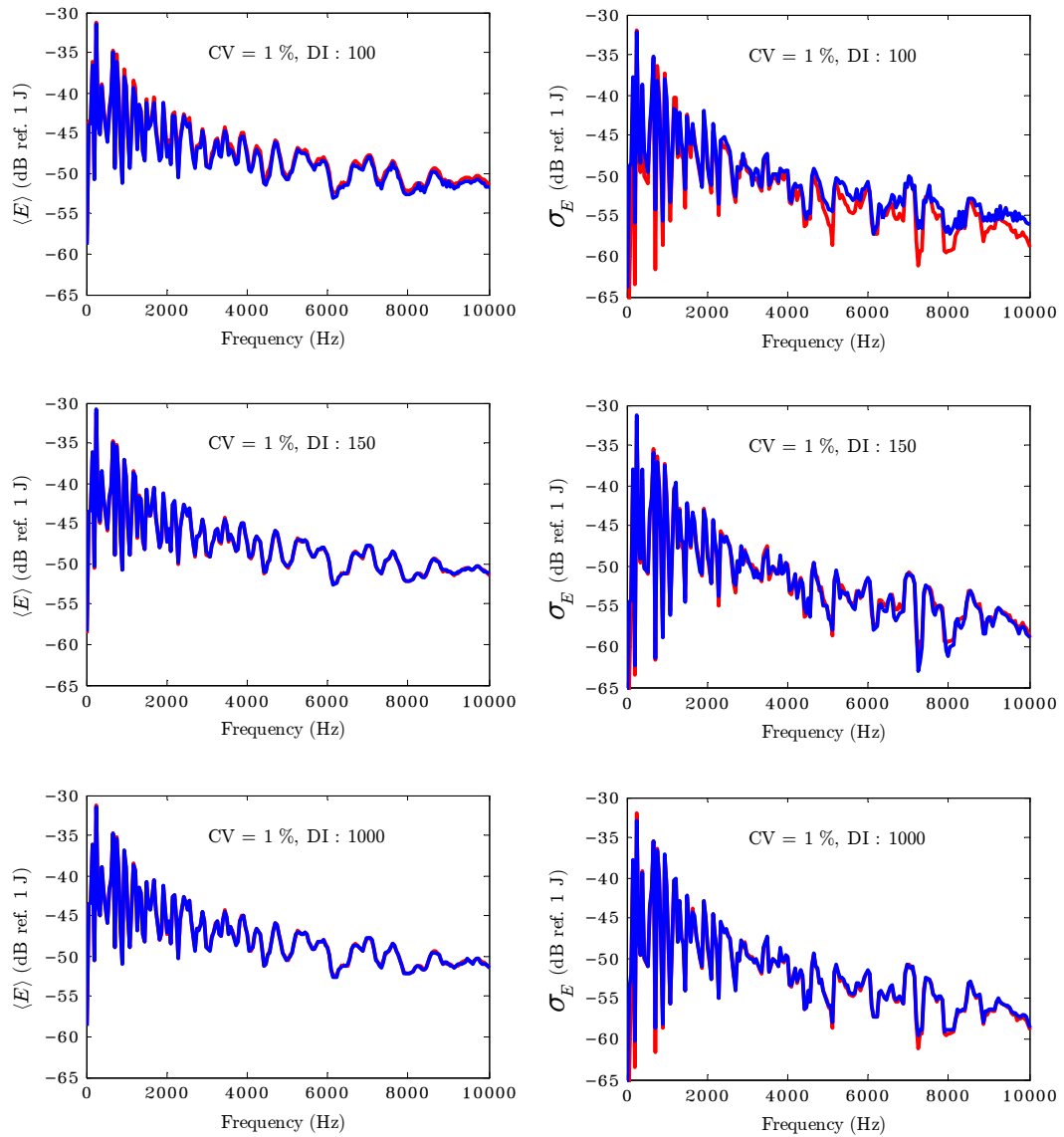


Figure 7.4: Comparison of mean and standard deviation of the energy, for a simply-supported plate with CV values of 1% for the thickness variation between Monte Carlo and DI with 100, 150, and 1000 subintervals. —: Monte Carlo; —: DI.

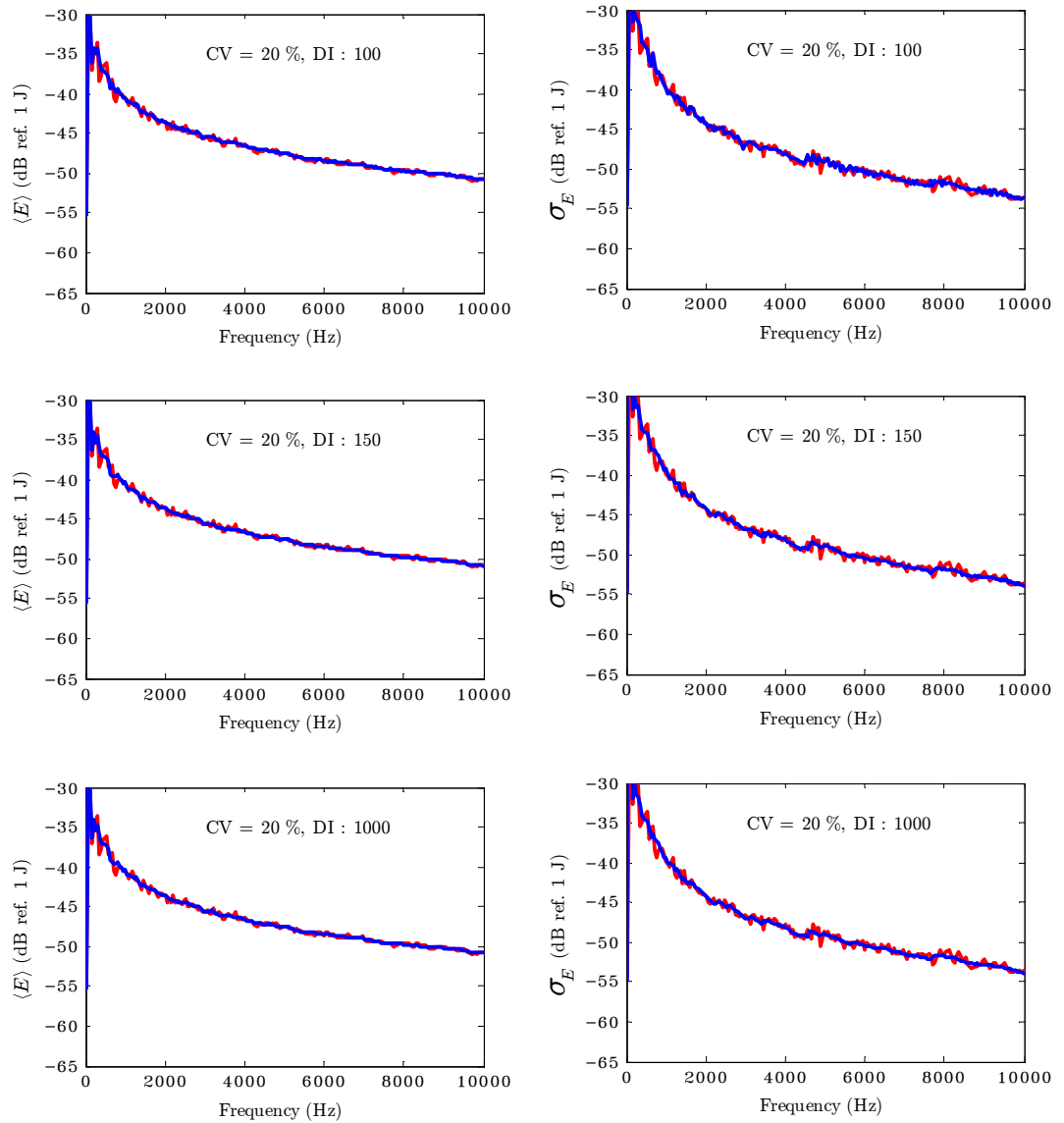


Figure 7.5: Comparison of the mean and standard deviation of the energy, for a simply-supported plate with CV values of 20% for the thickness variation between Monte Carlo and DI with 100, 150, and 1000 subintervals. —: Monte Carlo; —: DI.

To see a quantitative comparison, the percentage error of the mean and standard deviation of the energy, for a simply-supported plate with the plate dimension and thickness variation at CV value of 1% and 20% between Monte Carlo and DI with 100, 150, and 1000 subintervals are shown in Figs. 7.6–7.9. The percentage error of the energy is defined as the difference between the moments obtained by DI and Monte Carlo simulation. For example, for the mean this is:

$$\text{Error of } E[E](\%) = \frac{E[E]_{\text{DI}} - E[E]_{\text{Monte Carlo}}}{E[E]_{\text{DI}}} \times 100$$

Strictly this measure is subjected to statistical fluctuation from Monte Carlo simulation.

Fig. 7.6 shows that the ranges of percentage error for the mean of the energy, for a simply-supported plate with CV values of 1% for the plate dimension variation, are around -40% to 20%, -10% to 10%, and -5% to 5% for DI with 100, 150, and 1000 subintervals, respectively. The peaks in the range of the percentage error of the mean of the energy are -90%, -37%, and -19% for DI with 100, 150, and 1000 subintervals, respectively. For the percentage error in the standard deviation of the energy, for a simply-supported plate with CV values of 1% for the plate dimension variation, it also shows that the ranges of the percentage error, are around -40% to 60%, -40% to 30%, and -10% to 20% for DI with 100, 150, and 1000 subintervals, respectively. The peaks in the range of percentage error in the standard deviation of the energy are -160%, -100%, and 60% for DI with 100, 150, and 1000 subintervals, respectively.

For a simply-supported plate with CV values of 20% for the plate dimension variation, Fig. 7.7 shows that the ranges of percentage error for the mean of the energy are around -7% to 5%, -5% to 4%, and -3% to 3% for DI with 100, 150, and 1000 subintervals, respectively. With 150, and 1000 subintervals, the scatter of percentage error for the mean of the energy continuously decreases when frequency increases. For the percentage error in the standard deviation of the energy, for a simply-supported plate with CV values of 1% for the plate dimension variation, It also shows that the ranges of the percentage error are around -20% to 20%, -10% to 10%, and -5% to 5% for DI with 100, 150, and 1000 subintervals, respectively. The peaks in the range of percentage error in the standard deviation of the energy are -60%, -50%, and 25% for DI with 100, 150, and 1000 subintervals, respectively.

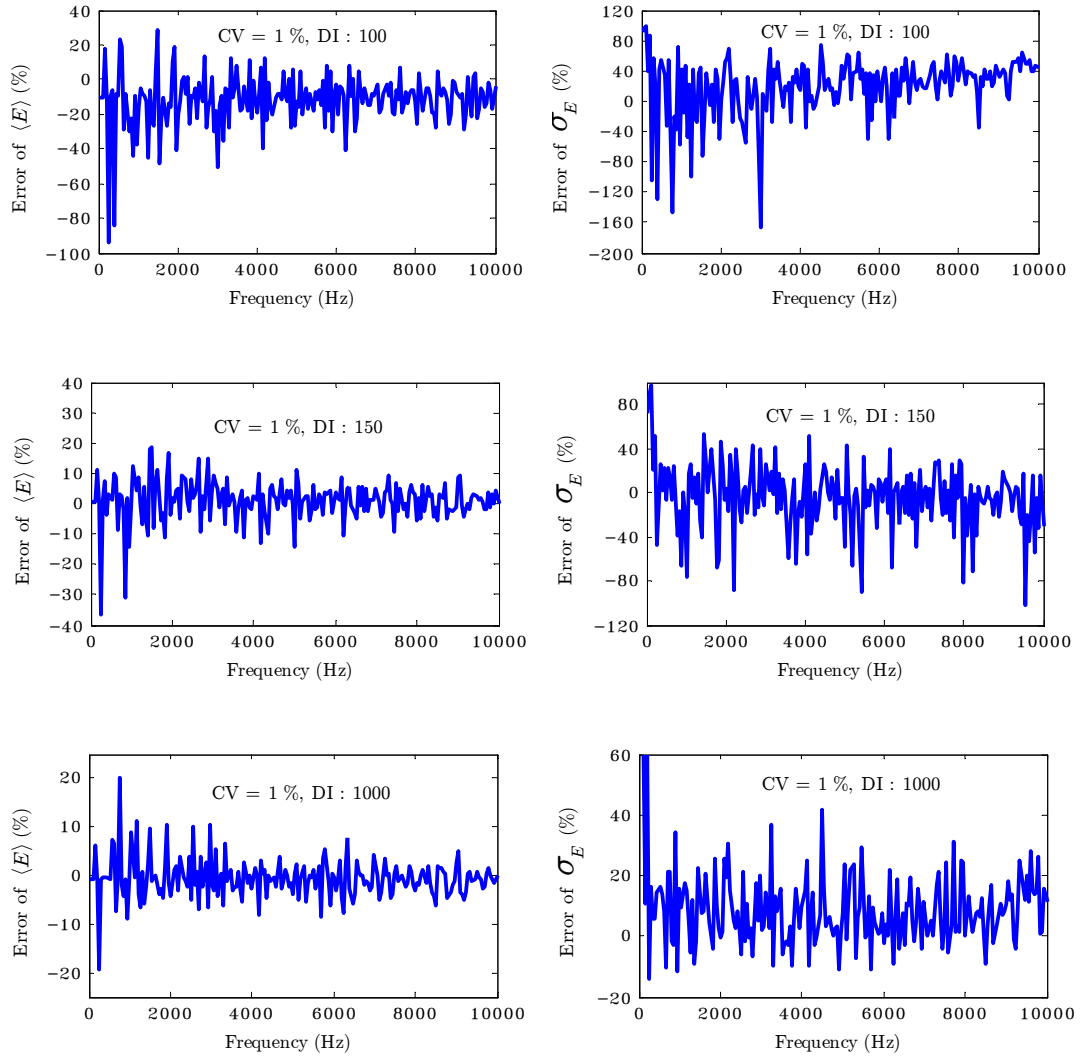


Figure 7.6: Comparison of the percentage error of the mean and standard deviation of the energy, for a simply-supported plate with CV values of 1% for the plate dimension variation between Monte Carlo and DI with 100, 150, and 1000 subintervals.

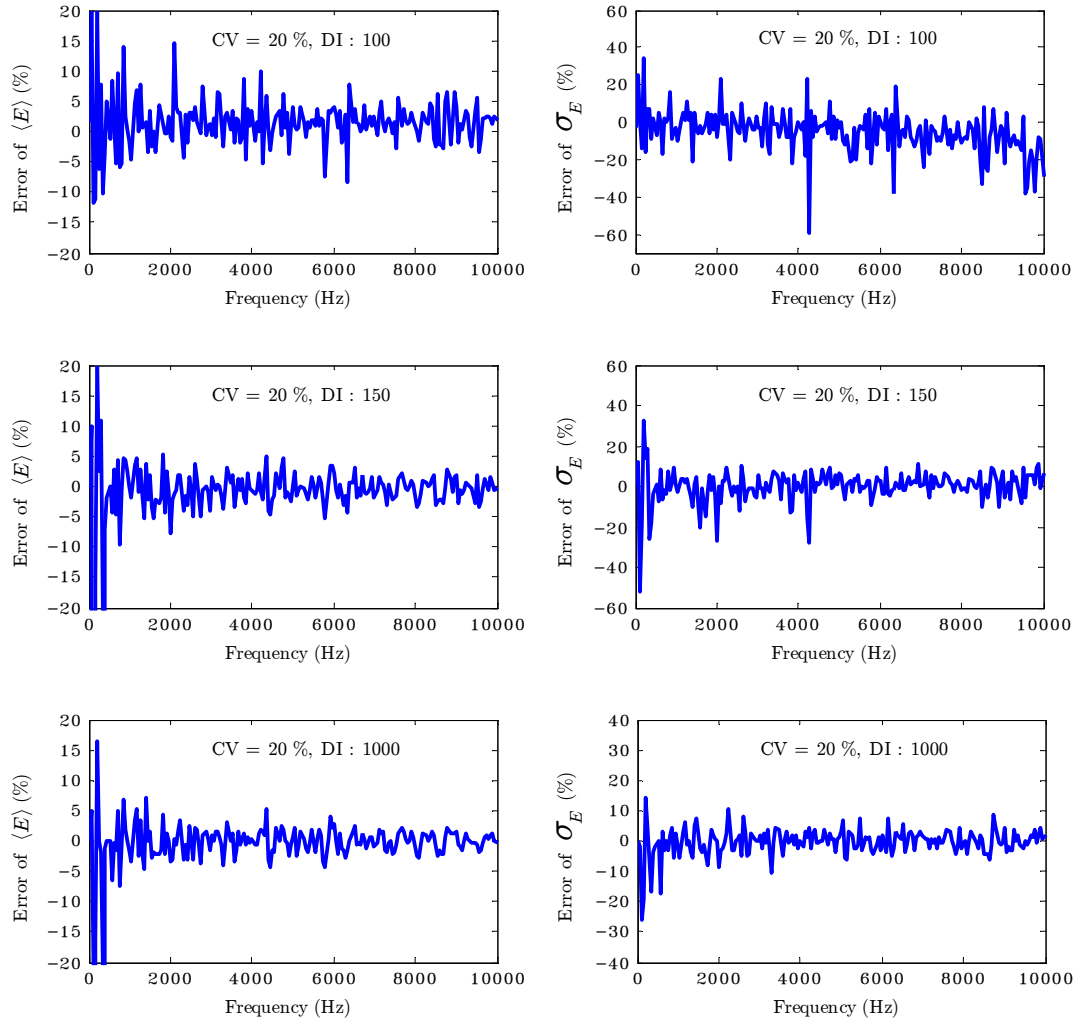


Figure 7.7: Comparison of the percentage error of the mean and standard deviation of the energy, for a simply-supported plate with CV values of 20% for the plate dimension variation between Monte Carlo and DI with 100, 150, and 1000 subintervals.

Fig. 7.8 shows that the ranges of the percentage error of the mean of the energy, for a simply-supported plate with CV values of 1% for the plate thickness variation, are around -20% to 0%, -4% to 5%, and -2.5% to 2.5% for DI with 100, 150, and 1000 subintervals, respectively. The peaks of the ranges of the percentage error of the mean of the energy are -25%, 10%, and -6% for DI with 100, 150, and 1000 subintervals, respectively. For the percentage error in the standard deviation of the energy, for a simply-supported plate with CV values of 1% for the plate thickness variation, it also shows that the ranges of the percentage error, are around -20% to 40%, -30% to 15%, and -10% to 10% for DI with 100, 150, and 1000 subintervals, respectively. The peaks in the range of percentage error in the standard deviation of the energy are 100%, -70%, and 60% for DI with 100, 150, and 1000 subintervals respectively.

For a simply-supported plate with CV values of 20% for the plate thickness variation, Fig. 7.9 shows that the ranges of percentage error for the mean of the energy are around -4% to 8%, -4% to 4%, and -3% to 3% for DI with 100, 150, and 1000 subintervals, respectively. With 100, 150, and 1000 subintervals, the scatter of percentage error for the mean of the energy continuously decreases when frequency increases. For the percentage error in the standard deviation of the energy, for a simply-supported plate with CV values of 1% for the plate thickness variation, It also shows that the ranges of the percentage error are around -15% to 10%, -6% to 6%, and -5% to 5% for DI with 100, 150, and 1000 subintervals, respectively. The peaks in the range of percentage error in the standard deviation of the energy are -60%, -50%, and 25% for DI with 100, 150, and 1000 subintervals respectively.

From Figs. 7.6–7.9, we can say that DI with 150-subinterval is acceptable to use for predicting the mean and standard deviation of the energy. The next subsection will show the comparison of the mean and standard deviation of the energy for a simply-supported plate from SEA, DI, and Monte Carlo simulation.

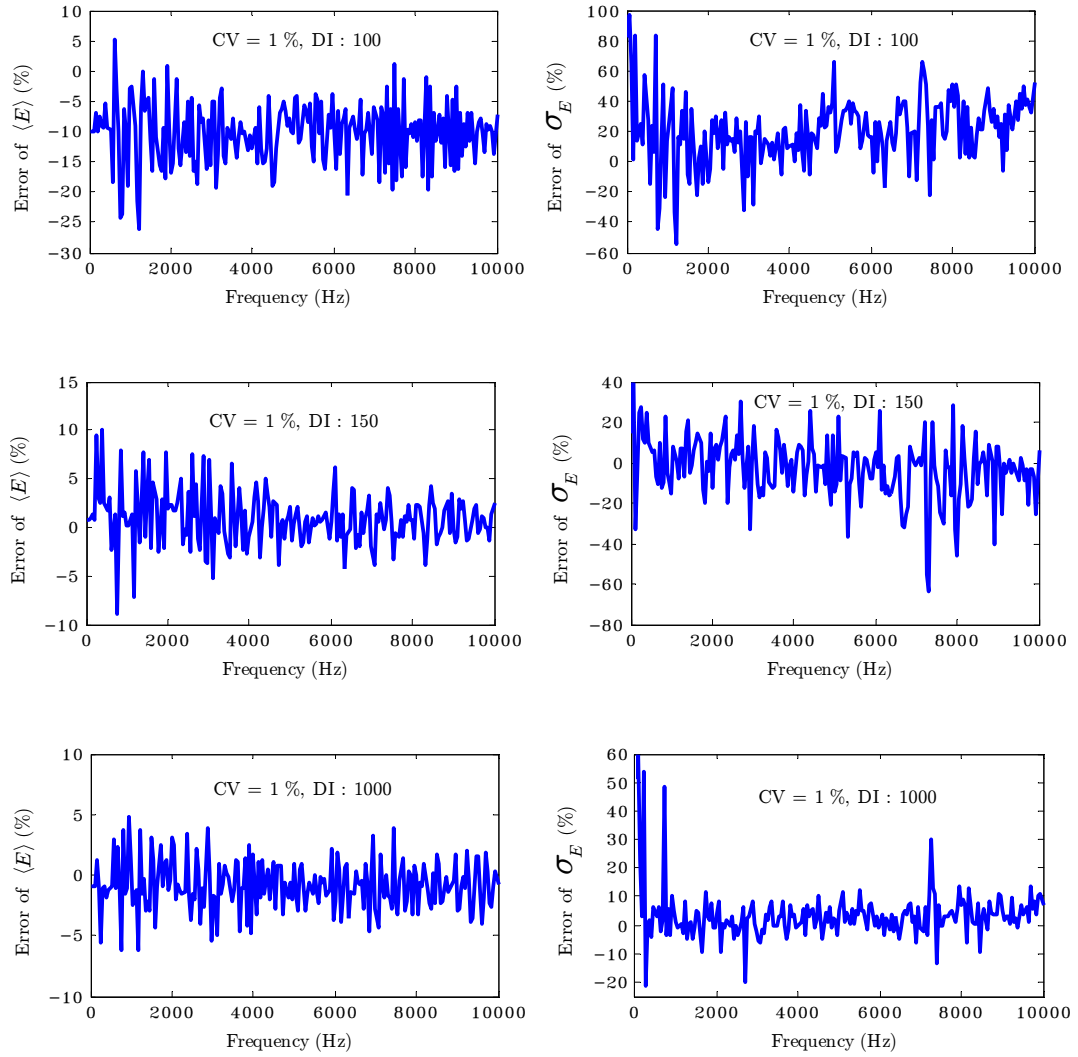


Figure 7.8: Comparison of the percentage error of the energy, for a simply-supported plate with CV values of 1% for the plate thickness variation between Monte Carlo and DI with 100, 150, and 1000 subintervals.

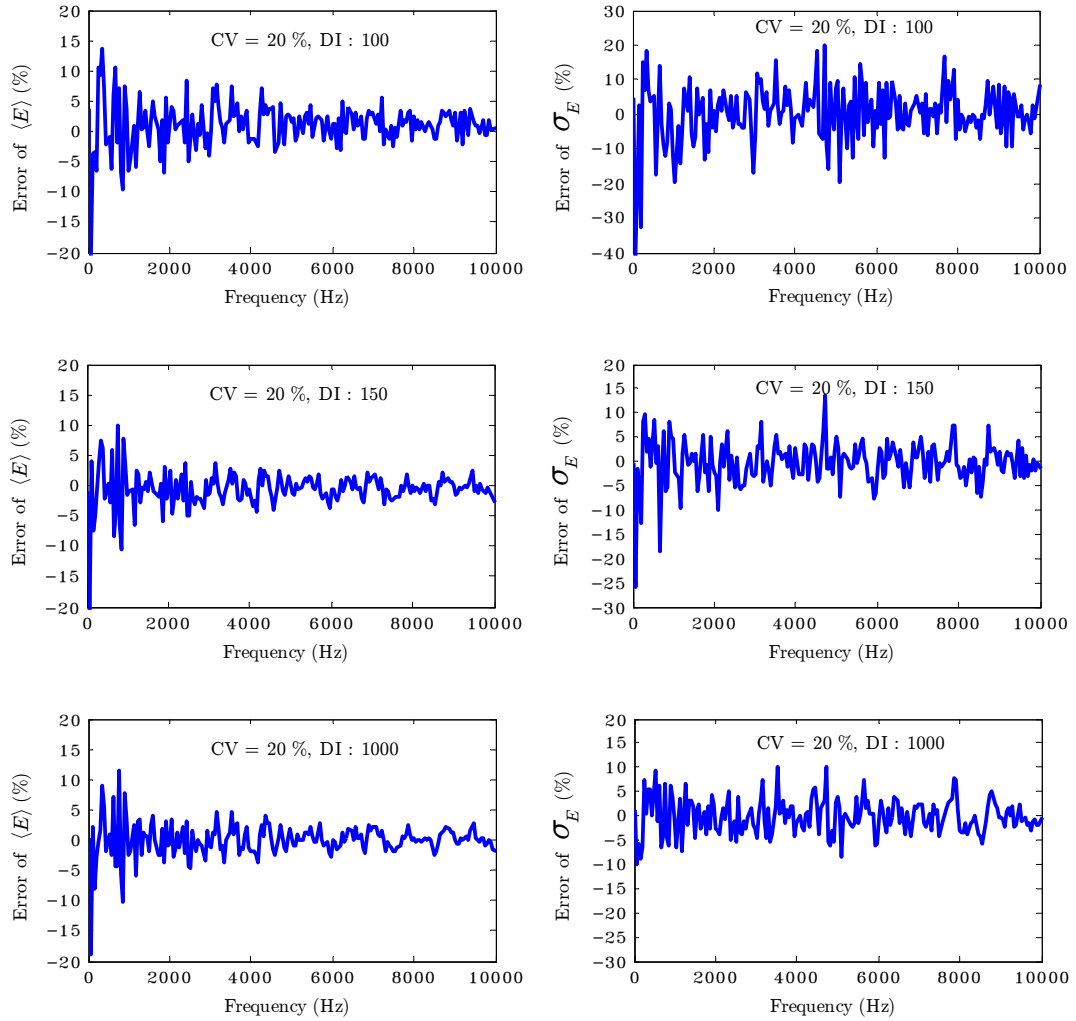


Figure 7.9: Comparison of the percentage error of the mean and standard deviation of the energy, for a simply-supported plate with CV values of 20% for the plate thickness variation between Monte Carlo and DI with 100, 150, and 1000 subintervals.

Application of DI to a Simple Structure

This section will show the capability of DI with 150 subintervals to predicting the mean and standard deviation of the energy with frequencies from 10 Hz up to 10000 Hz in 201 intervals, for a simply-supported plate from Chapter 4 with the plate dimension and thickness variation for CV value of 1%, 5%, 10%, 20%, and 30% compared with SEA and Monte Carlo results from Chapter 4.

To apply DI prediction for a simply-supported plate, first the energy as functions of the plate length or thickness for each frequency ($g(X)$ in Eq. (6.5)) needs to be constructed. Then $g(X)$ for each frequency is used in Eqs. (6.6) and (6.7) to calculate the mean and standard deviation of the energy for the plate.

Fig. 7.10 shows the energy of a plate as functions of the plate length and thickness with 150 subintervals at frequencies 5005 Hz and 10000 Hz, for a simply-supported plate subjected to a single point load. The nominal values are 0.4 m and 1 mm for the plate length and thickness variation, respectively. The parameters a for CV value 30% are 0.208 mm and 0.520 mm for the plate length and thickness variation, respectively.

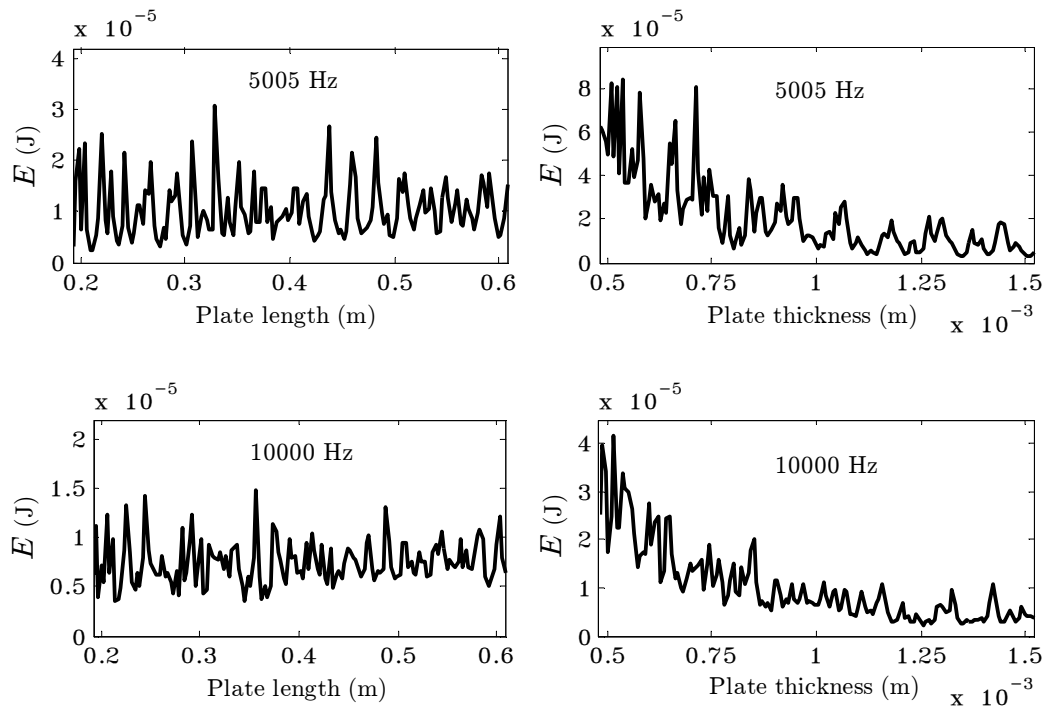


Figure 7.10: The energy of a plate as functions of the plate dimension with 150 subintervals at frequencies 5005 Hz and 10000 Hz, for a simply-supported plate subjected to a single harmonic load.

Figs. 7.11 and 7.12 show the mean and standard deviation of the energy, for a simply-supported plate subjected to a single load with CV values of 1%, 5%, 10%, 20%, and 30%, for the plate dimension and thickness variation as a function of frequency. The DI, SEA predictions, and Monte Carlo simulations are blue lines, smooth dashed lines, and red lines, respectively.

The results clearly show that DI method gives much better predictions for the mean and standard deviation of the energy than the SEA predictions for those in all CV cases and frequency ranges. Even for the plate thickness variation, SEA predictions of the mean and standard deviation are not accurate for at CV values higher than 20%. By contrast DI predictions of all values of CV give excellent agreement with Monte Carlo simulations.

The computation time for the results shown in Figs. 7.11 and 7.12 from SEA predictions just takes a few seconds whereas that for DI uses about 3.82 hours, and Monte Carlo simulations take 127.43 hours by using intel core i5 M520 at 2.4 GHz.

The next subsection will show the comparison of the mean and standard deviation of the energy for a built-up structure from SEA, DI, and Monte Carlo simulation.

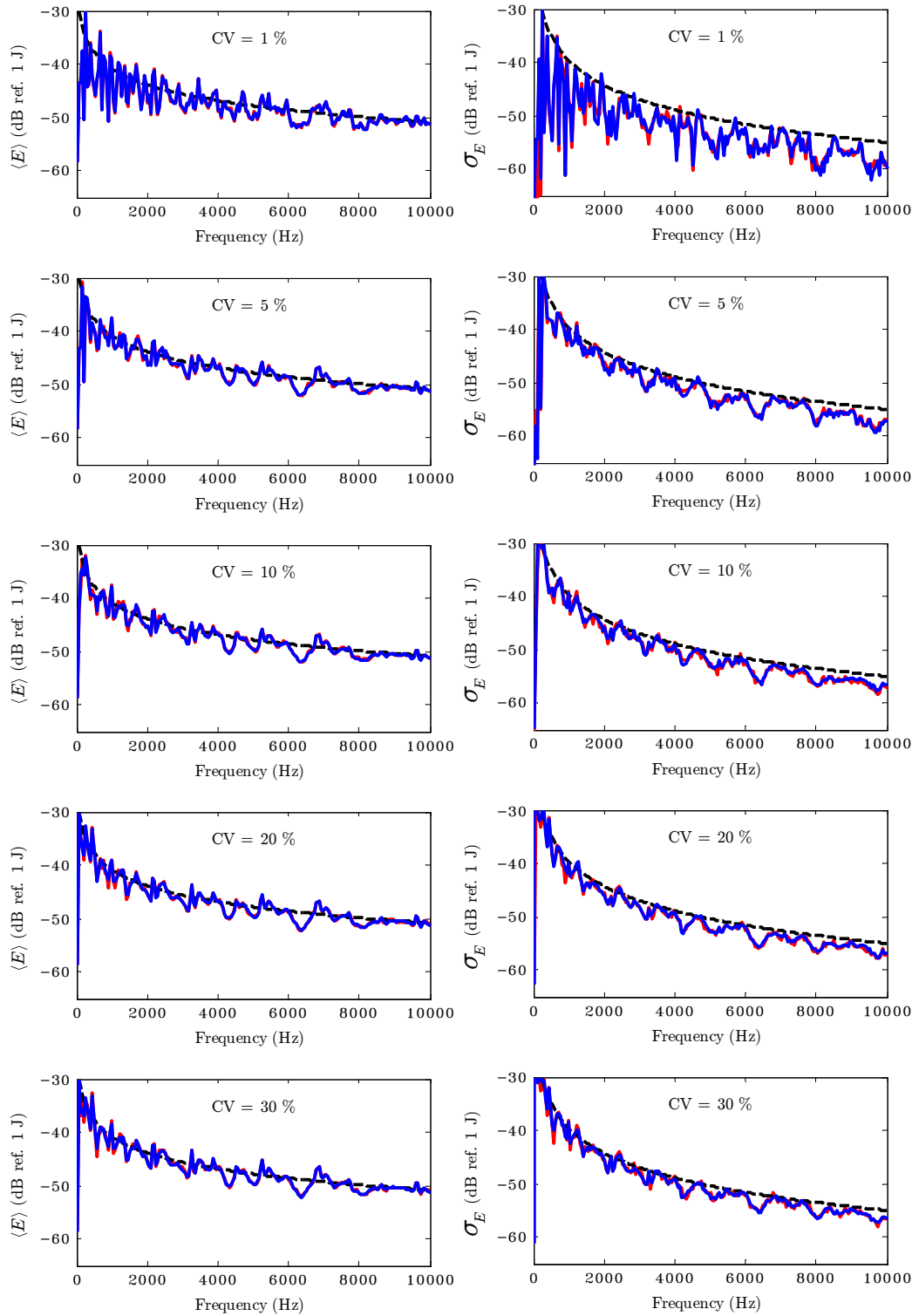


Figure 7.11: Comparison of the mean and standard deviation of the energy, for a simply-supported plate with the plate dimension variation; —, Monte Carlo simulation; —, DI; - -, SEA.

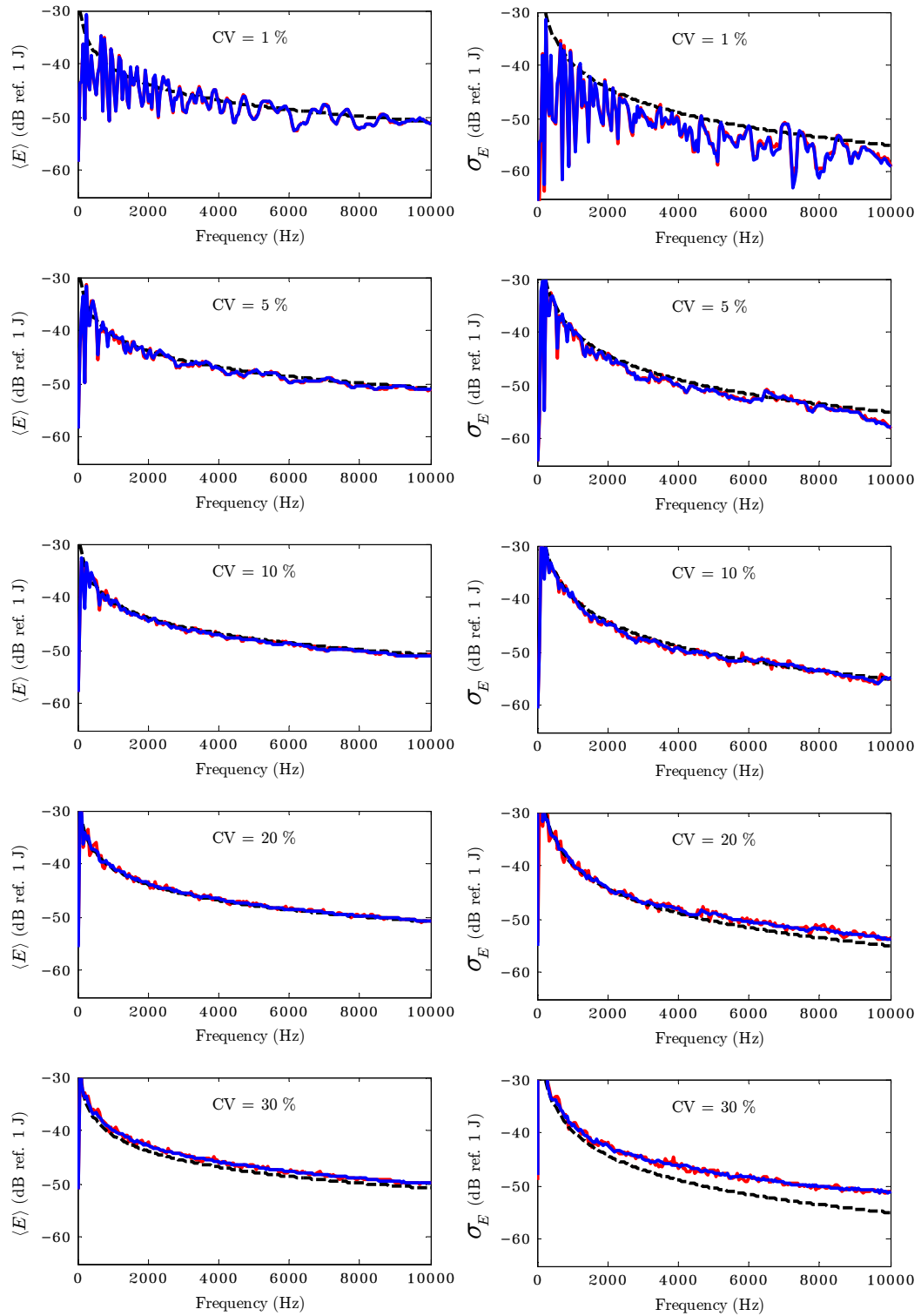


Figure 7.12: Comparison of the mean and standard deviation of the energy, for a simply-supported plate with the plate thickness variation; —, Monte Carlo simulation; —, DI; - -, SEA.

Application of DI to a Built-Up Structure

This section will show the capability of DI with 150 subintervals for predicting the mean and standard deviation of the energy with frequencies from 10 Hz up to 10000 Hz in 201 intervals, for an L-shaped plate in Fig. 5.1 with the plate dimension (length) and thickness variation compared with SEA and FE Monte Carlo results from Chapter 5.

To apply DI prediction for an L-shaped plate, first the energy as functions of the plate length or thickness for each plate ($g(X)$ in Eq. (6.5)) needs to be constructed. Then each $g(X)$ for each frequency is used in Eqs. (6.6) and (6.7) to calculate the mean and standard deviation of the energy for each plate. Fig. 7.13 shows the energy of Plates 1 and 2 as functions of the plate length with 150 subintervals at frequencies 5005 Hz and 10000 Hz, for an L-shaped plate subjected to a single point load on Plate 1. The nominal value and parameter a for CV value 30% are 0.3 m and 0.156 m, respectively.

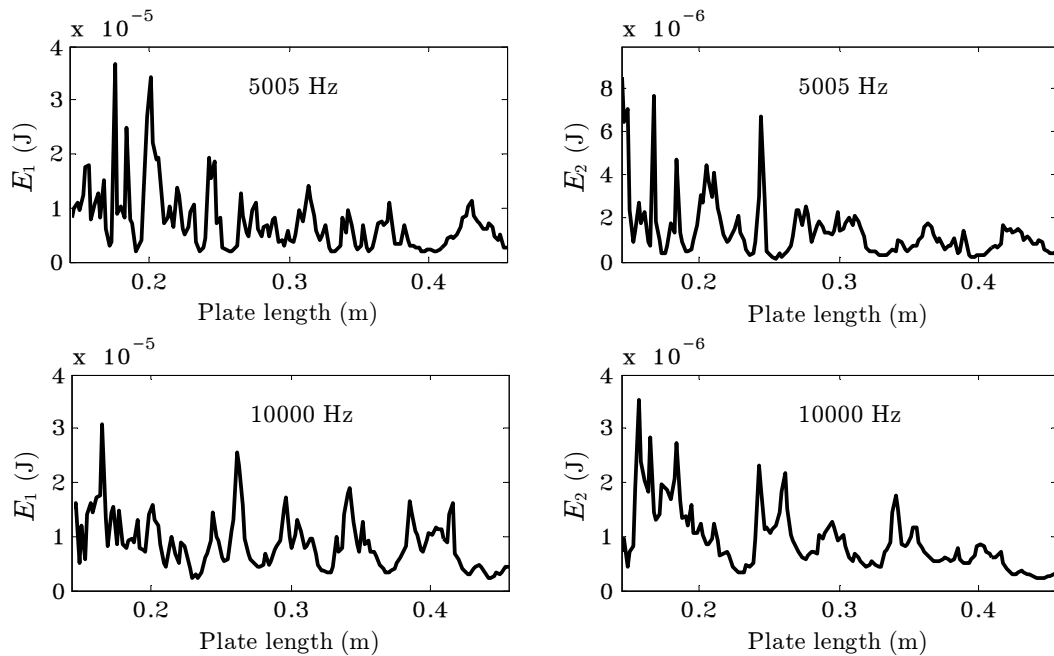


Figure 7.13: The energy of Plates 1 and 2 as functions of the plate dimension with 150 subintervals at frequencies 5005 Hz and 10000 Hz, for an L-shaped plate subjected to a single harmonic load on Plate 1.

Figs. 7.14 and 7.15 show the mean and standard deviation of the energy of Plates 1 and 2, for an L-shaped plate subjected to a single load on Plate 1 with CV value of 1%, 5%, 10%, 20%, and 30% for the plate dimension variation as a function of frequency. The DI, SEA predictions, and FE Monte Calo simulations are blue lines, smooth dashed lines, and red lines, respectively.

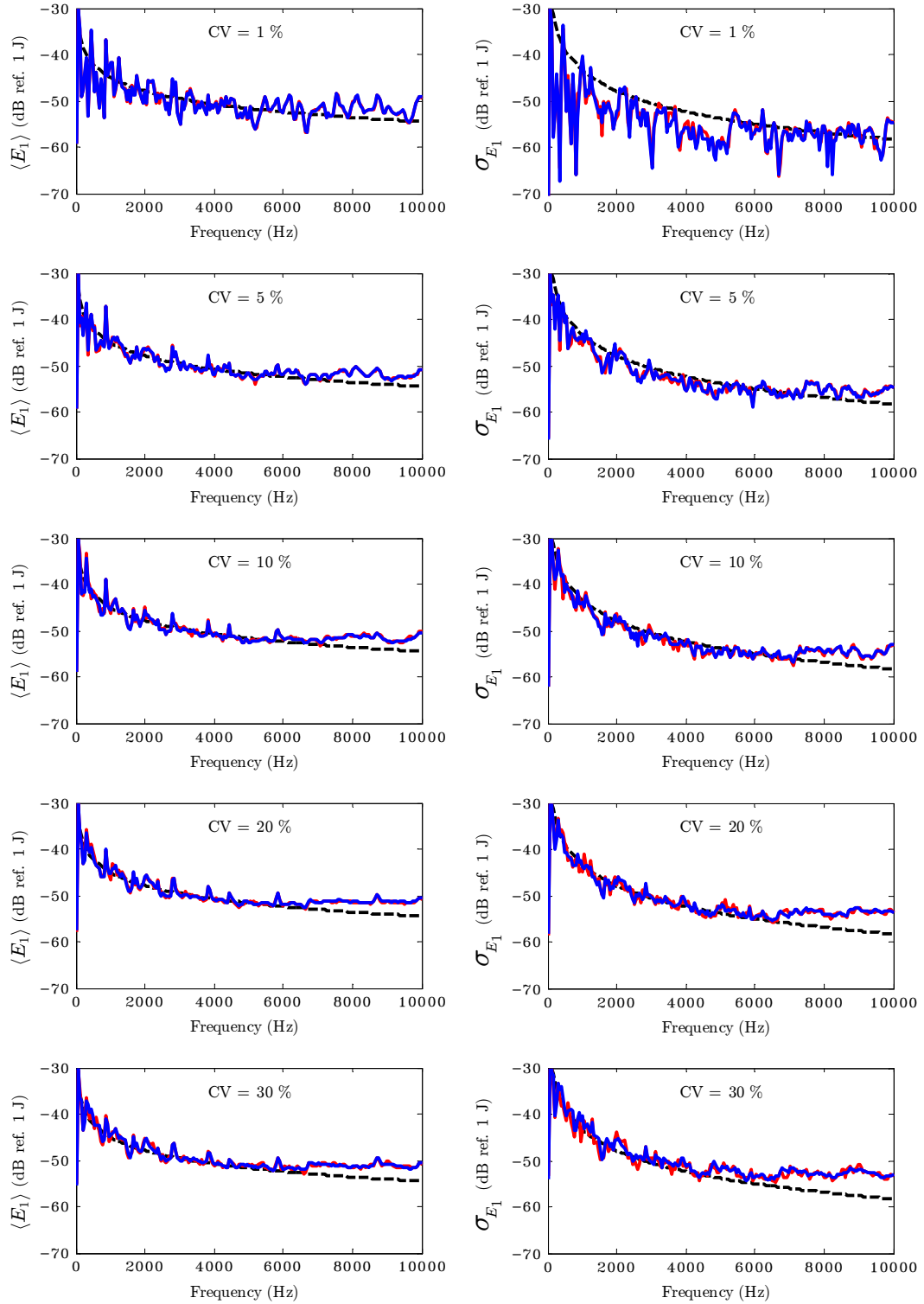


Figure 7.14: Comparison mean and standard deviation of the energy of Plate 1, for an L-shaped plate with the plate dimension variation; —, FE Monte Carlo simulation; —, DI; --, SEA.

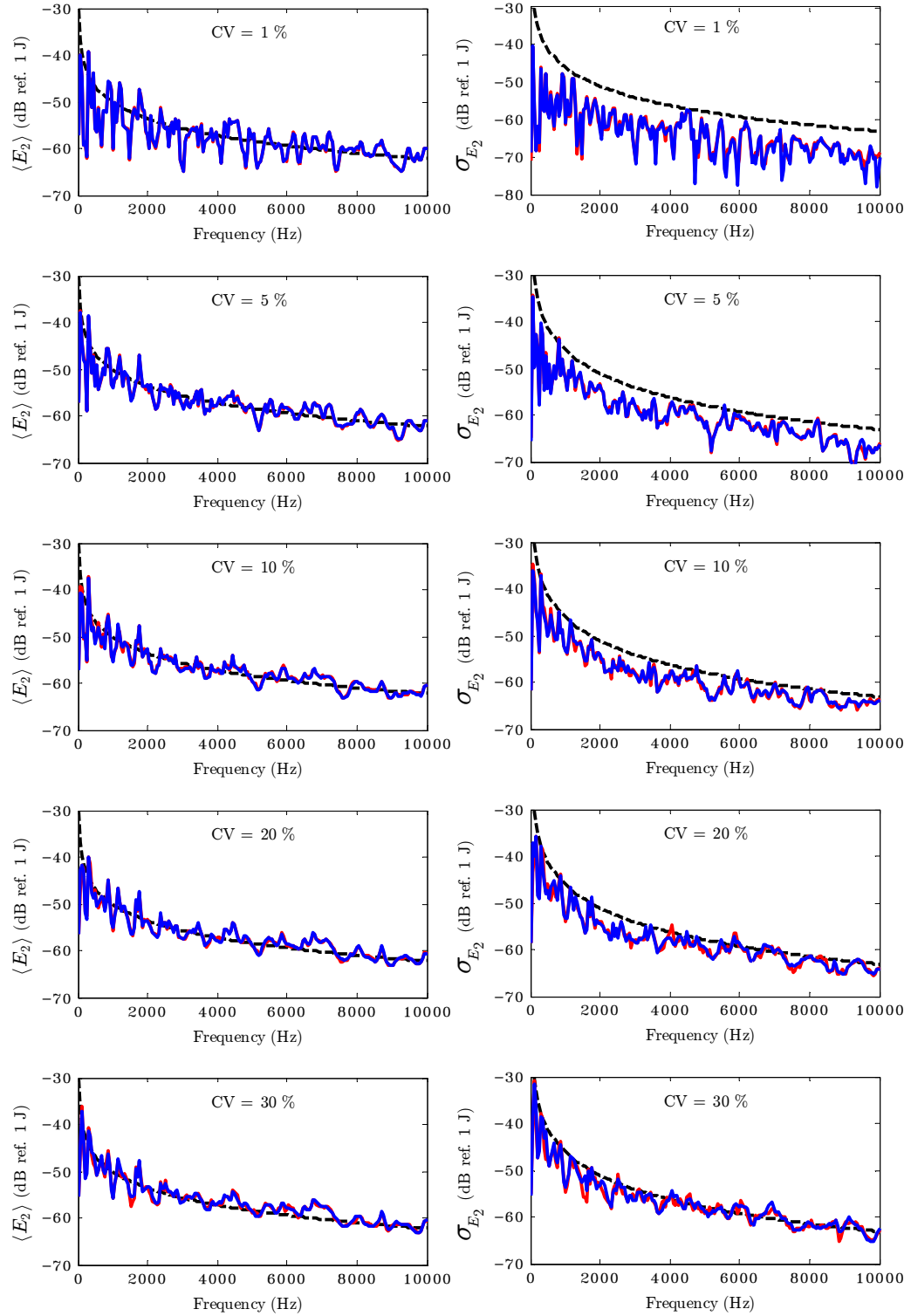


Figure 7.15: Comparison mean and standard deviation of the energy of Plate 2, for an L-shaped plate with the plate dimension variation; —, FE Monte Carlo simulation; —, DI; - -, SEA.

Fig. 7.16 shows the energy of Plates 1 and 2 as functions of the plate thickness with 150 subintervals at frequencies 5005 Hz and 10000 Hz, for an L-shaped plate subjected to a single point load on Plate 1. The nominal value and parameter a for CV value 20% are 1 mm and 0.346 mm, respectively.

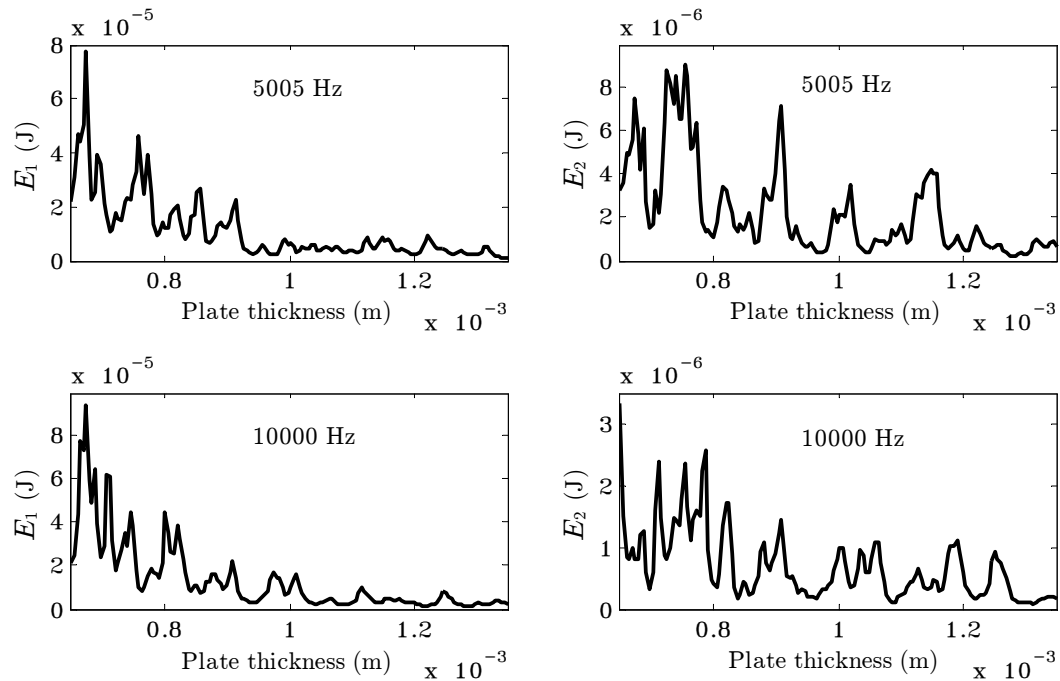


Figure 7.16: The energy of Plates 1 and 2 as functions of the plate thickness with 150 subintervals at frequencies 5005 Hz and 10000 Hz, for an L-shaped plate subjected to a single harmonic load on Plate 1.

Figs. 7.17 and 7.18 show the mean and standard deviation of the energy of Plates 1 and 2, for an L-shaped plate subjected to a single load on Plate 1 with CV value of 1%, 5%, 10%, 15%, and 20% for the plate thickness variation as a function of frequency. The DI, SEA predictions, and Monte Carlo simulations are blue lines, smooth dashed lines, and red lines, respectively.

From Figs 7.14, 7.15, 7.17, and 7.18, it can be clearly seen that DI method gives excellent prediction of the mean and standard deviation of the energy with FE Monte Carlo simulations, and much better than the SEA predictions for those in all CV cases and frequency ranges on both plates. Even for the plate thickness variation on Plate 1, SEA predictions of the mean and standard deviation are unable to handle at CV of values 15% and 20% of all frequency range, DI predictions for those CV values still gives excellent agreement with FE Monte Carlo simulations.

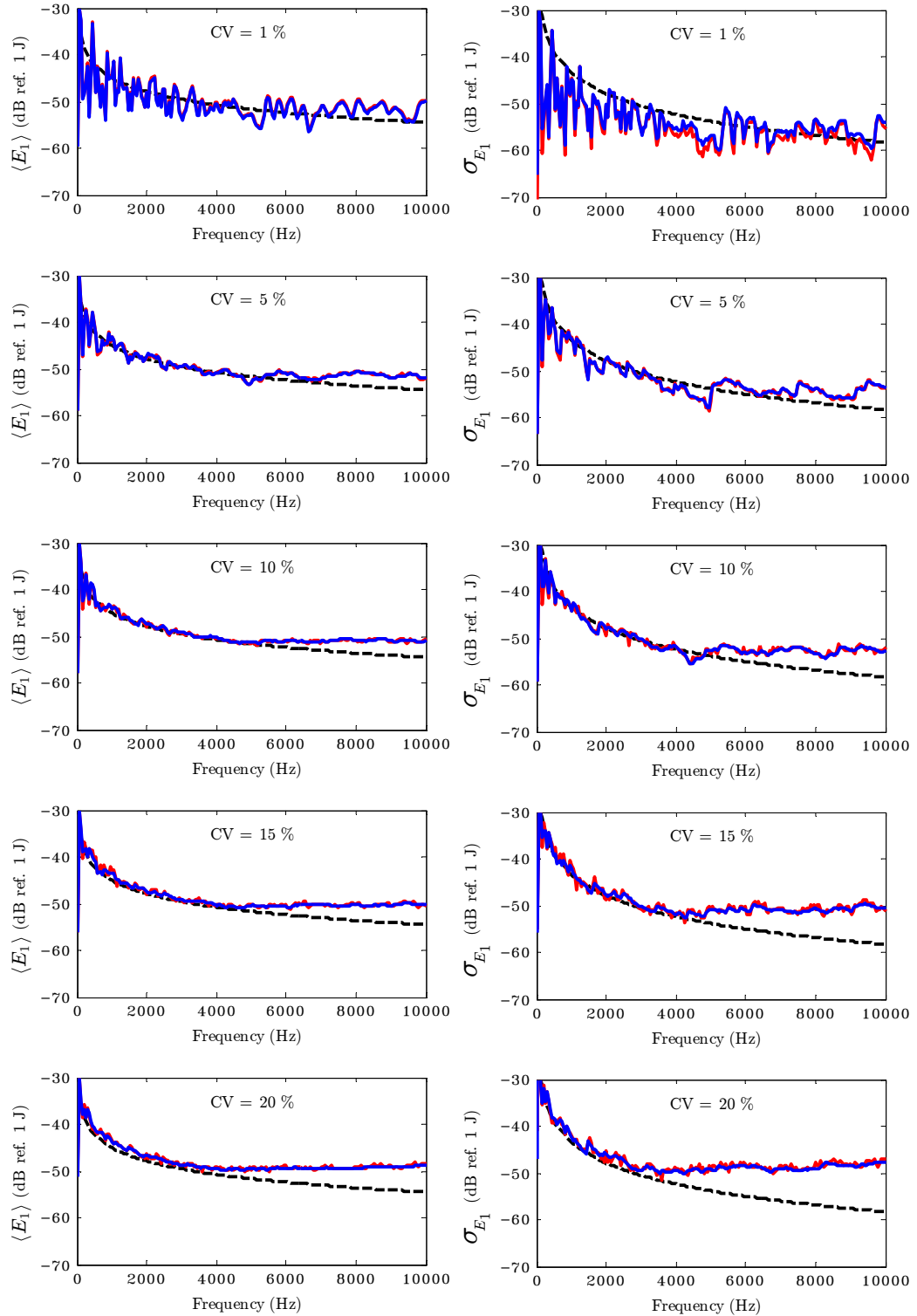


Figure 7.17: Comparison of the mean and standard deviation of the energy of Plate 1, for an L-shaped plate with the plate thickness variation; —, FE Monte Carlo simulation; —, DI; - -, SEA.

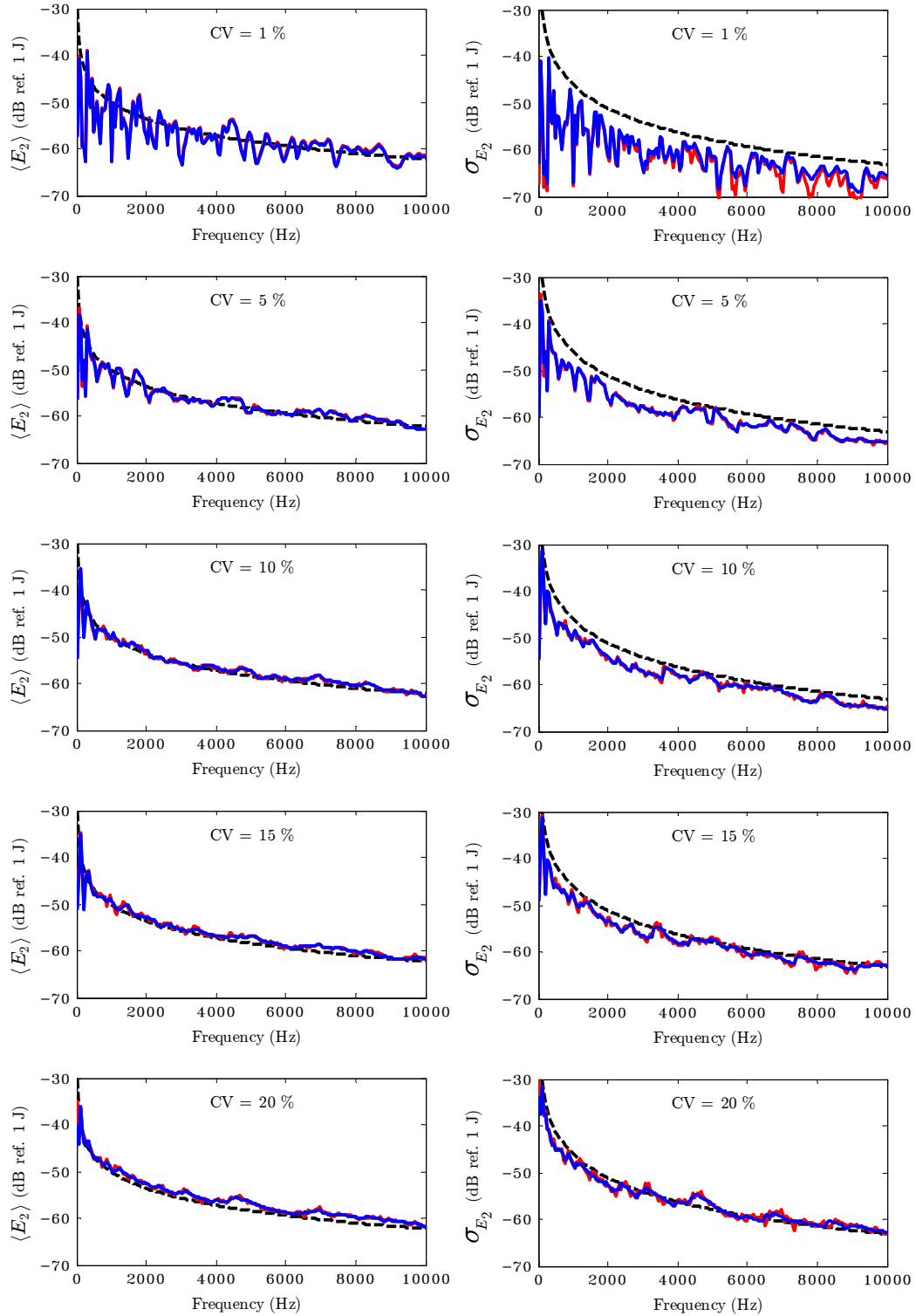


Figure 7.18: Comparison of the mean and standard deviation of the energy of Plate 2, for an L-shaped plate with the plate thickness variation; —, FE Monte Carlo simulation; —, DI; - -, SEA.

The computation time for the results shown in Figs 7.14, 7.15, 7.17, and 7.18 from SEA predictions takes around a few minutes, whereas DI in total uses about 1005 hours but Monte Carlo simulations take 3350 hours by using intel core i5 M520 at 2.4 GHz.

The next section will show the application of bounding prediction using the SEA-EV and DI-EV methods.

7.2 Application of DI-EV and SEA-EV Bounding Methods.

This section is the most important part in the thesis. The new bounding methods, DI-EV and SEA-EV, will be tested for the simple and built-up structures with plate dimension and thickness variation subjected to a harmonic point load, as described in Chapters 4 and 5. To use the DI-EV and SEA-EV bounding methods to predict the response bound, first, the mean and standard deviation obtained from both DI (with 150 subintervals) and SEA methods, are needed in constructing the probability density function $f(x)$ for each frequency by using Assumption-2 that $f(x)$ is log-normally distributed, and then the distribution function $F(x)$ is computed. Second, $F_n(x)$ is constructed by using Eq. (6.2). Finally, after $F_n(x)$ known, the bound for n finite samples can then be computed for a particular exceedance probability level.

7.2.1 Simple Structure: a Single Plate

In this section, a simply-supported plate (of Chapter 4) is used to apply the DI-EV and SEA-EV bounding methods. The energy response bounds for a simply-supported plate with uniform distributed dimension variation are shown in Fig. 7.19 and those with uniform distributed thickness variation are also shown in Fig. 7.20, which are obtained from Monte Carlo simulations based on the Mode Superposition plate-structure solutions (1000 generated samples). Each sample and ensemble mean from Monte Carlo simulations are shown in grey and blue lines, respectively.

Fig. 7.19, which shows the energy response bounds with a 50% probability level, for a simply-supported plate with the plate dimension variation, confirms that the predicting bounds from SEA-EV method are highly conservative (overpredicting) compared to those predictions obtained from DI-EV.

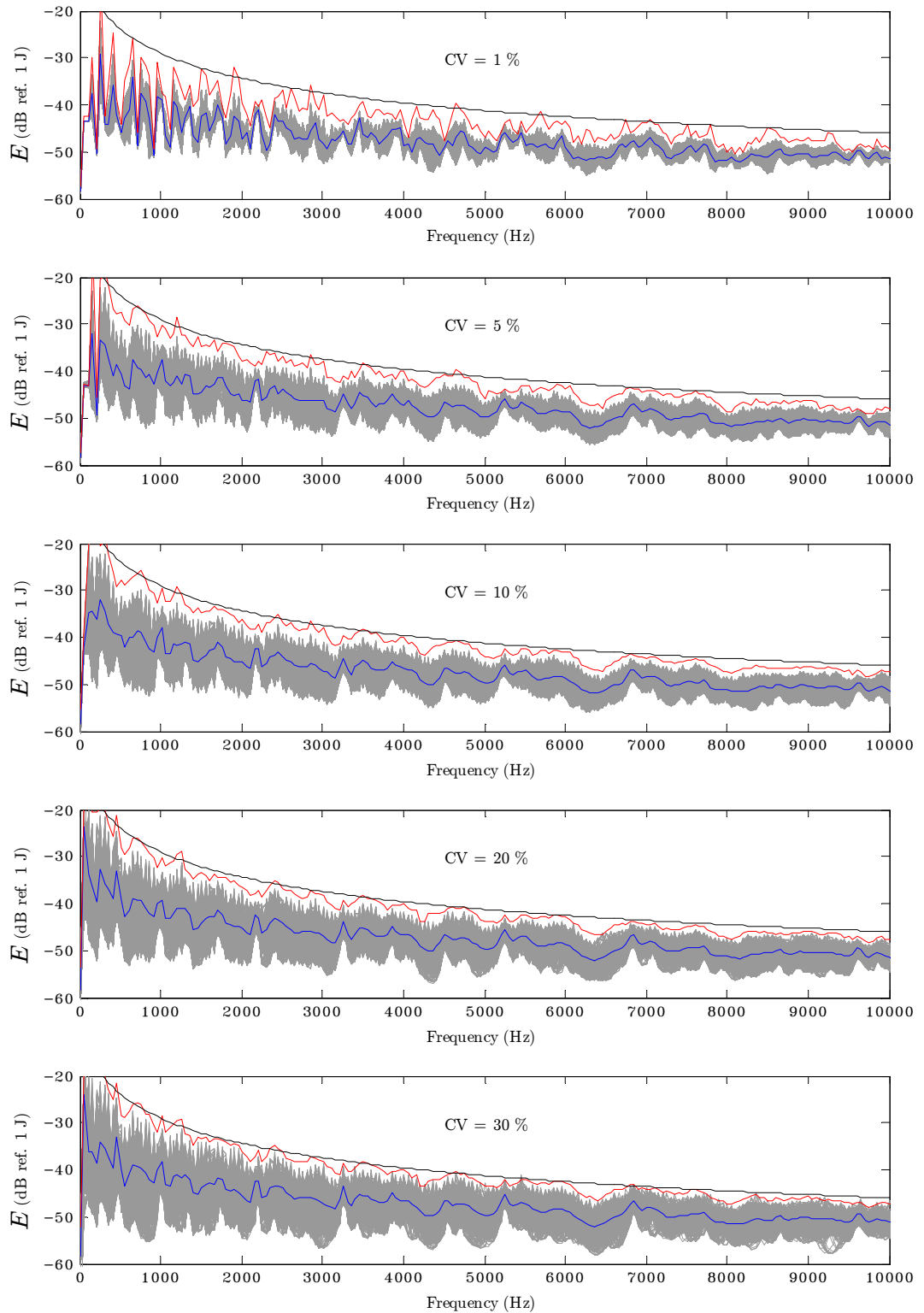


Figure 7.19: The energy response bounds with a 50% probability level for a simply-supported plate with the plate dimension variation; —, DI-EV bound; —, SEA-EV bound; —, ensemble mean (1000 samples).

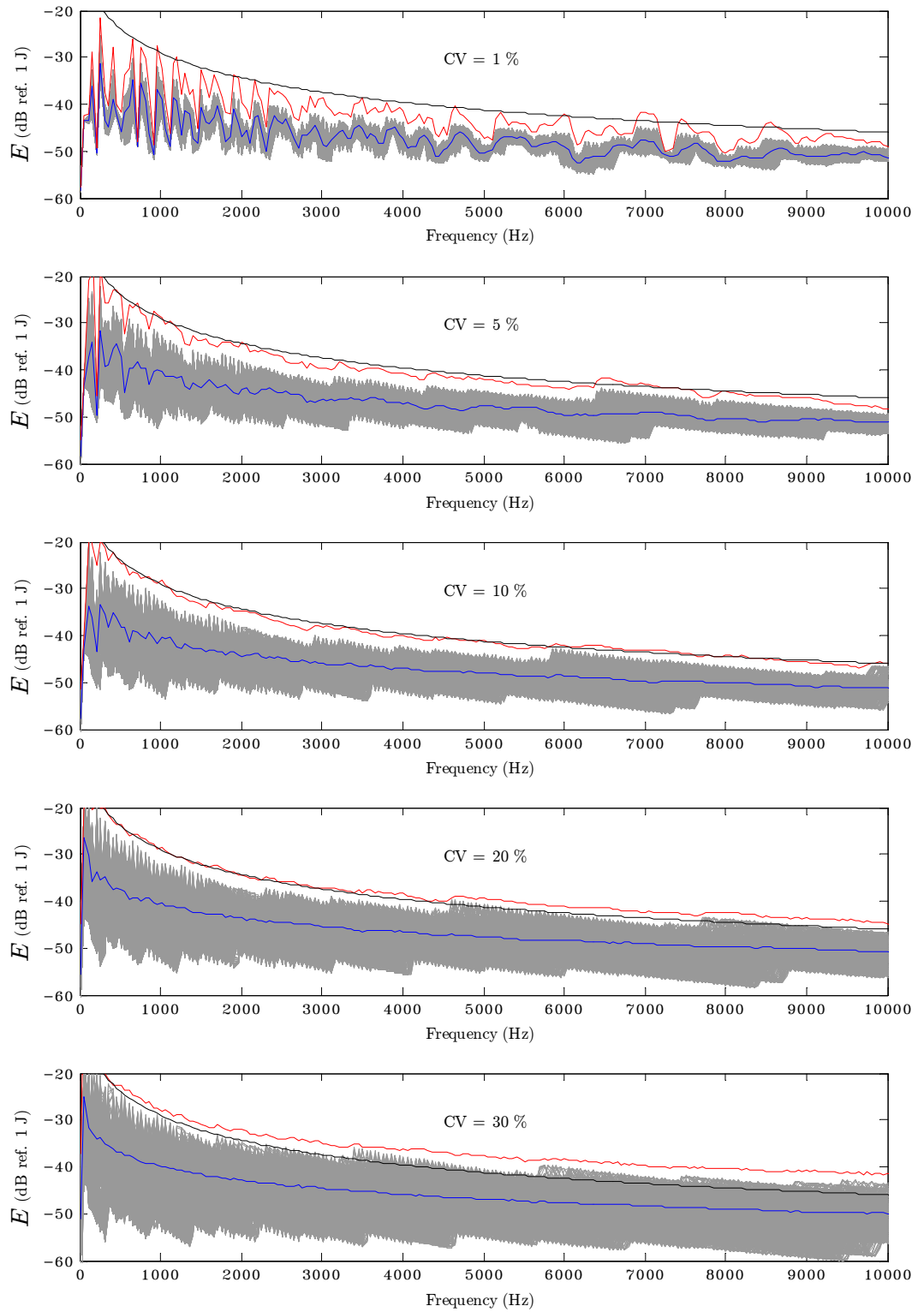


Figure 7.20: The energy response bounds with a 50% probability level for a simply-supported plate with the plate thickness variation; —, DI-EV bound; —, SEA-EV bound; —, ensemble mean (1000 samples).

Both methods give better bounding when the level of CV increases (i.e. the ratio of the distance between the bound to the peak of ensemble and the ensemble mean to the peak of ensemble). There are only a very few frequency points at CV value of 30%, for which the DI-EV bounding method gives underpredictions.

Fig. 7.20, which shows the energy response bounds with a 50% probability level for a simply-supported plate with the plate dimension variation, confirms that the predicted bounds from SEA-EV method are highly conservative (overpredicting) at level of CV value 1%. When the level of CV increases, the ratio of the distance between the bound to the peak of ensemble, and the ensemble mean to the peak of ensemble, decreases for both methods. At the level of CV 20%, SEA-EV bounding becomes an underprediction at some frequency range. SEA-EV bounding is underpredicted at frequency between from 3500–10000 Hz. In contrast, all ensembles, with all levels of CV values, stay within the DI-EV bounds. The DI-EV bounds of plate thickness variation are smoother than those of the plate dimension variation, compared with the same level of CV.

The reason why DI-EV bounding gives a better prediction when the level of CV increases may come from the distribution of the responses. From Figs. 4.16 and 4.17, the pdf of the responses is more similar to lognormal when CV value is higher. It means that at a low level of CV, the pdf is not similar to lognormal, hence the assumption that responses have a lognormal pdf can lead to an error in Eq. (6.2). In contrast, at high level of CV, the responses have a pdf very similar to a lognormal, therefore Eq. (6.2) give a good response bound.

To test that the DI-EV and SEA-EV bounding methods still work if the number of n corresponding to the number of finite samples change, the DI-EV and SEA-EV bounding are tested again with 100 samples. The energy response bounds for a simply-supported plate with uniformly distributed dimension variation are shown in Fig. 7.21 and those with uniformly distributed thickness variation are shown in Fig. 7.22, obtained from Monte Carlo simulations based on the Mode Superposition plate-structure solutions (100 generated samples). The DI-EV and SEA-EV bounds with 50% probability level and 100 finite samples, are shown in red and black lines, respectively. Each sample and ensemble mean from Monte Calo simulations, are shown in grey and blue lines, respectively.

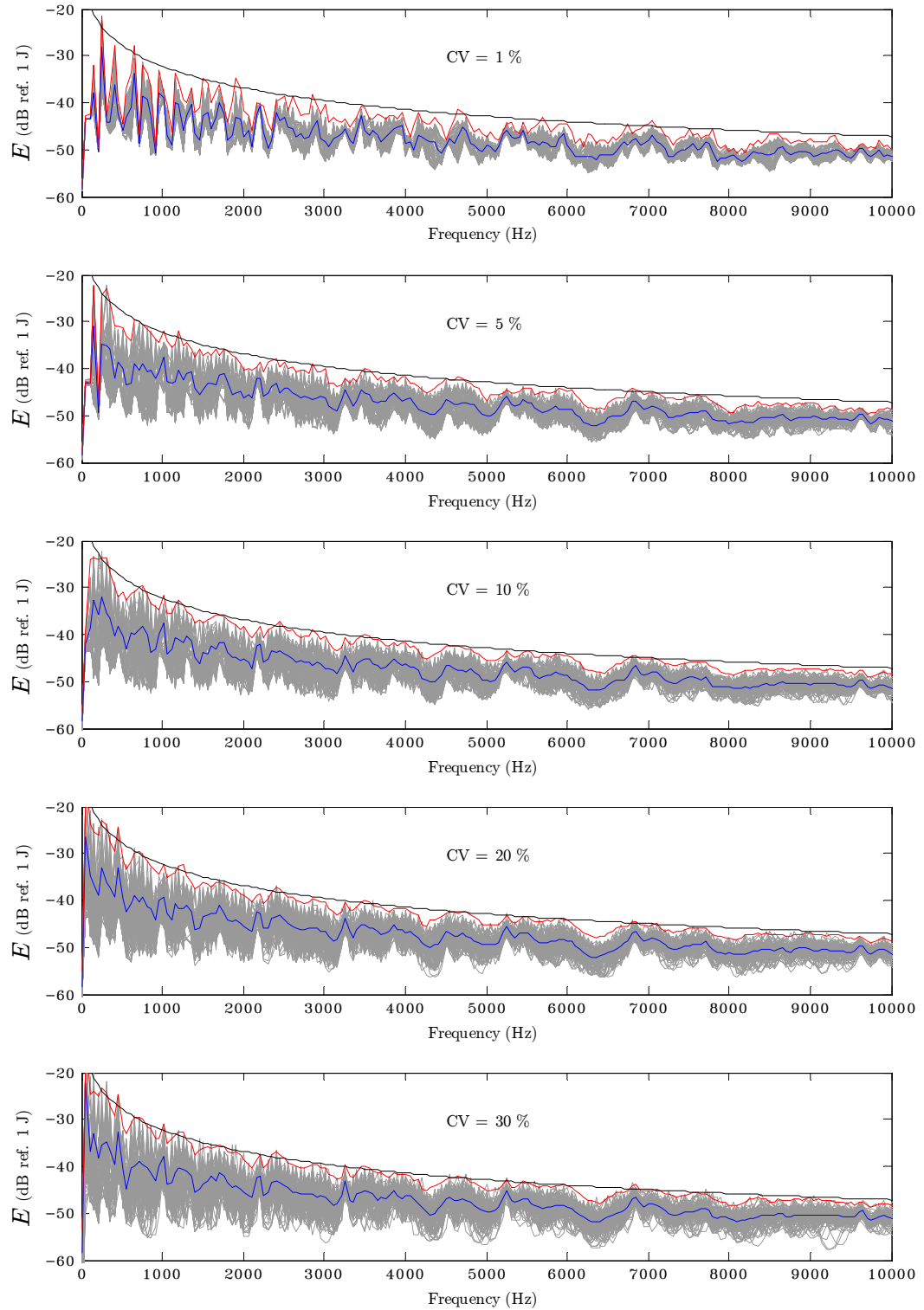


Figure 7.21: The energy response bounds with a 50% probability level for a simply-supported plate with the plate dimension variation; —, DI-EV bound; —, SEA-EV bound; —, ensemble mean (100 samples).

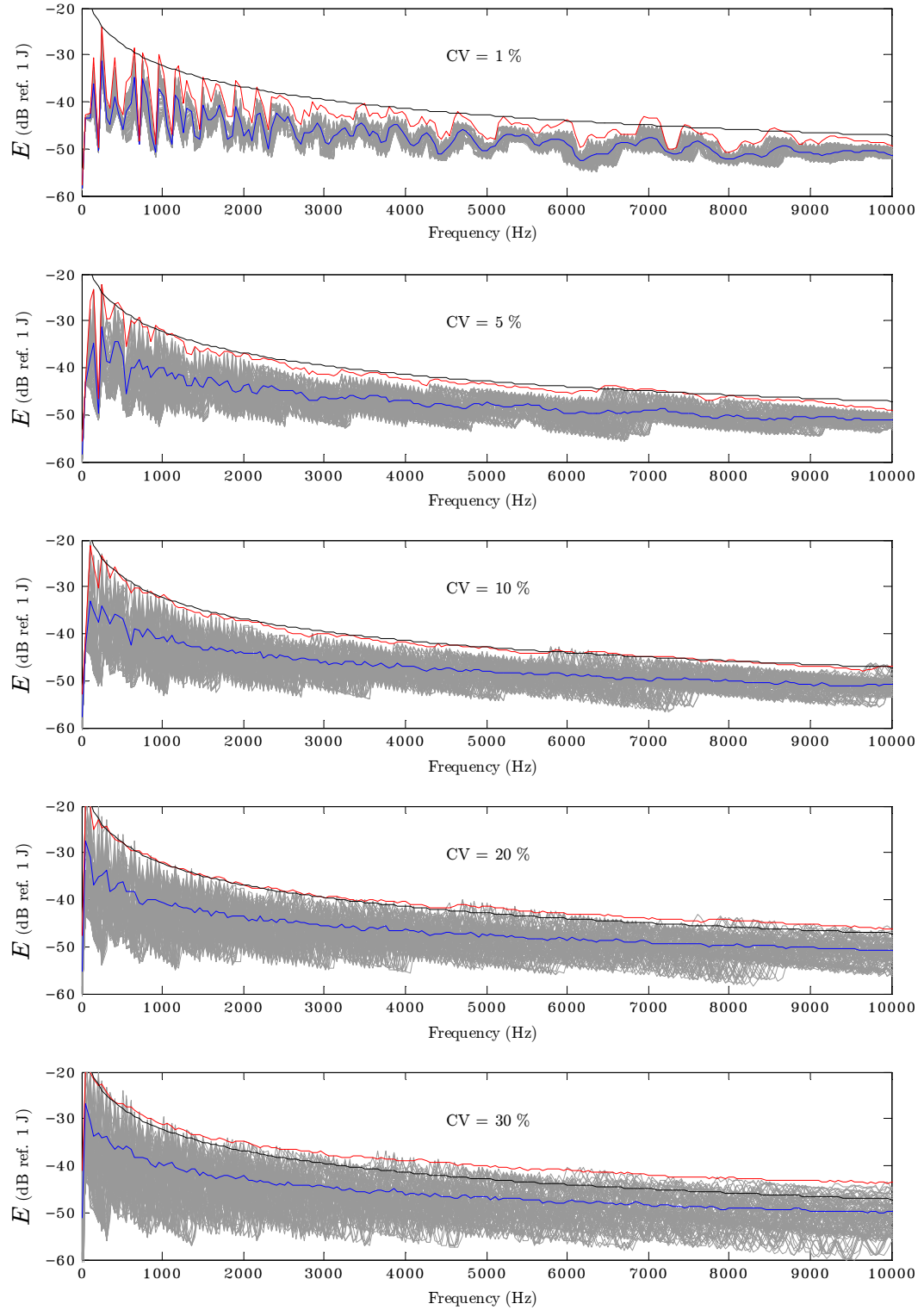


Figure 7.22: The energy response bounds with a 50% probability level for a simply-supported plate with the plate thickness variation; —, DI-EV bound; —, SEA-EV bound; —, ensemble mean (100 samples).

Fig. 7.21, which shows the energy response bounds with a 50% probability level for a simply-supported plate with the plate dimension variation for 100 samples, confirms that the SEA-EV bounding method still gives conservative predictions for all CV values, and both methods give the bounds closer to the peak of ensembles than those with 1000 samples in Fig. 7.19. It is also evident that the bounds move closer to the ensemble mean than those with 1000 samples. For 100 samples, there are more frequency points at CV value of 30% therefore the DI-EV bounding method gives underpredictions compared with 1000 samples in Fig. 7.19.

Fig 7.22, which shows the energy response bounds with a 50% probability level for a simply-supported plate with the plate thickness variation for 100 samples, demonstrates that both methods give the bounds closer to the peak of ensembles than those with 1000 samples (in Fig. 7.19). It is also evident that the bounds move closer to the ensemble mean than those with 1000 samples. With CV values of 1% and 5%, all ensembles with all levels of CV values, still stay within the DI-EV bounds. At CV value of 10%, DI-EV bounding method gives underpredictions at frequency ranges from 5800–6050 Hz and 9700–10000 Hz. At CV value of 20%, DI-EV bounding method gives underpredictions at frequency ranges from 4500–7000 Hz and 7500–10000 Hz. At CV value of 30%, DI-EV bounding method gives underpredictions for all of the frequency range.

7.2.2 Built-Up Structure: an L-Shaped Plate

In this section, the L-shaped plate structure Fig. 5.1 subjected to a harmonic point load with uniformly distributed dimension and thickness variation is used to apply the DI-EV and SEA-EV bounding methods to bound the energy response of Plates 1 and 2.

Figs. 7.23 and 7.24 show the energy response bounds for an L-shaped plate with uniform distributed dimension variation of Plates 1 and 2, which are obtained from FE Monte Carlo simulations (ANSYS) (100 generated samples). Figs. 7.25 and 7.26 show the energy response bounds for an L-shaped plate with uniform distributed thickness variation of Plates 1 and 2, which are obtained from FE Monte Carlo simulations (ANSYS) (100 generated samples).

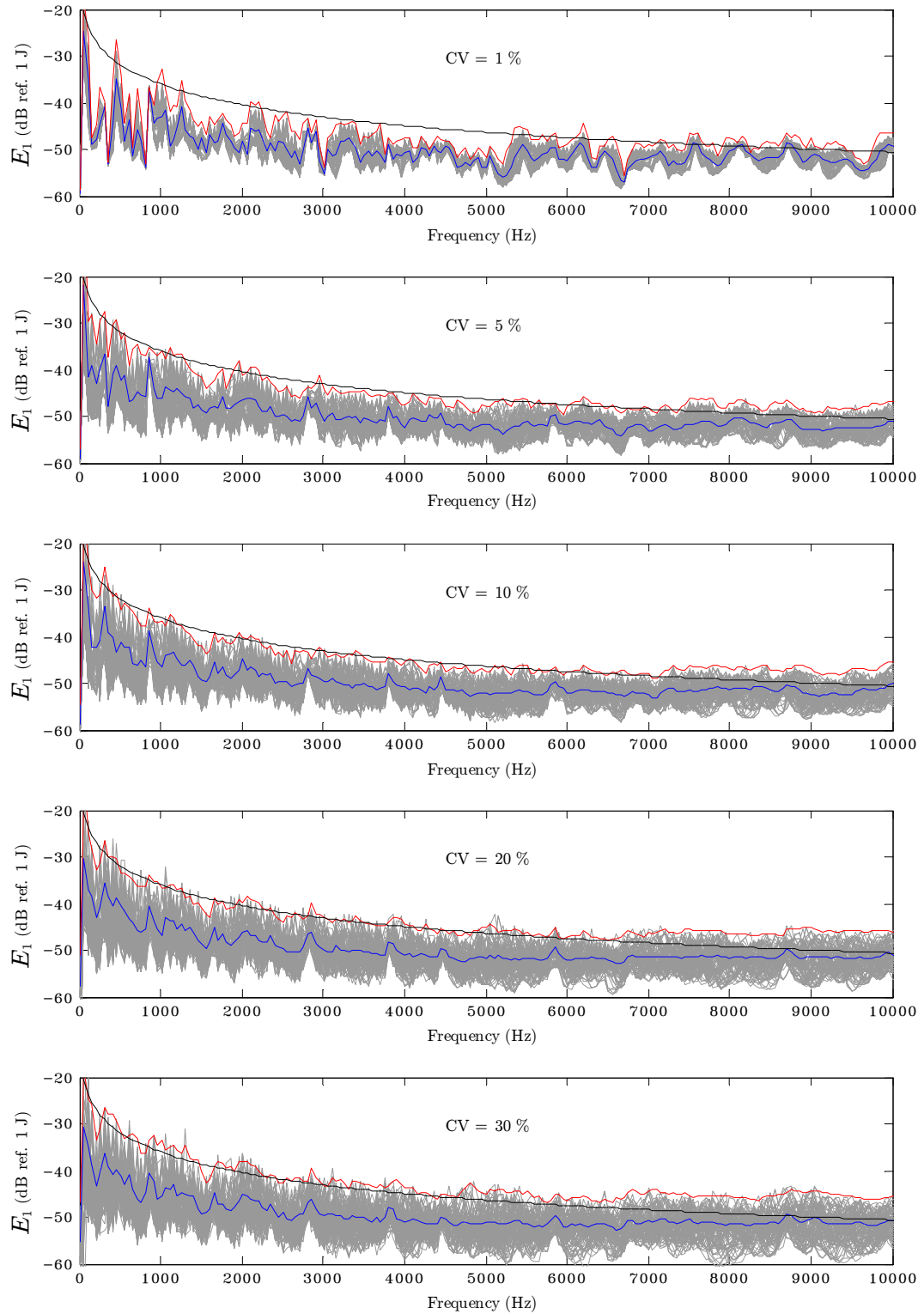


Figure 7.23: The energy response bounds of Plate 1 with a 50% probability level for an L-shaped plate with the plate dimension variation; —, DI-EV bound; —, SEA-EV bound; —, ensemble mean (100 samples).

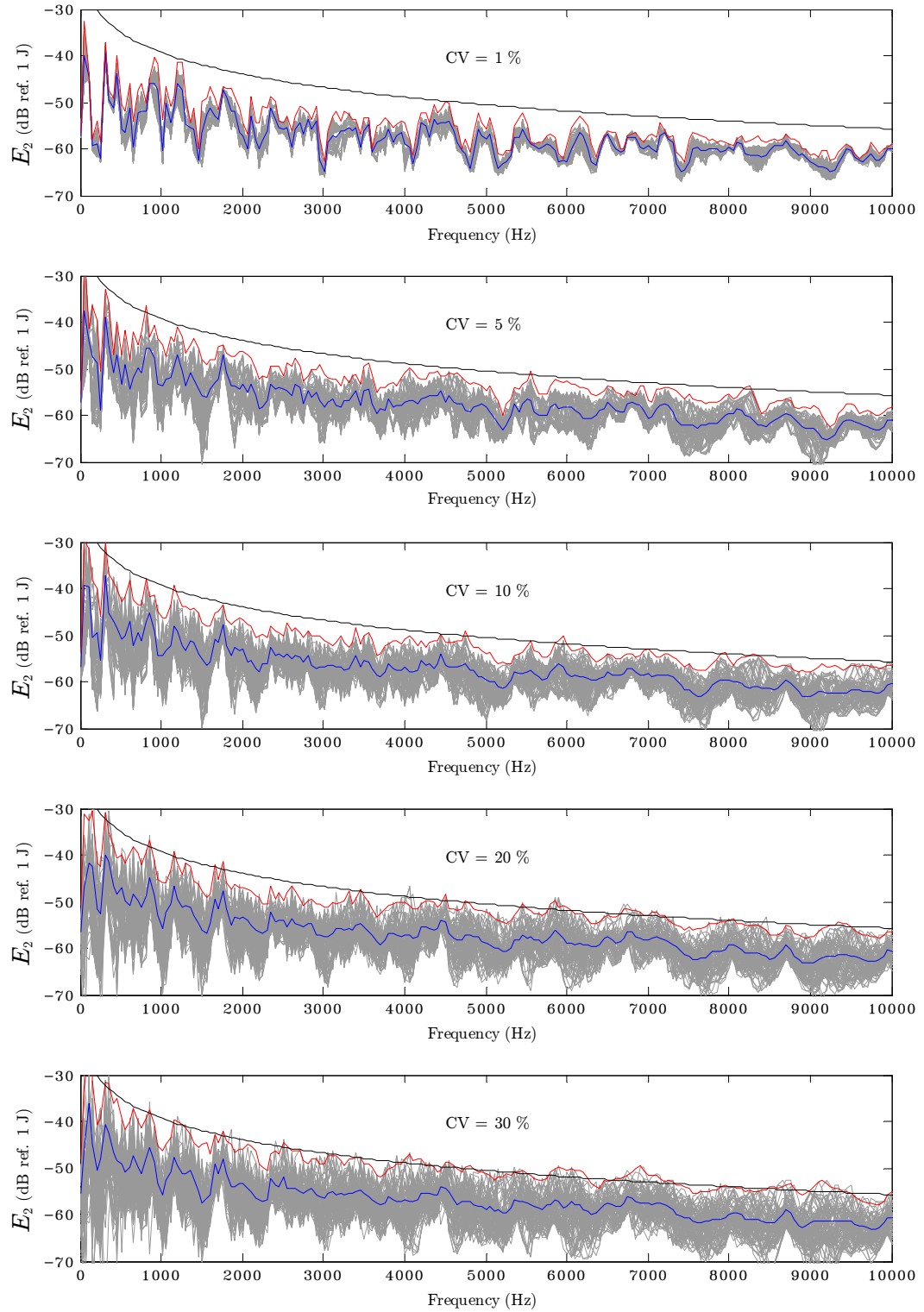


Figure 7.24: The energy response bounds of Plate 2 with a 50% probability level for an L-shaped plate with the plate dimension variation; —, DI-EV bound; —, SEA-EV bound; —, ensemble mean (100 samples).

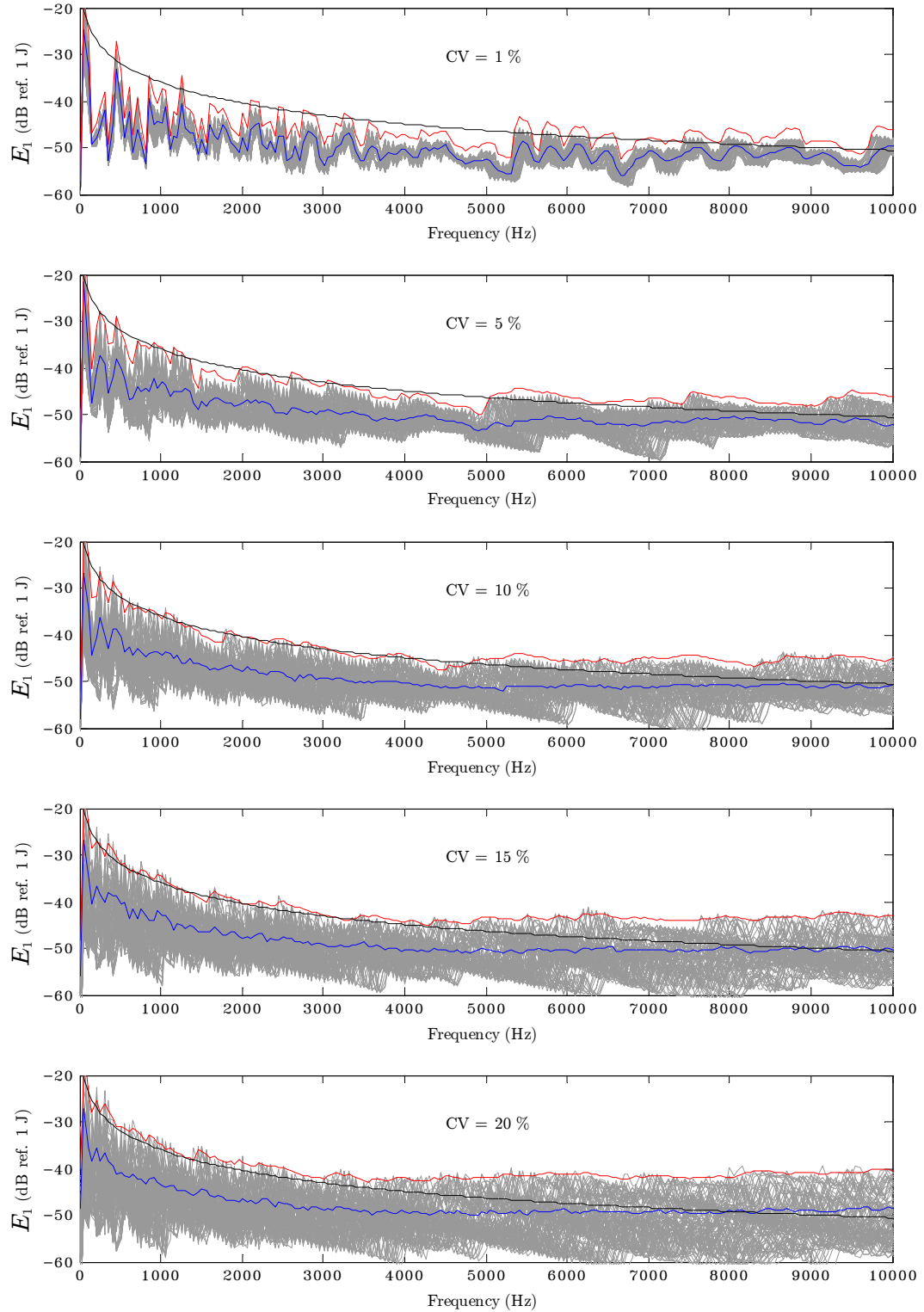


Figure 7.25: The energy response bounds of Plate 1 with a 50% probability level for an L-shaped plate with the plate thickness variation; —, DI-EV bound; —, SEA-EV bound; —, ensemble mean (100 samples).

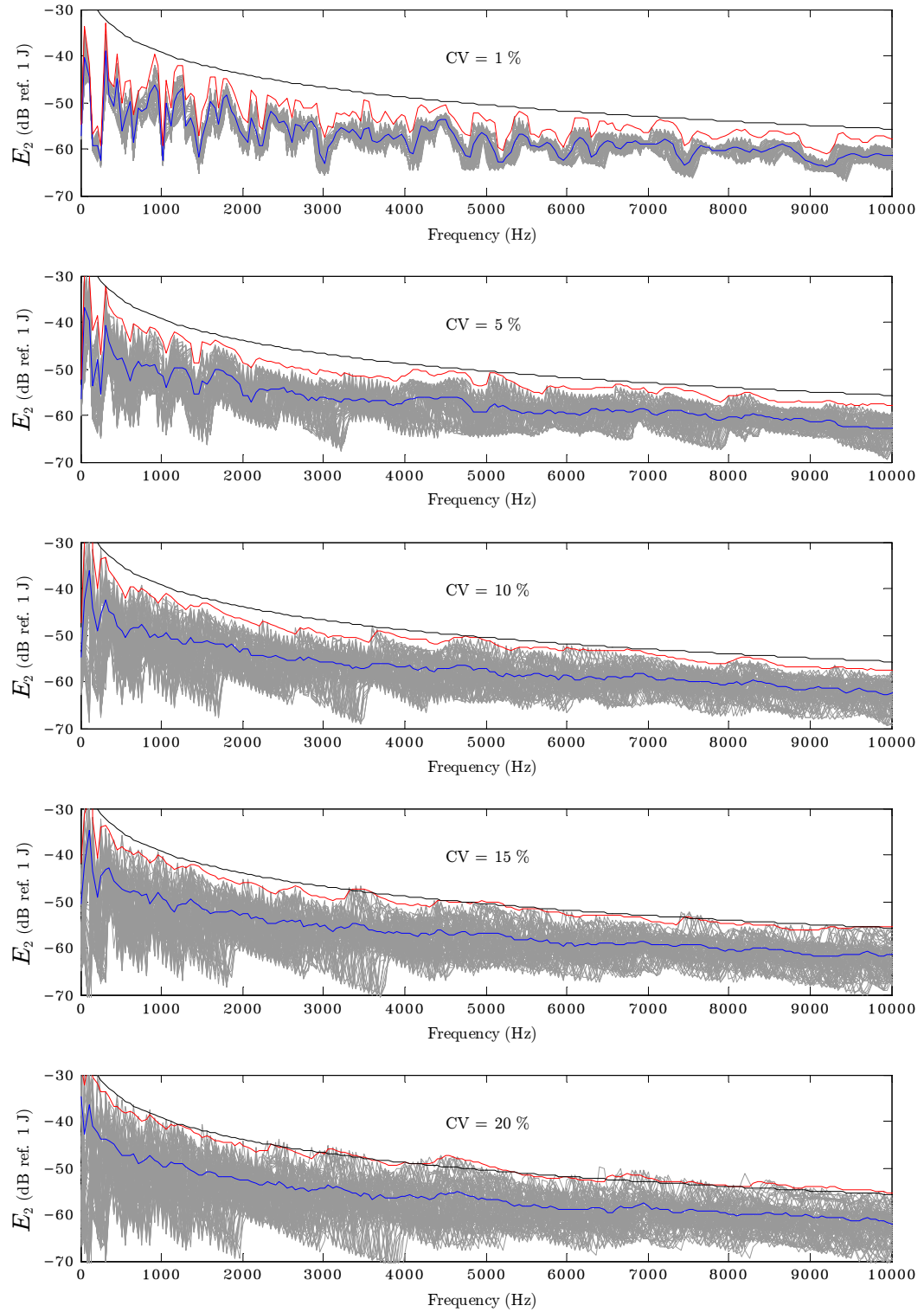


Figure 7.26: The energy response bounds of Plate 2 with a 50% probability level for an L-shaped plate with the plate thickness variation; —, DI-EV bound; —, SEA-EV bound; —, ensemble mean (100 samples).

The DI-EV and SEA-EV bounds with 50% probability level and 100 finite samples, are shown in red and black lines, respectively. Each sample and ensemble mean from Monte Carlo simulations are shown in grey and blue lines, respectively.

For the plate dimension variation, from Figs. 7.23 and 7.24, which show the energy response bounds for an L-shaped plate, it can clearly be seen that the SEA-EV bounding method gives an appropriate prediction for Plate 2 but for Plate 1, it can only predict the bound at low CV, whereas the DI-EV bounding method gives excellent prediction for both plates at all levels of CV values. Besides, the SEA-EV bounding method is conservative at low levels of CV when level of CV increases, the SEA-EV bound becomes an underestimate, especially on Plate 1.

Tuning attention to the plate thickness variation, from Figs. 7.25 and 7.26, which show the energy response bounds for an L-shaped plate, it is confirmed that the SEA-EV bounding method gives an appropriate prediction only for Plate 2. For Plate 1, SEA-EV gives an underprediction for almost all cases, whereas the DI-EV bounding method still gives an excellent prediction for both plates at all level of CV values. when the level of CV increases, the SEA-EV bound becomes more underestimated on Plate 1.

When the bounds of the built-up structure are compared with the simple structure at the same n finite samples in Figs. 7.21 and 7.22, it is found that the ratio of the distance between the bound to the peak of ensemble and the ensemble mean to the peak of ensemble is much smaller.

7.3 Conclusions of Chapter 7

The results show that the DI method has the high ability to predict the mean and standard deviation of the energy response for both simple and built-up structures when the plate dimension and thickness varies. However, this method takes considerably more computation time than SEA, but is still quicker than Monte Carlo simulations when working with many different CVs (for example, five CVs in our experiment). In case only one CV is considered, the DI method could be slower or quicker than Monte Carlo simulations, depending on whether the CV is high or low, respectively. For example, in our experiment, at 30% CV, 150 DI calculations are needed, whereas at 1%

CV, approximately 20 DI calculations are needed. Monte Carlo simulations require 100 samples for each CV.

The hypothesis from Chapter 6 has been tested and shown to be true. The results from DI-EV bounds show that DI-EV bounding method gives very good bounds not only for all levels of dimension and thickness variation but also at all frequencies. In contrast, SEA-EV bounding approach gives good bounds only at particular frequencies and for some levels of variation.

Both DI-EV and SEA-EV bounding methods confirm that these methods can be used to compute the response bound not limited to a level of variation without using expensive Monte Carlo simulation.

Chapter 8

Conclusions

The thesis has developed the DI-EV-based bounding approaches to predict the response bounds of structures that are subject to variability in the geometric parameters across a nominally identical ensemble. It has addressed two main problems. The first is that Monte Carlo modelling of an ensemble of complex built-up structures using methods such as FEA can become increasingly difficult and computationally expensive, owing to both small wavelengths of deformation and the number of input variables involved. The second problem is that the statistics of the structural parameters themselves are often not known, so even when methods are available to predict the variance of the response, such as probabilistic methods, they often cannot be used with a high level of confidence.

It has been shown that the DI-EV bounding approach, our new approach proposed, applied to simple and built-up structures with dimension and thickness variation compares extremely well with Monte Carlo simulations not only at all frequencies but also with both low-level and high-level uncertainties. In contrast, the SEA-EV bounding approach, an existing approach already used in the literature, applied to a simple structure gives conservative prediction when compared with Monte Carlo simulations across the entire frequency range with both low-level and high-level uncertainties for dimension variation. For the thickness variation, it gives underprediction at high-levels of uncertainty and high frequency. For a built-up structure, SEA-EV bounding gives reasonable results for Plate 2, but for Plate 1, it gives underprediction at high frequency for both low-level and high-level uncertainties. The DI-EV method by contrast takes much longer computation time than SEA but is still quicker than Monte Carlo simulations when working with many different CVs (for example, five CVs in Chapter 7).

In summary, it can be stated in overall conclusion that all the objectives of the study have been met. The approach that has been developed, have the ability to predict the response bounds for realistic structures with varying levels of uncertainty without the need to undertake expensive Monte Carlo simulation. However, when the number of

uncertain parameters increases, the number of DI calculations required increases exponentially. (For example, if one parameter requires n calculations, m parameters require n^m calculations.) It may not be practical to extend the proposed approach to the case of multiple certainties, but there could be a workaround. Further investigation is needed.

Further Work

The work in this thesis lends itself to several avenues of further research. Some of the further work is suggested as follows:

- Further parameter variation. For instance, add two or three parameter variation, which are realistically random in the system, e.g. variation in manufacturing processes and material variability.
- Explore larger numbers of parameter variation with different distributions because in the real problem, the parameter variation can be mixed, with many distributions, not only uniform. For example, it would be of interest to combine normal with uniformly distributed data.

The approaches developed in this research may be used to address industrial problems involving real complex structures. Currently, Monte Carlo simulations are still the default method for studying them as they have no limitations regarding the number of parameters and so on. The state of the art in the propagation of parametric uncertainties includes COSSAN, a general purpose software package for uncertainty quantification and management, sensitivity optimization and reliability analysis.

References

Anderson H. (1986): “Metropolis, Monte Carlo and the Maniac”. Los Alamos Science, No. 14, pp. 96–108.

Anderson J. and Naeim F. (2012): “Basic Structural Dynamics”, John Wiley & Sons.

Arenas J. (2003): “On the vibration analysis of rectangular clamped plates using the virtual work principle”. Journal of Sound and Vibration, 2003, Vol. 266, pp. 912-918.

Arnoux A., Batou A., Soize C., and Gagliardini L. (2012): “Stochastic Reduced-Order Model for Dynamical Structures Having A Modal Density in The Low Frequency Range”. International Symposium on the Computational Modelling and Analysis of Vehicle Body Noise and Vibration, Brighton, 2012.

Aydogdu M. (2005): “Vibration analysis of cross-ply laminated beams with general boundary conditions by Ritz method Original Research Article”. International Journal of Mechanical Sciences, 2005, Vol. 47, No. 11, pp. 1740-1755.

Baeurle S. (2009): “Multiscale modeling of polymer materials using field-theoretic methodologies: A survey about recent developments”. Journal of Mathematical Chemistry, 2009, Vol. 46, No. 2, pp. 363–426.

Benaroya H. and Rehak M. (1988): “Finite element methods in probabilistic structural analysis: A selective review”. Applied Mechanics Reviews, 1988, Vol. 41, No. 5, pp. 201-213.

Bendat J. and Piersol A. (2000): “Random data: Analysis and Measurement Procedures”. John Wiley & Sons, NewYork, pp. 96-99.

Beranek, L. (1971): “Levels,decibels and spectra, in Noise and Vibration Control”, McGraw-Hill.

Breitung K. and Faravelli L. (1996): “Response surface methods and asymptotic approximations, Mathematical Models for Structural Reliability Analysis”. CRC Press, Boca Raton.

Bremner P. (1999): “AUTOSEA 2- A new design evaluation tool for noise and vibration engineering”. ASME Design Technology Conferences, 1999, Las Vegas, Nevada.

Burroughs C., Fischer R., and Kern F. (1997): “An Introduction to Statistical Energy Analysis”. Journal of the Acoustical Society of America, 1997, Vol. 101, No. 4, pp. 1779-1789.

Castillo E., Hadi A., Balakrishnan N., and Sarabia J. (2005): “Extreme-value and Related Models with Applications in Engineering and Science”. Wiley, NewYork.

- Charpentier A., Cotoni V., and Fukui K. (2006): "Using the hybrid FE-SEA method to predict structure-borne noise in a car body-in-white". Proceedings of Internoise 2006, Honolulu, Hawaii.
- Chen N., Glazier J., Izaguirre J., and Alber M. (2007): "A parallel implementation of the Cellular Potts Model for simulation of cell-based morphogenesis". Computer Physics Communications, 2007, Vol. 176, No. 11–12, pp 670-681.
- Clough R. (2003): "Dynamics of structures". 3rd edition, McGraw-Hill.
- Coles S. (2001): "An Introduction to Statistical Modelling of Extreme-Values". Springer, London.
- Cotoni V., Langley R., and Kinder M. (2005): "Numerical and experimental validation of variance prediction in the statistical energy analysis of built-up systems". Journal of Sound and Vibration, 2005, Vol. 288, No. 3, pp. 701-728.
- Cotoni V., Shorter P., and Langley R. (2007): "Numerical and experimental validation of a hybrid finite element-statistical energy analysis method". Journal of the Acoustical Society of America, 2007, Vol. 122, No. 1, pp. 259-270.
- Cotoni V., Gardner B., Carneal J., and Fuller C. (2007): "Modelling methods for vibro-acoustic analysis of commercial Aircrafts". 14th International Congress on Sound and Vibration, Carin, 2007.
- Cremer L., Heckl M., and Petersson B. (1973): "Structure borne sound". Springer-Verlag.
- Crocker M. (1967): "Multimode response of panels to normal and to travelling sonic booms". Journal of Acoustical Society of America, Vol. 42, pp.1070-1079.
- De Gerssem H., Moens D., Desmet W., and Vandepitte D. (2005): "A fuzzy finite element procedure for the calculation of uncertain frequency response functions of damped structures: Part 2—Numerical case studies". Journal of Sound and Vibration, 2005, Vol. 288, No. 3, pp. 463-486.
- Donders S., Vandepitte D., Van de Peer J., and Desmet W. (2005): "Assessment of uncertainty on structural dynamic responses with The Short Transformation method". Journal of Sound and Vibration, 2005, Vol. 288, pp. 523–549.
- Dunne L. and Dunne J. (2009): "An FRF Bounding Method for Randomly Uncertain Structures with or without Coupling to an Acoustic Cavity Journal of Sound and Vibration 2009, Vol. 322 (1-2), pp. 98–134.
- Gorman D. (1999): "Vibration Analysis of Plates by the Superposition Method". World Scientific Publishing Co Pte Ltd.

Guoqing G. and Dunne J. (2010): "Efficient exceedance probability computation for randomly uncertain nonlinear structures with periodic loading". *Journal of Sound and Vibration*, 2011, Vol. 330, pp. 2354–2368.

Hanss M. (2002): "The transformation method for the simulation and analysis of systems with uncertain parameters". *Fuzzy Sets and Systems*, 2002, Vol. 130, No. 3, pp. 277–289.

Hasofer A. (1996): "Non-parametric estimation of failure probabilities". in: Casciati F. and Roberts J. (Eds.), *Mathematical Models for Structural Reliability Analysis*, Mathematical Modelling Series, CRC Press, Boca Raton, pp.195–226.

Ichchou M., Mencik J., and Zhou W. (2009): "Wave finite elements for low and mid-frequency description of coupled structures with damage". *Computer Methods in Applied Mechanics and Engineering*, 2009, Vol. 198, No. 15–16, pp. 1311-1326.

Kreyszig E. (1994): "Advanced engineering mathematics". 7th edition, John Wiley.

Langley R. and Heron K. (1990): "Elastic wave transmission through plate/beam junctions". *Journal of Sound and Vibration*, 1990, Vol 143. pp. 241-253.

Langley R. (1999): "An introduction to statistical energy analysis". ESDU limited.

Langley R. (2000): "The dynamic analysis of uncertain structures (Plenary Paper)". *The Seventh International Conference on Recent Advances in Structural Dynamics*, ISVR, Southampton, 2000.

Langley R. (2000): "Unified approach to probabilistic and possibilistic analysis of uncertain systems". *Journal of Engineering Mechanics*, 2000, Vol. 126, No. 11, pp. 1163-1172.

Langley R. (2004): "Mid and high-frequency vibration analysis of structures with uncertain properties". In: *11th International Congress on Sound and Vibration*, 5-7-2004 to 8-7-2004, St. Petersburg, Russia.

Langley R. and Cotoni V. (2004): "Response variance prediction in the statistical energy analysis of built-up systems". *Journal of the Acoustical Society of America*, Vol 115. pp. 706-718.

Langley R. (2011): "Universal eigenvalue statistics and vibration response prediction". *IUTAM Symposium on the Vibration Analysis of Structures with Uncertainties*, 2011, Volume 27, pp. 115-127.

Langley R., Legault J., Woodhouse J., and Reynders E. (2013): "On the applicability of the lognormal distribution in random dynamical systems". *Journal of Sound and Vibration*, 2013, Vol. 332, pp. 3289-3302.

Le Bot A. and Cotoni V. (2010): "Validity diagrams of statistical energy analysis". *Journal of Sound and Vibration*, 2010, Vol. 329, pp. 221-235.

Lyon R. and Dejong R. (1995): “Theory and Application of Statistical Energy Analysis”. 2nd edition, Butterworth-Heinemann.

Mace B. (2005): “Preface—uncertainty in dynamics”. *Journal of Sound and Vibration*, 2005, Vol. 288, pp. 423–429.

Madsen H., Krenk S., and Lind N. (2006): “Methods of Structural Safety”. Dover Publications.

Manson G. (2005): “Calculating frequency response functions for uncertain systems using complex affine analysis”. *Journal of Sound and Vibration*, 2005, Vol. 288, No. 3, pp. 487–521.

Manohar C. and Ibrahim R. (1999): “Progress in structural dynamics with stochastic parameter variation: 1987-1998”. *Applied Mechanics Reviews*, 1999, Vol. 52, No. 5, pp. 177-197.

Melchers R., Ahammed M., and Middleton C. (2003): “FORM for discontinuous and truncated probability density functions”. *Structural Safety*, 2003, Vol. 25, No. 3, pp. 305–313.

Moeckel C. (2006): “Probabilistic Turbine Blade Thermal Analysis of Manufacturing Variability and Toleranced Designs”. in Department of Aeronautics and Astronautics, Massachusetts Institute of Technology.

Moens D. and Hanss M. (2011): “Non-probabilistic finite element analysis for parametric uncertainty treatment in applied mechanics: Recent advances”. *Finite Elements in Analysis and Design*, 2011, Vol. 47, No. 1, pp. 4–16.

Papanicolaou G. (2011): “The Central Limit Theorem, Law of Large Numbers and Monte Carlo Methods”. Lecture note for Stochastic Methods in Engineering, Stanford University, California.

Pradlwarter H. and Schueller G. (2005): “A Consistent Concept for High and Low Frequency Dynamics Based on Stochastic Modal Analysis”. *Journal of Sound and Vibration*, 2005, Vol. 288, No. 3, pp. 653–667.

Rabbiolo G., Bernhard R., and Milner F. (2004): “Definition of a High-Frequency Threshold for Plates and Acoustical Spaces”. *Journal of Sound and Vibration*, 2004, Vol. 277, pp. 647-667.

Ragnarsson P., Pluymers B., Donders S., and Desmet W. (2010): “Subcomponent modelling of input parameters for statistical energy analysis by using a wave-based boundary condition”. *Journal of Sound and Vibration*, 2010, Vol. 329, pp. 96–108.

Rao S. (2004): “The Finite Element Method in Engineering”. 4th edition, Butterworth-Heinemann.

Ringner B. (2009): “Law of the unconscious statistician”. Unpublished note, Centre for Mathematical Sciences, Lund University, Sweden.

Secgin A., Dunne J., and Zoghaib L. (2012): “Extreme-Value-Based Statistical Bounding of Low, Mid, and High Frequency Responses of a Forced Plate with Random Boundary Conditions”. *Journal of Vibration and Acoustics*, 2012, Vol. 134.

Shorter P. and Langley R. (2005): “Vibro-acoustic analysis of complex systems”. *Journal of Sound and Vibration*, 2005, Vol. 288, pp. 669–699.

Vlasov V. (1949): “Some new problems on shell and thin structures”. National advisory committee for Aeronautics, Naca Tech. Memo No. 1204, 1949.

Xie G., Dunne L., Secgin A., Zoghaib L, and Dunne J. (2012): “Mid-Frequency Modelling of a car floor structure with Hybridge Method and SEA”. *International Symposium on the Computational Modelling and Analysis of Vehicle Body Noise and Vibration*, University of Sussex, UK.

Appendix A

Relationship between Edge Displacements and Edge Tractions

The relationship between edge displacements and edge tractions for the transmission coefficient calculation in Eq. (2.29) in Chapter 2 is derived in detail here.

Substituting Eq. (2.28) into Eq. (2.12):

$$\begin{aligned} S_j &= -D_j[\alpha_{B1}\mu_{B1}^3 - (2 - \nu_j)\alpha_{B1}\mu_{B1}k^2 + \alpha_{B2}\mu_{B2}^3 - (2 - \nu_j)\alpha_{B2}\mu_{B2}k^2] \\ &= D_j[\alpha_{B1}\mu_{B1}^3 + \alpha_{B2}\mu_{B2}^3 - (2 - \nu_j)(\alpha_{B1}\mu_{B1} + \alpha_{B2}\mu_{B2})k^2] \end{aligned} \quad (\text{A.1})$$

Rearranging the first two terms

$$\begin{aligned} &(\alpha_{B1} + \alpha_{B2})(\mu_{B1}^3 + \mu_{B2}^3) - (\alpha_{B1} + \alpha_{B2})(\mu_{B1}^3 + \mu_{B2}^3) + \alpha_{B1}\mu_{B1}^3 + \alpha_{B2}\mu_{B1}^3 \\ &= (\alpha_{B1} + \alpha_{B2})(\mu_{B1}^3 + \mu_{B2}^3) - (\alpha_{B2}\mu_{B1}^3 + \alpha_{B1}\mu_{B2}^3) \end{aligned}$$

Substituting the above back into Eq. (A.1)

$$\begin{aligned} S_j &= -D_j[(\alpha_{B1} + \alpha_{B2})(\mu_{B1}^3 + \mu_{B2}^3) - (\alpha_{B2}\mu_{B1}^3 + \alpha_{B1}\mu_{B2}^3) - (2 - \nu_j)(\alpha_{B1}\mu_{B1} + \alpha_{B2}\mu_{B2})k^2] \\ &= -D_j \frac{(\mu_{B1} - \mu_{B2})}{(\mu_{B1} - \mu_{B2})} [(\alpha_{B1} + \alpha_{B2})(\mu_{B1}^3 + \mu_{B2}^3) - (\alpha_{B2}\mu_{B1}^3 + \alpha_{B1}\mu_{B2}^3) \\ &\quad - (2 - \nu_j)(\alpha_{B1}\mu_{B1} + \alpha_{B2}\mu_{B2})k^2] \\ &= \frac{-D_j}{(\mu_{B1} - \mu_{B2})} [(\alpha_{B1} + \alpha_{B2})(\mu_{B1} - \mu_{B2})(\mu_{B1}^3 + \mu_{B2}^3) - (\mu_{B1} - \mu_{B2})(\alpha_{B2}\mu_{B1}^3 + \alpha_{B1}\mu_{B2}^3) \\ &\quad - (2 - \nu_j)(\mu_{B1} - \mu_{B2})(\alpha_{B1}\mu_{B1} + \alpha_{B2}\mu_{B2})k^2] \\ &= \frac{-D_j}{(\mu_{B1} - \mu_{B2})} [(\alpha_{B1} + \alpha_{B2})(\mu_{B1} - \mu_{B2})(\mu_{B1}^3 + \mu_{B2}^3) \\ &\quad - (\alpha_{B2}\mu_{B1}^4 - \alpha_{B2}\mu_{B2}\mu_{B1}^3 + \alpha_{B1}\mu_{B1}\mu_{B2}^3 - \alpha_{B1}\mu_{B2}^4) - (2 - \nu_j)(\mu_{B1} - \mu_{B2})(\alpha_{B1}\mu_{B1} + \alpha_{B2}\mu_{B2})k^2] \end{aligned} \quad (\text{A.2})$$

Consider the middle term above:

$$\alpha_{B2}\mu_{B1}^4 - \alpha_{B2}\mu_{B2}\mu_{B1}^3 + \alpha_{B1}\mu_{B1}\mu_{B2}^3 - \alpha_{B1}\mu_{B2}^4$$

$$\begin{aligned}
&= (\alpha_{B1} + \alpha_{B2})(\mu_{B1}^4 - \mu_{B2}^4) - (\alpha_{B1} + \alpha_{B2})(\mu_{B1}^4 - \mu_{B2}^4) + \alpha_{B2}\mu_{B1}^4 - \alpha_{B1}\mu_{B2}^4 - \alpha_{B2}\mu_{B2}\mu_{B1}^3 + \alpha_{B1}\mu_{B1}\mu_{B2}^3 \\
&= (\alpha_{B1} + \alpha_{B2})(\mu_{B1}^4 + \mu_{B2}^4) - \alpha_{B1}\mu_{B1}^4 - \alpha_{B2}\mu_{B1}^4 + \alpha_{B1}\mu_{B2}^4 + \alpha_{B2}\mu_{B2}^4 + \alpha_{B2}\mu_{B1}^4 - \alpha_{B1}\mu_{B2}^4 - \alpha_{B2}\mu_{B2}\mu_{B1}^3 \\
&\quad + \alpha_{B1}\mu_{B1}\mu_{B2}^3 \\
&= (\alpha_{B1} + \alpha_{B2})(\mu_{B1}^4 - \mu_{B2}^4) - \alpha_{B1}\mu_{B1}^4 + \alpha_{B2}\mu_{B2}^4 - \alpha_{B2}\mu_{B2}\mu_{B1}^3 + \alpha_{B1}\mu_{B1}\mu_{B2}^3
\end{aligned}$$

Substituting the above back into Eq. (A.2)

$$\begin{aligned}
S_j &= \frac{-D_j}{(\mu_{B1} - \mu_{B2})} [(\alpha_{B1} + \alpha_{B2})(\mu_{B1} - \mu_{B2})(\mu_{B1}^3 + \mu_{B2}^3) - \{(\alpha_{B1} + \alpha_{B2})(\mu_{B1}^4 - \mu_{B2}^4) - \alpha_{B1}\mu_{B1}^4 \\
&\quad + \alpha_{B2}\mu_{B2}^4 - \alpha_{B2}\mu_{B2}\mu_{B1}^3 + \alpha_{B1}\mu_{B1}\mu_{B2}^3\} - (2 - \nu_j)(\mu_{B1} - \mu_{B2})(\alpha_{B1}\mu_{B1} + \alpha_{B2}\mu_{B2})k^2] \\
&= \frac{-D_j}{(\mu_{B1} - \mu_{B2})} [(\alpha_{B1} + \alpha_{B2})(\mu_{B1} - \mu_{B2})(\mu_{B1}^3 + \mu_{B2}^3) - (\alpha_{B1} + \alpha_{B2})(\mu_{B1}^4 - \mu_{B2}^4) + \alpha_{B1}\mu_{B1}^4 \\
&\quad - \alpha_{B2}\mu_{B2}^4 + \alpha_{B2}\mu_{B2}\mu_{B1}^3 - \alpha_{B1}\mu_{B1}\mu_{B2}^3 - (2 - \nu_j)(\mu_{B1} - \mu_{B2})(\alpha_{B1}\mu_{B1} + \alpha_{B2}\mu_{B2})k^2] \\
&= \frac{-D_j}{(\mu_{B1} - \mu_{B2})} [(\alpha_{B1} + \alpha_{B2})\{(\mu_{B1} - \mu_{B2})(\mu_{B1}^3 + \mu_{B2}^3) - (\mu_{B1}^4 - \mu_{B2}^4)\} + \alpha_{B1}\mu_{B1}^4 \\
&\quad - \alpha_{B2}\mu_{B2}^4 + \alpha_{B2}\mu_{B2}\mu_{B1}^3 - \alpha_{B1}\mu_{B1}\mu_{B2}^3 - (2 - \nu_j)(\mu_{B1} - \mu_{B2})(\alpha_{B1}\mu_{B1} + \alpha_{B2}\mu_{B2})k^2] \\
&= \frac{-D_j}{(\mu_{B1} - \mu_{B2})} [(\alpha_{B1} + \alpha_{B2})\{\mu_{B1}^4 - \mu_{B2}\mu_{B1}^3 + \mu_{B1}\mu_{B2}^3 - \mu_{B2}^4 - \mu_{B1}^4 + \mu_{B2}^4\} + (\alpha_{B1}\mu_{B1}^4 \\
&\quad - \alpha_{B2}\mu_{B2}^4 + \alpha_{B2}\mu_{B2}\mu_{B1}^3 - \alpha_{B1}\mu_{B1}\mu_{B2}^3) - (2 - \nu_j)(\mu_{B1} - \mu_{B2})(\alpha_{B1}\mu_{B1} + \alpha_{B2}\mu_{B2})k^2] \\
&= \frac{-D_j}{(\mu_{B1} - \mu_{B2})} [(\alpha_{B1} + \alpha_{B2})(-\mu_{B2}\mu_{B1}^3 + \mu_{B1}\mu_{B2}^3) + (\alpha_{B1}\mu_{B1}^4 - \alpha_{B2}\mu_{B2}^4 + \alpha_{B2}\mu_{B2}\mu_{B1}^3 \\
&\quad - \alpha_{B1}\mu_{B1}\mu_{B2}^3) - (2 - \nu_j)(\mu_{B1} - \mu_{B2})(\alpha_{B1}\mu_{B1} + \alpha_{B2}\mu_{B2})k^2] \tag{A.3}
\end{aligned}$$

The last two terms above can be rearranged as

$$\begin{aligned}
&(\alpha_{B1}\mu_{B1}^4 - \alpha_{B2}\mu_{B2}^4 + \alpha_{B2}\mu_{B2}\mu_{B1}^3 - \alpha_{B1}\mu_{B1}\mu_{B2}^3) - (2 - \nu_j)(\mu_{B1} - \mu_{B2})(\alpha_{B1}\mu_{B1} + \alpha_{B2}\mu_{B2})k^2 \\
&= (\alpha_{B1}\mu_{B1} + \alpha_{B2}\mu_{B2}) \left[\frac{(\alpha_{B1}\mu_{B1}^4 - \alpha_{B2}\mu_{B2}^4 + \alpha_{B2}\mu_{B2}\mu_{B1}^3 - \alpha_{B1}\mu_{B1}\mu_{B2}^3)}{(\alpha_{B1}\mu_{B1} + \alpha_{B2}\mu_{B2})} - (2 - \nu_j)(\mu_{B1} - \mu_{B2})k^2 \right]
\end{aligned}$$

Rewriting the numerator above:

$$\alpha_{B1}\mu_{B1}^4 - \alpha_{B2}\mu_{B2}^4 + \alpha_{B2}\mu_{B2}\mu_{B1}^3 - \alpha_{B1}\mu_{B1}\mu_{B2}^3 = -(\alpha_{B1}\mu_{B1} + \alpha_{B2}\mu_{B2})(\mu_{B1}^3 - \mu_{B2}^3)$$

Substituting back into Eq. (A.3)

$$\begin{aligned}
S_j &= \frac{-D_j}{(\mu_{B1} - \mu_{B2})} [(\alpha_{B1} + \alpha_{B2})(-\mu_{B2}\mu_{B1}^3 + \mu_{B1}\mu_{B2}^3) \\
&\quad + (\alpha_{B1}\mu_{B1} + \alpha_{B2}\mu_{B2})[-(\mu_{B1}^3 - \mu_{B2}^3) - (2 - \nu_j)(\mu_{B1} - \mu_{B2})k^2] \\
&= \frac{D_j}{(\mu_{B1} - \mu_{B2})} [(\alpha_{B1} + \alpha_{B2})(\mu_{B2}\mu_{B1}^3 - \mu_{B1}\mu_{B2}^3) \\
&\quad + (\alpha_{B1}\mu_{B1} + \alpha_{B2}\mu_{B2})[(\mu_{B1}^3 - \mu_{B2}^3) + (2 - \nu_j)(\mu_{B1} - \mu_{B2})k^2] \\
&= \frac{D_j}{(\mu_{B1} - \mu_{B2})} [\mu_{B2}\mu_{B1}^3 - \mu_{B1}\mu_{B2}^3 \quad (\mu_{B1}^3 - \mu_{B2}^3) + (2 - \nu_j)(\mu_{B1} - \mu_{B2})k^2] \begin{pmatrix} \alpha_{B1} + \alpha_{B2} \\ \alpha_{B1}\mu_{B1} + \alpha_{B2}\mu_{B2} \end{pmatrix} \\
&= \frac{D_j}{(\mu_{B1} - \mu_{B2})} [\mu_{B2}\mu_{B1}^3 - \mu_{B1}\mu_{B2}^3 \quad (\mu_{B1}^3 - \mu_{B2}^3) + (2 - \nu_j)(\mu_{B1} - \mu_{B2})k^2] \begin{pmatrix} 1 & 1 \\ \mu_{B1} & \mu_{B2} \end{pmatrix} \begin{pmatrix} \alpha_{B1} \\ \alpha_{B2} \end{pmatrix}
\end{aligned}$$

The traction S_j can then be written as follows:

$$S_j = \frac{D_j}{(\mu_{B1} - \mu_{B2})} [\mu_{B2}\mu_{B1}^3 - \mu_{B1}\mu_{B2}^3 \quad (\mu_{B1}^3 - \mu_{B2}^3) + (2 - \nu_j)(\mu_{B1} - \mu_{B2})k^2] \begin{pmatrix} w_{ej} \\ \theta_{ej} \end{pmatrix} \quad (\text{A.4})$$

For the traction M_j , substituting Eq. (2.28) into Eq. (2.11) yields:

$$\begin{aligned}
M_j &= D_j [\alpha_{B1}\mu_{B1}^2 + \alpha_{B2}\mu_{B2}^2 - \nu_j k^2 (\alpha_{B1} + \alpha_{B2})] \\
&= \frac{D_j}{(\mu_{B1} - \mu_{B2})} [(\mu_{B1} - \mu_{B2})(\alpha_{B1}\mu_{B1}^2 + \alpha_{B2}\mu_{B2}^2) - \nu_j (\mu_{B1} - \mu_{B2})k^2 (\alpha_{B1} + \alpha_{B2})] \\
&= \frac{D_j}{(\mu_{B1} - \mu_{B2})} [(\mu_{B1} - \mu_{B2})(\alpha_{B1}\mu_{B1}^2 + \alpha_{B2}\mu_{B2}^2) \\
&\quad + (\alpha_{B1} + \alpha_{B2})\{(2 - \nu_j)(\mu_{B1} - \mu_{B2})k^2 - 2(\mu_{B1} - \mu_{B2})k^2\}] \quad (\text{A.5})
\end{aligned}$$

Expanding the term $(\mu_{B1} - \mu_{B2})(\alpha_{B1}\mu_{B1}^2 + \alpha_{B2}\mu_{B2}^2)$ and rearranging

$$\begin{aligned}
&(\mu_{B1} - \mu_{B2})(\alpha_{B1}\mu_{B1}^2 + \alpha_{B2}\mu_{B2}^2) \\
&= \alpha_{B1}\mu_{B1}^3 - \alpha_{B2}\mu_{B2}^3 - \alpha_{B1}\mu_{B2}\mu_{B1}^2 + \alpha_{B2}\mu_{B1}\mu_{B2}^2 + (\alpha_{B1}\mu_{B1} + \alpha_{B2}\mu_{B2})(\mu_{B1}^2 - \mu_{B2}^2) \\
&\quad - (\alpha_{B1}\mu_{B1} + \alpha_{B2}\mu_{B2})(\mu_{B1}^2 - \mu_{B2}^2) \\
&= \alpha_{B1}\mu_{B1}^3 - \alpha_{B2}\mu_{B2}^3 - \alpha_{B1}\mu_{B2}\mu_{B1}^2 + \alpha_{B2}\mu_{B1}\mu_{B2}^2 + (\alpha_{B1}\mu_{B1} + \alpha_{B2}\mu_{B2})(\mu_{B1}^2 - \mu_{B2}^2) \\
&\quad - (\alpha_{B1}\mu_{B1}^3 - \alpha_{B2}\mu_{B2}^3 - \alpha_{B1}\mu_{B1}\mu_{B2}^2 + \alpha_{B2}\mu_{B2}\mu_{B1}^2) \\
&= \alpha_{B1}\mu_{B1}^3 - \alpha_{B2}\mu_{B2}^3 - \alpha_{B1}\mu_{B2}\mu_{B1}^2 + \alpha_{B2}\mu_{B1}\mu_{B2}^2 + (\alpha_{B1}\mu_{B1} + \alpha_{B2}\mu_{B2})(\mu_{B1}^2 - \mu_{B2}^2) \\
&\quad - \alpha_{B1}\mu_{B1}^3 + \alpha_{B2}\mu_{B2}^3 + \alpha_{B1}\mu_{B1}\mu_{B2}^2 - \alpha_{B2}\mu_{B2}\mu_{B1}^2 \\
&= (\alpha_{B1}\mu_{B1} + \alpha_{B2}\mu_{B2})(\mu_{B1}^2 - \mu_{B2}^2) - \alpha_{B1}\mu_{B2}\mu_{B1}^2 + \alpha_{B2}\mu_{B1}\mu_{B2}^2 + \alpha_{B1}\mu_{B1}\mu_{B2}^2 - \alpha_{B2}\mu_{B2}\mu_{B1}^2
\end{aligned}$$

$$\begin{aligned}
&= (\alpha_{B1}\mu_{B1} + \alpha_{B2}\mu_{B2})(\mu_{B1}^2 - \mu_{B2}^2) + (\alpha_{B1} + \alpha_{B2})\mu_{B1}\mu_{B2}^2 - (\alpha_{B1} + \alpha_{B2})\mu_{B2}\mu_{B1}^2 \\
&= (\alpha_{B1}\mu_{B1} + \alpha_{B2}\mu_{B2})(\mu_{B1}^2 - \mu_{B2}^2) + (\alpha_{B1} + \alpha_{B2})(\mu_{B1}\mu_{B2}^2 - \mu_{B2}\mu_{B1}^2) \\
&= (\alpha_{B1}\mu_{B1} + \alpha_{B2}\mu_{B2})(\mu_{B1}^2 - \mu_{B2}^2) + (\alpha_{B1} + \alpha_{B2})(\mu_{B1}\mu_{B2}^2 - \mu_{B2}\mu_{B1}^2)
\end{aligned} \tag{A.6}$$

Consider the term $\mu_{B1}\mu_{B2}^2 + \mu_{B2}\mu_{B1}^2$:

$$\begin{aligned}
&\mu_{B1}\mu_{B2}^2 + \mu_{B2}\mu_{B1}^2 \\
&= \mu_{B1}\mu_{B2}^2 - \mu_{B2}\mu_{B1}^2 + (\mu_{B1} - \mu_{B2})(\mu_{B2}^2 + \mu_{B1}^2) - (\mu_{B1} - \mu_{B2})(\mu_{B2}^2 + \mu_{B1}^2) \\
&= (\mu_{B1} - \mu_{B2})(\mu_{B2}^2 + \mu_{B1}^2) - \mu_{B1}\mu_{B2}^2 + \mu_{B2}\mu_{B1}^2 + \mu_{B2}^3 - \mu_{B1}^3 + \mu_{B1}\mu_{B2}^2 - \mu_{B2}\mu_{B1}^2 \\
&= (\mu_{B1} - \mu_{B2})(\mu_{B2}^2 + \mu_{B1}^2) + \mu_{B2}^3 - \mu_{B1}^3
\end{aligned}$$

Substituting the above back into Eq. (A.6):

$$\begin{aligned}
&(\mu_{B1} - \mu_{B2})(\alpha_{B1}\mu_{B1}^2 + \alpha_{B2}\mu_{B2}^2) \\
&= (\alpha_{B1}\mu_{B1} + \alpha_{B2}\mu_{B2})(\mu_{B1}^2 - \mu_{B2}^2) + (\alpha_{B1} + \alpha_{B2})\{(\mu_{B1} - \mu_{B2})(\mu_{B2}^2 + \mu_{B1}^2) + \mu_{B2}^3 - \mu_{B1}^3\}
\end{aligned}$$

Substituting the above back into Eq. (A.5):

$$\begin{aligned}
M_j &= \frac{D_j}{(\mu_{B1} - \mu_{B2})} [(\alpha_{B1}\mu_{B1} + \alpha_{B2}\mu_{B2})(\mu_{B1}^2 - \mu_{B2}^2) \\
&\quad + (\alpha_{B1} + \alpha_{B2})\{(\mu_{B1} - \mu_{B2})(\mu_{B2}^2 + \mu_{B1}^2) + \mu_{B2}^3 - \mu_{B1}^3\} \\
&\quad + (\alpha_{B1} + \alpha_{B2})\{(2 - \nu_j)(\mu_{B1} - \mu_{B2})k^2 - 2(\mu_{B1} - \mu_{B2})k^2\}] \\
&= \frac{D_j}{(\mu_{B1} - \mu_{B2})} [(\alpha_{B1}\mu_{B1} + \alpha_{B2}\mu_{B2})(\mu_{B1}^2 - \mu_{B2}^2) \\
&\quad + (\alpha_{B1} + \alpha_{B2})\{(\mu_{B1} - \mu_{B2})(\mu_{B2}^2 + \mu_{B1}^2) + \mu_{B2}^3 - \mu_{B1}^3 \\
&\quad + (2 - \nu_j)(\mu_{B1} - \mu_{B2})k^2 - 2(\mu_{B1} - \mu_{B2})k^2\}] \\
&= \frac{D_j}{(\mu_{B1} - \mu_{B2})} [(\alpha_{B1}\mu_{B1} + \alpha_{B2}\mu_{B2})(\mu_{B1}^2 - \mu_{B2}^2) \\
&\quad + (\alpha_{B1} + \alpha_{B2})\{(\mu_{B1} - \mu_{B2})(\mu_{B2}^2 + \mu_{B1}^2) + \mu_{B2}^3 - \mu_{B1}^3 \\
&\quad + (2 - \nu_j)(\mu_{B1} - \mu_{B2})k^2 - 2(\mu_{B1} - \mu_{B2})k^2\}] \\
&= \frac{D_j}{(\mu_{B1} - \mu_{B2})} [(\alpha_{B1}\mu_{B1} + \alpha_{B2}\mu_{B2})(\mu_{B1}^2 - \mu_{B2}^2) + (\alpha_{B1} + \alpha_{B2})\{\mu_{B2}^3 - \mu_{B1}^3 + (2 - \nu_j)(\mu_{B1} - \mu_{B2})k^2 \\
&\quad + (\mu_{B1} - \mu_{B2})(\mu_{B2}^2 + \mu_{B1}^2 - 2k^2)\}]
\end{aligned}$$

because $\mu_{B2}^2 + \mu_{B1}^2 - 2k^2 = k^2 - k_B^2 + k^2 + k_B^2 - 2k^2 = 0$;

$$M_j = \frac{D_j}{(\mu_{B1} - \mu_{B2})} [(\alpha_{B1}\mu_{B1} + \alpha_{B2}\mu_{B2})(\mu_{B1}^2 - \mu_{B2}^2) \\ + (\alpha_{B1} + \alpha_{B2})\{\mu_{B2}^3 - \mu_{B1}^3 + (2 - \nu_j)(\mu_{B1} - \mu_{B2})k^2\}]$$

$$M_j = \frac{D_j}{(\mu_{B1} - \mu_{B2})} (\mu_{B2}^3 - \mu_{B1}^3 + (2 - \nu_j)(\mu_{B1} - \mu_{B2})k^2) \frac{\mu_{B1}^2 - \mu_{B2}^2}{(\alpha_{B1}\mu_{B1} + \alpha_{B2}\mu_{B2})} \left(\frac{\alpha_{B1} + \alpha_{B2}}{\alpha_{B1}\mu_{B1} + \alpha_{B2}\mu_{B2}} \right)$$

$$M_j = \frac{D_j}{(\mu_{B1} - \mu_{B2})} (\mu_{B2}^3 - \mu_{B1}^3 + (2 - \nu_j)(\mu_{B1} - \mu_{B2})k^2) \frac{\mu_{B1}^2 - \mu_{B2}^2}{(\theta_{ej})} \left(\frac{W_{ej}}{\theta_{ej}} \right)$$

The traction M_j can then be written as follows:

$$M_j = \frac{D_j}{(\mu_{B1} - \mu_{B2})} (\mu_{B2}^3 - \mu_{B1}^3 + (2 - \nu_j)(\mu_{B1} - \mu_{B2})k^2) \frac{\mu_{B1}^2 - \mu_{B2}^2}{(\theta_{ej})} \left(\frac{W_{ej}}{\theta_{ej}} \right) \quad (\text{A.7})$$

Appendix B

Relationship between the parameter a and the CV

The relationship between parameter a (the half width of the uniform distribution) and CV in Eq. (6.4) can be described as follows.

The variance of x can be written as

$$\sigma_x^2 = E[X^2] - E[X]^2 \quad (\text{B.1})$$

where

$$E[X]^2 = \mu_x^2$$

When $f_X(x)$ is a uniform distribution, $E[X^2]$ can be computed as follows:

$$\begin{aligned} E[X^2] &= \int_{\mu_x-a}^{\mu_x+a} x^2 f_X(x) dx = \int_{\mu_x-a}^{\mu_x+a} x^2 \left(\frac{1}{2a}\right) dx \\ &= \frac{1}{2a} \frac{x^3}{3} \Big|_{\mu_x-a}^{\mu_x+a} = \frac{1}{2a} \left(\frac{2}{3}a^3 + 2a\mu_x^2\right) \\ E[X^2] &= \frac{a^2}{3} + \mu_x^2 \end{aligned} \quad (\text{B.2})$$

Substituting Eq. (B.2) into Eq. (B.1) yields

$$\begin{aligned} \sigma_x^2 &= E[X^2] - E[X]^2 \\ &= \frac{a^2}{3} + \mu_x^2 - \mu_x^2 = \frac{a^2}{3} \end{aligned}$$

$$a = \sqrt{3}\sigma_x$$

because $CV = \sigma_x/\mu_x$;

$$a = \sqrt{3}\mu_x CV \quad (\text{B.3})$$